Evaluating Vadose Zone Moisture Dynamics using Ground-Penetrating Radar

by

Colby Michael Steelman

A thesis
presented to the University of Waterloo
in fulfillment of the
thesis requirement for the degree of
Doctor of Philosophy
in
Earth Sciences

Waterloo, Ontario, Canada, 2012

Author's Declaration

I hereby declare that I am the sole author of this thesis. This is a true copy of the thesis, including any required final revisions, as accepted by my examiners.

I understand that my thesis may be made electronically available to the public.

Colby Steelman

Abstract

Near-surface sediments in the vadose zone play a fundamental role in the hydrologic system. The shallow vadose zone can act as a buffer to delay or attenuate surface contaminants before they reach the water table. It also acts as a temporary soil moisture reservoir for plant and atmospheric uptake, and regulates the seasonal groundwater recharge process. Over the past few decades, geophysical methods have received unprecedented attention as an effective vadose zone characterization tool offering a range of non-invasive to minimally invasive techniques with the capacity to provide detailed soil moisture information at depths typically unattainable using conventional point-measurement sensors. Ground-penetrating radar (GPR) has received much of this attention due to its high sensitivity to the liquid water phase in geologic media. While much has been learned about GPR soil moisture monitoring and characterization techniques, it has not been evaluated across highly dynamic natural soil conditions. Consequently, GPR's capacity to characterize a complete range of naturally occurring vadose zone conditions including wetting/drying and freeze/thaw cycles, is not yet fully understood. Further, the nature of GPR response during highly dynamic moisture periods has not been thoroughly investigated.

The objective of this thesis is to examine the capacity of various surface GPR techniques and methodologies for the characterization of soil moisture dynamics in the upper few meters of vadose zone, and to develop measurement strategies capable of providing quantitative information about the current and future state of the shallow hydrologic system. To achieve this, an exhaustive soil moisture monitoring campaign employing a range of GPR antenna frequencies and survey acquisition geometries was initiated at three different agricultural field sites located in southern Ontario, Canada, between May 2006 and October 2008. This thesis represents the first attempt to evaluate multiple annual cycles of soil conditions and associated hydrological processes using high-frequency GPR measurements. Summaries of the seven major works embodied in this thesis are provided below.

Direct ground wave (DGW) measurements obtained with GPR have been used in a number of previous studies to monitor volumetric water content changes in the root zone; however, these studies have involved controlled field experiments or measurements collected across limited ranges in soil moisture. To further investigate the capacity of the DGW method, multi-frequency (i.e., 225 MHz, 450 MHz and 900 MHz) common-midpoint (CMP) measurements were used to monitor a complete annual cycle of soil water content variations at three sites with different soil textures (i.e., sand, sandy loam and silt loam). CMP surveys permitted characterization of the nature and evolution of the near-surface electromagnetic wavefields, and their subsequent impact on DGW velocity measurements. GPR results showed significant temporal variations in both the near-surface wavefield and multi-frequency DGW velocities corresponding to both seasonal and shorter term variations in soil conditions. While all of the measurement sites displayed similar temporal responses, the rate and magnitude of these velocity variations corresponded to varying soil water contents which were primarily controlled by the soil textural properties. Overall, the DGW measurements obtained using

higher frequency antennas were less impacted by near-surface wavefield interference due to their shorter signal pulse duration.

The estimation of soil water content using GPR velocity requires an appropriate petrophysical relationship between the dielectric permittivity and volumetric water content of the soil. The ability of various empirical relationships, volumetric mixing formulae and effective medium approximations were evaluated to predict near-surface volumetric soil water content using high-frequency DGW velocity measurements obtained from CMP soundings. Measurements were collected using 225, 450 and 900 MHz antennas across sand, sandy loam and silt loam soil textures over a complete annual cycle of soil conditions. A lack of frequency dependence in the results indicated that frequency dispersion had minimal impact on the data set. However, the accuracy of soil water content predictions obtained from the various relationships ranged considerably. The best fitting relationships did exhibit some degree of textural bias that should be considered in the choice of petrophysical relationship for a given data set. Further improvements in water content estimates were obtained using a field calibrated third-order polynomial relationship and three-phase volumetric mixing formula.

While DGW measurements provide valuable information within the root zone, the characterization of vertical moisture distribution and dynamics requires a different approach. A common approach utilizes normal-moveout (NMO) velocity analysis of CMP sounding data. To further examine this approach, an extensive field study using multi-frequency (i.e., 225 MHz, 450 MHz, 900 MHz) CMP soundings was conducted to monitor a complete annual cycle of vertical soil moisture conditions at the sand, sandy loam and silt loam sites. The use of NMO velocity analysis was examined for monitoring highly dynamic vertical soil moisture conditions consisting of wetting/drying and freeze/thaw cycles with varying degrees of magnitude and vertical velocity gradient. NMO velocity analysis was used to construct interval-velocity-depth models at a fixed location collected every 1 to 4 weeks. Time-lapse models were combined to construct temporal interval-velocity fields, which were converted into soil moisture content. These moisture fields were used to characterize the vertical distribution, and dynamics of soil moisture in the upper few meters of vadose zone. Although the use of multiple antenna frequencies provided varying investigation depths and vertical resolving capabilities, optimal characterization of soil moisture conditions was obtained with 900 MHz antennas. The integration of DGW and NMO velocity data from a single CMP sounding could be used to assess the nature of shallow soil moisture coupling with underlying vadose zone conditions; however, a more quantitative analyses of the surface moisture dynamics would require definitive knowledge of GPR sampling depth.

Although surface techniques have been used by a number of previous researchers to characterize soil moisture content in the vadose zone, limited temporal sampling and low resolution near the surface in these studies impeded the quantitative analysis of vertical soil moisture distribution and its associated dynamics within the shallow subsurface. To further examine the capacity of surface GPR, an extensive 26 month field study was undertaken using concurrent high-frequency (i.e., 900 MHz) reflection profiling and CMP soundings to quantitatively monitor soil moisture distribution and

dynamics within a sandy vadose zone environment. An analysis on the concurrent use of reflection and CMP measurements was conducted over two contrasting annual cycles of soil conditions. Reflection profiles provided high resolution traveltime data between four stratigraphic reflection events while cumulative results of the CMP sounding data set produced precise depth estimates for those reflecting interfaces, which were used to convert interval traveltime data into soil water content estimates. The downward propagation of episodic infiltration events associated with seasonal and transient conditions were well resolved by the GPR data. The GPR data also revealed variations in the nature of these infiltration events between contrasting annual cycles. The use of CMP soundings also permitted the determination of DGW velocities, which enabled better characterization of short-duration wetting/drying and freezing/thawing processes. This higher resolution information can be used to examine the nature of the coupling between shallow and deep moisture conditions.

High-resolution surface GPR measurements were used to examine vertical soil moisture distribution and its associated dynamics within the shallow subsurface over a 26 month period. While the apparent ability of surface GPR methods to give high quality estimates of soil moisture distribution in the upper 3 meters of the vadose zone was demonstrated, the nature of these GPR-derived moisture data needed to be assessed in the context of other hydrological information. As a result, GPR soil moisture estimates were compared with predictions obtained from a well-accepted hydrological modeling package, HYDRUS-1D (Simunek et al., 2008). The nature of transient infiltration pulses, evapotranspiration episodes, and deep drainage patterns were examined by comparing them with vertical soil moisture flow simulations. Using laboratory derived soil hydraulic property information from soil samples and a number of simplifying assumptions about the system, very good agreement was achieved between measured and simulated soil moisture conditions without model calibration. The overall good agreement observed between forward simulations and field measurements over the vertical profile validated the capacity of surface GPR to provide detailed information about hydraulic state conditions in the upper few meters of vadose zone.

A unique DGW propagation phenomenon was observed during early soil frost formation. High-frequency DGW measurements were used to monitor the seasonal development of a thin, high velocity frozen soil layer over a wet low velocity unfrozen substratum. During the freezing process, the progressive attenuation of a low velocity DGW and the subsequent development of a high velocity DGW were observed. Numerical simulations using GPRMAX2D (Giannopoulos, 2005) showed that low velocity DGW occurring after freezing commenced was due to energy leaking across the frozen layer from the spherical body wave in the unfrozen half space. This leaky phase progressively dissipated until the frozen layer reached a thickness equivalent to one quarter of the dominant wavelength in the frozen ground. The appearance of the high velocity DGW was governed by its destructive interference with the reflection events from the base of the frozen layer. This interference obscured the high velocity DGW until the frozen layer thickness reached one half of the dominant wavelength in the frozen ground.

While GPR has been extensively used to study frozen soil conditions in alpine environments, its capacity to characterize highly dynamic shallow freeze-thaw processes typically observed in temperate environments is not well understood. High-frequency reflection profiles and CMP soundings were used to monitor the freezing and thawing process during the winter seasonal period at the sand and silt loam sites. Reflection profiles revealed the long-term development of a very shallow (<0.5 m) soil frost zone overlying unfrozen wet substratum. During the course of the winter season, long-term traveltime analysis yielded physical properties of the frozen and unfrozen layers as well as the spatial distribution of the base of the soil frost zone. Short-term shallow thawing events overlying frozen substratum formed a dispersive waveguide for both the CMP and reflection profile surveys. Inversion of the dispersive wavefields for the CMP data yielded physical property estimates for the thawed and frozen soils and thawed layer thickness. It was shown that GPR can be used to monitor very shallow freezing and thawing events by responding to changes in the relative dielectric permittivity of the soil water phase.

The works embodied in this thesis demonstrate the effectiveness of high-frequency GPR as a non-invasive soil moisture monitoring tool under a full range of naturally occurring moisture conditions with the temporal and vertical resolution necessary to quantitatively examine shallow vadose zone moisture dynamics. Because this study encompassed an unprecedented range of naturally occurring soil conditions, including numerous short and long duration wetting/drying and freezing/thawing cycles, complex geophysical responses were observed during highly dynamic soil moisture processes. Analysis and interpretation of these geophysical responses yielded both qualitative and quantitative information about the state of the hydrologic system, and hence, provided a non-invasive means of characterizing soil moisture processes in shallow vadose zone environments. In the future, these GPR soil moisture monitoring strategies should be incorporated into advanced land-surface hydrological modeling studies to improve our understanding of shallow hydrologic systems and its impacts on groundwater resources.

Acknowledgements

This work was supported by a Post Graduate Scholarship (PGS-M and PGS-D) and an Individual Discovery Grant by the Natural Sciences and Engineering Research Council of Canada (NSERC) as well as a President's Graduate Scholarship from the University of Waterloo.

I can honestly say that I did not know what I was getting myself into when I accepted this challenge. It was not an easy road but I am grateful to have taken it. One of the things I enjoyed most was all the people I met along the way, many of which contributed in one way or another to this work. For that I thank you!

First and foremost, I have to thank my supervisor, Dr. Anthony L. Endres, without whom I would not have been able to accomplish what I did during my time at Waterloo. There are no words to describe Tony's level of commitment and dedication to his students. Tony is as an outstanding scientist, an inspirational role model, and a wonderful friend. I am forever indebted to you Tony.

I would like to thank my committee members, Dr. A. Peter Annan, Dr. Walter A. Illman, and Dr. Garry W. Parkin for their contributions and guidance over the years, and the time they invested in me. It was a privilege and honor to have you at my side along the way. I would also like to thank Dr. Jan van der Kruk and Dr. Jon Paul Jones for their specific contributions to this work, as well as my internal-external examiner Dr. Richard E.J. Kelley and my external-external examiner Dr. Andrew Binley.

This work would not have happened without the contribution of two wonderful people, Alicia and Murray Smith, who provided me with a field site near Waterloo, Ontario. This research would not have happened without you. Thank you for your hospitality.

As I think back, I am truly amazed at the thought of those who contributed to this work, either in the field collecting data, working on auxiliary projects, or simply listening to my frustrations. Starting from the beginning, I would like to thank Dr. Dave Rudolph and Dr. Brewster Conant Jr. for giving me the initial opportunity as a co-op student to work with them at the Woodstock site. I would like to thank Scott Piggott, Melissa Bunn, Cameron McNaughton, John Mosquera, Jon Rigg, Ryan Ruthart, Adam Ramer, Daniel Sponagle, Monica Pal, Anisa Kassam, Shaun Dempsey, Mojtaba Nilu, Richard Simms, Cameron Toy, and Lee Zhi for all their contributions.

Finally, I would like to thank my parents, Michael and Maria Steelman and my wonderful wife Alisha for their continued support. I couldn't have done it without you

Dedication

To my wife Alisha.

Table of Contents

List of Figures

List of Tables

Chapter 1
Introduction

1.1 Background

Soil moisture plays a crucial role in our understanding of hydrological, ecohydrological and biogeochemical processes (e.g., Vereecken et al., 2008). Regional and global spatial soil moisture distribution in the vadose zone, i.e., geologic media between land surface and the regional water table (Figure 1.1), is an important parameter in weather and climate predictions as it controls the exchange and partitioning of water and energy fluxes across the land surface (Seneviratne et al., 2010). Regional watershed scale information plays a critical role in water resource and ecohydrological management strategies (e.g., Robinson et al., 2008). Practitioners concerned with making predictions of fluid and contaminant transport from the surface to the regional groundwater system rely on effective characterization and monitoring strategies within vadose zone environments (Stephens, 1996). At the field-scale, soil moisture is important to precision agriculturalists; for instance, optimum crop yield and quality is achieved through appropriate irrigation management practices which rely on continuous high-resolution temporal and spatial moisture information (Robinson et al., 2008). Since a comprehensive understanding of soil moisture dynamics in the vadose zone is of utmost importance to the sustainable management of our water resources, and production and longevity of our crops, novel measurement strategies facilitating the attainment of soil moisture information will continue to play a fundamental role in future management practices of our water and food resources.

As soil scientists, hydrologists, ecologists and agronomists rely more and more on soil moisture measurements, a wide range of sensors and measurement methodologies are being developed to achieve the spatial and temporal resolution necessary to address the problems at hand (Robinson et al., 2008). Figure 1.2 summarizes some of the available measurement techniques and their spatial support scales. Spatial soil moisture distribution over regional and global scales is primarily achieved using space-borne sensors (e.g., Wagner et al., 2007) which are capable of producing high-resolution spatial and temporal soil moisture maps. However, the low depth of investigation achieved by remote sensing has restricted its usefulness in characterizing vadose zone hydrological processes. Hydrologists and soil scientists examining deeper vadose zone processes have historically relied on thermogravimetric and thermal neutron probes; however, these methods are highly invasive and are becoming more difficult and costly to implement. Technological advances over the past few decades

have resulted in the development of robust ground-based electromagnetic sensors such as time-domain reflectometry (TDR) and capacitance probes. The development of a wide range of petrophysical relationships between soil electrical properties and volumetric water content has enabled thes0e methods to become the standard for in-situ soil moisture measurements. While these two methods have the capacity to provide accurate soil moisture information with unprecedented temporal sampling, they are generally invasive and require permanent installation which makes them less suitable for field-scale spatial investigations. Although some innovative designs for mounting TDR and capacitive sensors to mobile platforms have been proposed (e.g., Wraith et al., 2005), sampling depths are significantly reduced which limits their usefulness for deeper vadose zone studies.

Alternatively, geophysical methods offer a range of non-invasive to minimally invasive techniques with the capacity to provide spatial soil moisture information at depths typically unattainable using conventional point-measurement sensors. These geophysical methods measure ground electrical conductivity, such as DC resistivity (e.g., Samouelian et al., 2005) and electromagnetic induction (e.g., Sheets and Hendrickx, 1995), or electromagnetic wave propagation velocity such as ground-penetrating radar (GPR) (e.g., Huisman et al., 2003a). GPR has received unprecedented attention over the last decade as a viable high-resolution soil moisture sensor for vadose zone environments. This system employs high-frequency electromagnetic waves (i.e., similar to TDR) that respond primarily to the bulk dielectric permittivity of the medium. As the permittivity of liquid water is much larger than other geologic constituents, the device is highly suited for measuring volumetric water content. Technological advances in GPR antenna performance and signal processing have furthered the tools capacity to image highly dynamic spatial and temporal hydrologic processes over a range of depth scales. GPR systems are typically available in three configurations: (i) air-launched units operating at some distance above the ground surface providing surface moisture conditions, (ii) those designed for cross-borehole applications, and (iii) surface-based systems used primarily for spatial subsurface mapping. Surface-based GPR systems are particularly suitable for vadose zone studies because of their mobility and robust ability to measure from sub-meter to tens of meters or more into the subsurface depending on soil conditions and antenna frequency (e.g., Davis and Annan, 1989; Neal, 2004; Annan, 2005; Jol, 2009).

Employing GPR with the intent of obtaining high-resolution spatial and temporal soil moisture information may require different survey methodologies depending on the desired depth of

investigation, lateral resolution and site conditions. While a variety of survey methods have been shown to provide detailed soil moisture information (e.g., Huisman et al., 2003a), researchers have not yet fully explored the robustness of this geophysical method under a full range of naturally occurring moisture conditions with the temporal and vertical resolution necessary to examine the dynamics associated with shallow vadose zone hydrologic processes. Consequently, GPR's capacity to characterize a complete range of naturally occurring vadose zone conditions is not yet fully understood. Past studies using surface GPR in unsaturated environments have been focused on (1) laboratory flow experiments (e.g., Loeffler and Bano, 2004; Grote et al., 2010b; Moysey, 2010); (2) plot-scale monitoring of controlled irrigation and infiltration fronts (e.g., Galagedara et al., 2003; Galagedara et al., 2005a; Cassiani et al., 2009; Wijewardana and Galagedara, 2010, Haarder et al., 2011); (3) measurement of lateral and vertical soil moisture fields with limited resolution (e.g., Greaves et al., 1996; Hubbard et al., 2002; Huisman et al., 2002; Grote et al., 2003; Turesson, 2005; Weihermüller et al., 2007; Gerhards et al., 2008; Grote et al., 2010a); (4) time-lapse monitoring of natural moisture changes with limited spatial or temporal sampling (e.g., van Overmeeren et al., 1997; Lunt et al., 2005; Grote et al., 2005; Wollschläger and Roth, 2005).

1.2 Objectives

The main objective of this thesis is to examine the capacity of surface GPR for the characterization of highly dynamic soil moisture processes while developing novel measurement strategies that provide valuable hydrological information about the vadose zone. To achieve this objective, a long-term soil moisture monitoring campaign employing a range of GPR antenna frequencies (i.e., 225, 450 and 900 MHz) and survey acquisition geometries (i.e., common-midpoint and reflection profiles) was initiated at three different agricultural field sites. The geophysical investigations presented in this thesis were conducted over variable periods between May 2006 and October 2008. A detailed description of the field sites is provided in Appendix A. The study period encompassed a wide range of naturally occurring soil conditions including numerous short and long duration wetting/drying and freezing/thawing cycles. As a result, unique geophysical responses were observed during highly dynamic soil moisture processes; interpretation of these responses yielded valuable information about the state of the shallow hydrologic system.

The specific objectives of this thesis revolve around the applied methodologies, observed geophysical responses and the hydrologic information obtained from GPR measurements. The specific objectives are to:

- evaluate the use of multi-frequency GPR direct ground wave (DGW) measurements to monitor soil moisture variations over a complete annual cycle of soil conditions (i.e., natural wetting/drying and freeze/thaw cycles);
- compare various petrophysical relationships between bulk dielectric permittivity and volumetric water content in terms of their ability to estimate soil moisture using multi-frequency DGW measurements;
- assess the use of multi-frequency CMP soundings for monitoring vertical soil moisture dynamics and the nature of the coupling between the soil moisture profile and surface conditions;
- examine the use of high-frequency GPR reflection traveltime measurements for monitoring vertical soil moisture distribution and migration over multiple annual cycles in the shallow vadose zone, and further examine of the coupling between the soil moisture profile and surface conditions;
- assess the capacity of surface GPR to monitory highly dynamic vadose zone processes and examine the nature of the soil moisture patterns observed in GPR reflection traveltime data series using a one-dimensional variably saturated flow model;
- investigate the observed DGW response during the development of a thin frozen soil layer during early wintertime conditions;
- evaluate the use of high-frequency GPR measurements for monitoring highly dynamic freeze-thaw cycles and associated hydraulic processes.

1.3 Thesis Organization

This thesis is organized in 9 chapters, including 7 core chapters [Chapters 2–8] written as independent research papers. Each core chapter includes the necessary background information so that they can be read independently of the thesis document. Finally, the main contributions of this thesis and recommendations for future work are summarized in Chapter 9.

While GPR has been proven to be an effective non-invasive soil moisture tool capable of providing hydrologic information from the vadose zone, it has not been exhaustively tested over a wide range of natural soil conditions. The majority of existing research has focused on the DGW method as a soil

moisture measurement technique in shallow root zone environments; however, there has been very limited analysis of this method over a wide range of natural soil conditions and textural environments. To address this, Chapter 2 presents a multi-frequency DGW velocity monitoring study conducted at three agricultural field sites characterized by different soil textures over a complete annual cycle of soil conditions. The goal of this chapter is to effectively demonstrate the capabilities and limitations of CMP-derived DGW soil moisture measurements under natural conditions.

Although numerous petrophysical relationships are available in the literature to convert bulk dielectric permittivity into volumetric water content, many of these relationships were developed using other dielectric sensors or under controlled laboratory conditions; consequently, their suitability for GPR measurements is not well known. Chapter 3 compares the performance of various petrophysical relationships for estimating volumetric water content using the DGW velocity measurements and gravimetrically-derived volumetric water content data presented in Chapter 2. A wide range of empirical, volumetric mixing formulae and effective medium approximations are considered. The goal of this chapter is to provide some insight into the relative performance of commonly applied petrophysical relationships to GPR measurements.

A comprehensive understanding of vadose zone hydrologic conditions requires both surface and vertical moisture information to examine the nature of the coupling between soil moisture profile and surface conditions. While previous studies have demonstrated the application of GPR for the characterization of spatial soil moisture distribution in the vadose zone, they lack the temporal component necessary to critically examine vertical moisture dynamics. To address this, Chapter 4 examines the application of multi-frequency CMP soundings for monitoring vertical soil moisture conditions at three field sites over an annual cycle of soil conditions; Chapter 5 builds upon this by examining the use of higher resolution reflection traveltime and CMP sounding measurements for monitoring vertical soil moisture distribution and migration over multiple annual cycles. In Chapter 6, a 1-D variably saturated numerical flow model is used to assess the capacity of surface GPR to monitor highly dynamic vadose zone processes and examine the nature of the observed GPR soil moisture data series presented in Chapter 5. These three chapters show GPR's capacity to provide qualitative and quantitative hydrological information across a range of depth scales in the upper vadose zone.

Wintertime periods in temperate climates significantly impact seasonal hydrologic processes. The development of a seasonal frost zone can affect the timing and magnitude of annual recharge

(Johnsson and Lundin, 1991; Nyberg et al., 2001; Bayard et al., 2005), and can also play an important role in soil functioning (Henry, 2007). GPR can provide valuable information during highly dynamic freeze and thaw cycles, thereby improving our understanding of seasonal hydrologic conditions. Chapter 7 presents a numerical evaluation of a DGW response observed during early frost development, while Chapter 8 examines novel GPR field-observations of dynamic freeze and thaw processes during the winter periods. The goal of these two chapters is to establish the capacity of high-frequency GPR for the characterization of highly dynamic and hydrologically relevant wintertime conditions.

Although each chapter was independently developed and written by the author under the direct supervision of Dr. Anthony L. Endres, some chapters did receive additional collaboration from other authors as indicated below. As a result, the terms "we", "us" and "our" are occasionally used to describe the works embodied in this thesis. In addition, many of the chapters have been published or submitted to peer-reviewed journals; as a result, they may have received some revision based on the comments of two or three anonymous reviewers.

1.4 Contributions to Research and Development

This thesis contains 9 major contributions to research and development that have been published or submitted for publication in peer-reviewed international journals. The details of each contribution, including all collaborative authors and original copyright material is provided below:

1. **Chapter 2:** Steelman, C.M., and Endres, A.L. (2010). An examination of direct ground wave soil moisture monitoring over an annual cycle of soil conditions. *Water Resources Research, 46*, W11533, doi:10.1029/2009WR008815.
2. **Chapter 3:** Steelman, C.M., and Endres, A.L. (2011). Comparison of petrophysical relationships for soil moisture estimation using GPR ground waves. *Vadose Zone Journal, 10*, 1–16, doi:10.2136/vzj2010.0040.
3. **Chapter 4:** Steelman, C.M., and Endres, A.L. Assessing vertical soil moisture dynamics using multi-frequency GPR common-midpoint soundings. *Journal of Hydrology,* doi: 10.1016/j.jhydrol.2012.02.041 (accepted 21/02/2012).
4. **Chapter 5:** Steelman, C.M., and Endres, A.L. (in review). High-resolution GPR monitoring of soil moisture dynamics 1. Field results and interpretation. Submitted to *Water Resources Research,* 16/09/2011.

5. **Chapter 6:** Steelman, C.M., Jones, J.P., and Endres, A.L. (in review). High-resolution GPR monitoring of soil moisture dynamics 2. Comparison with unsaturated flow model. Submitted to *Water Resources Research*, 16/09/2011.

6. **Chapter 7:** Steelman, C.M., and Endres, A.L. (2009). Evolution of high-frequency ground-penetrating radar direct ground wave during thin frozen soil layer development. *Cold Regions Science Technology*, *57*, 116–122, doi:10.1016/j.coldregions.2009.01.007. ©2009 Elsevier B.V. Reproduced/modified by permission of Elsevier B.V.

7. **Chapter 8:** Steelman, C.M., Endres, A.L., and van der Kruk, J. (2010). Field observations of freeze and thaw processes using high-frequency ground penetrating radar. *Hydrological Processes*, *24*, 2022–2033, doi:10.1002/hyp.7688. ©2010 John Wiley & Sons, Inc. Reproduced/modified by permission of John Wiley & Sons, Inc.

8. **Appendix B:** van der Kruk, J., Steelman, C.M., Endres, A.L., and Vereecken, H. (2009). Dispersion inversion of electromagnetic pulse propagation within freezing and thawing soil waveguides. *Geophysical Research Letters*, *36*, L18503, doi:10.1029/2009GL039581. ©2009 American Geophysical Union. Reproduced/modified by permission of American Geophysical Union.

9. **Supplementary:** Hamann, G., Tronicke, J., Steelman, C.M., and Endres, A.L. Spectral velocity analysis for determination of ground wave velocities and their uncertainties in multi-offset GPR data. *Near-Surface Geophysics* (accepted 30/11/2011).

In addition, portions of this thesis have been published in peer-reviewed conference proceedings. The details of each proceedings paper, including all collaborative authors, are provided below:

1. Steelman, C.M., and Endres, A.L. (2011). Vertical soil moisture dynamics in the vadose zone: a high resolution GPR reflection study. In *Proceedings of the 6th International Workshop on Advanced Ground Penetrating Radar*, Aachen, Germany.

2. Steelman, C.M., and Endres, A.L. (2010). Inference of soil water flux using high-frequency GPR reflection traveltime and NMO velocity analysis. In *Proceedings of the 13th International Conference on Ground Penetrating Radar*, Lecce, Italy, 2010.

3. Steelman, C.M., Endres, A.L. and van der Kruk, J. (2009). Field observations of shallow freeze and thaw processes using high-frequency ground-penetrating radar. In *Proceedings of the 66th Annual Meeting of the Eastern Snow Conference*, Niagara on the Lake, Ontario, Canada.

4. van der Kruk, J., Steelman, C.M., and Endres, A.L. (2009). Dispersion inversion of GPR data recorded across freezing and thawing induced waveguides. In *Proceedings of the 5th International Workshop on Advanced Ground Penetrating Radar*, Granada, Spain.

5. Steelman, C.M., and Endres A.L. (2008). Monitoring seasonal variations in soil water content using multiple high-frequency GPR direct ground waves. In *Proceedings of the 12th International Conference on Ground Penetrating Radar*, Birmingham, United Kingdom.
6. Steelman, C.M., and Endres, A.L. (2008). Monitoring seasonal variations in soil moisture profile using high-frequency velocity and reflection traveltime analysis. In *Proceedings of the 12th International Conference on Ground Penetrating Radar*, Birmingham, United Kingdom.
7. Steelman, C.M., and Endres, A.L. (2007). Monitoring temporal soil moisture variations using multi-frequency ground penetrating radar under natural field conditions. In *Proceedings of the 60th Canadian Geotechnical Conference/8th Joint IAH and CGS Groundwater Conference*, Canadian Geotechnical Society/International Association of Hydrogeologists–Canadian National Chapter, Ottawa, 499 – 506.

Finally, various components of this thesis have been presented at regional, national and international conferences. A list of abstract presentations, including all collaborative authors, is provided below:

1. Endres, A.L., Steelman, C.M., Jones, J.P., Busch S., and J. van der Kruk. Evaluating soil moisture dynamics using High Frequency Ground-Penetrating Radar. American Geophysical Union International Fall Meeting, 5th – 9th December 2011, San Francisco, USA.
2. van der Kruk, J., Bakker, J.G., Bikowski, J., Steelman, C.M., Endres, A.L., and H. Vereecken. Multi-layer inversion of freezing induced dispersive ground penetrating radar data, European Geoscience Union General Assembly, 3rd – 8th April 2011, Vienna, Austria
3. Steelman, C.M., and A.L. Endres. Monitoring Vertical Soil Moisture Dynamics using GPR Reflection Traveltimes. Symposium on the Application of Geophysics to Environmental and Engineering Problems (SAGEEP), 10th – 14th April 2011, Charleston, USA.
4. Steelman, C.M., and A.L. Endres. Evaluating Soil Moisture Dynamics using Time-Lapse GPR Velocity Analysis. Canadian Geophysical Union – Hydrology Section, Eastern Regional Student Conference, 4th December 2010, Guelph, Canada.
5. Steelman, C.M., and A.L. Endres. High-Resolution Investigation of Vertical Soil Moisture Distribution and Migration using Ground-Penetrating Radar Reflection Traveltime Signals. Association Hydrogéophysique Québec 2010, September 2010, Montreal, Canada.
6. Steelman, C.M., and A.L. Endres. Evaluating seasonal soil water dynamics using high-frequency ground penetrating radar. 3rd Joint Canadian Meteorological and Oceanographic

Society (CMOS) – Canadian Geophysical Union (CGU) Congress, 31st May – 4th June 2010, Ottawa, Canada.

7. van der Kruk, J., Jacob, R., Steelman, C.M., Endres, A.L., and H. Vereecken. Identifying dispersive GPR signals and inverting for surface waveguide properties. EGU2010-13969, European Geosciences Union General Assembly 2010, 2nd – 7th May 2010, Vienna, Austria.

8. Steelman, C.M., and A.L. Endres. Monitoring of temporal variations in shallow soil water content using multi-frequency GPR common-midpoint soundings. American Geophysical Union Joint Assembly – Hydrogeophysics: The State of the Science, 24th – 27th May 2009, Toronto, Canada.

9. van der Kruk, J., Jacob, R.W., Steelman, C.M., Endres, A.L., and H. Vereecken. Inversion of dispersive GPR data recorded across precipitation and thawing induced waveguides. American Geophysical Union Joint Assembly – Hydrogeophysics: The State of the Science, 24th – 27th May 2009, Toronto, Canada.

10. van der Kruk, J., Steelman, C.M., Endres, A.L., and H. Vereecken. Dispersion inversion of GPR data recorded across freezing and thawing induced waveguides. 69. Jahrestagung der Deutschen Geophysikalischen Gesellschaft, 23rd – 26th March 2009, Kiel, Germany.

11. van der Kruk, J., Steelman, C.M., and A.L. Endres. Inversion of dispersive GPR data recorded across freezing and thawing induced waveguides. American Geophysical Union International Fall Meeting, 15th – 19th December 2008, San Francisco, USA.

12. Steelman, C.M., and A.L. Endres. Evaluating near-surface soil water content variations and seasonal infiltration using high frequency ground penetrating radar. American Geophysical Union International Fall Meeting, 15th – 19th December 2008, San Francisco, USA.

13. Steelman, C.M., and A.L. Endres. The effect of petrophysical relationship on water content estimates from GPR direct wave data. Joint International Annual Meeting GAC-MAC-SEG-SGA, 26th – 28th May 2008, Quebec City, Canada.

14. Steelman, C.M., and A.L. Endres. Monitoring soil freeze-thaw process using high frequency ground penetrating radar. Canadian Geophysical Union – Hydrology Section, Eastern Regional Student Conference, 7th – 8th December 2007, Waterloo, Canada.

15. Steelman, C.M., and A.L. Endres. Monitoring shallow freeze and thaw processes using high frequency surface ground penetrating radar. American Geophysical Union International Fall Meeting, 10th – 14th December 2007, San Francisco, USA.

1.5 Tables and Figures

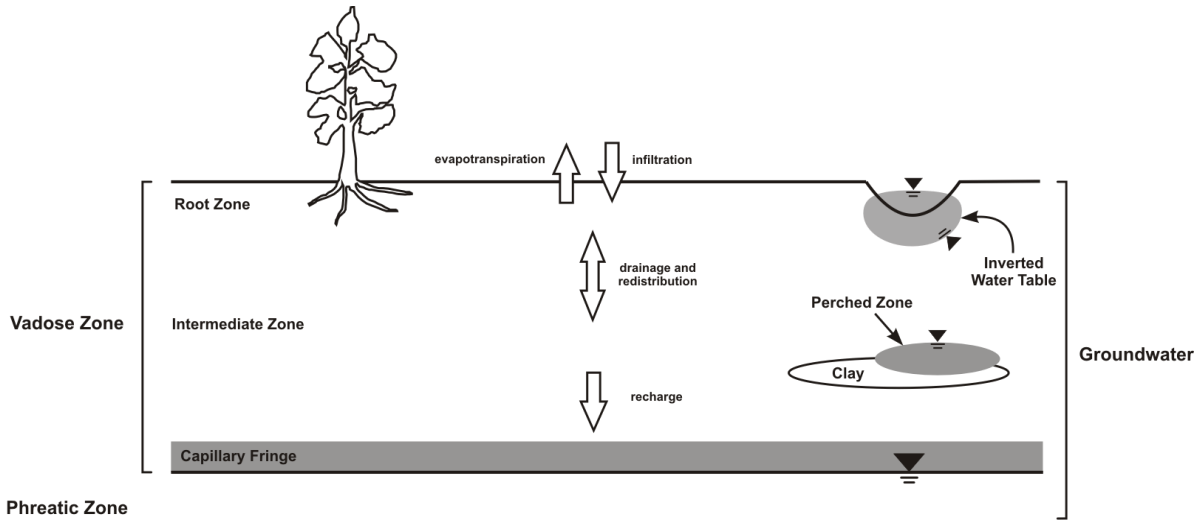

Figure 1.1 The vadose zone lies below the land surface and above the regional water table and is primarily composed of unsaturated material. Water pressure within most of the vadose zone is less than atmospheric pressure, although some areas of complete saturation and positive fluid pressure may occur (e.g., within the capillary fringe or above an isolated low permeable layer). Flow properties are dependent upon the degree of saturation in the pore space. Figure/caption modified from Stephens (1996).

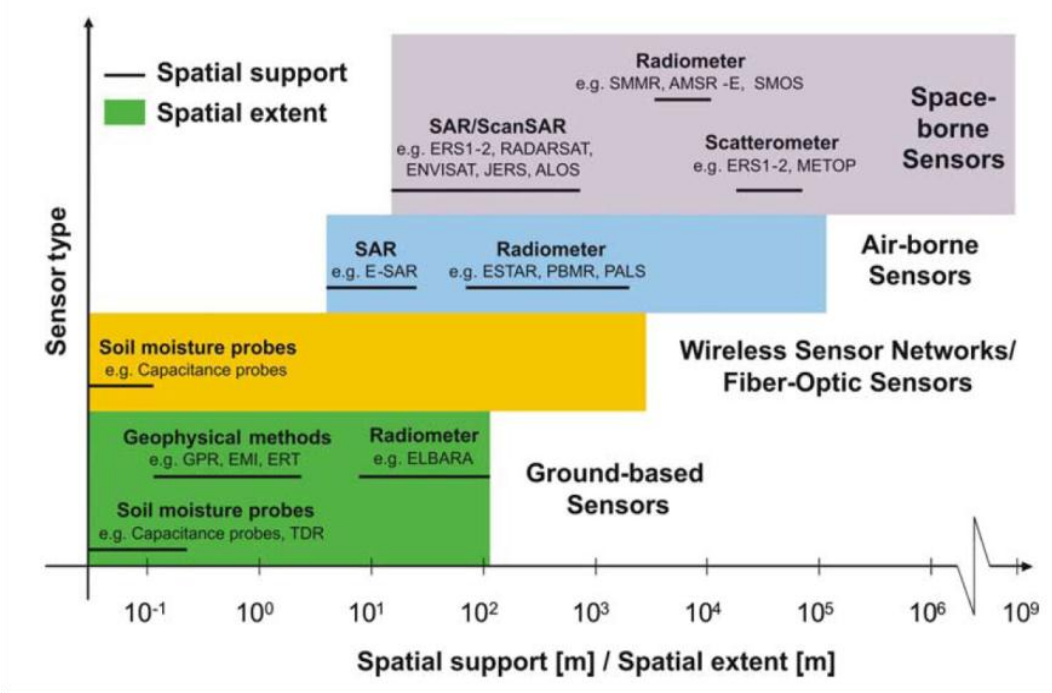

Figure 1.2 Support scale of soil moisture observations or measurements obtained from ground-based sensors (GPR, ground penetrating radar; TDR, time domain reflectometry; EMI, electromagnetic induction; ELBARA, L band radiometer), wireless sensor networks, airborne sensors (SAR, synthetic aperture radar; E-SAR, experimental airborne SAR; ESTAR, electronically scanned thinned aperture radiometer; PBMR, L band push broom microwave radiometer; PALS, passive and active L/S band sensor), and spaceborne sensors (ALOS, Advanced Land Observing Satellite; AMSR-E, Advanced Microwave Scanning Radiometer; ENVISAT, Environmental Satellite; ERS1–2, European Remote Sensing Satellite 1–2; JERS, Japanese Environmental Remote Sensing; SMOS, Soil Moisture and Ocean Salinity Satellite; SMMR, Scanning Multichannel Microwave); from Vereecken et al. (2008).

Chapter 2
An Examination of Direct Ground Wave Soil Moisture Monitoring Over an Annual Cycle of Soil Conditions[1]

2.1 Executive Summary

Direct ground wave (DGW) measurements obtained with ground-penetrating radar have been used in a number of previous studies to estimate volumetric water content in the shallow soil zone; however, these studies have generally involved controlled field experiments or measurements collected across limited natural ranges of soil moisture conditions. To further investigate the capacity of this method, we have undertaken an extensive field study using multi-frequency (i.e., 225 MHz, 450 MHz and 900 MHz) DGW measurements to monitor a complete annual cycle of soil water content variations typical of mid-latitude climates at three sites with different soil textures. The use of common-midpoint (CMP) surveys allowed us to understand the nature and evolution of the near-surface electromagnetic wavefields and their impact on DGW moisture predictions. We present the novel characterization of a wide-range of seasonal moisture dynamics including soil freezing and thawing process using multi-frequency DGW measurements for a range of soil textures. These data showed significant temporal variations in both the near-surface wavefield and multi-frequency DGW velocities corresponding to both seasonal and shorter term variations in soil conditions. While all of the measurement sites displayed similar temporal responses, the rate and magnitude of these velocity variations corresponded to varying soil water contents which were controlled by the soil textural properties. While there were no observed systematic differences in DGW velocities due to frequency dispersion for the 225–900 MHz range, the DGW measurements obtained using higher frequency antennas was less impacted by near-surface wavefield interference due to their shorter signal pulse duration. DGW velocity measurements combined with an appropriate dielectric mixing formula provided quantitative predictions of soil water content that accurately replicated the soil sample data over the annual cycle of moisture conditions.

[1] Steelman, C.M., and Endres, A.L. (2010). An examination of direct ground wave soil moisture monitoring over an annual cycle of soil conditions. *Water Resources Research, 46*, W11533, doi:10.1029/2009WR008815.

2.2 Introduction

The measurement of soil water content is important for the prediction of hydrological state variables (e.g., soil moisture fields, soil water storage), soil parameters (e.g., relative hydraulic conductivity, residual saturation) and hydraulic fluxes (e.g., evapotranspiration, infiltration, groundwater recharge) at the field and catchment scale. Soil moisture also governs microbial activity which is important for a range of biochemical processes. Numerous studies have demonstrated the value of soil moisture data and associated measurement techniques to the characterization of vadose zone hydrology; recent reviews on these topics have been published by Vereecken et al. (2008) and Robinson et al. (2008). Measurement of soil water content is also important for the characterization of soil freeze and thaw processes (Luo et al., 2003), which is vital to studies examining overland flow potential (Nyberg et al., 2001), melt water recharge (Bayard et al., 2005; Iwata et al., 2010) and soil thermal conductivity, as well as for the evaluation of soil functioning (e.g., soil physical properties, microorganisms, carbon and nutrient dynamics); a review of the effects of freeze-thaw processes on soil functioning has been published by Henry (2007). Therefore, techniques that can provide accurate information of soil water content conditions are extremely important for understanding vadose zone hydrology.

Commonly used techniques to measure soil water content such as time-domain reflectometry (TDR), gravimetric sampling, capacitive sensors and thermal neutron probes are effective tools; however, these methods can be invasive and may not be suitable for spatial investigations. Ground-penetrating radar (GPR) is a non-invasive geophysical technique capable of monitoring and quantifying shallow soil water content (Huisman et al., 2003a). Direct ground wave (DGW) GPR techniques utilize waves that propagate along the air-ground interface; hence, they are highly suited for soil water content monitoring in shallow root zone environments.

The DGW technique is well suited for field-scale soil water content measurements due to its larger sampling volume (i.e., dm^3) relative to conventional TDR sensors (i.e., cm^3) (e.g., van Overmeeren et al., 1997; Hubbard et al., 2002; Huisman et al., 2002; Grote et al., 2003; Huisman et al., 2003b; Weihermüller et al., 2007). The larger sampling volume and non-invasive nature of DGW techniques make them less prone to measurement errors associated with macropores (e.g., root and worm holes) and air gaps along sensors compared to TDR (Robinson et al., 2003). Further, the availability of a wide-range of GPR antenna frequencies (e.g., 50–1000 MHz) permits the measurement of different soil depth ranges (i.e., measurement volumes) in the near-surface.

However, the research involving DGW soil water content monitoring to date has been limited to controlled irrigation experiments (e.g., Huisman et al., 2002; Galagedara et al., 2005a), minimal natural variations in soil water content (e.g., Weihermüller et al., 2007), minor variations in soil texture (e.g., Hubbard et al., 2002), or measurements collected at large temporal intervals (e.g., van Overmeeren et al., 1997). Given the potential impact of soil water content conditions and soil texture on the DGW method, there is a need for an examination of this method conducted across a wide range of seasonal soil water contents and differing soil textural conditions to develop an improved understanding of DGW capabilities and limitations under natural field environments.

To address these issues, an extensive field study was initiated to investigate the use of multi-frequency (i.e., 225 MHz, 450 MHz and 900 MHz) DGW measurements for monitoring a complete annual cycle of soil water content variations (i.e., dry summer, wet spring and autumn, frozen winter soil conditions) typical of mid-latitude climates at sites with three different soil textures (i.e. sand, sandy loam and silt loam). The common-midpoint (CMP) method was used so that the complexity of the near-surface wavefield during DGW measurements (i.e., wavefield interference mechanisms) could be examined. The impact of long and short time scale soil water content changes on both the near-surface wavefield and measured DGW velocities is examined. Using gravimetric soil moisture data that were concurrently collected with a number of GPR surveys, we assess the capacity of the DGW method to provide quantitative estimates of soil water content over the annual cycle of soil conditions.

2.3 Elements of the DGW Method

The DGW method uses a transmitting antenna positioned along the ground surface (i.e., air-ground interface) which radiates short pulses of electromagnetic (EM) waves commonly in the bandwidth between 10 MHz and 1 GHz. These propagating EM fields respond to changes in subsurface electrical properties. Figure 2.1 illustrates the various wavefronts associated with the transmission of a point source (S) on the earth's surface that propagates spherical waves upward into the air (A) and downward into the earth (B). The spherical wave in the air gives rise to a lateral head wave in the ground (C), while the spherical ground wave gives rise to the evanescent wave in the air (D) which is present due to the boundary conditions that enforce continuity of the horizontal electric field (Annan, 1973). The DGW is an interfacial wave represented by a combination of the spherical wave in the ground and the evanescent wave in the air that propagates along the air-ground interface between a transmitting and receiving antennae.

The near-surface EM wavefield becomes more complicated when heterogeneity, such as layering, is presented within the earth, giving rise to the generation of additional events. The use of multi-offset CMP soundings that systematically separate a transmitting and receiving antenna about a central fixed point produces a data set that can result in a distinct separation of the wavefields. Figure 2.2 shows a schematic diagram (Figure 2.2a) and a representative CMP data set (Figure 2.2b) illustrating the direct air wave and DGW, critically refracted air and ground waves, and reflected ground waves. It should be noted that refracted ground waves occur when a higher permittivity (i.e., lower EM wave velocity) layer is underlain by lower permittivity (i.e., higher EM wave velocity) material (Bohidar and Hermance, 2002). The DGW possesses a linear traveltime-offset relationship such that the inverse of its slope is equal to its velocity. The simplicity of a linear relationship (i.e., simple identification of the wavefield and straightforward linear curve-fitting procedure) permits determination of EM wave velocity in near-surface environments.

An important aspect of DGW techniques for soil water content measurements is its effective sampling depth (Huisman et al., 2001; Hubbard et al., 2002; Grote et al., 2003; Galagedara et al., 2005a). Due to the unguided nature of this EM wave, it is difficult to quantify the soil volume influencing DGW propagation. Nevertheless, a number of studies have attempted to empirically define the effective DGW sampling depth (e.g., Du, 1996; Sperl, 1999; Galagedara et al., 2005b). Alternatively, van Overmeeren et al. (1997) adapted the theoretical relationship based on seismic wave propagation principles (Hagedoorn, 1954) for DGW propagation. This relationship proposes that the DGW sampling depth (d) is equal to half the Fresnel zone:

$$d = \frac{1}{2}\sqrt{\frac{vS}{f}}, \tag{2.1}$$

where v is the measured velocity of the DGW, S is the transmitter-receiver antenna separation distance and f is the central frequency of the DGW signal. This relationship indicates that DGW sampling depth increases with decreasing soil permittivity (e.g., dry soils) and dominant central frequency (i.e., lower antenna frequencies); DGW sampling depth is also dependent on antenna separation distance. However, researchers have not reached a consensus for a functional relationship between DGW propagation and effective sampling depth.

Neglecting the effects of magnetic permeability and electrical conductivity, the propagation velocity (v) of EM waves in a medium within GPR bandwidth is determined from its relative

dielectric permittivity (κ) (i.e., the effective permittivity ε of the bulk material relative to the free space permittivity ε_o) using the equation

$$v = \frac{c}{\sqrt{\kappa}}, \tag{2.2}$$

where c is the EM velocity in free space (0.2998 m/ns). Within this bandwidth, the permittivity of liquid water (κ_w = 78–88) contrasts strongly with other common components of the soil system (i.e., mineral soil grains κ_s = 4–6 and air κ_a = 1), as well as ice (κ_i = 3.2) (Cassidy, 2009); hence, providing the basis for estimating volumetric water content using EM wave velocity measurements.

The estimation of soil water content from EM velocity requires an appropriate petrophysical relationship to convert the bulk permittivity κ of the material into an accurate volumetric water content θ measurement. Volumetric mixing formulae are a type of commonly used petrophysical relationships that relates the permittivity of the bulk material to the dielectric properties of the individual components within the system through their volume fractions. Geological material is typically considered a three phase system (e.g., Roth et al., 1990) composed of air, solids and water that can be expressed as

$$\theta = \frac{\kappa^{\alpha} - (1-\phi)\kappa_s^{\alpha} - \phi\kappa_a^{\alpha}}{\kappa_w^{\alpha} - \kappa_a^{\alpha}}, \tag{2.3}$$

where ϕ represents soil porosity, while κ_a, κ_s and κ_w represent the permittivities of the air, solid mineral and water constituents, respectively. The geometric fitting parameter, α, theoretically ranges between -1 and 1 for electric fields which are oriented perpendicular and parallel to a layered medium. If it is assumed that the traveltime through the mixture is equivalent to the sum of the volume weighted traveltimes through the individual components, the geometric factor is equal to 0.5; and Equation (2.3) becomes the well-known Complex Refractive Index Model (CRIM) (Birchak et al., 1974; Wharton et al., 1980; Dobson et al., 1985; Heimovaara et al., 1994). However, it has been found that α for partially saturated soils can range between 0.25–0.8 (Brovelli and Cassiani, 2008 and references therein). As a result, we have elected to use site calibrated α values based on our gravimetrically measured soil water contents rather than the general CRIM relationship.

2.4 Experimental Description

2.4.1 Field Sites

Soil water content variations were monitored at three active agricultural field sites; each site is characterized by a different soil texture: sand, sandy loam and silt loam soils. Both the sand (528878E, 4814702N) and sandy loam (528938E, 4814594N) soil sites are 3 km west of Waterloo, Ontario, Canada, while the silt loam soil site (519845E, 4770361N) is 2 km south of Woodstock, Ontario, Canada. While haying operations were conducted during the study period, other agricultural disturbances, such as plowing and tilling, were not performed at these sites during or in the recent past (i.e., within the preceding 2–5 years) prior to this study.

Average soil characteristics were determined from a single sample at each site extracted using a 3/4 inch diameter soil sampling probe in the upper half meter positioned approximately 1.0 m adjacent to the midpoint of each GPR survey line. Soil samples were extracted over 0.1 m depth intervals; analyses included hydrometer and dry sieve for grain size distribution, as well as the loss-on-ignition method (Dean, 1974) to estimate percentage of organics. Dry soil bulk densities were estimated in the upper 0.2 m by extracting a known volume of soil using small aluminum cylinders and measuring their mass after they were oven dried at 105˚C for 24 hours; relative uncertainties in bulk density estimates were inferred from repeat samples (e.g., 2–4 cores) that were collected 1–2 m adjacent to the midpoint of the GPR lines. Dry bulk densities were used to estimate soil porosities by assuming an average grain density of 2.65 g/cm^3. A detailed summary of the soil properties are provided in Table 2.1.

The Waterloo sites are located on the Waterloo moraine, which is characterized as an irregular tract of gently rolling to hummocky terrain with some exposures of ice-contact stratified sand and gravel deposits (Russell et al., 2007). The two soil water content monitoring sites at this location were separated by ~125 m laterally and ~7 m vertically with the sand site on a topographic high and the sandy loam site in a topographic low. Shallow core logs collected at the Waterloo sites showed that the sand site is characterized by a sequence of stratified sand deposits, while the sandy loam site grades downward into loamy sand below a depth of 0.4–0.5 m. The water table at the Waterloo site is believed to be 10–15 m below ground surface based on nearby springs. Precipitation and atmospheric temperature for the Waterloo sites were monitored using the University of Waterloo weather station located approximately 7 km east of the study sites.

The Woodstock silt loam site is situated in a localized valley described as a glaciofluvial outwash channel (Cowan, 1975); it is located 45 km southwest of the Waterloo sites. A nearby core log shows that this monitoring location is characterized by approximately 0.5–0.7 m of silt loam grading downward into a silty gravel with sand. The water table varies seasonally between 2–3 m below ground surface based on water level data collected in the vicinity of the study area. Precipitation and atmospheric temperature was monitored using an on-site meteorological station located approximately 0.5 km west of the GPR monitoring site.

2.4.2 Data Acquisition and Analysis

CMP surveys were conducted along a fixed survey line at each of the three sites using a Sensors and Software PulseEKKO™ 1000 (Sensors and Software Inc., Mississauga, Ontario, Canada) GPR system equipped with three sets of high-frequency, bistatic antennae (i.e., 225 MHz, 450 MHz and 900 MHz). A total of 304 individual CMP data sets were collected between May 2006 and November 2007 at intervals ranging from two days to four weeks. A summary of the CMP surveys performed at each site is provided in Table 2.2. When time constraints limited data acquisition at the sand and sandy loam sites, higher frequency soundings (e.g., 450 MHz and 900 MHz) were preferentially performed due to their better signal resolution in the near-surface. We have included these data sets in this paper to improve the temporal resolution of the DGW phenomena.

Field conditions during the wintertime period (i.e., January–March 2007) were characterized by variable snow pack thicknesses which were removed prior to CMP data collection. While the sand and silt loam sites were characterized by relatively thin snow packs (up to ~0.3 m), the sandy loam site was frequented by deep snow packs (up to ~1.0 m). To maintain natural field conditions (i.e., minimize effects of altering overlying snow pack) the removed snow was placed back over the survey lines after completing the CMP soundings whenever possible.

The GPR data were collected using a time window of 100 ns, sampling interval of 0.1 ns and 64 stacks per trace. Transmitter and receiver antennas were manually separated at 0.02 m increments during the CMP surveys and remained stationary during the recording time. Data acquisition was done with a manual trigger. The GPR surveys were collected using standard antenna offset ranges of 0.3–3.0 m, 0.2–2.5 m and 0.2–2.0 m for the 225 MHz, 450 MHz and 900 MHz antennas, respectively. These GPR data were processed using Sensors and Software's Ekko View Deluxe™ software program. All data sets were dewowed using the software's default time windows to remove low-

frequency signal saturation arising from the radar equipment. While the DGW was clearly visible in the radar sections, additional signal processing was applied to improve the quality of later arriving events that approached the first arrivals at wider antenna offsets. Hence, bandpass frequency filtering using cut-off frequency sets were applied to the 225 MHz, 450 MHz and 900 MHz data, respectively: 25–125–475–550 MHz, 100–150–800–1000 MHz and 100–200–1100–1400 MHz, respectively. Finally, a spreading and exponential compensation gain was used to compensate for spherical spreading and exponential losses. A fixed set of gain parameters were applied to all of the data collected at the sand (i.e., start value = 1, attenuation = 0.4, gain max = 100), sandy loam (i.e., start value = 1, attenuation = 0.6, gain max = 100) and silt loam (i.e., start value = 1, attenuation = 1.0, gain max = 100).

Traveltime-offset measurements used to determine the DGW velocity values were obtained using Sensors and Software's Picker™ software program. The wavelet of the DGW events were composed of an initial peak (i.e., positive first half-cycle) followed by a trough (i.e., negative second half-cycle) and subsequent positive peak. Due to increased distortion along the leading edge of the first half-cycle as a result of wavefield interferences (e.g., direct and refracted air waves), the zero-value between the first and second half-cycle was used to determination DGW velocity; these arrivals were manually picked by the user along the standard antenna offset ranges. The identification of zero-amplitude value at the cross-over point was a more objective criteria then trying to identify the maximum or minimum peak values along the wavelet phase. For instance, peak values were sometimes smeared across a range of times particularly when the peaks flattened out as a result of wavefield superposition. A least squares linear analysis was applied to these traveltime-offset data points to obtain an estimate and standard error for the DGW velocity derived from the slope of the best fitting line. A manual (i.e., user defined) curve-fitting routine was used to delineate which offset range yielded a linear traveltime-offset relationship. This procedure ensured that only optimal portions of the standard offset range were used to determine DGW velocity.

2.4.3 Gravimetric Soil Sampling

Soil samples were concurrently collected over the upper 0.5 m of soil at 0.1 m depth intervals in the proximity (i.e., 1–2 m) of each GPR survey location for a substantial subset of CMP surveys (i.e., bracketed values in Table 2.2) to obtain field estimates of soil moisture for comparison with the GPR results. Sampling was performed using a standard 3/4 inch diameter soil sampling probe during unfrozen soil conditions. Soil samples were oven dried at 105˚C for 24 hours to obtain their

gravimetric water content, which were subsequently converted to volumetric water content using dry soil bulk densities obtained from the separate samples collected with an aluminum cylinder within the upper 0.2 m of soil. Volumetric water contents obtained from soil samples were used to establish an appropriate petrophysical relationship to convert DGW velocity measurements to a corresponding soil water content estimate. Relative uncertainties in gravimetrically derived water contents were inferred from the range in soil bulk density measurements collected at each site.

2.5 Results and Discussion

2.5.1 Characterization of Near-Surface Wavefields

An important element of using the DGW for shallow soil moisture monitoring is the quality of the DGW velocity measurement. This process is dependent on the accurate determination of DGW traveltimes over a sufficiently broad range of antenna offset distances which, in turn, is dependent on the nature of the near-surface EM wavefields. The complexity of these varying wavefields is readily apparent in our CMP data.

Major variations in DGW velocity occurred over longer (i.e., seasonal) time scales. These variations are seen in Figure 2.3 which shows representative 900 MHz CMP data from the three textural sites acquired during dry (summer), wet (spring and autumn) and frozen (winter) soil conditions. DGW propagation during both dry (Figures 2.3a–c) and frozen (Figures 2.3g–i) periods are characterized by high velocities and variable degrees of lateral coherency over longer offset distances. In comparison, DGW propagation during wet periods (Figure 2.3d–f) exhibit low velocities and strong lateral coherency.

Superimposed on these seasonal trends are shorter (daily to weekly) time scale variations in DGW propagation that are due to precipitation events and subsequent soil drying, as well as freezing and thawing events. For example, Figure 2.4 shows the temporal changes in the 900 MHz CMP data during 4 May–4 June 2007 period at the sand site caused by significant rainfall events during a longer term drying trend. Prior to the major precipitation events, a high velocity DGW was observed on 4 May (Figure 2.4a) that exhibited reduced lateral coherency at antenna offsets greater than 0.75 m. Approximately 61% of the precipitation during this one month period occurred as two events on 9 May (8.8 mm) and 15 May (33.4 mm); the CMP data collected after each of these events on 11 May and 16 May (Figure 2.4b and 2.4c, respectively) show a progressive slowing of the DGW. Further, the major precipitation event one day prior to 16 May survey resulted in the formation of a refraction

event at 1.65 m antenna offset. While this refraction is consistent with a pre-existing stratigraphic reflection event observed in the previous CMP data, these wide-angle arrivals (i.e., at offsets >1.65 m) did not affect the DGW until the soil surface was sufficiently wet. Afterward, increasing DGW velocities can be observed in the CMP data acquired on 22 May and 4 June (Figure 2.4d and 2.4e, respectively) during the following drying period. While both of these periods yielded similar DGW velocity measurements, significant differences were observed in lateral coherency. In particular, the survey collected on 22 May shows a substantial reduction in DGW beyond 0.80 m antenna offset while 4 June shows a relatively strong DGW across the entire offset range.

The potential cause of these reduced lateral coherencies for variable soil conditions could be due to the formation of a high-velocity surface soil layer. Recent studies showed that DGW propagation across a thin high-velocity layer (i.e., dry or frozen soil) underlain by lower velocity material would result in interfering multiple reflections off the base of the high-velocity layer which could eventually propagate as dispersive waves (Steelman and Endres, 2009; van der Kruk et al., 2009). Under these soil conditions the apparent DGW would be less pronounced, particularly at wider antenna offsets. While the rapid drying (e.g., Figure 2.4d) or seasonal freezing (e.g., Figure 2.3h) of surface soil could have resulted in a thin high-velocity layer over relatively wetter soil, further analysis (i.e., numerical modeling) with these data sets is necessary to validate this waveguide mechanism hypothesis.

In addition to the variable lateral coherency, other wavefield events can be superimposed on the DGW, causing interference that may affect the accuracy of DGW traveltime measurements. Since a GPR wavelet has a finite duration that is related to its dominant period, the range of offset distances in the CMP data where this interference occurs will be a function of the antenna frequency used to acquire the data. In general, the interference due to a particular event will likely occur over increasingly larger offset ranges as antenna frequency decreases due to the associated lengthening of the wavelet duration (i.e., dominant period).

In our data sets, interference between the direct air wave and DGW was observed over short offset distances where there was insufficient separation between the two wavefields. The rate at which this separation occurred was determined by the DGW velocity; hence, direct air wave interference extended to longer offsets during higher DGW velocity conditions. A related phenomenon was the interference between the DGW and refracted air waves. While refracted air waves have the same horizontal velocity on the CMP data as the direct air wave, their traveltimes were greater due to an initial reflection raypath within the ground. Hence, the nature of the interaction between the DGW

and refracted air waves was similar to that which occurred with the direct air wave, except that it occurred at wider offset distances. Multiple air refraction events were also observed across the antenna offset range. The severity of refracted air wave interference with DGW was more prominent during dry and frozen soil conditions; these soil conditions are characterized by a lower permittivity contrast at the air-ground interface that may have resulted in increased transmission of energy into air (e.g., formation of refracted air waves).

To illustrate the nature of these air wave interferences as a function of wavelet duration (i.e., antenna frequency), Figure 2.5 shows 225 MHz, 450 MHz and 900 MHz CMP data collected at the silt loam site during dry soil conditions on 1 August 2007. The 225 MHz CMP data (Figure 2.5a) is characterized by strong direct air and DGW interference at offsets less than 0.85 m; similar interferences are also evident with later arriving refracted air waves (e.g., 1.4–1.6 m and 2.0–2.2 m). In this case, clear DGW events are difficult to identify across the entire antenna offset range. The 450 MHz data (Figure 2.5b) shows reduced direct air wave and DGW interference at near offsets and reduced air refraction interferences relative to the 225 MHz data. Finally, the 900 MHz CMP data (Figure 2.5c) shows further reduced direct air wave and DGW interference, as well as relatively minor air refraction interference across the entire measurement offset range compared to the 450 MHz and 225 MHz data.

While air wave interference with DGW is evident throughout the antenna offset range for each frequency, these interferences primarily affected the first positive half-cycle of the DGW. This illustrates the importance of using the zero-amplitude cross-over point between the first and second half-cycle to pick DGW events. Although this portion of the DGW wavelet is still affected by air wave interferences, a relatively consistent picking procedure can be used to obtain traveltimes over a sufficiently wide range of offsets which would not be possible using the first break or peak amplitude values. As a result, each DGW velocity in Figure 2.5 was computed from 0.5 m to 2.0 m offset to obtain an overall best fit for the entire offset range. This type of approach was used because we could not accurately identify specific ranges containing clear DGW arrivals. In this case, lower frequency DGW were more strongly affected by air wave interference which seemed to result in progressively higher DGW velocity measurements.

Reflection and refraction events from shallow subsurface interfaces were near-surface wavefield components that also interfered with the DGW. Because of their additional raypath lengths relative to the DGW, these events limited the maximum offset distance available for DGW velocity

determination. The formation of ground refraction events requires a downward velocity increase in the shallow subsurface, such as a wet surface layer overlying dryer substratum. Hence, ground refraction interference with the DGW was particularly severe after rainfall events following a prolonged drying period, particularly at the sandy loam site, where this type of near-surface velocity structure occurred.

The 450 MHz CMP data in Figure 2.6 shows the impact of subsurface refractions and reflections on the DGW at the sandy loam site during the period between 24 April and 11 May 2007. DGW traveltimes were initially identified across the full offset range for linear regression analysis. Occasionally these data were characterized by distinct changes in the slope of the traveltime-offset relationship. For instance, a slight decrease in slope was typically observed at offsets <0.5 m. The relatively shallower slope characterizing the direct events at these near-offsets in Figure 2.6 may be the result of air wave interference or possibly a shallow reflection phase superimposed on the DGW wavelet. Further changes in the slope were observed at wider offset distances. These portions of the direct arrival data were again more accurately fit using a linear regression characterized by a higher velocity (i.e., shallower slope). Hence, these arrivals were interpreted as refraction events that arrived prior to the true DGW. In some cases, destructive interference by these reflection/refraction events eliminated wider-offset DGW arrivals, thereby significantly reducing the DGW offset range available for velocity determination.

For example, the CMP data collected on 24 April (Figure 2.6a) shows a prominent ground refraction event at antenna offsets greater than ~1.65 m, limiting the maximum antenna offset available for DGW velocity determination. However, the linear regression analysis also indicated the presence of a less pronounced ground refraction event between offsets 0.8–1.65 m, which further limited the offset range available for DGW velocity determination. This data set also shows interference at near-offsets (i.e., less than 0.5 m). The following CMP sounding collected on 4 May (Figure 2.6b) during relatively higher velocity conditions shows significant destructive interference between the DGW and a shallow reflection event initiating at 0.8 m that greatly reduced the maximum offset range available for DGW velocity determination; near-surface interference is evident at offsets less than 0.34 m. After a 9 May precipitation event, interference from the ground refraction event was observed at offsets beyond ~1.35 m for the CMP survey conducted on 11 May (Figure 2.6c); however, additional phase interference at offsets less than 0.26 m and between 0.8–1.35 m significantly limited the DGW offset range. While these variations in refraction and reflection offset

distance are associated with changes in soil water content conditions, the presence of finer grained sediments and increased percentage of organics in the upper few decimeters of soil at the sandy loam site likely ensures a persistent velocity increase with depth. This contrast appears to be enhanced by wetting events and continues under dryer conditions due to the ability of the surface layer to retain water.

Clearly, accurate determination of DGW traveltimes required the individual interpretation of each CMP survey to establish an appropriate offset range where it was not obscured by other events in the near-surface wavefield. Initially, we attempted to use a fixed offset range (e.g., 0.5–2.0 m) for all data sets to maintain a more consistent soil sampling volume during the annual period; however, we found that the offset ranges containing clear DGW events varied significantly in terms of soil texture and soil water content conditions as illustrated above. As a result, variable offset ranges (i.e., between 0.5–2.0 m) were used in the determination of DGW velocity and are shown in Figure 2.7.

The use of wider offsets at the sandy loam site (Figures 2.7d–f) was severely restricted by the frequent occurrence of shallow ground refractions during the entire monitoring period. It is probable that the presence of finer grained sediments with increased organic content in the top 0.3–0.4 m overlying coarser sediments at the sandy loam site (refer to Table 2.1) would consistently produce a downward velocity increase due to the inherent soil moisture differences between these textures. Shallow ground refractions occasionally restricted the use of wide offsets (e.g., greater than 0.75 m) at the sand site (Figure 2.7a–c) during the months of September to December when a relatively wetter surface layer formed over less wet substratum. In comparison, the dryer July to August period at the sand site was characterized by relatively wider initial offset positions (e.g., greater than 0.7 m) due to more pronounced direct air wave and DGW interference combined with reduced DGW coherency that severely restricted the available offset ranges. A relatively consistent offset range was available for DGW analysis at the silt loam site during the entire measurement period (Figure 2.7g–i).

2.5.2 Temporal Variations in Direct Ground Wave Velocity

The DGW velocity results for the three soil textural sites are presented in Figure 2.8. The uncertainties (i.e., standard errors) in the DGW velocity values are indicated as vertical error bars that are generally very small and covered by the data points. It should be noted that these velocity uncertainties represent the linear fitting error in the DGW arrivals and do not necessarily encompass errors associated with wavefield interference. Nevertheless, these linear fitting uncertainties in DGW

were only significant during the early soil freezing and thawing process, during which DGW propagation in the thin frozen/thawed upper layer was partially obscured by the interfering multiple reflections at wider antenna offsets.

In general, the DGW velocities are consistently faster at the sand site (Figure 2.8a) (i.e., 0.0965–0.1653 m/ns). The DGW velocities at the sandy loam (Figure 2.8b) and silt loam (Figure 2.8c) sites are comparable (i.e., 0.0593–0.1302 m/ns and 0.0583–0.1385 m/ns, respectively), and both show a wider range of absolute and relative variation compared to the sand site. Further, there appears to be little, if any, systematic differences in DGW velocities as a function of antenna frequency, indicating that frequency dispersion effects were negligible. An examination of the data sets where significant frequency differences occurred found that variations in wavefield interference due to differing source wavelet duration (i.e., signal frequency) and dominant soil conditions were likely contributing factors. Larger velocity differences between antenna frequencies were observed during relatively high DGW velocity conditions. These conditions were typically encountered during the dry summer and frozen winter periods, during which large changes in vertical soil conditions occurred (e.g., dry soil over wet soil and frozen soil over thawed soil). For instance, faster velocities at the sand site exhibited greater frequency differences during the monitoring period compared to the generally slower sandy loam and silt loam sites. The silt loam site was characterized by more variable DGW coherencies during the early freezing process which also depended on the antenna frequency. While these uncertainties associated with wavefield interference with the DGW are difficult to quantify, higher frequency antennas (i.e., 450 and 900 MHz) were generally characterized by less wavefield superposition; hence, higher frequency antennas likely provided more reliable DGW measurements for the range of soil conditions in this study.

The velocity data shown in Figure 2.8 exhibits both long-period (i.e., seasonal) and short-period (i.e., semi-daily) variations in soil dielectric permittivity. The seasonal trends consist of (i) increasing spring-early summer velocities, (ii) relatively high mid-summer velocities and (iii) decreasing late summer-autumn velocities, reflecting the annual drying and wetting cycle. While all three sites exhibit this pattern, the length of the phase differs with soil texture. In particular, the drying phase (i) is extended at the loam sites relative to the sand site; as a result, the sand site has a comparatively longer mid-summer dry period (ii).

As water freezes, it becomes part of a crystalline ice structure which decreases the polarizability of the water molecule, causing an increase in the EM wave velocity measurement. Numerous studies

have evaluated the dielectric response of freezing pore water using TDR (e.g., Patterson and Smith, 1980; Patterson and Smith, 1981; Stein and Kane, 1983). The high velocity winter period (iv) is demarcated by a large initial velocity increase and subsequent decrease corresponding to freezing (F) and thawing (T) periods, respectively. While the soil thaw appears to be a relatively short duration process in this study, the freezing process appears to vary with location, with the sandy loam site having the slower freezing rate. This slower rate is thought to be associated with its lower topographic position within the agricultural field, which permitted greater accumulation of overlying snow pack that may have partially insulated the soil during the early freezing process.

Superimposed on these seasonal trends are relatively short-period velocity decreases caused by major precipitation events (P) followed by rapid drying of the near-surface soil. While the definition of these events depends on the temporal sampling interval, it can be seen that the impact of these events varies with soil texture. In particular, it can be seen that the sand site has a stronger response to these events in comparison to the loam soil sites.

2.5.3 Temporal Variations in Volumetric Water Content

It is necessary to establish an appropriate petrophysical $\kappa - \theta$ relationship to convert the DGW velocity information into volumetric water content estimates. However, this calibration requires information about DGW sampling depth during the study period for each antenna frequency and soil texture. Due to the relatively large gravimetric sampling interval (i.e., 0.1 m) used to obtain the field volumetric water content measurements, we have elected to simply compute the mean DGW sampling depth during the monitored unfrozen soil conditions for each antenna frequency and soil measurement site.

Our sampling depth estimates are based on the coefficient of determination r^2 from a linear regression analysis of the field-derived volumetric water contents and the index of refraction, $\sqrt{\kappa}$, from DGW during thawed soil conditions. The sampling depth analysis used the average water content from the 0.1 m sample intervals for cumulative depths between 0.1 to 0.5 m below ground surface. A summary of these r^2 results is provided in Table 2.3.

Given that r^2 is a measure of the dependence between the average water contents and dielectric permittivity, our DGW sampling depth estimates were determined using the cumulative soil sampling depth interval with the maximum r^2 value. Due to the gross soil sampling interval (i.e., 0.1 m) used in this study, our measured sampling depths in Table 2.3 are assumed to have an uncertainty of ±10

cm (i.e., on the order of the soil sampling interval). These results given in Table 2.3 predict DGW sampling depths of 30 cm for the 225 MHz antennas and 20 cm for the 450 MHz and 900 MHz antennas at the sand site. For the sandy loam site, the estimated DGW sampling depths are 10 cm for the 225 MHz and 900 MHz antennas and 20 cm for the 450 MHz. The estimated sampling depth at the silt loam was 20 cm for all three frequencies.

While our DGW sampling depth estimates represent an approximate average value for the measurement period, these results were within the predicted sampling depth ranges using Equation (2.1) for the sand but were typically less than those predicted for the loam soils. These predicted ranges (shown in Table 2.3) were calculated using the range of velocity and offsets presented in Figures 2.7 and 2.8, respectively, while approximate average central frequencies were obtained from the amplitude spectrums. It should be noted that the lower DGW sampling depth interpreted at the sandy loam site with 225 MHz and 900 MHz antenna clearly disagrees with those found at the sand and silt loam sites. While it is possible that the lower sampling depth measured at the sandy loam site may be partially associated with the typically shorter antenna offset ranges used to measure DGW velocity at this site, similar offset ranges were also used for the 450 MHz antennas. However, a closer examination of the 450 MHz results at the sandy loam site shows that very similar r^2 values were obtained for the upper 10 and 20 cm intervals, and hence the effective sampling depth of the 450 MHz is generally consistent with the other two frequencies.

For this study, we have utilized the volumetric mixing formulae for the three-phase system given by Equation (2.3) that was independently calibrated for each soil texture to estimate water content from the DGW derived permittivity values. The soil porosity ϕ values used are given for each texture in Table 2.1. The dielectric permittivity values assigned to the air, solid mineral and liquid water constituents were κ_a = 1, κ_s = 5 and κ_w = 82.232, respectively. Our dielectric value for water corresponds to a temperature T = 15˚C as this represents a reasonable average value over our range of unfrozen field conditions (i.e., 5–25˚C). Although our permittivity value for solid phase is generally accepted for quartz grains, typical values for sand and loamy soils can range between 4 and 6 (Cassidy, 2009).

While the absence of in-situ soil temperature data restricted our ability to vary the κ_w value, our sensitivity analysis using κ_w values between 86.1 and 78.5 corresponding to limiting temperature condition indicates a maximum uncertainty in water content of ±0.01 m^3m^{-3} when assuming a constant ground temperature of 15˚C and κ_s = 5 (i.e., based on CRIM). It should be noted that this

maximum uncertainty of ±0.01 m^3m^{-3} coincides with very wet conditions at the loam sites and would become less significant as the soil dries. While more systematic uncertainties associated with solid phase permittivity range (i.e., $\kappa_s = 4 – 6$) could account for as much as +0.019 m^3m^{-3} to -0.017 m^3m^{-3} deviations in water content from that obtained using $\kappa_s = 5$ with CRIM for sand soil, the relative contribution of soil phase permittivity decreases with increasing porosity (e.g., loam soils). This maximum sensitivity to solid phase permittivity corresponds to very warm dry soil conditions. However, we can reduce these solid phase uncertainties significantly by calibrating α to each site.

The best fitting volumetric mixing formula for the combined frequency data set for each soil corresponds to the exponent value α that yielded the lowest root-mean-squared-error (RMSE). These results indicate best fit exponent values of $\alpha = 0.51$ (RMSE = 0.018 m^3m^{-3}), $\alpha = 0.19$ (RMSE = 0.051 m^3m^{-3}) and $\alpha = 0.40$ (RMSE = 0.020 m^3m^{-3}) for the sand, sandy loam and silt loam soils, respectively. The results of this analysis are shown in Figure 2.9 where each of the calibrated mixing formulae are superimposed on a plot of the DGW dielectric permittivity measurements as a function of their corresponding gravimetrically derived volumetric water content from the soil sampling. While the uncertainties in measured dielectric permittivity (i.e., linear fit) were generally small during unfrozen soil conditions, more significant uncertainties are possible in the sample derived volumetric water content data. Inference of these uncertainties in gravimetrically derived water content was based on the repeat soil bulk density measurements collected at each site. As a result, the sand, sandy loam and silt loam sites were given water content uncertainties of 0.01 m^3m^{-3}, 0.03 m^3m^{-3} and 0.02 m^3m^{-3}, respectively; however, these uncertainties are not shown in Figure 2.9 for clarity.

It is clear that the sand data forms a distinct group over a lower range of permittivity ($3 \leq \kappa \leq 10$) which is well described by the best fit mixing formula. While the data for the sandy and silt loams display appreciable overlap in a higher range of permittivity ($6 \leq \kappa \leq 26$), these data are more variable, particularly for the sandy loam. For instance, the sandy loam exhibits relatively lower and higher water contents for $\kappa > 15$ and $\kappa < 12$, respectively, that resulted in a relatively lower α value compared to the silt loam. Similar results were obtained for each of the GPR antenna frequencies; this indicates that frequency dispersion has minimal impact on our data set.

These field calibrated mixing formulae were used with Equation (2.2) to convert the DGW velocity data into volumetric soil water content estimates; these water contents are presented in Figure 2.10 with corresponding precipitation and air temperature data. For comparison, the residual water content

θ_r, field capacity θ_{fc} at -33 kPa and saturated water content θ_s for these three soil textures were predicted with Rosetta™ software (Schaap et al., 2001) using the information provided in Table 2.1 (e.g., grain size and soil bulk density). This software provides a simple means of predicting probable soil hydraulic parameters from existing databases using minimal soil textual information. The Rosetta™ estimates for our soil textures are given in Table 2.4 and denoted in Figure 2.10.

As anticipated from the velocity results shown in Figure 2.8, the DGW soil water content estimates exhibit both long-period and short-period variations caused by seasonal wetting/drying trends and major precipitation events, respectively. The autumn wetting and summer drying trends correlate well with the frequency and intensity of measured precipitation at each site. While each site shows similar seasonal trends in Figure 2.10, the rate and magnitude of these variations correspond to varying soil water contents which is controlled by the soil textural properties. In particular, the sand site (Figure 2.10a) displays a more limited and lower range of soil water content conditions (<0.01 m^3m^{-3}–0.16 m^3m^{-3}) compared to the sandy loam (0.12 m^3m^{-3}–0.48 m^3m^{-3}) and silt loam (0.09 m^3m^{-3}–0.47 m^3m^{-3}) soils (Figures 2.10b and 2.10c, respectively). When compared with the Rosetta™ estimates, it can be seen that both loam sites attained full saturation during the wet autumn and post thaw spring conditions while the sand site achieved only about half of its fully saturated value during these wet periods. Further, the sand site reached residual saturation conditions during the spring and remained in that state for much of the summer. In comparison, both loam sites exhibited a longer drying period and did not reach residual saturation conditions.

This contrast in textural response is particularly interesting given the meteorological conditions that occurred during the study period. Data from the University of Waterloo weather station show that the autumn of 2006 was exceptionally wet (293.8 mm versus the 30 year average of 220.9 mm) and the summer of 2007 was both hot (0.9 ˚C warmer than average) and dry (143.4 mm versus the 30 year average of 274.0 mm). The sand clearly exhibits a lower capacity to store water, as predicted by its field capacity, compared to the loam soils even during very wet seasonal conditions. In addition, while water content in both loam textures were relatively low compared to their wet autumn and post thaw spring conditions, residually saturated conditions were not attained under extraordinarily hot and dry seasonal conditions.

Due to the low dielectric permittivity of ice (e.g., κ_i = 3.2), the DGW-derived water content estimates during winter conditions (roughly denoted by subzero atmospheric temperatures) measure the unfrozen liquid fraction within the frozen soil. GPR data collected in the late-January to early-

March winter period indicate lower unfrozen water content for the sand (~0.02 m^3m^{-3}) in comparison to the sandy loam and silt loam soils (~0.15 m^3m^{-3} and ~0.12 m^3m^{-3}, respectively). Through laboratory tests, Patterson and Smith (1981) showed that finer textured soils will exhibit relatively larger liquid water contents at a given frozen soil temperature, and that the rate of decrease in liquid water content per change in soil temperature would be more rapid for coarser soil particularly during the early freezing process. These findings are consistent with our DGW data.

As can be seen in Figure 2.10, our three phase volumetric mixing formula with best fitting α values for each soil texture yielded quantitative estimates of soil water content that replicated the soil sampling data at both the sand and silt loam sites. Although the DGW moisture estimates at the sandy loam site were greater than the soil sample data during the wet autumn and drying spring conditions (by as much as 0.12 m^3m^{-3}) and less during the wet dry summer conditions (by as much as 0.08 m^3m^{-3}), the overall results at the three sites demonstrate the capacity of the DGW method to provide quantitative estimates of soil water content over the annual cycle of soil conditions, particularly at the sand and silt loam sites.

The more variable soil moisture estimates at the sandy loam site are thought to be associated with increased complexity of near-surface wavefield. Here, the presence of finer grained sediments and an increased percentage of organics in the upper few decimeters of soil likely caused a persistent velocity increase with depth which was enhanced by wetting events and was maintained under dryer soil conditions due to the surface layers ability to retain water. During the dry summer period, significant wavefield interference was observed at shorter antenna offsets (i.e., initiating at offsets less than 0.5 m), and as a result the apparent DGW events may have been impacted by both the direct air wave and refraction events. Hence, what we interpreted as a DGW during this dry period may have in fact been the ground refraction which would have resulted in an under estimation of soil water content.

To demonstrate the impact these dry condition data had on the determination of α for the complete annual cycle at the sandy loam site, we excluded the dry period data (last 10 soil samples) from the calibration procedure; this procedure resulted in a revised geometric parameter α = 0.33 (RMSE = 0.040 m^3m^{-3}). This revised value is more consistent with the geometric parameter obtained for the silt loam. However, the recalibrated GPR-derived volumetric soil water content estimates for the sandy loam site still overestimate water contents during the wet autumn period (by as much as 0.10 m^3m^{-3}), and underestimate the soil sample data during the dry summer period (by as much as 0.11 m^3m^{-3}). It

is clear that complexities in the near-surface wavefield during the dry summer period could have had a significant impact on our DGW soil water content estimates over the annual cycle at this site.

2.6 Conclusions

While the DGW technique for monitoring near-surface soil moisture is conceptually straightforward, its successful application requires an understanding of the nature of the near-surface EM wavefields. In this study, the use of CMP surveys has permitted us to examine the complexity of this wavefield as it evolved in response to long-term soil moisture variations and short-term precipitation events. Although these data did not show systematic differences in DGW velocity as a result of frequency dispersion for the 225–900 MHz range, the measurements obtained using higher frequency antennas (i.e., 450 MHz and 900 MHz) were less susceptible to near-surface wavefield interference. The application of CMP surveys enabled us to determine the appropriate antenna offset range for DGW velocity measurements under the conditions encountered at the time of data acquisition, which allowed us to study the nature of the interference caused by the superposition of other events, such as the air wave phases and subsurface refractions, upon the DGW event. We showed that significant variations can occur in the nature of the near-surface EM wavefields over both long and short time scales that significantly impact the usable range of antenna offsets for DGW velocity determination and corresponding soil moisture estimation.

Large variations in DGW velocities that followed seasonal trends and short-term velocity decreases due to precipitation events were observed during the annual cycle. While the overall DGW velocity patterns were similar for all three soil types, there were systematic textural differences associated with the hydraulic properties of the soil (e.g., due to differences in residual saturation and field capacity parameters). Using an appropriate petrophysical relationship calibrated to field data, we found that the DGW velocities provided quantitative estimates of soil water content that accurately replicated the soil sample data over the annual cycle of moisture conditions at both the sand and silt loam sites; however, slightly less accurate moisture estimates were obtained at the sandy loam site. Nevertheless, DGW measurements can be used to monitor soil wetting and drying cycles, thereby permitting the characterization of soil hydraulic processes (e.g., infiltration and evapotranspiration) in the near-surface.

For instance, the sand soil consistently exhibited lower water contents and completed the spring to early summer drying phase sooner than the loam textures. While the definition of precipitation events

depends on the temporal sampling interval, our results indicate that the sand site experienced a more variable response to these events in comparison to the loam soil sites. The variable conditions at the sand site are due to its lower capacity to store water which effectively permits water to drain more readily compared to the finer grained loam sites. The observed soil moisture characteristics at each site are directly related to seasonal hydraulic processes. The spring and autumn periods were characterized by persistently high soil water content conditions, thereby suggesting infiltration process. The effect of evapotranspiration was also shown to vary between the three sites during the summer period where rapid soil drying in the near-surface resulted in reduced DGW coherency. During the winter period, the progress of soil freezing was found to be slower at the sandy loam site which may have been the result of a thicker overlying snow pack; the timing and rate of freeze-thaw processes will affect seasonal recharge.

While the DGW technique has been previously shown to provide reliable soil moisture data, we have shown its suitability during a full range of natural soil conditions including temporally dynamic periods (e.g., precipitation events, rapid soil drying and seasonal frost development), during which we observed abrupt changes in the character of the near-surface wavefield. DGW measurements can be used to define moisture conditions at the air-soil interface which is a fundamental component of the hydrologic studies. In particular, near-surface processes such as infiltration, evapotranspiration, and moisture redistribution during the annual period can be characterized. The characterization of seasonal freeze-thaw processes is also important because a large portion of the annual recharge occurs before and after freezing commences; the DGW may be a viable technique to characterize both unfrozen and frozen soil conditions (i.e., estimate liquid water content). The non-invasive nature and larger sampling volume of DGW surveys can provide improved characterization of soil moisture dynamics for a complete range of seasonal soil conditions.

2.7 Tables and Figures

Table 2.1 Textural classification of upper 0.5 m of soil, including grain size and organic content expressed as weight percent, dry bulk density and porosity for the three water content monitoring sites.

Site	Texture	Sampling Depth	Sand	Silt	Clay	Organic	Bulk Density	Porosity
		cm		*% wt*			*g/cm^3*	-
Waterloo	sand	0 - 10	97.0	3.0	0.0	1.6		
		10 - 20	98.0	2.0	0.0	1.4	1.68[a]	0.37[a]
		20 - 30	98.0	2.0	0.0	1.1		
		30 - 40	96.0	4.0	0.0	1.1		
		40 - 50	97.0	3.0	0.0	-		
Waterloo	sandy loam	0 - 10	64.0	32.0	4.0	5.6		
		10 - 20	69.0	27.0	4.0	3.2	1.59[a]	0.40[a]
		20 - 30	68.0	29.0	3.0	5.5		
		30 - 40	72.0	23.0	5.0	4.0		
		40 - 50	87.0	10.0	3.0	0.7		
Woodstock	silt loam	0 - 10	24.0	71.0	5.0	8.2		
		10 - 20	17.0	78.0	5.0	6.9	1.23[a]	0.54[a]
		20 - 30	16.0	81.0	3.0	3.2		
		30 - 40	13.0	81.0	6.0	3.3		
		40 - 50	15.0	83.0	2.0	3.8		

[a] dry bulk density measurements and corresponding porosity estimates refer to the upper 20 cm of soil.

Table 2.2 Summary of DGW data sets acquired using 225 MHz, 450 MHz and 900 MHz antennas at the sand, sandy loam and silt loam. Number of GPR surveys collected with coincident gravimetric soil moisture samples are provided in brackets.

Soil Texture	**Sand**	**Sandy Loam**	**Silt Loam**
	28-Aug-06 to 13-Nov-07	28-Aug-06 to 13-Nov-07	19-May-06 to 31-Aug-07
225 MHz	30 (22)	27 (19)	31 (20)
450 MHz	34 (26)	33 (23)	32 (20)
900 MHz	52 (34)	33 (23)	32 (20)
Total	116	93	95

Table 2.3 Summary of r^2 results obtained from cumulative depth averaged gravimetric water content and $\sqrt{\kappa}$ from DGW velocity measurements with estimated mean effective sampling depths. The predicted effective sampling depth ranges from Equation (2.1) using data in Figure 2.7 and 2.8 is also provided for reference.

Soil Texture	**Sand**			**Sandy Loam**			**Silt Loam**		
	225	**450**	**900**	**225**	**450**	**900**	**225**	**450**	**900**
	MHz			*MHz*			*MHz*		
Cumulative Depths (cm)									
10	0.723	0.675	0.697	0.819[a]	0.839	0.910[a]	0.942	0.934	0.935
20	0.884	0.873[a]	0.881[a]	0.792	0.849[a]	0.895	0.973[b]	0.968[a]	0.964[a]
30	0.890[a]	0.870	0.852	0.720	0.800	0.833	0.973	0.967	0.960
40	0.888	0.833	0.780	0.650	0.732	0.760	0.966	0.960	0.949
50	0.861	0.740	0.670	0.611	0.696	0.714	0.962	0.955	0.943
Sampling Depth (cm)	30	20	20	10	20	10	20	20	20
Range of Predicted Sampling Depths (cm), Eqn. (2.1)	26-59	18-38	13-31	18-42	15-34	13-29	28-45	24-37	19-31

[a] approximate DGW sampling depths.
[b] DGW sampling depth determined using four significant figures (values not shown).

Table 2.4 Residual water content, field capacity at -33 kPa, and saturated water content values estimated with Rosetta™ software using grain size distribution and dry bulk density data.

Saturation Value	**Residual** θ_r	**Field Capacity** θ_{fc}	**Saturated** θ_s
	m^3m^{-3}	m^3m^{-3}	m^3m^{-3}
Soil Texture			
Sand	0.048	0.049	0.330
Sandy Loam	0.033	0.106	0.349
Silt Loam	0.051	0.285	0.440

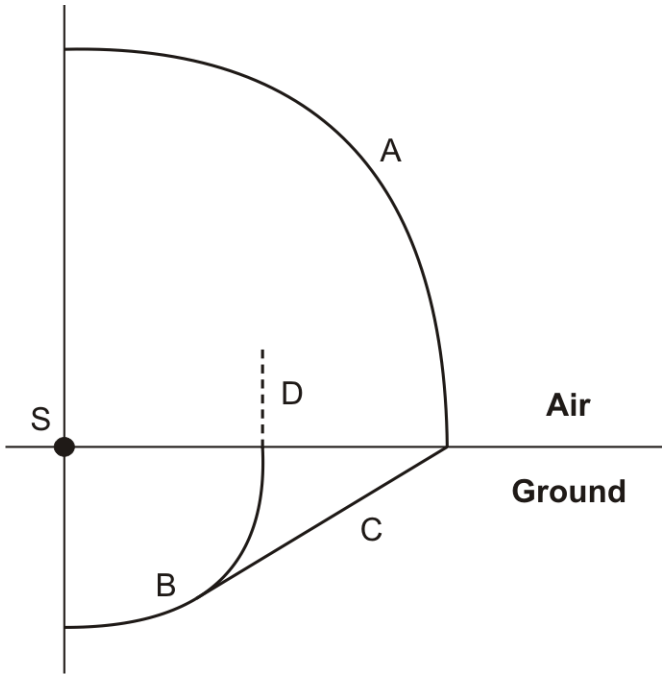

Figure 2.1 An illustration of the various wavefronts associated with a point source (S): spherical air wave (A), spherical ground wave (B), lateral head wave (C) and interfacial evanescent wave (D). The DGW is a combination of the spherical ground wave and evanescent wave; after Annan (1973).

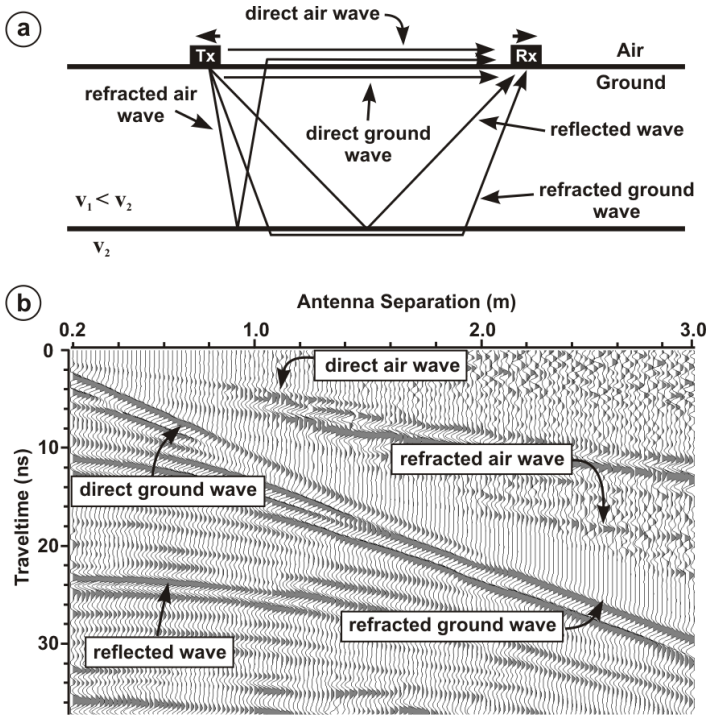

Figure 2.2 (a) Schematic showing the typical raypaths of GPR energy and (b) a representative CMP sounding; modified from Huisman et al. (2003a).

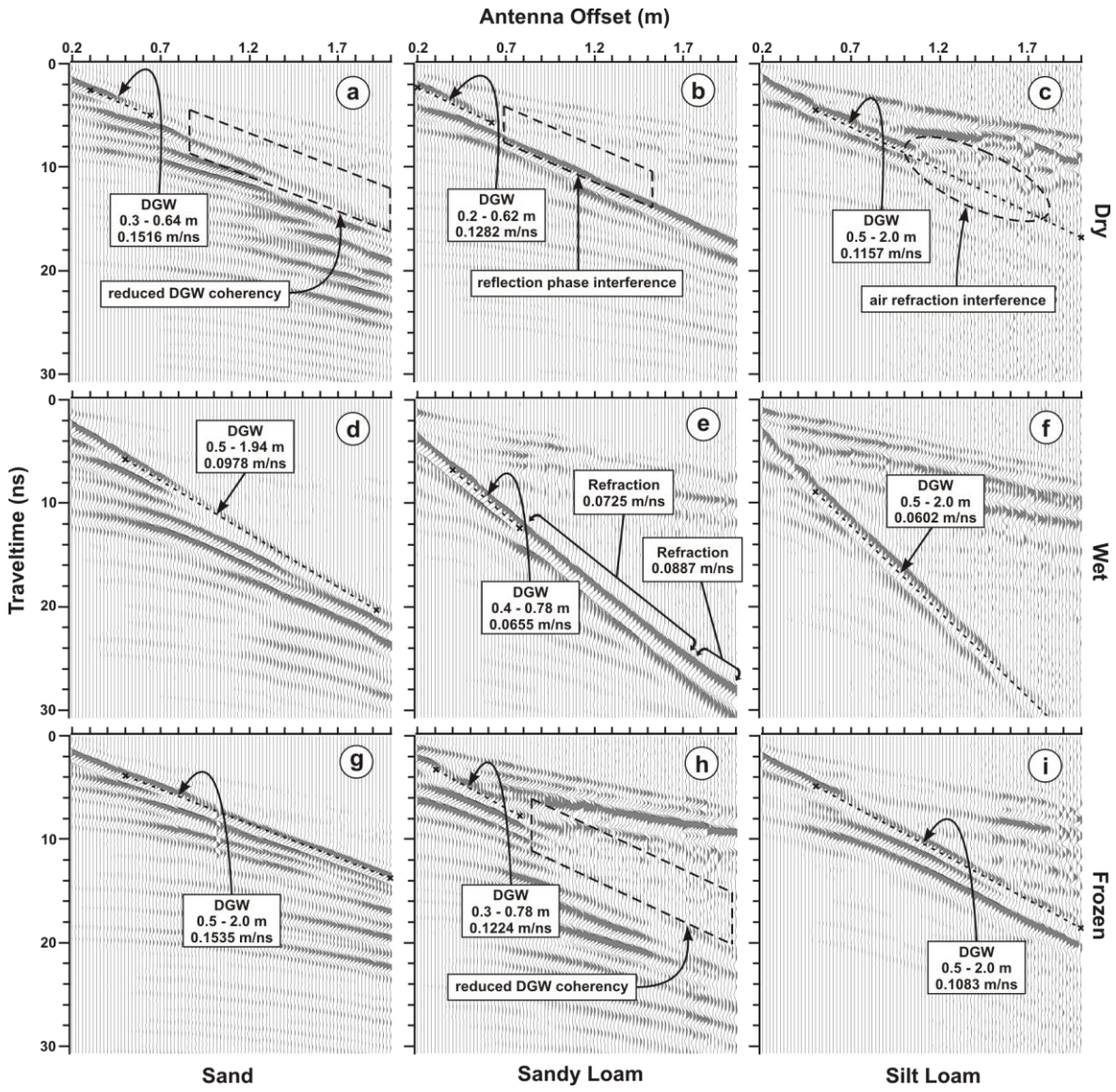

Figure 2.3 CMP soundings collected using 900 MHz antennae showing representative seasonal variations during dry (a–c), wet (d–f) and frozen (g–i) soil conditions at the sand, sandy loam and silt loam sites. The antenna offset range used to measure DGW velocity is also shown.

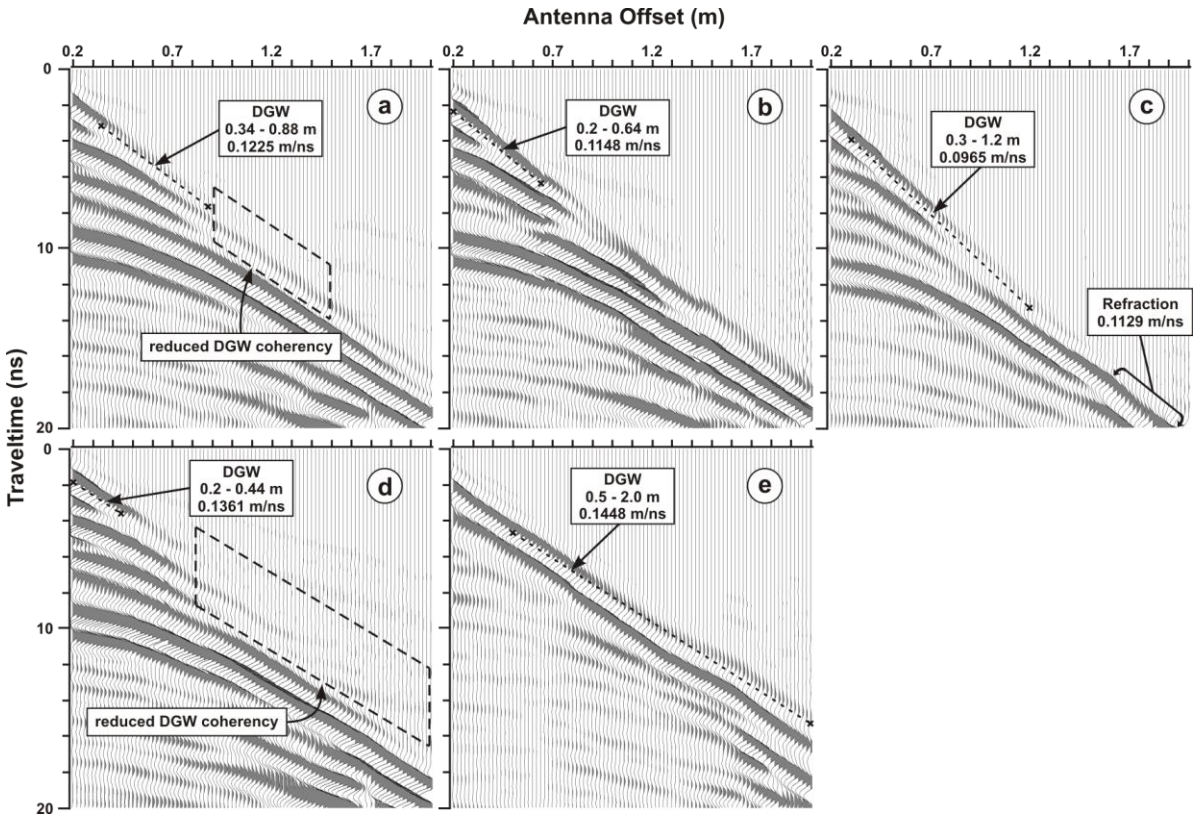

Figure 2.4 CMP sounding collected using 900 MHz antenna at the sand site illustrating shorter time scale wavefield variations. Surveys were conducted on (a) 4 May 2007, (b) 11 May 2007, (c) 16 May 2007, (d) 22 May 2007 and (e) 4 June 2007. The antenna offset range used to measure DGW velocity is also shown.

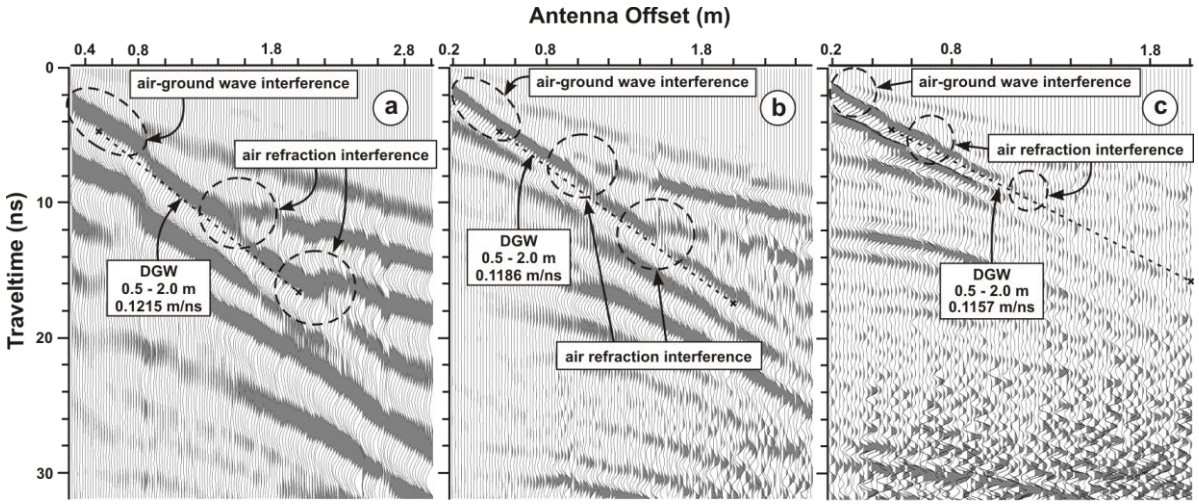

Figure 2.5 CMP soundings collected on 1 August 2007 at the silt loam site using (a) 225 MHz, (b) 450 MHz and (c) 900 MHz antennas illustrating direct air and DGW interference at near-offsets and air refraction interference at far-offsets. The antenna offset range used to measure DGW velocity is also shown.

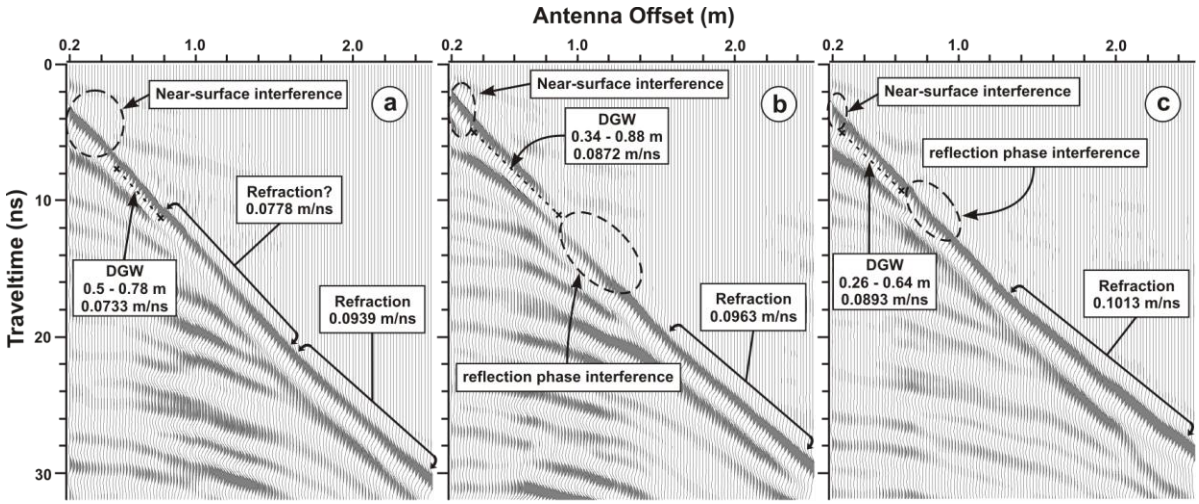

Figure 2.6 CMP soundings collected using 450 MHz antennas on (a) 24 April 2007, (b) 4 May 2007 and (c) 11 May 2007 at the sandy loam site exhibiting temporal variations in DGW interference between ground refractions and reflection events. The antenna offset range used to measure DGW velocity is also shown.

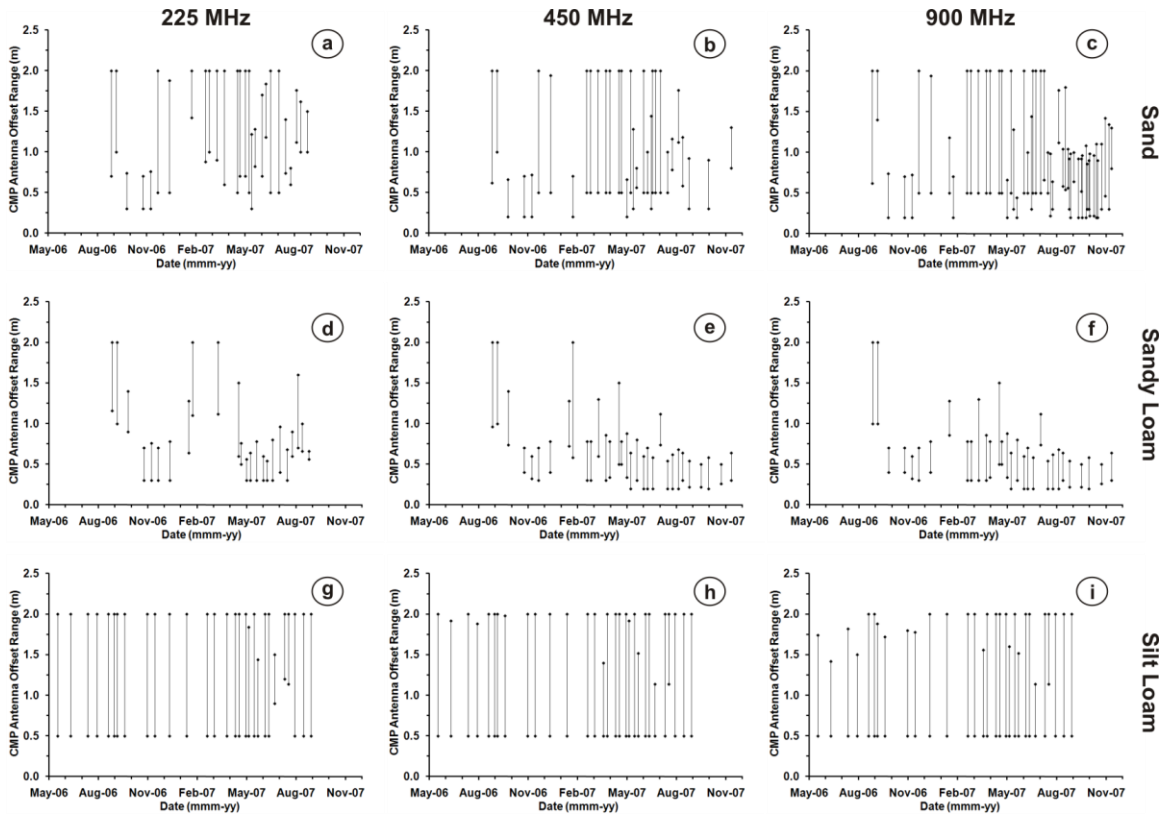

Figure 2.7 CMP antenna offset ranges used for DGW velocity determination with 225 MHz, 450 MHz and 900 MHz antennas at the sand (a–c), sandy loam (d–f) and silt loam (g–i) textural sites.

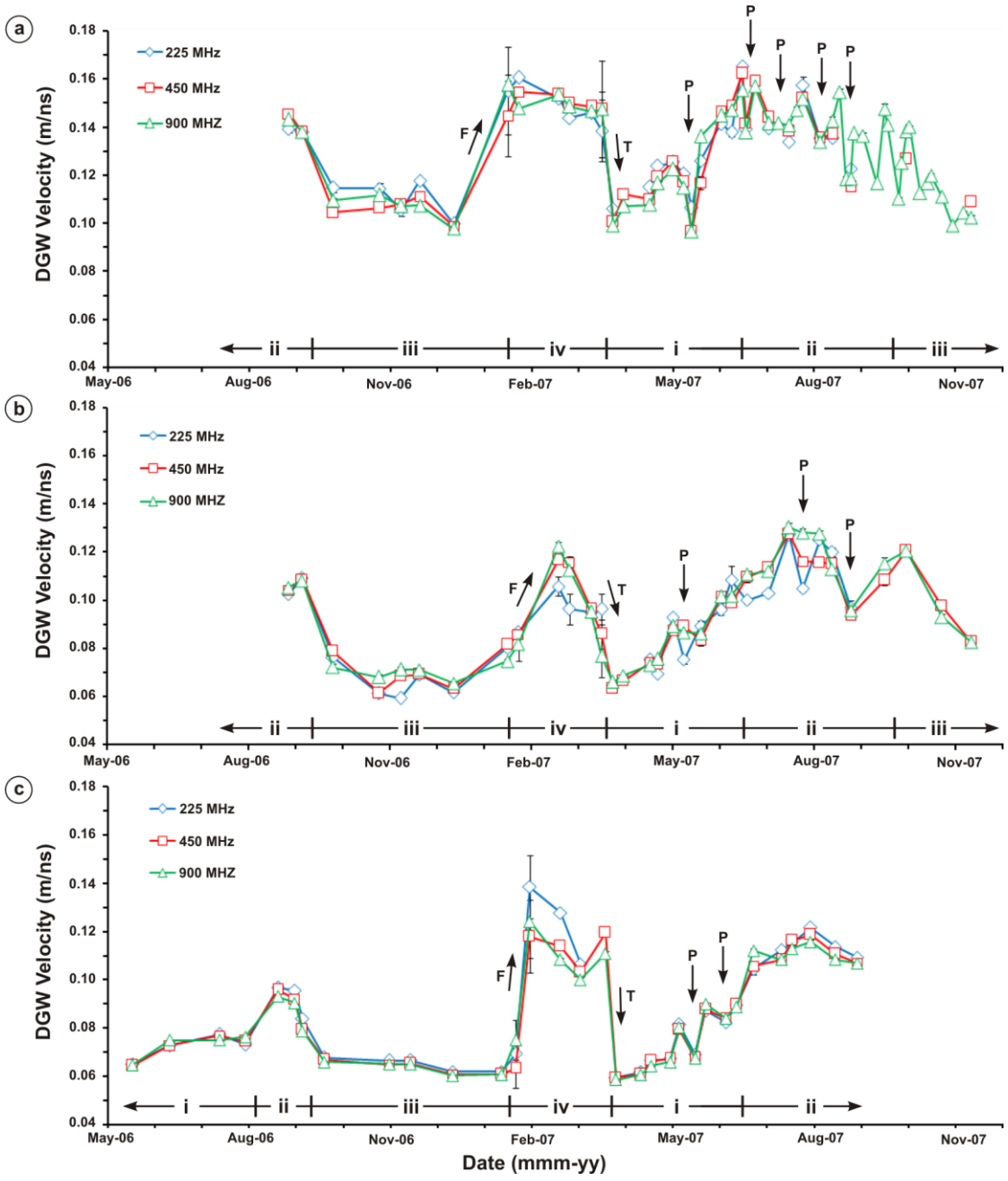

Figure 2.8 Temporal variations in DGW velocity using 225 MHz, 450 MHz and 900 MHz antennas for (a) sand, (b) sandy loam and (c) silt loam sites. Long-period seasonal patterns (i.e., (i) increasing spring-early summer velocities, (ii) relatively high mid-summer velocities, (iii) decreasing late summer-autumn velocities and (iv) high velocity winter periods) and short-period changes related to precipitation events (P) are denoted. The changes due to soil freezing (F) and thawing (T) processes are also indicated.

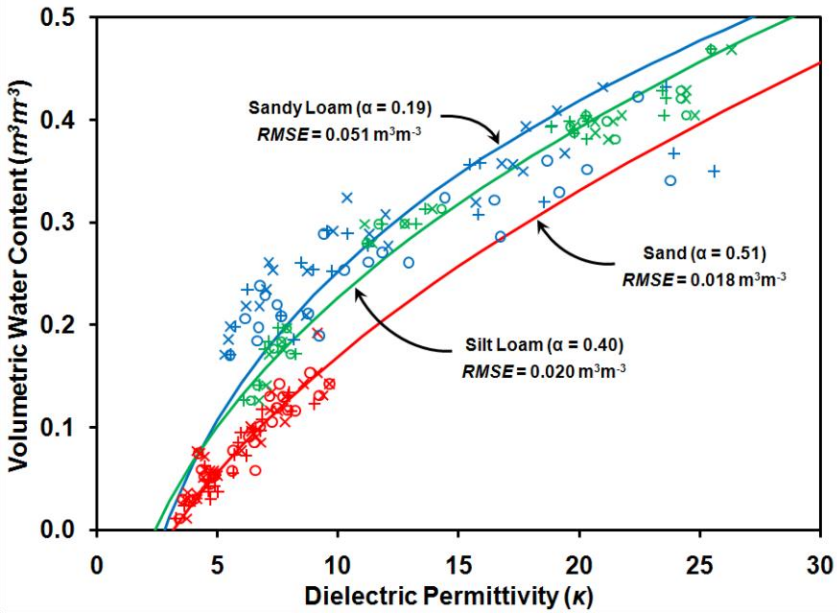

Figure 2.9 GPR dielectric permittivity with corresponding volumetric water content collected at (a) sand (red), (b) sandy loam (blue) and (c) silt loam (green) textural locations using 225 MHz (+), 450 MHz (○) and 900 MHz (×) antenna. Volumetric mixing formulae demonstrating best fit geometric parameter (i.e., lowest root-mean-squared-error) for each soil texture are also shown. Note: each antenna frequency was fitted using data corresponding to their measured sampling depth interval shown in Table 2.3.

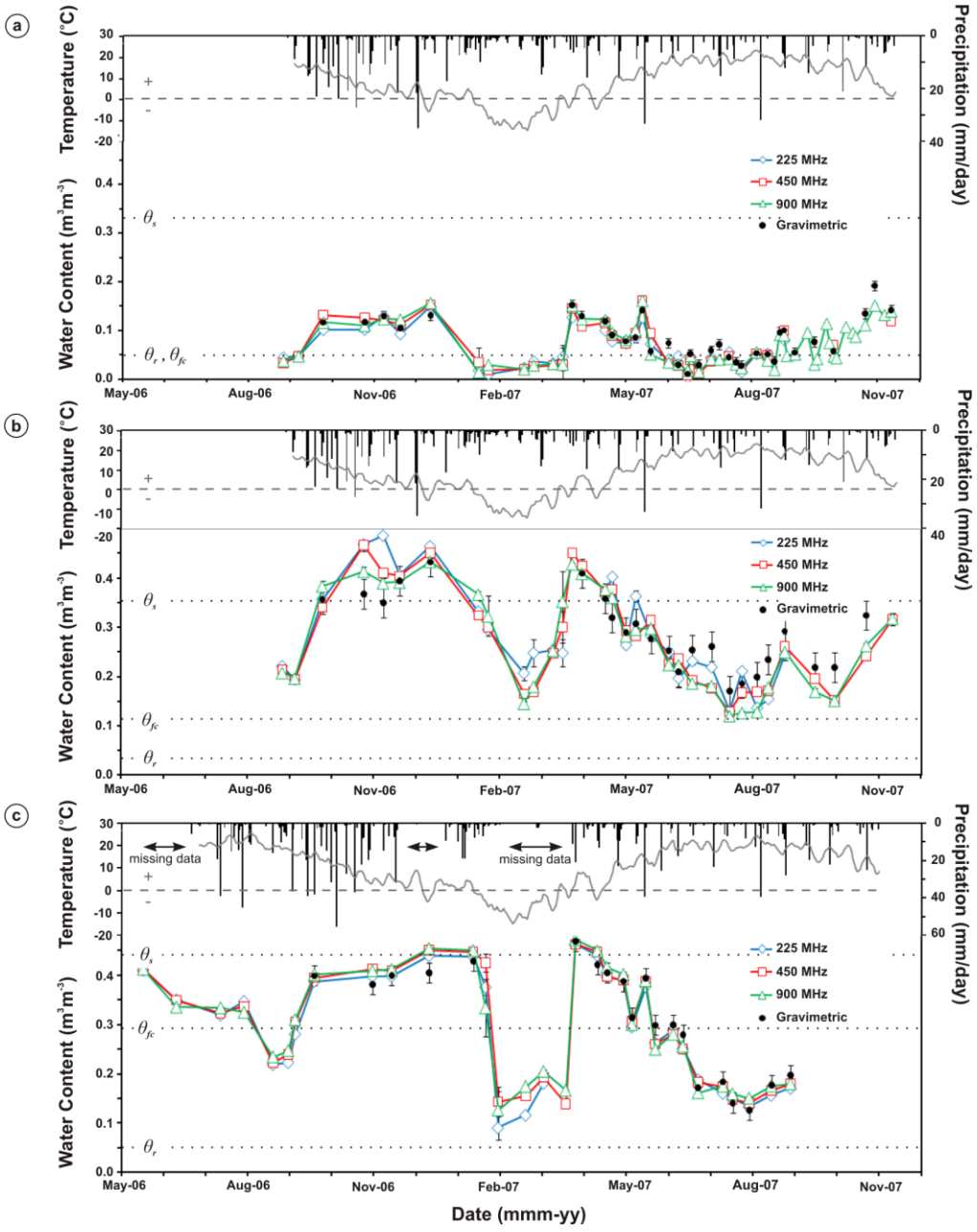

Figure 2.10 Temporal variations in DGW soil water content estimates for 225 MHz, 450 MHz and 900 MHz antennas at (a) sand, (b) sandy loam and (c) silt loam sites. Soil sampled water content from 20 cm interval is shown for sand and silt loam, while 10 cm interval is shown for sandy loam. The daily precipitation and mean weekly temperature data are provided for the corresponding soil textural locations. Soil hydraulic parameters predicted with Rosetta™ software (i.e., residual water content θ_r, field capacity θ_{fc} at -33 kPa and saturated water content θ_s) are shown for the three soil textures.

Chapter 3
Comparison of Petrophysical Relationships for Soil Moisture Estimation using GPR Ground Waves[2]

3.1 Executive Summary

Soil water content measurement using ground-penetrating radar (GPR) requires an appropriate petrophysical relationship between the dielectric permittivity and volumetric water content of the soil. The suitability of different relationships for GPR soil water content estimation has not been thoroughly investigated under natural field conditions for a complete range of seasonal soil conditions. The ability of various empirical relationships, volumetric mixing formulae and effective medium approximations to predict near-surface volumetric soil water content using high-frequency direct ground wave (DGW) velocity measurements was evaluated. DGW velocities were obtained from common-midpoint soundings collected using multiple antenna frequencies across three distinct soil textures (i.e., sand, sandy loam and silt loam). The estimated water contents were compared with values obtained from gravimetric sampling. The accuracy of soil water content predictions obtained from the various relationships ranged considerably. The best predictions for the overall data set in terms of root-mean-square-error (RMSE) were obtained with a differential effective medium approximation based on a coated sphere model (i.e., RMSE = 0.045 m^3m^{-3}). However, the empirical relationships proposed by Topp et al. (1980) and Roth et al. (1992) (i.e., RMSE = 0.052 m^3m^{-3}) and volumetric mixing formula given by Roth et al. (1990) (i.e., RMSE = 0.048 m^3m^{-3}) also performed well. These best fitting relationships do exhibit some degree of textural bias that should be considered in the choice of petrophysical relationship for a given data set. Further improvements in water content estimates were obtained using our best fit third-order polynomial relationship (i.e., RMSE = 0.041 m^3m^{-3}) and our three-phase volumetric mixing formula with geometric parameter α = 0.36 (i.e., RMSE = 0.042 m^3m^{-3}); these optimized relationships were developed using the DGW permittivity and soil water content data collected in this study.

[2] Steelman, C.M., and Endres, A.L. (2011). Comparison of petrophysical relationships for soil moisture estimation using GPR ground waves. *Vadose Zone Journal, 10*, 1–16, doi:10.2136/vzj2010.0040.

3.2 Introduction

The measurement and evaluation of soil water content is a fundamental component in hydrological and agricultural studies (Vereecken et al., 2008; Robinson et al., 2008). Knowledge of soil water content is necessary for optimizing crop yield, evaluating groundwater recharge and assessing overland flow potential. Methods that provide a quantitative assessment of the lateral and vertical distribution of soil water are important, particularly methods that are non-invasive and can easily be applied to the field scale. A standard method of measuring soil water content is the gravimetric method which is based on the loss of mass after a soil sample has been oven dried for a specified period of time. However, this method relies on accurate soil bulk density estimates to convert water content measurements from mass to volume, which can become labor intensive if a large number of samples are required. Another common method utilizes a thermal neutron probe which is lowered into an access tube installed at the site; this method measures the ability of a medium to moderate neutrons (i.e., slow down fast neutrons to the lower energy thermal regime) that are emitted from the source (Ellis, 1987). Although this method allows for repeatable measurements of soil water content directly in the field, it must be calibrated to the field conditions and is difficult to apply at the field scale. Furthermore, this method does not provide reliable estimates of soil water content in the shallow root zone due to air space contribution in the probe's sampling volume.

High-frequency electromagnetic methods such as time-domain reflectometry (TDR) and ground-penetrating radar (GPR) as well as low-frequency capacitive sensors are particularly well suited for measuring volumetric soil water contents due to the polar nature of liquid water molecules. Although TDR and capacitive sensors both utilize probes which have to be inserted into the soil, they are based on different principles. TDR is based on the two-way traveltime of a high-frequency electromagnetic pulse that propagates along the probes (Jones et al., 2002; Robinson et al., 2003), while a capacitive sensor is based on the charge time and output voltage of a capacitance probe for an applied voltage (Dean et al., 1987; Gardner et al., 1998; Francesca et al., 2010); both of these sensors are strongly dependent on the dielectric property of the medium immediately surrounding the probes. While TDR and capacitive sensors can be easily automated for high temporal resolution monitoring of volumetric water content, the need for permanent sensor installation within the soil limits these techniques to point measurements which would have to be extrapolated over large areas. Furthermore, probe size restrictions (i.e., on the order of a few decimeters) result in small measurement volumes (i.e., cm^3)

which makes them more susceptible to errors arising from macropores and air gaps that may occur during installation (Robinson et al., 2003).

GPR methods have been shown as a viable alternative technique to monitor and evaluate shallow soil water content (Huisman et al., 2003). This method is based on the measured traveltime of a high-frequency electromagnetic pulse transmitted and received by either a monostatic or bistatic radar system. Because GPR measures larger volumes of soil (i.e., on the order of dm^3 to m^3) in a non-invasive manner, it is much better suited for field scale applications than standard point measurement techniques (e.g., Hubbard et al., 2002; Grote et al., 2003; Lunt et al., 2005; Galagedara et al., 2005a; Weihermüller et al., 2007; Gerhards et al., 2008). Hence, this moisture measurement technique would also be suitable for calibrating airborne and spaceborne remote sensing products (e.g., Wagner et al., 2007).

However, accurate measurements of soil water content using GPR requires an appropriate petrophysical relationship between the dielectric permittivity and volumetric water content of the soil; water contents can be determined by calibrating the GPR measurements (e.g., Huisman et al., 2001; Huisman et al., 2002; Grote et al., 2003) or by using some previously defined relationship. While field calibrations may be the most accurate because they are site specific, they are not easily established due to the amount of auxiliary (i.e., calibration) measurements that would have to be collected. Therefore, pre-established petrophysical relationships are commonly used to estimate soil water content from GPR measurements (e.g., Greaves et al., 1996; Galagedara et al., 2005a; Turesson, 2006; Weihermüller et al., 2007; Gerhards et al., 2008). These relationships may include: empirical equations based on experimental data (e.g., Topp et al., 1980; Nadler et al., 1991; Roth et al., 1992; Jacobsen and Schjønning, 1993a; Malicki et al., 1996; Curtis, 2001), volumetric mixing formulae using component electrical properties (e.g., Birchak et al., 1974; Wharton et al., 1980; Dobson et al., 1985; Roth et al., 1990; Heimovaara et al., 1994) and effective medium approximations based on geometrical models (e.g., Sen et al., 1981; Sen et al. 1984; Kenyon, 1984; Tyč et al., 1988; Endres and Redman, 1996; Friedman, 1998; Jones and Friedman, 2000; Cosenza et al., 2003; Endres and Bertrand, 2006; Chen and Or, 2006). A review on the application of petrophysical relationships to the electromagnetic properties of composite materials is provided by Sihvola (1999; 2000).

While some petrophysical relationships have been tested under relatively controlled (e.g., Roth et al., 1990; Roth et al., 1992; Jacobsen and Schjønning, 1993a) and natural soil conditions (e.g., Jacobsen and Schjønning, 1993b) for a range of soil textures, the dielectric permittivity measurements

have been typically obtained using some form of TDR sensor. More recent studies (e.g., Weiler et al., 1998; Lambot et al., 2004; Lambot et al., 2008) have attempted to examine the performance of some petrophysical relationships using GPR signals. However, many relationships have still not been thoroughly tested using GPR measurements. Given the difference in operating frequency and sampling volume between TDR and GPR measurements, and the increasing use of GPR as a soil water content sensor, it is apparent that such a study into the effect of petrophysical relationships on water content estimates from in-situ GPR measurements needs to be conducted.

This paper examines the performance of various published petrophysical relationships used to obtain soil water content estimates from in-situ GPR direct ground wave (DGW) velocity measurements (i.e., the velocity of the transmission of electromagnetic energy between a transmitting and receiving antenna propagating along the air-ground interface). The DGW measurements were collected as part of a separate soil moisture monitoring study examining the effects of seasonal soil water dynamics on DGW propagation (i.e., Steelman and Endres, 2010), thereby providing an opportunity to evaluate the suitability of a wide range of petrophysical relationships for DGW soil moisture estimation. Hence, our study is unique in a number of aspects. For instance, the DGW dielectric permittivity measurements were collected across recently undisturbed agricultural soils and calibrated with gravimetric soil water content measurements. While haying operations were conducted during the study period, other agricultural disturbances, such as plowing and tilling did not occur within the preceding 2–5 years of this study. The GPR data were also collected over the annual range of naturally occurring seasonal soil conditions common to mid-latitude climates (i.e., wet autumn and spring; dry summer with occasional large storm events) for three distinct soil textures (i.e., sand, sandy loam and silt loam). Further, multiple GPR antenna frequencies (i.e., 225 MHz, 450 MHz and 900 MHz) were used to measure the soil dielectric permittivity.

3.3 Petrophysical Relationships for Estimating Soil Moisture Content

Both guided (e.g., TDR) and unguided (e.g., GPR) electromagnetic wave propagation are determined by the frequency dependent complex dielectric permittivity, $\varepsilon^* = \varepsilon' - \varepsilon''$, where ε' is the real part of the complex permittivity associated with the capacity to store energy in the presence of an alternating electric field, while ε'' is the imaginary part of the complex permittivity associated with energy dissipation. In the case of GPR measurements, which have bandwidths between 10 MHz to 1 GHz, ε'' is typically small compared to ε'; hence, the effective dielectric permittivity of a composite material is

commonly expressed as the relative permittivity, $\kappa = \varepsilon'/\varepsilon_o$, where ε_o is the electric permittivity of free space (8.854×10^{-12} Fm^{-1}). The relative permittivity is referred herein as the permittivity. For non-magnetic, low conductive soils, the propagation velocity (v) of electromagnetic waves is determined from

$$v = \frac{c}{\sqrt{\kappa}}, \tag{3.1}$$

where c is the electromagnetic velocity in free space (0.2998 m/ns).

Under these conditions the permittivity of liquid water varies over the range of 78–88 as a function of temperature while the permittivity of air is 1 and the permittivity of the solid grains of sand and loamy soils typically ranges between 4 and 6 (Cassidy, 2009). This large dielectric contrast between liquid water, soil solids and air resulting from the high polarizability of water molecules provides the basis for predicting volumetric soil water content using electromagnetic wave velocity measurements. However, obtaining a reliable estimate of water content requires the use of an appropriate petrophysical relationship between the permittivity of the bulk material and its volumetric soil water content.

3.3.1 Empirical Relationships

Empirically derived relationships, based on field and laboratory measurements, are less complex compared to physical models, and hence are easier to apply for a range of soil textures and water content conditions since they require very limited information about soil textural properties (e.g., bulk density, porosity, pore structure etc.). As a result, numerous researchers have developed relationships between volumetric soil water content (θ) and the permittivity of the bulk material ($\tilde{\kappa}$) using a range of soil textures.

The most widely used empirical relationship is the third-order polynomial proposed by Topp et al. (1980):

$$\theta = -5.3\times10^{-2} + 2.92\times10^{-2}\tilde{\kappa} - 5.5\times10^{-4}\tilde{\kappa}^2 + 4.3\times10^{-6}\tilde{\kappa}^3. \tag{3.2}$$

Their relationship was derived using four different fine grained soil textures ranging from sandy loam to clay with a range of fresh and salt water mixtures and saturation levels. TDR was used to measure the dielectric properties of soil samples placed in a coaxial transmission line. They concluded that this relationship could be appropriately applied over the range of moisture conditions

from air dry to water saturated with a prediction error of 0.013 m^3m^{-3}. In addition, they state that the permittivity measurement was almost independent of soil density, texture, dissolved salt content and temperature for the range of soil conditions tested (i.e., typical agricultural soils).

Nadler et al. (1991) investigated the effects of water content layering (e.g., dry over wet, wet over dry) in silt loam soil using different TDR probe designs. From their results, they obtained the following third-order polynomial relationship:

$$\theta = -7.25\times10^{-2} + 3.67\times10^{-2}\tilde{\kappa} - 12.3\times10^{-4}\tilde{\kappa}^2 + 15\times10^{-6}\tilde{\kappa}^3. \quad (3.3)$$

They concluded that accurate soil water content estimates could be obtained from the TDR method regardless of probe type and soil layering, except for the case of very dry soil overlying very wet soil which they attributed to difficult trace interpretation. However, they did not provide a quantitative error estimate for their petrophysical relationship.

Roth et al. (1992) established empirical relationships using TDR for mineral soils, organic soils and magnetic soils using eleven mineral soil horizons and seven organic soil horizons characterized by a range of chemical and physical properties. Based on measurements collected from nine non-magnetic mineral soil samples, they obtained the following third-order polynomial relationship with a prediction error of 0.015 m^3m^{-3}:

$$\theta = -7.28\times10^{-2} + 4.48\times10^{-2}\tilde{\kappa} - 19.5\times10^{-4}\tilde{\kappa}^2 + 36.1\times10^{-6}\tilde{\kappa}^3. \quad (3.4)$$

Curtis (2001) measured the dielectric properties of numerous soil samples with a range of dry bulk densities using a coaxial transmission/reflection apparatus operating at a frequency of 100 MHz, and proposed the following third-order polynomial:

$$\theta = -2.86 + 2.435\tilde{\kappa} - 3.421\times10^{-2}\tilde{\kappa}^2 + 2.37\times10^{-4}\tilde{\kappa}^3. \quad (3.5)$$

Further, Curtis (2001) stated that soil water content measurements were dependent on signal frequency with a potential 10% under prediction of volumetric water content using Equation (3.5) for high frequency (e.g., 500 MHz and 1000 MHz) measurements at higher permittivities (e.g., $\kappa \geq 30$). However, the relationships for the 500 MHz and 1000 MHz measurement frequencies that appear in the figures of that paper were not given.

Other researchers have considered explicitly incorporating the effects of soil texture, density and organic matter on permittivity measurements when developing empirical relationships. For example, Jacobsen and Schjønning (1993a) developed a standard third-order polynomial

$$\theta = -7.01\times10^{-2} + 3.47\times10^{-2}\tilde{\kappa} - 11.6\times10^{-4}\tilde{\kappa}^2 + 18\times10^{-6}\tilde{\kappa}^3, \tag{3.6}$$

with a prediction error of 0.012 m^3m^{-3} based on TDR measurements of packed soil samples. In addition, Jacobsen and Schjønning (1993a) proposed an enhanced third-order polynomial which incorporated the effects of dry bulk density (g/cm^3), clay content (wt. %) and organic matter (wt. %):

$$\begin{aligned}\theta = {} & -3.41\times10^{-2} + 3.45\times10^{-2}\tilde{\kappa} - 11.4\times10^{-4}\tilde{\kappa}^2 + 17.1\times10^{-6}\tilde{\kappa}^3 \\ & - 3.70\times10^{-2}\rho_b + 7.36\times10^{-4}\ (\%\ \text{clay}) + 47.7\times10^{-4}\ (\%\ \text{org. mat.}).\end{aligned} \tag{3.7}$$

These two relationships were obtained using a range of soil textures (e.g., coarse sand to sandy clay loam) which were packed at two different bulk densities (i.e., 1.35 g/cm^3 and 1.55 g/cm^3). The inclusion of soil bulk density (ρ_b), clay content and organic matter was shown to provide an improved prediction error (i.e., 0.0097 m^3m^{-3}) when compared to their standard equation.

Malicki et al. (1996) also developed an enhanced empirical relationship using data from Roth et al. (1992) that considered the effect of soil matrix. Their petrophysical relationship was based on the index of refraction, $\sqrt{\tilde{\kappa}}$, and the bulk density of the soil matrix (g/cm^3):

$$\theta = \frac{\sqrt{\tilde{\kappa}} - 0.819 - 0.168\rho_b - 0.159\rho_b^2}{7.17 + 1.18\rho_b}. \tag{3.8}$$

They concluded that for every 0.1 g/cm^3 deviation in soil bulk density around the value, ρ_o, used to define an insensitive-to-matrix relationship (e.g., Equation 3.2–3.6), an absolute error in moisture of $0.004 < \Delta\theta < 0.18$ m^3m^{-3} could be observed, depending on the ρ_o value and moisture conditions.

3.3.2 Volumetric Mixing Formulae

In contrast to the empirical relationships, volumetric mixing formulae relate the permittivity of the bulk material (i.e., $\tilde{\kappa}$) to the individual component permittivities within the system through their volume fractions. The general form of these mixing formulae for a system containing *n* dielectric components is

$$\left(\tilde{\kappa}\right)^{\alpha} = \sum_{i=1}^{n} \chi_i \left(\kappa_i\right)^{\alpha}, \tag{3.9}$$

where the exponent α is a geometrical fitting parameter representing the structure within the heterogeneous medium (Lichtenecker and Rother, 1931). The volume fraction and permittivity of the i^{th} component are given by χ_i and κ_i, respectively.

Near-surface soil is typically a three phase system (e.g., Roth et al., 1990) composed of air, solids and water that can be expressed as

$$\theta = \frac{\tilde{\kappa}^{\alpha} - (1-\phi)\kappa_s^{\alpha} - \phi\kappa_a^{\alpha}}{\kappa_w^{\alpha} - \kappa_a^{\alpha}}, \tag{3.10}$$

where ϕ represents soil porosity, while κ_a, κ_s and κ_w are the permittivities of the air, solid mineral and water constituents, respectively. Four phase mixing formulae have also been proposed that incorporate the contribution of bound water on the solid mineral grain to the bulk permittivity (e.g., Dobson et al., 1985).

The geometric fitting parameter theoretically ranges between -1 and 1 for electric fields which are oriented perpendicular and parallel to a layered medium. If it is assumed that the traveltime through the mixture is equivalent to the sum of the volume weighted traveltimes through the individual components, the geometric factor is equal to 0.5; setting κ_a = 1, Equation (3.10) becomes the Complex Refractive Index Model (CRIM) (Birchak et al., 1974; Wharton et al., 1980; Dobson et al., 1985; Heimovaara et al., 1994) given by

$$\theta = \frac{\sqrt{\tilde{\kappa}} - (1-\phi)\sqrt{\kappa_s} - \phi}{\sqrt{\kappa_w} - 1}. \tag{3.11}$$

Other experimental studies have proposed different values of the geometric parameter; for example, Roth et al. (1990) suggested α = 0.46 for a three phase system, while Dobson et al. (1985) suggested α = 0.65 for a four phase system. Other studies have shown that α can range between 0.25–0.8 (Brovelli and Cassiani, 2008 and references therein) depending on the geometry of the mineral grains and pore fluids. However, in most cases the CRIM has been found to produce adequate results (e.g., Roth et al., 1990; Robinson et al., 1999).

3.3.3 Effective Medium Approximations

Although volumetric mixing formulae account for the volume weighted contribution of each constituent, they do not explicitly connect the textural and structural contributions of the various constituents to the permittivity of a composite material. In contrast, effective medium approximations (e.g., the differential effective medium method) use microscale geometrical models to explicitly incorporate textural and structural information about the heterogeneous system into the prediction of dielectric properties. Various geometrical models have been developed that incorporate pore structure/geometry (e.g., Endres and Bertrand, 2006), grain shape (e.g., Sen, 1984; Kenyon, 1984; Tyč et al., 1988; Jones and Friedman, 2000) and pore-scale fluid distribution (e.g., Endres and Redman, 1996; Friedman, 1998; Cosenza et al., 2003; Chen and Or, 2006); these studies have demonstrated that the dielectric property of the medium is not solely a function of porosity and water content, which is the primary assumption of volumetric mixing formulae.

Given the versatility of geometrical models, there is a wide range of configurations (i.e., grain shape and pore fluid distributions) that could be used to represent partially saturated media. For the purposes of this study, we have elected to use simple models based on spherical geometries; this is a reasonable assumption given the low percentage of clay in our soils (e.g., Feng and Sen, 1985; Cosenza et al., 2003). By restricting the component shapes, we only require the permittivity and volume fractions of the individual components which results in a more straightforward model implementation (i.e., grain shape aspect ratios are not required).

The differential effective medium (DEM) approach (Norris et al., 1985) for deriving petrophysical relationships based on geometrical models has been extensively used to examine the dielectric properties of rocks and soils (e.g., Sen et al. 1984; Cosenza et al., 2003; Endres and Bertrand, 2006). The DEM method is based on an iterative inclusion embedding process where infinitesimally small volumes of the inclusions are sequentially embedded into the heterogeneous system; the electrical property of the effective medium that results from a given embedding constitute the electrical property of the background material for the next embedding step. The mathematical description of the embedding process (e.g., Endres and Bertrand, 2006) is parameterized in terms of a homogenization variable p that monotonically increases from 0 at the start to 1 when the embedding process is completed. In this study we consider three DEM type geometrical models that were applied in Endres and Redman (1996) to examine the permittivity dependence on soil water content.

Here, we consider a partially saturated porous soil composed of solid grains, air and water phases having permittivities κ_s, κ_a and κ_w, respectively. The porosity of soil is ϕ, and the pore water saturation is S_w. The effective dielectric permittivity of the resulting medium is given by κ^*. The first two models use different types of homogeneous spherical inclusions composed of either soil grains or air that are embedded into a water background. These models differ in terms of the embedding sequence used to construct the heterogeneous system. The sequential embedding model completely embeds the air spheres before embedding the mineral grain spheres; this sequence results in an effective two-phase composite with structures (e.g., air spheres) that have size scales significantly smaller than the subsequently embedded mineral spheres. The embedding of air spheres results in an effective pore filling having a permittivity κ_f given by the initial value problem

$$\frac{d\kappa(p)}{dp} = \frac{3(1-S_w)\kappa(p)}{S_w + p(1-S_w)} \quad \frac{\kappa_a - \kappa(p)}{\varepsilon_a + 2\kappa(p)}, \tag{3.12}$$

integrated from $\kappa(p = 0) = \kappa_w$ to $\kappa(p = 1) = \kappa_f$. The subsequent embedding of the spherical mineral grains into this effective pore filling is described by

$$\frac{d\kappa(p)}{dp} = \frac{3(1-\phi)\kappa(p)}{\phi + p(1-\phi)} \quad \frac{\kappa_s - \kappa(p)}{\kappa_s + 2\kappa(p)}, \tag{3.13}$$

integrated from $\kappa(p = 0) = \kappa_f$ to $\kappa(p = 1) = \kappa^*$. The effective pore filling is uniformly distributed throughout the composite system with the assumption that the air spheres are small in comparison to the size of the grains. Hence, the water phase remains interconnected for $S_w > 0$.

The second model uses a simultaneous embedding sequence that embeds both types of spherical inclusions (i.e., air and mineral grains) in a single process. In this case, the distribution of size scales is identical for both inclusion types. Further, the water phase remains interconnected through the embedding process. The effective dielectric permittivity of the resulting system is obtained from the following initial value problem

$$\frac{d\kappa(p)}{dp} = \frac{3\kappa(p)}{p(1-\theta)+\theta} \times \left[(1-\phi)\frac{\kappa_s - \kappa(p)}{\kappa_s + 2\kappa(p)} + (\phi-\theta)\frac{\kappa_a - \kappa(p)}{\kappa_a + 2\kappa(p)} \right], \tag{3.14}$$

which is integrated from $\kappa(p = 0) = \kappa_f$ to $\kappa(p = 1) = \kappa^*$. This simultaneous embedding scheme is the same as that used by Feng and Sen (1985) to examine partially saturated rock.

The third model uses coated grains consisting of an inner spherical mineral grain covered by a concentric shell of water that are embedded into an air background. Sen et al. (1981) have shown that the coated sphere can be represented by an equivalent homogeneous sphere with a dielectric permittivity, κ_{cs}, given by

$$\kappa_{cs} = \kappa_w \frac{3(1-\phi)\kappa_s + \theta(\kappa_s + 2\kappa_w)}{3(1-\phi)\kappa_w + \theta(\kappa_s + 2\kappa_w)}. \tag{3.15}$$

The effective dielectric permittivity of the composite material is obtained by integrating

$$\frac{d\kappa(p)}{dp} = \frac{3(1-\phi+\theta)\kappa(p)}{(\phi-\theta)+p(1-\phi+\theta)} \quad \frac{\kappa_{cs}-\kappa(p)}{\kappa_{cs}+2\kappa(p)} \tag{3.16}$$

from $\kappa(p = 0) = \kappa_a$ to $\kappa(p = 1) = \kappa^*$. This geometrical configuration specifically places the water on the grain surfaces, thereby permitting the air to form an interconnected phase.

The order in which inclusions are embedded and choice of background material controls the geometrical and structural conditions of the composite material. For instance, the sequential embedding sequence represents the case where very small, disconnected bubbles of air are uniformly distributed throughout the entire pore system, while the simultaneous embedding sequence represents the case of air being preferentially located in main pore bodies. In both of these scenarios, the water phase retains its connectivity throughout the porous material. Conversely, the coated grain configuration allows air to become the interconnected phase; this configuration could represent residually saturated soil conditions. While a number of different geometrical models could be constructed using the DEM approach, we examine three physically plausible models which are suitable for partially saturated media (e.g., Feng and Sen, 1985; Endres and Redman, 1996; Cosenza et al., 2003).

3.4 Description of the Field Measurements

Seasonal soil water content variations were monitored at three different locations characterized by sand, sandy loam and silt loam soils. The sand (528878E, 4814702N) and sandy loam (528938E, 4814594N) soils were located 3 km west of Waterloo, Ontario, Canada within a single agricultural field while the silt loam (519845E, 4770361N) soil was located 2 km south of Woodstock, Ontario, Canada. While haying operations were conducted during the study period, other agricultural

disturbances, such as plowing and tilling, were not performed at these sites during or in the recent past (i.e., within the preceding 2–5 years) prior to this study.

Average soil characteristics were determined in the upper half meter over 0.1 m depth intervals using a 3/4 inch diameter soil sampling probe; the samples were obtained approximately 1.0 m from each of the GPR lines. Analyses included hydrometer and dry sieve for grain size distribution, as well as the loss-on-ignition method (Dean, 1974) to estimate the percentage of organics. Dry soil bulk densities were estimated in the upper 0.2 m by extracting a known volume of soil using small aluminum cylinders and measuring their mass after they were oven dried at 105˚C for 24 hours; uncertainties in bulk density estimates were inferred from 2–4 repeat samples collected approximately 1.0 m from each of the GPR lines. Dry bulk densities were used to estimate soil porosities by assuming an average grain density of 2.65 g/cm^3. A detailed summary of the soil properties are provided in Table 3.1.

To assess direct ground wave (DGW) derived soil volumetric water content estimates, soil samples were concurrently collected over the upper half meter of soil at 0.1 m depth intervals in the immediate vicinity of each GPR line (i.e., within approximately 1–2 m of the GPR survey line) using the 3/4 inch diameter soil sampling probe. Soil samples were oven dried at 105˚C for 24 hours to obtain their gravimetric water content, which were converted to volumetric water content using dry soil bulk densities provided in Table 3.1. The number of CMP soundings collected at the three textural locations with corresponding gravimetric sampling is provided in Table 3.2 for each set of antenna frequencies. The uncertainties in gravimetric water content measurement used in this study represent an approximated confidence interval based on the soil bulk density variations.

DGW velocity measurements were obtained from CMP soundings that were conducted at a fixed midpoint position at each of the three textural locations using a Sensors & Software PulseEKKO 1000™ GPR system equipped with three sets of high frequency, bistatic antennae (i.e., 225 MHz, 450 MHz and 900 MHz). CMP surveys result in a distinct separation of the wavefields thereby permitting accurate DGW velocity determination over a sufficiently broad range of offset distances. Figure 3.1 shows a schematic diagram of a CMP survey (Figure 3.1a) and a representative CMP sounding (Figure 3.1b) illustrating the direct air wave and DGW, critically refracted air and ground waves, and reflected ground waves. The wavelet of the DGW events were composed of an initial peak (i.e., positive first half-cycle) followed by a trough (i.e., negative second half-cycle) and subsequent positive peak. Due to distortion along the leading edge of the first half-cycle as a result of wavefield

interference between DGW events and other arrivals (e.g., direct and refracted air waves), and the occasional superposition of wavelets, the zero-value between the first and second half-cycle was used to characterize DGW arrivals.

The GPR data was collected using a time window of 100 ns, sampling interval of 0.1 ns and 64 stacks per trace. Transmitter and receiver antennas were manually separated at 0.02 m increments from ~0.2 m to 2.0 m offset range. Prior to interpretation, all data sets were dewowed to remove low-frequency signal saturation arising from the radar equipment. Bandpass frequency filtering using cut-off frequencies of 25–550 MHz, 100–1000 MHz and 100–1400 MHz were applied to the 225 MHz, 450 MHz and 900 MHz data, respectively, to reduce incoherent noise. Variable spreading and exponential compensation gains were used to offset the effects of spherical spreading and exponential losses. A least squares linear analysis was applied to the DGW traveltime-offset measurements to obtain an estimate and standard error for the velocity derived from the slope of the best fitting line. The reader is referred to Steelman and Endres (2010) [Chapter 2] for a detailed discussion regarding the analysis of CMP soundings and DGW velocity measurements used in this study.

DGW velocity measurements were collected at the Woodstock silt loam site from May 2006 to the end of August 2007; data acquisition at the Waterloo sand and sandy loam sites took place between August 2006 and November 2007. Hence, these measurements encompass a wide range of unfrozen soil conditions typically observed in southern Ontario (i.e., wet autumn and spring; dry summer with occasional large storm events).

Due to the finite spatial dimensions of the DGW wavelet in the ground, its effective sampling depth had to be estimated to compare the GPR permittivities with the gravimetric soil moisture samples. While a number of studies have shown that DGW sampling depth is dependent on the in-situ signal wavelength and antenna offset (e.g., van Overmeeren et al., 1997; Huisman et al., 2003b; Galagedara et al., 2005b), the gross gravimetric sampling interval used to obtain the field volumetric water content measurement restricted our ability to rigorously evaluate DGW sampling depth at the centimeter scale. Therefore, we have simply estimated the average DGW sampling for the entire monitored period for each antenna frequency and soil site.

Our sampling depth estimates are based on the coefficient of determination r^2 from a linear regression analysis of the field-derived volumetric water contents and the index of refraction, $\sqrt{\tilde{\kappa}}$, obtained from DGW velocity; r^2 values were calculated using the data sets corresponding to each

antenna frequency at the three textural sites. The sampling depth analysis used the average water content from the 0.1 m sample depth intervals for cumulative depths between 0.1 to 0.5 m below ground surface. The cumulative sampling depth interval with the highest r^2 value was inferred to be the average DGW sampling depth. The results summarized in Table 3.3 indicate DGW sampling depths of 30 cm for the 225 MHz antennas and 20 cm for the 450 MHz and 900 MHz antennas at the sand site. For the sandy loam site, the DGW sampling depths are 10 cm for the 225 MHz and 900 MHz antennas and 20 cm for the 450 MHz antenna. The sampling depth at the silt loam site was 20 cm for all three frequencies. Steelman and Endres (2010) hypothesized that the lower sampling depths interpreted at the sandy loam site with 225 MHz and 900 MHz antenna were likely associated with the generally shorter antenna offset ranges used to measure DGW velocity due to the presence of a persistent ground refraction event at wide-angle offsets (e.g., at antenna offsets >1.0 m). It was also noted that the r^2 result for the 450 MHz 20 cm interval was similar to the 10 cm value (i.e., $r^2 = 0.849$ verses $r^2 = 0.839$, respectively) which suggests relatively consistent sampling depth results between the three frequencies at the sandy loam site.

3.5 Comparison of the Petrophysical Relationships

Our bulk soil permittivity $\tilde{\kappa}$ values calculated from the DGW velocity plotted as a function of their corresponding volumetric water content θ_{field} values determined from gravimetric soil sampling are presented in Figure 3.2 for 225 MHz, 450 MHz and 900 MHz antennae. It is clear that the sand data forms a distinct group over a lower range of permittivity ($3 \leq \tilde{\kappa} \leq 10$). While the data for the sandy and silt loams display appreciable overlap in a higher range of permittivity ($6 \leq \tilde{\kappa} \leq 26$), the sandy loam tends to exhibit lower water contents than the silt loams for comparable $\tilde{\kappa}$ values. Further, similar results were obtained for each of the GPR antenna frequencies; this lack of systematic frequency dependence indicates that frequency dispersion has minimal impact on our data set. While we only show the 450 MHz data in our petrophysical comparisons (i.e., Figures 3.3–3.5) for brevity, the results for each frequency is summarized in Tables 3.4 and 3.5.

To examine the suitability of these petrophysical relationships, we have superimposed them on plots of the soil permittivity and field water content measurements in Figure 3.3–3.5. The uncertainties in measured permittivity (i.e., horizontal error bars) were obtained from the least squares method used to calculate the standard error in the slope of a straight line that best fit the traveltime-

offset DGW data. These linear fitting uncertainties are generally small and are covered by the data points, particularly for the sand and silt loam data.

More significant levels of uncertainties are seen in the sample derived volumetric water content data that are represented by the vertical error bars. Our inference of these uncertainties (i.e., approximated confidence intervals) in water content was based on the soil bulk density measurements collected at each site. As a result, the sand, sandy loam and silt loam sites were given volumetric water content uncertainties of 0.01 m^3m^{-3}, 0.03 m^3m^{-3} and 0.02 m^3m^{-3}, respectively. It should be noted that because we collected repeat GPR measurements at each site, soil samples could not be collected directly along the GPR survey lines. A conscious effort was made to minimize the effects of inserting too many macropores (i.e., from the soil sampling probe) in the immediate vicinity of the GPR lines. Also, the number of bulk density samples which required a small pit had to be minimized. Consequently, there will be some level of inherent uncertainty associated with measurement location (i.e., possible small-scale spatial variability in moisture) and different sampling volumes between the GPR and soil samples which we could not rigorously account for in this study.

Both the volumetric mixing formulae and the effective medium approximations require values for the constituent permittivities (i.e., κ_a for air, κ_s for solids and κ_w for water). The air, solid mineral and liquid water constituents were assigned permittivities of $\kappa_a = 1$, $\kappa_s = 5$ and $\kappa_w = 82.232$. While the solid mineral permittivity value is appropriate for sand and loamy soils (Cassidy, 2009), we were not able to directly measure solid phase permittivity. Water content uncertainties resulting from the use of a fixed solid phase permittivity (i.e., $\kappa_s = 5$) could induce a static error in the petrophysical relationship. For instance, using a solid phase permittivity of 4 and 6 (rather than 5) would induce a static increase and decrease in the water content estimates, respectively; the magnitude of these static water content differences is dependent on the soil porosity. In the case of CRIM, a solid phase permittivity of 4 and 6 would shift water contents by as much as +0.019 m^3m^{-3} and –0.017 m^3m^{-3} for sand, +0.018 m^3m^{-3} and –0.016 m^3m^{-3} for sandy loam, +0.014 m^3m^{-3} and –0.013 m^3m^{-3} for silt loam relative to the value obtained using $\kappa_s = 5$. These moisture deviations are relatively independent on soil conditions (i.e., soil temperature and water contents).

Due to the absence of soil temperature measurements in this study, a water permittivity κ_w corresponding to a temperature $T = 15^{\circ}C$ was assumed; this seemed to represent a reasonable average value over our range of field conditions near the soil-air interface (i.e., approximately 5˚C to 25˚C).

For this temperature range, the permittivity of pure water can range between 86.1 (at 5˚C) and 78.5 (at 25˚C) (Weast et al., 1985). To evaluate the potential effect of temperature on the estimation of volumetric water content, we predicted water contents for each soil texture with a water permittivity value of κ_w = 86.1 and κ_w = 78.5, corresponding to the minimum and maximum range in near-surface soil temperatures. Since the empirical relationships discussed in this study do not have the capacity to account for changes in temperature, measures of volumetric water content using these water constituent values were obtained using the CRIM. Within the observed range of permittivities for each soil texture shown in Figure 3.2, the maximum potential difference (i.e., due to 20˚C temperature range) in predicted volumetric water content for dry and wet soil conditions at the sand site is 0.0003 m^3m^{-3} and 0.008 m^3m^{-3}, respectively. Similarly, the maximum potential difference in predicted volumetric water content at the sandy loam site for dry and wet soil conditions is 0.006 m^3m^{-3} and 0.021 m^3m^{-3}, respectively. Finally, the maximum potential difference in predicted volumetric water content at the silt loam site for dry and wet soil conditions is 0.006 m^3m^{-3} and 0.023 m^3m^{-3}, respectively. These results indicate that soil temperature variations could account for a maximum uncertainty of ±0.01 m^3m^{-3} if we assume a constant ground temperature of 15˚C. However, this level of uncertainty would only be observed during very wet soil conditions. While pore water temperature may have a variable effect on our water content estimates during the course of the annual period, we cannot explicitly account for these uncertainties in our analysis.

To quantitatively assess the accuracy of DGW volumetric soil water content estimates, the root-mean-squared-errors (RMSE) of the various petrophysical relationships were determined for each antenna frequency and soil texture using

$$RMSE = \sqrt{\frac{\sum_{i=1}^{N}\left(\theta_{field} - \theta_{pred}\right)^2}{N}}, \tag{3.17}$$

where N is the number of samples, θ_{field} is the volumetric water content obtained from soil sampling and θ_{pred} is the volumetric water content estimated from the GPR data using the petrophysical relationship. The RMSE results are summarized in Tables 3.4 and 3.5. Overall, these results indicate that the sand location was characterized by the lowest relative RMSE while the sandy loam and silt loam textural locations were characterized by relatively larger differences in volumetric water content values.

3.5.1 Empirical Relationships

In Figure 3.3a, we consider the empirical relationships proposed by Topp et al. (1980), Nadler et al. (1991), Roth et al. (1992), Curtis (2001) and Jacobsen and Schjønning (1993a) (Equation 3.2–3.6) where the prediction of water content is only a function of the measured permittivity. These empirical relationships give similar $\tilde{\kappa} - \theta$ relationships at lower permittivities (i.e., $\tilde{\kappa} < 10$) with the exception of Roth et al. (1992), which predicts volumetric water contents up to 0.025 m^3m^{-3} higher over this permittivity range. At higher permittivities (i.e., $\tilde{\kappa} > 15$), there is significant divergence between the empirical relationships with potentially 0.10 m^3m^{-3} difference in volumetric water content. In particular, both Nadler et al. (1991) and Jacobsen and Schjønning (1993a) consistently predict relatively lower water contents in comparison to the relationships of Topp et al. (1980), Roth et al. (1992) and Curtis (2001). When all of these empirical relationships are compared with our 450 MHz data, it can be seen that they over predict water contents for the sand texture, while under predict water contents for both loam textures.

Versions of enhanced empirical relationship by Jacobsen and Schjønning (1993a) (Equation 3.7) that incorporates additional information about soil bulk density, clay content and organic content, and Malicki et al. (1996) (Equation 3.8) that incorporates soil bulk density are shown in Figure 3.3b for our sand, sandy loam and silt loam soil textures. The incorporation of soil property information from Table 3.1 (i.e., corresponding to DGW sampling depths) into these empirical relationships progressively shifts them upward on the $\tilde{\kappa} - \theta$ plots as texture becomes increasingly finer grained. Both the Jacobsen and Schjønning (1993a) and Malicki et al. (1996) relationships produce a better match for the sand data in comparison to the other empirical relationships that are only dependent on permittivity. For the loam soils, however, the relationships proposed by Malicki et al. (1996) yields a much better fit to these data compared those obtained with Jacobsen and Schjønning (1993a). In particular, the Malicki et al. (1996) relationship strongly fits the silt loam data over the full range of water content conditions.

The RMSE results in Table 3.4 for these empirically derived relationships varied significantly in terms of both the petrophysical relationship and soil texture. For the sand soil, the enhanced empirical relationship proposed by Jacobsen and Schjønning (1993a) (Equation 3.7) resulted in the most accurate predictions of volumetric water content (i.e., RMSE = 0.012–0.017 m^3m^{-3}). The standard relationship proposed by Roth et al. (1992) gave the most accurate predictions for the sandy loam

(RMSE = 0.044–0.057 m^3m^{-3}) while the enhanced relationship proposed by Malicki et al. (1996) gave the best results for the silt loam (RMSE = 0.023–0.025 m^3m^{-3}) soil.

In addition, we developed a best fit third-order polynomial corresponding to our GPR permittivity measurements (i.e., using all the data in Figure 3.2). A reasonable fit, r^2 = 0.90, was found for the combined 225 MHz, 450 MHz 900 MHz measurements at the sand, sandy loam and silt loam data set:

$$\theta = -0.157 + 5.65\times10^{-2}\tilde{\kappa} - 2.03\times10^{-3}\tilde{\kappa}^2 + 2.97\times10^{-5}\tilde{\kappa}^3. \quad (3.18)$$

This GPR-derived relationship is plotted in Figure 3.3c with the sand, sandy loam and silt loam soil textures while a summary of its relative performance with respect to the individual antenna frequencies for each soil texture is summarized in Table 3.5. This relationship gave the most accurate predictions for the silt loam (RMSE = 0.016–0.020) soil while the least accurate predictions were obtained for the sandy loam (RMSE = 0.051–0.062 m^3m^{-3}) soil. The sand (RMSE = 0.038–0.043 m^3m^{-3}) soil showed marginally improved results compared to the sandy loam soil.

3.5.2 Volumetric Mixing Formulae

The three phase (i.e., air, solid and water) volumetric mixing formulae defined by Equation 3.10 are given in Figure 3.4a–c for sand, sandy loam and silt loam soils, respectively; the version for each soil texture uses the appropriate value of porosity ϕ given in Table 3.1. Mixing formulae having the geometric parameter values of α = 0.5 and 0.46 in Figure 3.4a–c are the CRIM and Roth et al. (1990) formulae, respectively. Additional mixing formulae are included for each soil texture to show the potential geometrical parameter range necessary to account for most of the variability in the field measurement.

The sand soil data presented in Figure 3.4a are nearly confined within the region defined by the exponent values α = 0.3 and α = 0.7. While the CRIM provides a better fit than the Roth et al. (1990) formula to the measured data, both tend to over predict volumetric water content for $\tilde{\kappa} \geq 6$. Much of the sandy loam data in Figure 3.4b is bounded by the relatively broader region between the exponent values of α = 0.1 and α = 0.7 due to scatter in the data; however, a number of data points are plotted outside this range at lower permittivity values. While the Roth et al. (1990) formula provides a slightly better fit to the sandy loam data, both the CRIM and Roth et al. (1990) formulae significantly under predict the soil water content data, particularly for $\tilde{\kappa} \leq 15$. The silt loam soil data in Figure 3.4c are confined between a more limited range of exponent values between α = 0.3 and α = 0.6

compared to the sandy loam and sand soil, reflecting the lower variability in the silt loam data. The volumetric mixing formulae for the silt loam (Figure 3.4c) showed better correlation to the field data compared to the sandy loam. For the silt loam case, the Roth et al. (1990) formula again provides the better fit to the data relative to the CRIM; however, both generally under predicted water content for this texture.

The RMSE results in Table 3.4 for both the CRIM and Roth et al. (1990) formulae indicate improved agreement with field data compared to the general empirical relationships; however, the results of these formulae were very similar to those observed with the enhanced empirical relationships. The RMSE results confirm that the CRIM provides better predictions for the sand soil (RMSE = 0.013–0.017 m^3m^{-3}) while the Roth et al. (1990) formula gives a better fit to the sandy loam (RMSE = 0.069–0.090 m^3m^{-3}) and silt loam (RMSE = 0.027–0.029 m^3m^{-3}) soils. It should be noted that these water content estimates could be improved slightly by adjusting the solid phase permittivity value, thereby applying a bulk shift in the $\tilde{\kappa} - \theta$ curve. For instance, increasing the solid phase value (i.e., $\kappa_s > 5$) for sand and decreasing the value (i.e., $\kappa_s < 5$) for loam soils would reduce a portion of the over and under predictions in water content.

In addition, exponent values for the best fitting volumetric mixing formulae were also determined for each soil texture. The best fitting formulae corresponding to 450 MHz data is plotted in Figure 3.4a–c, while a summary of the best fit exponents for all data sets is provided in Table 3.5. This analysis was conducted by determining the exponent value that yielded the lowest RMSE while maintaining the same constituent parameter values. These results indicate best fit exponent values of α = 0.52, α = 0.26 and α = 0.40 for the sand, sandy loam and silt loam soils, respectively, for the 450 MHz measurements. It should be noted that by optimizing the geometric parameter for each soil type we are effectively reducing some of the uncertainty associated with solid phase permittivity range. The range in the geometric parameter in this study is generally consistent with the range found by Ponizovsky et al. (1999); their results indicate that the best fit geometric parameter ranged from α = 0.25 to α = 0.52 using a range of soils (e.g., sand, loamy sand, sandy clay, clay and silt loam). However, the 225 MHz and 900 MHz parameter results at the sandy loam site in this study are somewhat lower (i.e., α = 0.21 and α = 0.11, respectively). These results clearly demonstrate the potential variability in the geometric parameter in terms of soil texture and to a lesser degree antenna frequency.

3.5.3 Effective Medium Approximations

Figure 3.5a–c show the computed $\tilde{\kappa} - \theta$ curves for sand, sandy loam and silt loam textures for the three geometrical models; as with the mixing formulae, each model used the appropriate value of porosity ϕ given in Table 3.1. The sand data matches well with all of the model-based relationships in Figure 3.5a. The sandy loam data in Figure 3.5b were only roughly matched by the geometrical models. Finally, the silt loam data in Figure 3.5c appears to be well represented by the coated mineral grain model across the entire range of $\tilde{\kappa} - \theta$ measurements. In this case, both embedded inclusion models significantly under predicted volumetric water content by up to 0.07 m^3m^{-3}. The RMSE results in Table 3.4 for the effective medium approximations show that the model based on the coated mineral grain gave the best prediction for sand (RMSE = 0.013–0.016 m^3m^{-3}), sandy loam (RMSE = 0.075–0.092 m^3m^{-3}) and silt loam (RMSE = 0.016–0.017 m^3m^{-3}) soils relative to the other geometrical models. In the case of silt loam, the difference in RMSE results between the coated sphere and the other embedding models is substantial (i.e., ~0.045 m^3m^{-3}).

3.5.4 Combined Petrophysical Datasets

It can be readily seen that the accuracy of a petrophysical relationship significantly varies in terms of the type of relationship and soil texture. In general, an appropriate petrophysical relationship for estimating soil volumetric water content would be one that could be applied to a range of soil textures with relatively low uncertainty. To make this evaluation, the RMSE results for combined single frequency data sets (e.g., combined soil textures for each antenna frequency) and the overall data set (e.g., combined soil textures with all three antenna frequencies) are also given in Table 3.4. These results indicate that the general empirical relationships proposed by Topp et al. (1980) and Roth et al. (1992) provided the most accurate estimates of volumetric water content for a range of soil textures and water content conditions (i.e., RMSE = 0.052 m^3m^{-3}) relative to the other empirical relationships. However, the incorporation of soil bulk density in the enhanced empirical relationship by Malicki et al. (1996) resulted in slightly improved water content estimates (i.e., RMSE = 0.048 m^3m^{-3}). With regards to volumetric mixing formulae, the geometric parameter used by Roth et al. (1990) (α = 0.46) yielded relatively better estimates of soil water content compared to those obtained with the standard CRIM (i.e., α = 0.5). However, the Roth et al. (1990) volumetric formula results are only marginally better than the Topp et al. (1980) and Roth et al. (1992) empirical relationships (i.e., 0.004 m^3m^{-3}), but is identical to that obtained with the enhanced empirical relationship of Makicki et al. (1996). Finally, the coated mineral grain geometric model was the most accurate for the range of soil textures and

conditions presented in this study (i.e., RMSE = 0.045 m^3m^{-3}). While the coated grain geometric model was the most accurate petrophysical relationship for the range of soil textures and water content conditions in this study, the overall improvement achieved by the effective medium approximation was minor (i.e., <0.01 m^3m^{-3}) relative to the other best fit relationships.

In addition, the RMSE results for our best fit GPR polynomial (Equation 3.18) and optimized volumetric mixing formulae (i.e., best fit geometric parameters) were also determined for combined single frequency data sets and the overall data set for each soil texture; these results are provided in Table 3.5. Our best fit GPR polynomial yielded a RMSE = 0.041 m^3m^{-3} for the range of soil textures and water contents considered in this study. Further, our results indicate a volumetric mixing formulae with α = 0.36 (RMSE = 0.042 m^3m^{-3}) would yield the most accurate estimates of soil water content. While these results are better than those obtained with the coated grain geometric model, the overall improvement achieved by these optimized relationships is only about 0.01 m^3m^{-3} water content.

Figure 3.6 illustrates the capacity of the best fitting petrophysical relationships to provide estimates of soil volumetric water content for the range of soil textures and measurement frequencies considered in this study. While these data confirm minimal frequency dependence, slight differences in their relative ability to provide water content estimates for the three soil textures are observed. For instance, one of the best fitting empirical relationships (i.e., Topp et al., 1980) (Figure 3.6a) over predicted water content for the sand while it under predicted water content for the loam soils. While the enhanced empirical relationship by Malicki et al. (1996) (Figure 3.6b) shows similar predictions to Topp et al. (1980), the relative magnitude of the deviations are reduced. The Roth et al. (1990) volumetric mixing formula (Figure 3.6c) shows improved estimates for sand and silt loam relative to the Topp et al. (1980) and Malicki et al. (1996) relationships; however, significant under predictions still occurred for the sandy loam soil during low to moderate water content conditions. Although the coated mineral grain effective medium approximation model (Figure 3.6d) shows further improvements for sand and silt loam soil, poorer results were obtained for the sandy loam site compared to the Roth et al. (1990) formula.

The best fit GPR polynomial relationship and optimized volumetric mixing formulae with the best fit geometric parameter (Figure 3.7a and b, respectively) yielded similar RMSE for the combined data set; however, their textural performance varied considerably. For instance, the sand data was much better predicted using the best fit volumetric mixing formula while the loam data was better predicted

using the best fit GPR polynomial. Clearly, all of these relationships (Figure 3.6 and 3.7) show textural biases that may not necessarily be reflected in the overall RMSE value; hence, the choice of petrophysical relationship for a particular data set should also consider the dominant textural conditions.

3.6 Conclusions

We have examined the effect of the choice of petrophysical relationship on the estimates of volumetric water content derived from soil permittivities obtained from high-frequency GPR DGW velocity data. The GPR field data were obtained for three distinct soil textures (i.e., sand, sandy loam and silt loam) covering a complete range of natural soil moisture conditions common to mid-latitude climates. While a range of antenna frequencies were used (i.e., 225 MHz, 450 MHz and 900 MHz), the lack of frequency dispersion produced very similar results for each frequency analyzed.

Empirical relationships, volumetric mixing formulae and effective medium approximations using spherical inclusions were used to predict water content from the DGW velocity measurements. Soil water content estimates varied significantly depending on the type of petrophysical relationship used to predict volumetric water content and soil textural conditions (i.e., by as much as 0.07 m^3m^{-3}). While differences were also observed between the three antenna frequencies, they were typically <0.01 m^3m^{-3}.

The results of this study found that empirical relationships primarily over predicted water contents at the sand site while under predicted water content at the sandy loam and silt loam sites. The relative performance of these relationships varied with soil texture. For instance, the enhanced empirical relationship incorporating soil property information (e.g., soil bulk density, organic and clay content) proposed by Jacobsen and Schjønning (1993a) producing the best agreement with the soil sampling for the sand soil (i.e., RMSE = 0.012–0.017 m^3m^{-3}). The general empirical equation by Roth et al. (1992) provided the best fit for the sandy loam soil (i.e., RMSE = 0.044–0.057 m^3m^{-3}). Finally, the enhanced empirical relationship that incorporated soil bulk density by Malicki et al. (1996) yielded the best fit for the silt loam soil (i.e., RMSE = 0.023–0.025 m^3m^{-3}). When the entire data set was analyzed using the general empirical expressions, we found that the Topp et al. (1980) and Roth et al. (1992) relationships provided the most accurate predictions of volumetric water content (i.e., RMSE = 0.052 m^3m^{-3}). However, slightly improved predictions were achieved by using the enhanced

empirical equation by Malicki et al. (1996) (i.e., RMSE = 0.048 m^3m^{-3}) for the full range of soil textures and water content conditions considered in this study.

Similar to the empirical relationships, we found that the CRIM and Roth et al. (1990) volumetric mixing formulae slightly over predicted water contents at the sand site, while under predicted water contents at the sandy loam and silt loam sites. When we consider each texture, it was shown that the CRIM provided more accurate estimates of water content at the sand site (i.e., RMSE = 0.013–0.017 m^3m^{-3}) while the Roth et al. (1990) model was better suited for the sandy loam (i.e., RMSE = 0.069–0.090 m^3m^{-3}) and silt loam (i.e., RMSE = 0.027–0.029 m^3m^{-3}) soils. For the entire data set, the Roth et al. (1990) formulae produced better results than the CRIM (i.e., 0.048 m^3m^{-3} verses 0.054 m^3m^{-3}, respectively), but only performed slightly better than the general empirical relationships.

The functional relationships defined by the three effective medium approximations showed contrasting degrees of fit to the data for the three soil textures. While the sequential embedding, simultaneous embedding and coated mineral grain models all matched well with the data collected at the sand site, the coated mineral grain model yielded slightly better results (i.e., RMSE = 0.013–0.016 m^3m^{-3}). In comparison, the data collected at the sandy loam site were only loosely fitted with any of the geometric models, while the silt loam data were very well predicted by only the coated mineral grain model. Here, the coated grain models provided the most accurate predictions for the sandy loam (RMSE = 0.075–0.092 m^3m^{-3}) and silt loam (RMSE = 0.016–0.017 m^3m^{-3}) soils. Although the coated grain model yielded the best fit for the entire data set (i.e., RMSE = 0.045 m^3m^{-3}) compared to any other established empirical equation or volumetric mixing model considered in this study, the overall improvement was less than 0.01 m^3m^{-3} water content.

Further improvements in water content could be obtained using our best fit third-order polynomial relationship, Equation (3.18), based on our GPR permittivity measurements and gravimetric water contents. This relationship was determined using the combined 225 MHz, 450 MHz 900 MHz measurements at the sand, sandy loam and silt loam data set with a RMSE = 0.041 m^3m^{-3}. In addition, we determined an optimal geometric parameter in the volumetric mixing formula for each of the three soil textures. The range of optimal values we found in our analysis (i.e., sand: α = 0.49–0.53 with RMSE = 0.012–0.017 m^3m^{-3}; sandy loam: α = 0.11 – 0.26 with RMSE = 0.041–0.055 m^3m^{-3}; silt loam: α = 0.38–0.41 with RMSE = 0.018–0.022 m^3m^{-3}) demonstrates the variability in the geometric parameter with changing soil texture and to a less degree antenna frequency. However, due to this dependence on soil texture, less overall improvement was achieved for the sand and silt loam soil

when we optimized the geometric parameter using the total data sets (i.e., combining data from all three soil textures). Here, we obtained a best fit geometric parameter α = 0.36 with RMSE = 0.042 m^3m^{-3}.

Using our multi-frequency DGW field measurements for a complete annual cycle of unfrozen soil conditions, we have illustrated the effect of petrophysical relationship on the estimation of volumetric soil water content. The accuracy of soil water content predictions obtained from the various petrophysical relationships within each of our three categories (i.e., empirical relationship, volumetric mixing formulas and effective medium approximation) ranged considerably. For the complete data set, we found the best fitting empirical relationship, volumetric mixing formula and effective medium approximation yield comparable estimates of soil water content. These best fitting relationships do exhibit some degree of textural bias that should be considered in the choice of petrophysical relationship for a given data set.

3.7 Tables and Figures

Table 3.1 Textural properties in the upper 0.5 m of soil, including textural classification, grain size distribution (wt %), organic content (wt. %), dry bulk density (g/cm^3) and porosity.

Site	Texture	Sampling Depth	Sand	Silt	Clay	Organic	Bulk Density	Porosity
		cm	*% wt*				*g/cm^3*	-
Waterloo	sand	0 - 10	97.0	3.0	0.0	1.6		
		10 - 20	98.0	2.0	0.0	1.4	1.68[a]	0.37[a]
		20 - 30	98.0	2.0	0.0	1.1		
		30 - 40	96.0	4.0	0.0	1.1		
		40 - 50	97.0	3.0	0.0	-		
Waterloo	sandy loam	0 - 10	64.0	32.0	4.0	5.6		
		10 - 20	69.0	27.0	4.0	3.2	1.59[a]	0.40[a]
		20 - 30	68.0	29.0	3.0	5.5		
		30 - 40	72.0	23.0	5.0	4.0		
		40 - 50	87.0	10.0	3.0	0.7		
Woodstock	silt loam	0 - 10	24.0	71.0	5.0	8.2		
		10 - 20	17.0	78.0	5.0	6.9	1.23[a]	0.54[a]
		20 - 30	16.0	81.0	3.0	3.2		
		30 - 40	13.0	81.0	6.0	3.3		
		40 - 50	15.0	83.0	2.0	3.8		

[a] dry bulk density measurements and corresponding porosity estimates refer to the upper 20 cm of soil.

Table 3.2 Summary of r^2 results based on the linear regression of field-derived volumetric water contents and $\sqrt{\tilde{\kappa}}$ from DGW velocity measurements.

Soil Texture	**Sand**	**Sandy Loam**	**Silt Loam**
	28-Aug-06 to 13-Nov-07	28-Aug-06 to 13-Nov-07	19-May-06 to 31-Aug-07
225 MHz	23	19	20
450 MHz	26	23	20
900 MHz	34	23	20

Table 3.3 Summary of the CMP soundings collected with corresponding gravimetric samples.

Soil Texture	**Sand**			**Sandy Loam**			**Silt Loam**		
	225	**450**	**900**	**225**	**450**	**900**	**225**	**450**	**900**
	MHz			*MHz*			*MHz*		
Cumulative Sampling Depth (cm)									
10	0.723	0.675	0.697	0.819[a]	0.839	0.910[a]	0.942	0.934	0.935
20	0.884	0.873[a]	0.881[a]	0.792	0.849[a]	0.895	0.973[b]	0.968[a]	0.964[a]
30	0.890[a]	0.870	0.852	0.720	0.800	0.833	0.973	0.967	0.960
40	0.888	0.833	0.780	0.650	0.732	0.760	0.966	0.960	0.949
50	0.861	0.740	0.670	0.611	0.696	0.714	0.962	0.955	0.943

[a] approximate DGW sampling depths.
[b] DGW sampling depth determined using four significant figures (values not shown).

Table 3.4 The RMSE for GPR-derived water content estimated using the empirical relationships, volumetric mixing formulae and effective medium approximations.

Petrophysical Relationship	Sand			Sandy Loam			Silt Loam			Combined Data			
	225	450	900	225	450	900	225	450	900	225	450	900	All
	MHz			*MHz*			*MHz*			*MHz*			
Empirical Relationships													
Topp et al., 1980; Eq. (2)	0.027	0.026	0.023	0.075	0.065	0.086	0.050	0.047	0.045	0.053	0.048	0.056	0.052
Nadler et al., 1991; Eq. (3)	0.028	0.028	0.024	0.087	0.073	0.099	0.090	0.088	0.087	0.073	0.066	0.072	0.070
Roth et al., 1992; Eq. (4)	0.053	0.052	0.048	0.057	0.045	0.044	0.048	0.044	0.042	0.053	0.048	0.054	0.052
Curtis, 2001; Eq. (5)	0.030	0.028	0.025	0.078	0.066	0.089	0.054	0.050	0.048	0.056	0.050	0.057	0.055
Jacobsen and Schjønning, 1993a; Eq. (6)	0.024	0.023	0.020	0.086	0.074	0.101	0.078	0.074	0.072	0.067	0.060	0.067	0.065
Jacobsen and Schjønning, 1993a; Eq. (7)	0.012	0.015	0.017	0.090	0.077	0.104	0.064	0.060	0.058	0.063	0.051	0.060	0.080
Malicki et al., 1996; Eq. (8)	0.022	0.021	0.018	0.078	0.066	0.090	0.025	0.023	0.023	0.048	0.042	0.052	0.048
Volumetric Mixing Formulae													
Complex Refractive Index (α=0.5)	0.013	0.016	0.017	0.086	0.075	0.099	0.039	0.036	0.035	0.053	0.049	0.058	0.054
Roth et al., 1990 (α=0.46)	0.016	0.019	0.017	0.079	0.069	0.090	0.029	0.027	0.027	0.048	0.044	0.053	0.048
Effective Medium Approximations													
Sequential Embedding	0.014	0.019	0.022	0.102	0.091	0.108	0.065	0.060	0.059	0.069	0.066	0.071	0.069
Simultaneous Embedding	0.013	0.017	0.020	0.098	0.087	0.104	0.061	0.057	0.055	0.065	0.064	0.068	0.056
Coated Rock Grains	0.013	0.015	0.016	0.086	0.075	0.092	0.016	0.016	0.017	0.049	0.038	0.047	0.045

Table 3.5 Results of our best fit GPR third-order polynomial and optimized volumetric mixing formulae.

Soil Texture	**Sand**			**Sandy Loam**			**Silt Loam**			**Combined Data**			
	225	***450***	***900***	***225***	***450***	***900***	***225***	***450***	***900***	***225***	***450***	***900***	***All***
	MHz			*MHz*			*MHz*			*MHz*			
Best Fit Polynomial; Eq (18)													
RMSE	0.038	0.043	0.038	0.054	0.051	0.062	0.020	0.017	0.016	0.040	0.041	0.043	0.041
Best Fit Mixing Formulae													
Geometric Parameter (α)	0.53	0.52	0.49	0.21	0.26	0.11	0.38	0.40	0.41	0.36	0.38	0.34	0.36
RMSE	0.012	0.016	0.017	0.055	0.050	0.041	0.018	0.020	0.022	0.041	0.039	0.044	0.042

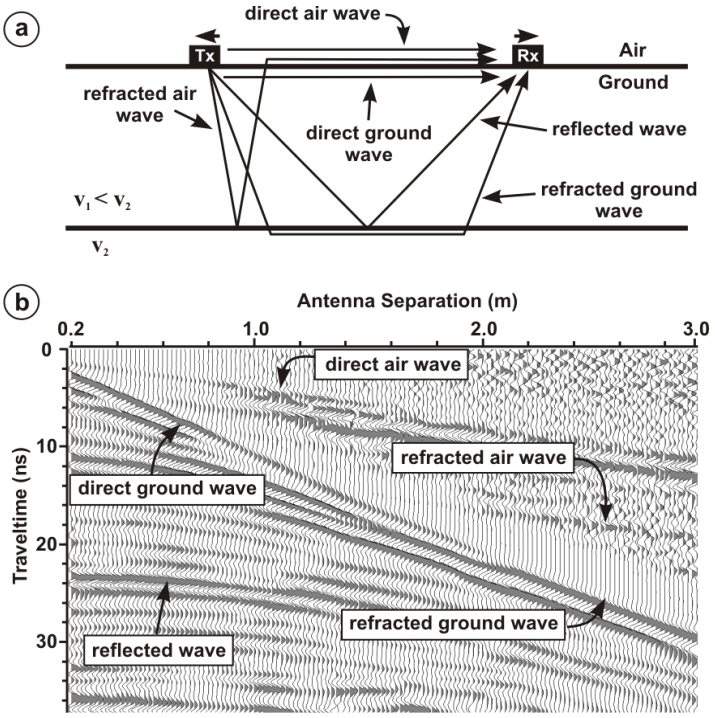

Figure 3.1 (a) Schematic diagram of a CMP survey illustrating typical wavefields and (b) a representative CMP sounding. The direct ground wave is characterized by a linear traveltime-antenna offset relationship; modified from Huisman et al. (2003a).

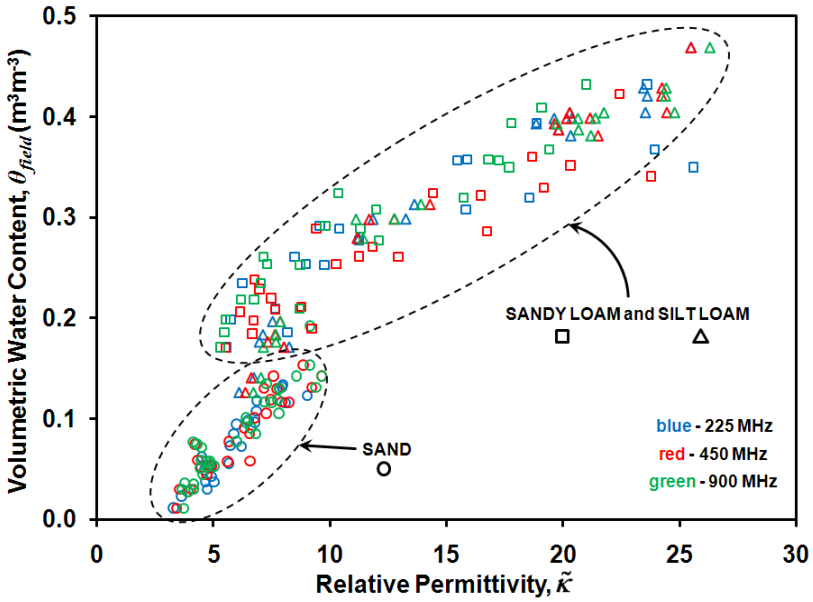

Figure 3.2 Soil permittivity calculated from the DGW velocity for 225 MHz (blue), 450 MHz (red) and 900 MHz (green) antennae with corresponding volumetric water content determined from gravimetric soil sampling. The sand (○) data forms a distinct group over a lower range in permittivity while the sandy loam (□) and silt loam (△) data display appreciable overlap in a higher range of permittivity. Note: error bars have been removed for clarity.

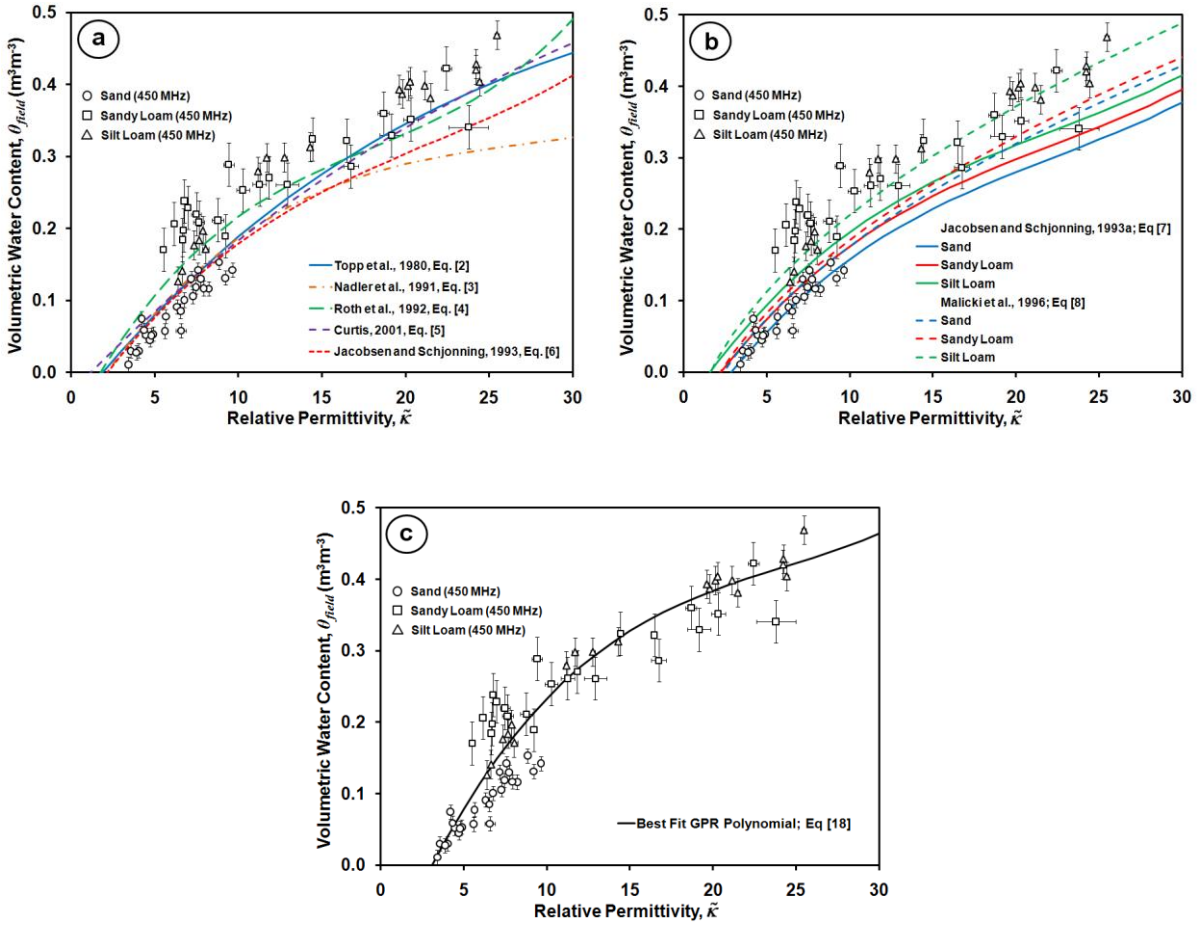

Figure 3.3 GPR permittivity with corresponding volumetric water content collected at the sand (○), sandy loam (□) and silt loam (△) textural locations with 450 MHz antennas. (a) Data superimposed with empirical equations proposed by Topp et al. (1980), Nadler et al. (1991), Roth et al. (1992), Curtis (2001) and Jacobsen and Schjønning (1993a) (Equation 3.2–3.6). (b) Data superimposed with Jacobsen and Schjønning (1993a) (Equation 3.7) and Malicki et al. (1996) (Equation 3.8) using additional soil textural information provided in Table 3.1. (c) Data superimposed with our best fit third-order polynomial (Equation 3.18) determined using the data presented in this study (i.e., Figure 3.2).

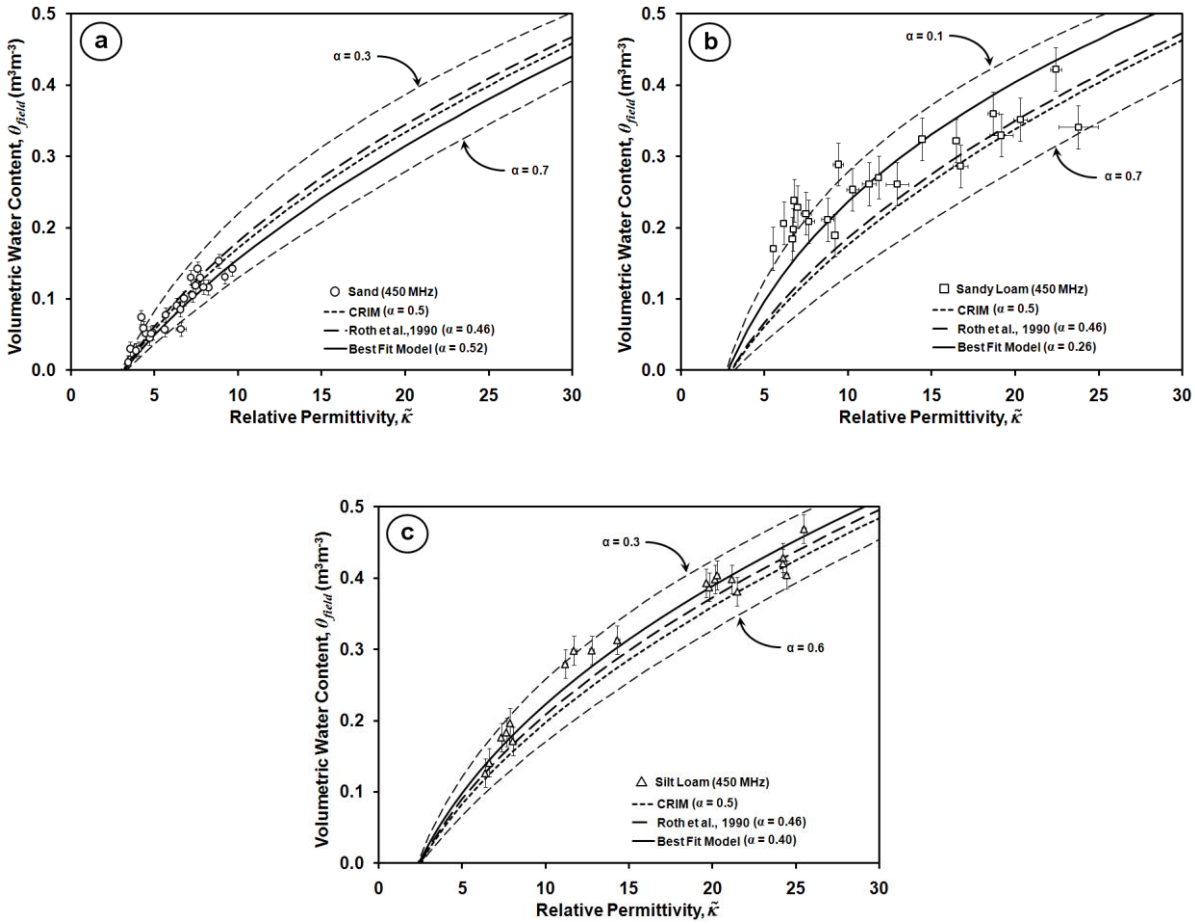

Figure 3.4 GPR permittivity with corresponding volumetric water content collected at (a) sand (○), (b) sandy loam (□) and (c) silt loam (△) textural locations with 450 MHz antennas. Geometric parameters (α) encompassing GPR data at each soil texture are presented. Data are superimposed with CRIM (α = 0.5) and Roth et al. (1990) formula (α = 0.46). Models demonstrating best fit geometric parameter for 450 MHz data are also shown.

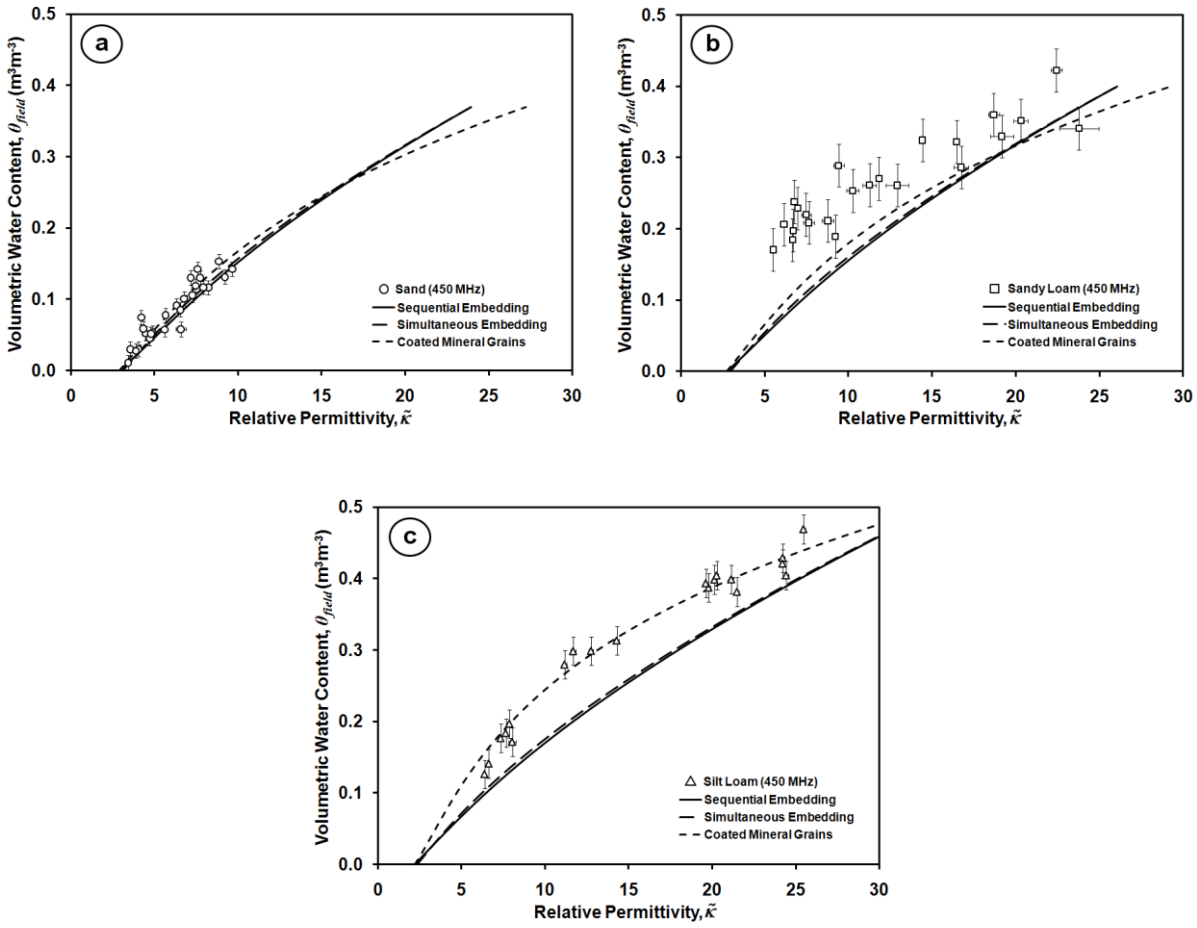

Figure 3.5 GPR permittivity with corresponding volumetric water content collected at (a) sand (○), (b) sandy loam (□) and (c) silt loam textural (△) locations with 450 MHz antennas. Effective medium approximation models are plotted for the corresponding soil textures.

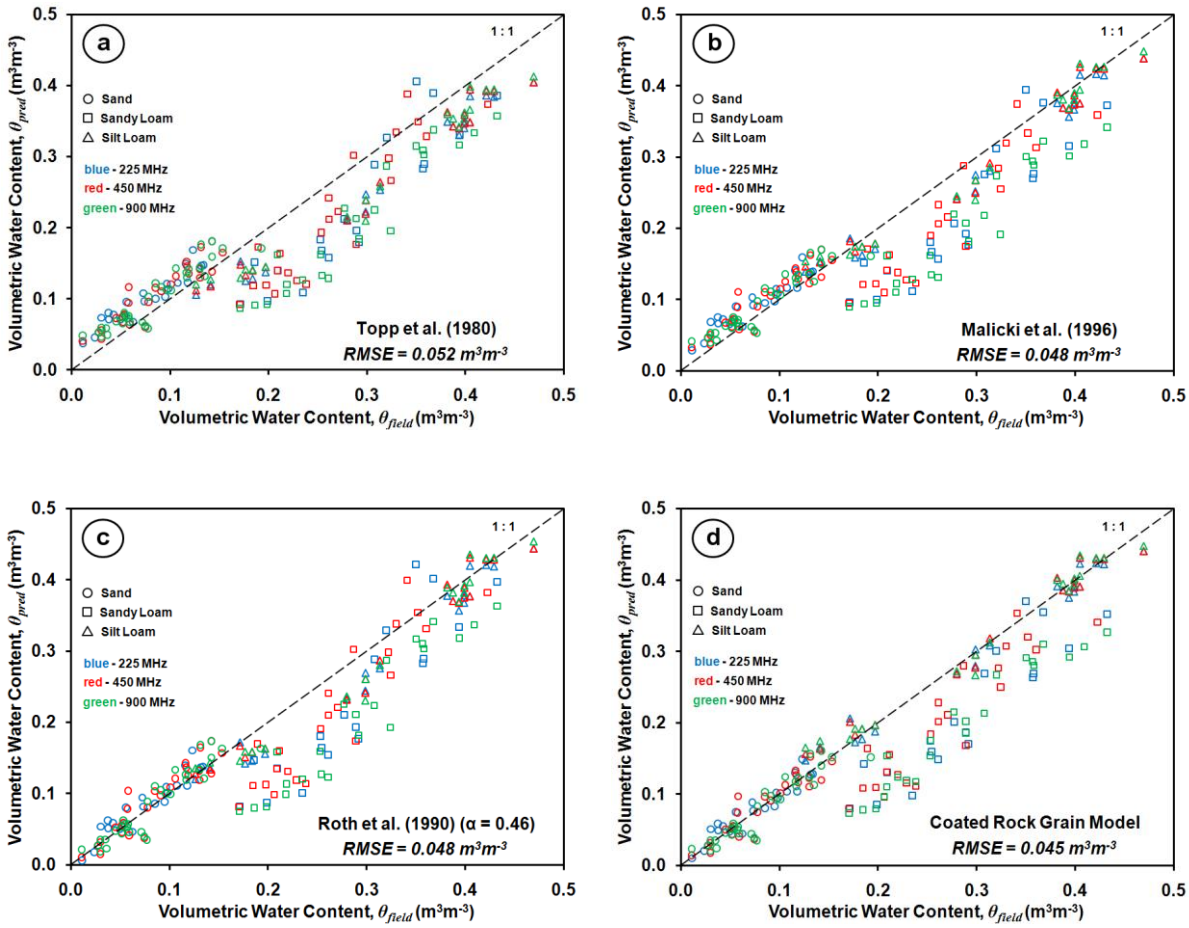

Figure 3.6 The correlation between field-derived volumetric water content and GPR-derived volumetric water content for sand (○), sandy loam (□) and silt loam (△) soils using 225 MHz (blue), 450 MHz (red) and 900 MHz (green) for (a) Topp et al. (1980) empirical equation, (b) Malicki et al. (1996) enhanced empirical equation, (c) Roth et al. (1990) mixing formulae, (d) coated mineral grain effective medium approximation. Note: error bars have been removed for clarity.

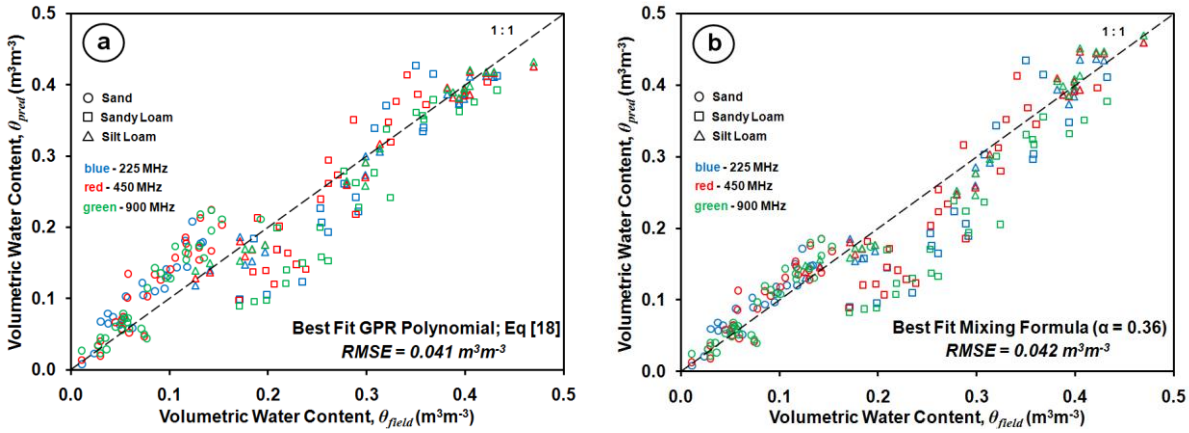

Figure 3.7 The correlation between field-derived volumetric water content and GPR-derived volumetric water content for sand (○), sandy loam (□) and silt loam (△) soils using 225 MHz (blue), 450 MHz (red) and 900 MHz (green) for (a) best fit third-order polynomial (Equation 3.18) and (b) volumetric mixing formula with optimized geometric parameter for the combined multi-frequency data set. Note: error bars have been removed for clarity.

Chapter 4

Assessing Vertical Soil Moisture Dynamics using Multi-Frequency GPR Common-Midpoint Soundings[3]

4.1 Executive Summary

Soil moisture measurement techniques are of utmost importance to vadose zone hydrologists. Surface hydrogeophysical methods, such as ground-penetrating radar (GPR), have the capacity to provide field-scale soil moisture information across a range of depth scales. This paper presents an extensive field study using multi-frequency (i.e., 225 MHz, 450 MHz, 900 MHz) GPR common-midpoint (CMP) soundings to monitor a complete annual cycle of soil moisture conditions at three distinct sites. We examine the use of normal-moveout (NMO) velocity analysis applied to CMP data for monitoring highly dynamic vertical soil moisture conditions in a mid-latitude climate consisting of wetting/drying and freeze/thaw cycles with varying degrees of magnitude and vertical velocity gradient. NMO velocity analysis is used to construct interval-velocity-depth models at a fixed location collected every 1 to 4 weeks. These time-lapse models are combined to construct temporal interval-velocity fields, which are converted into soil moisture content using an appropriate petrophysical relationship. Using these moisture fields, we were able to characterize the vertical distribution and dynamics of soil moisture in the shallow vadose zone. Although the use of multiple antenna frequencies provided varying investigation depths and vertical resolving capabilities, optimal characterization of soil moisture conditions was obtained with high-frequency 900 MHz antennas. The integration of direct ground wave and NMO velocity data from a single CMP sounding allowed us to better refine the shallow soil moisture profile and underlying vadose zone conditions during seasonal wetting, drying and freezing cycles. This study demonstrates the capacity of GPR to characterize vertical moisture dynamics, and highlights the importance of collecting high-resolution data along the air-soil interface to resolve the water content profile from the surface down to the deeper vadose zone conditions.

[3] Steelman, C.M., and Endres, A.L. Assessing vertical soil moisture dynamics using multi-frequency GPR common-midpoint soundings. *Journal of Hydrology*, doi: 10.1016/j.jhydrol.2012.02.041 (accepted 21/2/2012).

4.2 Introduction

Soil water content is a fundamental component in the prediction of hydrological state variables (e.g., soil moisture fields, soil water storage), soil hydraulic properties (e.g., hydraulic conductivity function, water retention curve) and hydraulic fluxes (e.g., infiltration, redistribution, drainage) at both the field and catchment scale. Numerous studies have demonstrated the value of soil moisture data to the characterization of vadose zone hydrology; recent reviews on this topic have been published by Vereecken et al. (2008) and Robinson et al. (2008). The vadose zone is also a fundamental component of the climate system because it governs plant transpiration and photosynthesis, and acts as a storage component for water and energy (Seneviratne et al., 2010). Moisture conditions are also important for the characterization of seasonal freeze and thaw cycles (Luo et al., 2003), and hence the evaluation of overland flow potential (Nyberg et al., 2001), melt water recharge (Bayard et al., 2005) and soil thermal conductivity. Freeze and thaw processes also play an important role in the evolution of soil functioning (i.e., changes in soil physical properties, microorganisms, carbon and nutrient dynamics) (Henry, 2007). Techniques that provide in-situ estimates of soil moisture distribution are fundamental to hydrologic studies.

Conventional moisture monitoring techniques such as gravimetric sampling, thermal neutron probes and time-domain reflectometry (TDR) provide highly localized information and are generally invasive; further, these methods are not well suited for efficient acquisition of spatial data. Alternately, remote sensing imagery has low spatial resolution and lacks the depth of investigation necessary to estimate vertical hydraulic fluxes. Hence, surface hydrogeophysical methods are increasingly recognized (e.g., Vereecken et al., 2008; Robinson et al., 2008) as an important source of soil moisture information at the field scale due to their sampling volume (i.e, dm3–m3 scale), non-invasive nature, good depth of investigation (1–10 m) and high resolving power. In particular, ground-penetrating radar (GPR) techniques have been proven to be very useful for monitoring vadose zone soil water content at the field scale (Huisman et al., 2003). While GPR data are dependent on the same electromagnetic (EM) properties that govern TDR response, its larger sampling volume and non-invasive nature makes it much less affected by measurement errors associated with macropores (e.g., root and worm holes) and air gaps along sensors that may impact TDR measurements (Robinson et al., 2003).

Two important requirements of vadose zone hydrology are the vertical soil moisture distribution within the vadose zone and the nature of its coupling with soil moisture variations at the surface

(Vereecken et al., 2008); this information is needed to quantify moisture storage, estimate groundwater recharge, and quantify exchange of water and energy between the soil and atmosphere. A technique for obtaining information about the vertical moisture profile from surface GPR measurements utilizes the normal-moveout (NMO) velocity analysis of the offset distance-traveltime relationship for subsurface reflection events in common-midpoint (CMP) data. The results of NMO velocity analysis are subsequently used to determine the interval velocities of layers in the subsurface. NMO velocity analysis and interval velocity determination were originally developed for application to seismic reflection data and have been extensively analyzed in the literature (e.g., Taner and Koehler, 1969; Shah and Levin, 1973; Castle, 1994; Yilmaz, 2001). Recently, their application to GPR data for obtaining subsurface EM wave velocity information has been examined in a number of papers (e.g., Tillard and Dubois, 1995; Jacob and Hermance, 2004; Becht et al., 2006; Barrett et al. 2007; Booth et al., 2010).

Studies by Greaves et al. (1996), Garambois et al. (2002) and Turesson (2006) have applied NMO velocity analysis and interval velocity determination to GPR CMP data to characterize the spatial distribution of soil moisture in the vadose zone. However, these studies lack the temporal component necessary to critically examine the ability of this approach to monitor over a range of annual conditions the vertical soil moisture distribution within the vadose zone and the nature of its coupling with very shallow soil moisture variations.

To address this point, we have undertaken an extensive field study to examine the use of NMO velocity analysis applied to CMP data for monitoring vertical soil moisture variations over a complete annual cycle of soil conditions (i.e., dry summer, wet spring and autumn, frozen winter soil conditions) typical of mid-latitude climates; as a result, our data set covers a wide range of in-situ vertical velocity conditions in terms of magnitude and gradient. By collecting multi-frequency (i.e., 225 MHz, 450 MHz and 900 MHz) data sets at three sites with different soil textures (i.e., sand, sandy loam and silt loam), we will examine the effects of the trade-off between resolving power and depth of penetration inherent in GPR surveys. Our ability to obtain reliable interval velocity measurements from NMO analysis will also be assessed. Further, the fact that these data yield information at discrete depth intervals in the shallow vadose zone enables us to evaluate the nature of the coupling between surface and deeper moisture conditions.

4.3 NMO Velocity Analysis and Interval Velocity Determination

Surface GPR techniques use a transmitting antenna positioned on the surface (i.e., air-ground interface) that radiates short pulses of EM waves commonly in the bandwidth between 10 MHz and 1 GHz. These propagating EM fields respond to changes in material electrical properties which are recorded by a receiving antenna also located on the surface. For non-magnetic low-loss soils, the propagation velocity (v) of EM waves within GPR bandwidth primarily depends on the relative permittivity (κ) (i.e., the effective permittivity of the bulk material ε relative to the free space permittivity, ε_o). This relationship is defined by the equation

$$v = \frac{c}{\sqrt{\kappa}}, \tag{4.1}$$

where c is the EM velocity in free space (0.2998 m/ns). Within this bandwidth, the relative permittivity of liquid water (κ_w = 78–88) contrasts strongly with other common components of the soil system (i.e., mineral soil grains κ_s = 4–6 and air κ_a = 1), as well as ice (κ_i = 3.2) (Cassidy, 2009). This relative permittivity contrast provides the basis for estimating liquid volumetric water content using EM wave velocity measurements.

CMP surveys systematically separate a transmitting and receiving antenna about a fixed midpoint (M) position (Figure 4.1a), which results in a separation of coherent events in the wavefield (e.g., direct waves and reflections) (Figure 4.1b). This separation allows the extraction of subsurface EM wave velocity information from the various events through the analysis of their respective traveltime-offset distance relationships. Direct ground waves (DGW) possess a linear traveltime-offset relationship in CMP data such that the velocity is obtained from a line-fitting procedure (Steelman and Endres, 2010) [Chapter 2]. The traveltime-offset relationship for the reflections in CMP data is more complicated and requires a different analysis technique.

Let us consider the reflection event from the Nth interface in a horizontally layered subsurface (Figure 4.2) where the N^{th} layer has a thickness and interval velocity h_N and v_N, respectively. The relationship between the antenna offset distance x and the corresponding two-way traveltime $t_x(N)$ for this event can be expressed in terms of the following power series expansion (Yilmaz, 2001):

$$\left[t_x(N)\right]^2 = C_0(N) + C_1(N)\,x^2 + \sum_{i=2}^{\infty} C_i(N)\,x^{2i}, \tag{4.2}$$

where $C_0(N) = \left[t_0(N)\right]^2$, $C_1(N) = 1 \Big/ \left[V_{RMS}(N)\right]^2$ and $C_i(N)$ are functions that depend on layer thicknesses and interval velocities. The normal incident two-way traveltime $t_0(N)$ and root-mean-squared velocity $V_{RMS}(N)$ in Equation (4.2) are defined as

$$t_0(N) = \sum_{i=1}^{N} \Delta\tau_i \tag{4.3}$$

and

$$\left[V_{RMS}(N)\right]^2 = \frac{1}{t_0(N)} \sum_{i=1}^{N} v_i^2 \, \Delta\tau_i, \tag{4.4}$$

where $\Delta\tau_i = 2h_i / v_i$ is the normal incident two-way traveltime through the i^{th} layer. If the source and receiver offset are small compared to the depth of investigation (i.e., small-spread approximation), the higher order terms in Equation (4.2) can be neglected; as a result, we obtain the hyperbolic offset-distance-traveltime equation

$$\left[t_x(N)\right]^2 = \left[t_0(N)\right]^2 + x^2 \Big/ \left[V_{RMS}(N)\right]^2. \tag{4.5}$$

NMO velocity analyses are based on an analogous hyperbolic form of the offset-distance-traveltime relationship for reflection events. For the reflection event from the N^{th} interface, this equation is

$$\left[t_x(N)\right]^2 = \left[t_0'(N)\right]^2 + x^2 \Big/ \left[V_{NMO}(N)\right]^2. \tag{4.6}$$

where the velocity V_{NMO} and two-way zero-offset traveltime t_0' define the "best fitting" hyperbola to its offset-distance-traveltime data. A commonly used technique for determining this hyperbola from CMP data is the semblance statistic *SE* which is a measure of signal coherency along the hyperbolic trajectory of a reflection event (Neidell and Taner, 1971). The semblance statistic expresses the normalized $(0 \le SE \le 1)$ output-to-input energy ratio on a velocity versus time plot, where a semblance peak (i.e., stacked velocity) corresponds to the optimal V_{NMO} and t_0' for the N^{th} reflection hyperbolae (Yilmaz, 2001).

If we assume the measured V_{NMO} and t_0' are approximately equivalent to V_{RMS} and t_0 for reflection events, interval velocity v_N for the material in the N^{th} layer located between these two reflecting interfaces can be determined using Dix's (1955) equation:

$$v_N = \sqrt{\frac{\left[V_{NMO}(N)\right]^2 \cdot t_0(N) - \left[V_{NMO}(N-1)\right]^2 \cdot t_0(N-1)}{t_0(N) - t_0(N-1)}}. \quad (4.7)$$

where $V_{NMO}(N)$ and $V_{NMO}(N-1)$ are the NMO velocities to the lower and upper reflecting boundaries, while $t_0(N)$ and $t_0(N-1)$ are the corresponding two-way zero-offset traveltimes. The corresponding interval thickness of the material between these successive reflection events is obtained from the measured zero-offset interval traveltime and calculated interval velocity using

$$h_N = v_N \left[t_0(N) - t_0(N-1)\right] / 2. \quad (4.8)$$

The estimates of interval velocity and thickness are potentially very sensitive to uncertainties in the NMO velocity and zero-offset traveltime values (e.g., Hajnal and Sereda, 1981). This sensitivity increases as the interval between selected reflecting interfaces thins due to the differencing process involved in Equation (4.7) and (4.8).

4.4 Experimental Description

4.4.1 Field Sites

Soil water content conditions were monitored at three active agricultural field sites used to produce hay; each site is characterized by different surficial soil textures: sand, sandy loam and silt loam soil. Both the sand (528878E, 4814702N) and sandy loam (528938E, 4814594N) soil sites are 3 km west of Waterloo, Ontario, Canada, while the silt loam soil site (519845E, 4770361N) is 2 km south of Woodstock, Ontario, Canada. While haying operations were conducted during the study period, other agricultural disturbances, such as plowing and tilling, were not performed at these sites during or in the recent past (i.e., within the preceding 2–5 years) prior to this study.

The Waterloo sites are located on top of the Waterloo moraine, which is described as an irregular tract of gently rolling to hummocky terrain with some exposures of ice-contact stratified sand and gravel deposits (Russell et al., 2007). The two soil water content monitoring sites at this location were separated by ~125 m laterally and ~7 m vertically with the sand site on a topographic high and

the sandy loam site in a topographic low. Shallow core logs collected at these locations showed that the sand site is characterized by a sequence of stratified fine to coarse sand along the entire measurement profile, while the sandy loam site grades downward into loamy sand below a depth of 0.4–0.5 m. The water table at the Waterloo site is assumed to be well below ground surface (i.e., >10–15 m) based on the presence of nearby springs and geophysical surveys. Precipitation and atmospheric temperature for the Waterloo sites were monitored using the University of Waterloo weather station located approximately 7 km to the east.

The Woodstock silt loam site is located 45 km southwest of the Waterloo sites, and is situated in a localized valley portion characterized as a glaciofluvial outwash channel (Cowan, 1975). A nearby core log indicates that this monitoring location is characterized by 0.5–0.7 m of silt loam grading downward into gravelly silt with sand between 0.7–1.7 m; this sequence is underlain by sandy gravel with silt deposits. Water level records from an adjacent monitoring well showed that the relatively shallow water table varied seasonally between 2.33–3.78 m below ground surface during the study period. Precipitation and atmospheric temperature at this location were monitored using an on-site meteorological station located 0.5 km to the west.

4.4.2 Data Acquisition and Analysis

CMP surveys were conducted along a fixed survey line at each of the three sites using a Sensors and Software PulseEKKO™ 1000 (Sensors & Software Inc., Mississauga, Ontario, Canada) GPR system equipped with three sets of high-frequency, bistatic antennae (i.e., 225 MHz, 450 MHz and 900 MHz). A total of 278 individual CMP data sets were collected between May 2006 and August 2007 at intervals ranging from 1–4 weeks. A summary of the CMP surveys performed at each textural site is provided in Table 4.1. When time constraints limited data acquisition, higher frequency soundings (e.g., 450 MHz and 900 MHz) were preferentially performed due to their better resolving capability in the near surface. We have included these data sets in this paper to improve the temporal resolution of the vertical velocity profile. Auxiliary reflection profiles collected along each CMP survey line (data not shown) for each antenna frequency indicate the presence of horizontally deposited stratigraphic interfaces.

Field conditions during the wintertime period (i.e., January–March 2007) at the three sites were characterized by variable snow packs which were removed prior to CMP data collection to maintain consistent antenna-ground coupling during the annual period. While the sand and silt loam sites were

characterized by relatively thin snow packs (up to ~0.3 m), the sandy loam snowpack was frequently much deeper (up to ~1.0 m). To maintain natural field conditions (i.e., minimize effects of altering overlying snow pack on soil freezing process) the removed snow was placed back over the survey lines after completing the CMP surveys whenever possible.

The GPR data were collected using a time window of 100 ns, sampling interval of 0.1 ns and 64 stacks per trace. Transmitter and receiver antennas were manually separated at 0.02 m increments during the CMP surveys and remained stationary during the recording time. Data acquisition was done with a manual trigger. The GPR surveys were collected using antenna offset ranges of 0.3–3.0 m, 0.2–2.5 m and 0.2–2.0 m for the 225 MHz, 450 MHz and 900 MHz antennas, respectively. These GPR data were processed using Reflex-Win™ software program (Sandmeier Software, Karlsruhe, Germany). The signal processing steps and parameters applied to the CMP data for subsequent velocity analysis are summarized in Table 4.2.

Vertical velocity information was obtained through a velocity analysis of each CMP data set using Reflex-Win™. A velocity spectrum was calculated for each processed CMP sounding using the semblance statistic; these spectra were used to manually determine the NMO velocity and zero-offset traveltime for prominent reflection events. An example of a velocity spectrum and its corresponding CMP sounding are shown in Figure 4.3.

The causal and multi-cycle nature of the GPR wavelet must be considered when using velocity spectra to determine the NMO velocity and zero-offset traveltime profile (Booth et al. 2010). Typically, the GPR wavelet for the reflection event is comprised of three or more half-cycles each possessing significant amplitude. As a result, a given reflection event will generate a series of semblance peaks where each corresponds to a particular half-cycle of the wavelet package. Further, the trailing peaks exhibit systematically slower apparent NMO velocities relative to the 1st half-cycle values due to a delay time effect (Booth et al., 2010). This phenomenon is illustrated in Figure 4.3.

The appropriate phase of the wavelet that should be used to extract velocity information is the “first break” or leading edge of the wavelet (Booth et al., 2010). Due to its relatively slow rise time, this wavelet phase is very difficult to identify in complex wavefields resulting from the superposition of various events and in the presence of noise. To compensate, we have adjusted the CMP zero-time using the first half-cycle of the direct air wave event (in our case a negative trough). Assuming the invariance of GPR pulse shape, this shifting procedure would make the first semblance peak of a reflection event on the velocity spectra equivalent to the first break arrival.

Successive pairs of NMO velocity and zero-offset traveltime from the velocity analyses were inserted into Equation (4.7) and (4.8) to obtain an estimate of interval-velocity and layer thickness, respectively. These results were used to construct individual interval-velocity models for each frequency over the entire study period; in turn, these models were used to infer the vertical soil moisture profile over the annual hydrological cycle for each site.

4.5 CMP Data and NMO Analysis Results

Figure 4.4 illustrates our velocity picking procedure for each antenna frequency at the sand (Figure 4.4a), sandy loam (Figure 4.4b) and silt loam (Figure 4.4c) sites during seasonally wet conditions on 19 April 2007 (Waterloo) and 20 April 2007 (Woodstock). This figure shows processed CMP soundings (upper series of panels) with prominent reflection events marked by dashed lines, semblance plots (middle series of panels) with $V_{NMO} - t_0$ function corresponding to the semblance picks, and calculated interval-velocity-depth models (lower series of panels). These data clearly demonstrate the more rapid decrease in the signal-to-noise ratio with traveltime that occurs as antenna frequency increases. As a result, lower antenna frequencies permitted greater depth of investigation while better resolution of the near-surface was achieved with higher antenna frequencies. A comparison between the three sites shows the decrease in depth of penetration associated with the increase in fine grain content of the soils.

In an effort to produce consistent results, we attempted to use the same reflection events throughout the study at each site. Three prominent reflection events were identified for each CMP sounding. However, the variable soil moisture conditions that occur over an annual cycle can significantly impact the subsurface wavefields by changing the relative reflectivity of the interfaces. As an example, Figure 4.5 shows data collected using 450 MHz antennas at the silt loam site during seasonally wet (Figure 4.5a), dry (Figure 4.5b) and frozen (Figure 4.5c) soil conditions. The wetter periods were characterized by more coherent reflections with relatively higher amplitude which resulted in improved semblance coherency and easier reflector identification compared to dry conditions. Further, the development and dissipation of the seasonal frost zone can produce significant vertical velocity gradients near the surface (Steelman et al., 2010). Such conditions are illustrated in Figure 4.5c, where a shallow frost layer (~0.4 m) is overlying wet unfrozen soil. While high velocities are limited to the near-surface, the semblance plot is significantly different than those obtained during wet and dry soil conditions. These factors affected our ability to maintain consistency (i.e., identification of consistent reflection events) in our NMO analysis procedure;

consequently, moderate variations in interval thickness estimates were encountered for each antenna frequency and soil site (refer to Section 4.6).

To examine the variations in the $V_{NMO} - t_0$ function, we constructed a temporal velocity field using the NMO velocity picks from 225 MHz, 450 MHz and 900 MHz data sets at each site. The velocity field results are provided in Figure 4.6 with corresponding precipitation and air temperature data collected at the nearby weather stations. These fields were constructed using the kriging interpolation method (Surfer™ 8, Golden Software, Inc.) using the semblance velocity picks positioned at their respective zero-offset traveltime t_0 and acquisition date. Because the $V_{NMO} - t_0$ function assumes a homogeneous velocity from the surface to the first interface (refer to Figure 4.4), the uppermost NMO velocity was replicated at the air-soil interface to better constrain the interpolation. While similar velocity fields could be constructed using other gridding methods (e.g., radial basis function, minimum curvature, natural neighbour), the kriging method better delineated short-duration events. Temporal variations in velocity are presented for each antenna frequency with the $V_{NMO} - t_0$ data points denoted by the symbol (•). For reference, the dates corresponding to the semblance analyses in Figure 4.4 have been indicated on their corresponding velocity field by the symbol (▾).

The precision of our NMO analysis is dependent on the resolution of semblance results which is defined by the width of the maximum peak value (Murray et al., 2007; Booth et al., 2010). This peak width is affected by a variety of factors. For example, the semblance plots in Figure 4.4 display well-known progressive broadening of the peak width as t_0 increases on individual semblance plot. This phenomenon produces growing uncertainty in the determination of $V_{NMO} - t_0$ values with increasing reflecting interface depth. In addition, the semblance plots in Figure 4.5 clearly show the variation in semblance resolution that occurred with changing soil moisture conditions. In particular, it can be seen that higher subsurface velocity conditions are accompanied by broader semblance peak values.

The complexity of GPR response during variable soil conditions encountered during the annual cycle complicates the quantitative estimation of uncertainty in the NMO analysis results. However, the evaluation of uncertainty for selected CMP data sets provides some insight. For example, the uncertainty levels for the data shows in Figure 4.4 (results not shown) were estimated as followed: ±0.002 m/ns to ±0.012 m/ns for sand site, ±0.002 m/ns to ±0.009 m/ns for sand loam site and 0.001 m/ns to ±0.004 m/ns for silt loam site. These uncertainty levels are comparable to those cited by previous studies (e.g., Jacob and Hermance, 2004).

While the V_{NMO} quantity represents a root-mean-square average of the subsurface EM wave velocity structure from the surface downwards to its corresponding reflecting interface, the results in Figure 4.6 clearly show the impact of the overall nature and evolution of soil moisture in the shallow vadose zone. The V_{NMO} fields display distinctive long-term temporal patterns that follow general seasonal moisture trends; calendar seasonal periods are shown for reference. It can be seen that lower V_{NMO} values are encountered during the wetter spring and autumn periods while higher V_{NMO} values were observed during the dryer summer and frozen winter conditions. The V_{NMO} fields exhibit increasing values with traveltime during both the spring and autumn when soil moisture is expected to be increasing in the very shallow near-surface due to the onset of higher precipitation. The downward decreasing V_{NMO} fields during the winter reflect the presence of the seasonal frost table at the surface.

While seasonal trends in velocity are consistent at each site, the temporal duration and resolution of these conditions varied with antenna frequency. For instance, the temporal periods encompassing lower velocity autumn and spring conditions were more clearly resolved, i.e., better definition of vertical velocity gradients, in 900 MHz data. However, poorer consistency between the three frequencies during higher velocity periods indicates the overall lower reliability of the data during these periods, particularly during the transitions between low-velocity autumn and spring, and high-velocity winter and summer conditions, respectively. These observed differences in seasonal conditions highlight the range in vertical resolution achieved with each frequency. The improved vertical resolution (i.e., upper 20–30 ns) achieved with higher frequency antennas (i.e., 450 MHz and 900 MHz) also seemed to result in better delineation of short-duration velocity variations. For instance, a major precipitation event in mid-May 2007 at the sand and silt loam sites (Figure 4.6a and 4.6c, respectively), which impacted the upper soil section, was better imaged with 900 MHz antennas.

4.6 Interval Velocity Profiles

These $V_{NMO} - t_0$ data were used with Equation (4.7) and (4.8) to construct interval velocity-depth models over the annual cycle at each site for each antenna frequency; these results are presented in Figure 4.7. In this figure, the interval velocity field is illustrated as a block diagram indicating the thickness and EM wave velocity of the intervals between the semblance data points. The temporal position of each interval-velocity model (i.e., date acquired) is denoted by a series of vertical lines intersecting the upper and lower boundary of each interval. The temporal (i.e., horizontal) limits of the block represents the midpoint time between successive GPR surveys. The interval-velocity field

results for the three sites are presented in Figure 4.7a–c with corresponding precipitation and air temperature data collected at the nearby weather stations.

These results show differing degrees of variability in terms of the site, antenna frequency, interval depth and seasonal condition, which reflect some of the inherent difficulties in interval velocity models obtained from the $V_{NMO} - t_0$ data. This variability is reflected in the mean interval thicknesses and standard deviations (SD) for the annual cycle summarized in Table 4.3. The SD values show increased interval thickness variability with decreasing antenna frequency and increasing depth of investigation. Overall, the least variation was observed at the sand site with 900 MHz antennas where we could confidently identify the same stratigraphic reflectors throughout the annual period (Steelman and Endres, in review) [Chapter 4]. While an absence of consistent reflection events throughout the annual cycle at the sandy loam and silt sites using 900 MHz antennas resulted in greater interval thickness variations than those from the sand site, the differences were considerably less than those observed with the lower 225 and 450 MHz frequencies. Therefore, the remainder of this paper will focus only on the 900 MHz results due to their lower variability and higher resolving power in the shallow soil zone.

While the observed velocity changes in the upper two intervals of the 900 MHz data seem to follow expected seasonal soil conditions (i.e., based on dominant weather patterns), the lowermost interval 3 results are considerably more variable. The complex GPR response during variable soil conditions may be partially responsible for the increased variability in interval 3. For instance, the development of a large vertical velocity gradient or sharp velocity changes at stratigraphic interfaces could cause significant ray bending, thereby violating the hyperbolic approximation assumption of NMO analysis (Becht et al., 2006). This problem may be compounded by survey acquisition limitations such as our maximum spread lengths and signal attenuation with depth (Barrett et al., 2007); however, a comprehensive investigation of these uncertainties is beyond the scope of this study. While the majority of the interval 3 results are of poorer quality, and at times deviate from the soil moisture pattern observed in the overlying intervals, results from intervals 1 and 2 appear to provide reliable qualitative information about shallow soil conditions.

Focusing on the upper two intervals, it is apparent that the overall magnitude of the velocity variations increases near the surface; this reflects the surface sensitivity to atmospheric forcing. The improved vertical resolution achieved using the 900 MHz antennas resulted in more consistent reflection event identification, and hence, more representative interval-velocity estimates with greater

sensitivity to short-duration velocity variations. For instance, the large mid-May 2007 precipitation event is marked by a dramatic velocity decrease at all three sites.

Similar to the V_{NMO} fields, these velocity data exhibit long-period seasonal changes in velocity reflecting seasonal weather pattern trends. As shown with the NMO velocities, the most distinctive vertical trends were observed during the wetter autumn and spring, and frozen winter periods, while significantly less vertical contrast was observed during the dryer summer period at each site. The autumn and spring periods are characterized by increasing velocity conditions with depth which signifies wetting period conditions. Conversely, the frozen winter period is characterized by decreasing velocity conditions with depth. While the 900 MHz antennas adequately describe shallow soil moisture dynamics in the upper few meters of vadose zone, the muted velocity response to highly dynamic surface moisture variations (i.e., due to short-duration precipitation and evapotranspiration processes) throughout the annual period highlights the importance of resolving surface soil moisture conditions to better define the hydraulic coupling between surface and deeper vadose zone conditions.

4.7 Soil Moisture Estimates

The estimation of soil water content from EM wave velocity measurements requires an appropriate petrophysical relationship to convert the relative permittivity κ information into volumetric water content θ. For this study, we have elected to use the simple empirical relationship proposed by Topp et al. (1980):

$$\theta = -5.3\times10^{-2} + 2.92\times10^{-2}\kappa - 5.5\times10^{-4}\kappa^2 + 4.3\times10^{-6}\kappa^3. \quad (4.9)$$

This relationship provides reliable estimates of soil water content for a range of soil moisture conditions and textural properties without the use of detailed soil textural information. A comparison between DGW and gravimetrically derived water content estimates collected in the upper few decimeters of soil at these three sites (Steelman and Endres, 2011) [Chapter 3] showed that Equation (4.9) provides reliable estimates of soil water content for the range of natural moisture conditions considered in this study. However, it should be noted that the performance of Equation (4.9) was not tested for the frozen soil conditions; this may result in larger uncertainties in liquid water content estimates during these periods.

Temporal soil moisture fields were computed from 900 MHz interval-velocity measurements (i.e., intervals 1 and 2 only) using Equation (4.9); results are shown for the sand and sandy loam (Figure

4.8), and silt loam (Figure 4.9) sites. As anticipated from the interval-velocity results, these water content data exhibit long-period variations caused by seasonal wetting and drying as well as freeze and thaw cycles. Intra-seasonal variations (i.e., on the order of a few weeks) is also observed within the upper meter in response to elevated precipitation rates followed by soil drying.

The rate and magnitude of moisture variations depends strongly on the dominant soil texture. The seasonally wetter periods at the sand site (Figure 4.8) are characterized by higher water contents within the upper soil interval which become progressively drier with depth. The wintertime and summer periods show more uniform moisture conditions along the measured vertical profile.

The sandy loam site (Figure 4.8) displays a slightly higher range of interval water content compared to the nearby sand site due to the presence of finer textured soil at the surface. Here, the upper interval encompasses water contents within the finer textured sandy loam soil at the surface, while the deeper measurements are sampling the underlying loamy sand which has a lower moisture capacity. This textural transition favours a sharp moisture transition that enhances during wetter periods. As a result, a significant portion of the seasonal moisture loading may be retained in the shallow root zone, which subsequently restricts flow to the underlying soil.

The silt loam site (Figure 4.9) is characterized by a wide range of interval water contents with less short-period variability compared to the other two sites. Seasonally wetter periods are characterized by decreasing water contents with depth. The wettest upper layer (~0.4–0.7 m) is composed of silt loam soil which has a relatively high capacity to store water. Underlying this upper root zone is coarser gravelly silt with sand that has a lower moisture capacity compared to the overlying silt loam. Similar to the other sites, there is a systematic decrease in moisture content between the surface and deeper soil zone during wet conditions which diminishes during seasonally drier periods. However, the gradual textural transition at this site reduces the potential for a sharp moisture transition between adjacent units due to the smoother change in moisture content and hydraulic connectivity. The freezing process was limited to a much shallower portion of soil and resulted in rapidly decreasing velocities with depth. Here, shallow water contents indicate frozen soil while the lower intervals reflect wet unfrozen conditions. As with the other sites, the freezing process resulted in a sharp transition between surface and deeper soil conditions that temporarily interrupted the autumn and spring wetting process.

In addition, a nearby well at the Woodstock site allowed us to monitor the water table elevation underlying our GPR survey line, and hence, the coupling between vadose zone moisture conditions

and underling aquifer response. The depth to water table varied between 2.33 to 3.78 meters below ground surface (mbgs) as shown in Figure 4.9. These data indicate that groundwater recharge primarily occurred during the mid-to-late autumn and early spring periods; here, increased water table elevation coincided with elevated moisture contents along the entire vertical profile. A reduction in water table elevation occurred during dryer summer periods and late-wintertime period and was accompanied by decreasing moisture conditions with depth.

4.8 Resolving Shallow Soil Moisture Dynamics

Previous work at these sites (Steelman and Endres, 2010) showed the capacity of DGW method employing CMP data to monitor soil moisture at the air-soil interface (i.e., upper 0.1 – 0.3 m) over the complete annual cycle. While the upper interval velocities from NMO analysis provides information near the surface, its larger sampling depth (i.e., compared to DGW) may lead to a misrepresentation of actual surface moisture conditions, particularly within the root zone.

To illustrate the potential differences between surface and deeper moisture conditions during the annual cycle, DGW water content data from Steelman and Endres (2010) is presented with corresponding 900 MHz interval 1 NMO data for each site in Figure 4.10. Although similar seasonal moisture trends are observed the DGW shows a larger range in measured water content over the annual period at each site. The magnitude of the moisture divergence between the measurement scales is dependent on soil texture, wetting/drying period, and the relative sampling depth of interval 1. For instance, DGW water contents at the sand site (Figure 4.10a) are typically less than that observed in the interval 1 data with the exception of major wetting events (e.g., late-May 2007) which results in temporarily higher water contents at the surface. Rather, more prominent discrepancies are seen during short-duration drying (evapotranspiration) periods during the late-spring and mid-summer months, and early-freezing conditions in the winter. The textural transition noted at the sandy loam site (Figure 4.10b) resulted in a sharp moisture gradient which enhances dramatically during wetter autumn and spring periods. However, more uniform surface moisture distribution occurred with depth as the finer surface soils began to freeze during the winter and dry during summer periods, respectively, relative to the underlying loamy sand. The silt loam (Figure 4.10c) DGW data shows slightly wetter conditions at the surface throughout the annual period.

These data clearly demonstrate the need for better resolution of the very shallow near surface and a method of augmenting the velocity profiling process with the DGW data, e.g., using piece-wise linear

velocity layers, in order to fully capture the near surface velocity variations. The improved resolution at the surface provided by the DGW method would enable better characterization of short-duration wetting (infiltration) and drying (evapotranspiration) processes, which, when combined with NMO data, would allow for a closer examination of the coupling between soil moisture profile through the vadose zone and surface soil moisture variations.

4.9 Discussion and Conclusions

While previous studies (e.g., Greaves et al., 1996; Garambois et al., 2002; Turesson, 2006) have demonstrated the application of NMO velocity analysis and interval-velocity determination for the characterization of spatial soil moisture distribution in the vadose zone, they did not incorporate the temporal component necessary to critically examine vertical moisture dynamics. Our field study has examined the use of NMO velocity analysis applied to CMP data by monitoring vertical soil moisture variations over a wide range of soil conditions at three distinct sites. Further, we considered a range of antenna frequencies to evaluate the resolving powers and depth of penetrations necessary to effectively characterize vertical moisture dynamics. Using NMO velocities, we successfully characterized major seasonal trends associated with dry summer, wet spring and autumn, and frozen winter soil conditions. Subsequent interval-velocity determination permitted soil moisture measurements at discrete depth intervals in the shallow vadose zone that, when combined with DGW data, allowed us to further examine the nature of the coupling between surface and deeper moisture conditions during the annual cycle.

Although our approach utilized three different antenna frequencies with inherently varying depths of investigation and resolving powers, we found that the high-frequency 900 MHz antennas yielded the most reliable velocity and water content measurements with respect to depth of investigation and resolving power. The improved resolving capability was particularly important during short-duration wetting and drying events and seasonal freeze-thaw cycles. Nevertheless, our ability to obtain reliable interval-velocity measurements was hindered by site conditions. Less reliable interval velocities occurred during decreasing velocity conditions with depth. For instance, seasonal frost development during early-wintertime and increased surface drying rates during late-spring periods were accompanied by erroneously low interval velocities (high water contents) in the lowermost interval at the sand and silt loam sites. Further examination of the sensitivity of interval-velocity measurements to varying site conditions (i.e., effects of vertical velocity gradient) should be conducted in future studies. Although the application of CMP soundings permitted simultaneous measurement of surface

and deeper soil moisture conditions, comparisons with DGW measurements highlighted the need for better resolution of the very shallow near-surface to further improve our ability to resolve short-duration events. This can be achieved by augmenting the NMO velocity profiling process with DGW data obtained from a single CMP sounding.

Assessment of systematic changes in vertical soil moisture profile can provide valuable information about the nature of seasonal moisture dynamics in the shallow vadose zone. Using NMO velocity measurements, we were able to monitor vertical soil moisture distribution and examine coupling characteristics between the surface and shallow vadose zone during an annual cycle of soil conditions. As expected, surface soil conditions were more variable than deeper soil conditions and exhibited a more dynamic range of water contents due to atmospheric forcing. The strongest difference between surface and subsurface moistures was observed during the wetter autumn and spring periods, and during early wintertime conditions. Shorter duration wetting events during dryer summer periods resulted in temporary differences between surface and deeper soil as moisture was partitioned between the atmosphere and root zone through evapotranspiration.

4.10 Tables and Figures

Table 4.1 Summary of CMP data sets for each site and antenna frequency.

Soil Texture	Sand	Sandy Loam	Silt Loam
	28-Aug-06 to 27-Aug-07	28-Aug-06 to 27-Aug-07	19-May-06 to 31-Aug-07
225 MHz	30	27	31
450 MHz	32	29	32
900 MHz	36	29	32
Total	98	85	95

Table 4.2 GPR processing steps and parameters.

Process	225 MHz	450 MHz	900 MHz
Subtract-Mean	time window = 4.444 ns	time window = 2.222 ns	time window = 1.111 ns
Mean Filter	range = 4 point	range = 4 point	range = 4 point
Adjust Zero Time[a]	static shift ± ns	static shift ± ns	static shift ± ns
Time Cut	max range = 80 ns	max range = 80 ns	max range = 80 ns
Bandpass Frequency	25–125–475–550 MHz	100–150–800–1000 MHz	100–200–1100–1400 MHz
Gain Function (sand)	linear = 0.1 pulsewidth^{-1} exponent = 4 db/m max gain = 1000	linear = 0.1 pulsewidth^{-1} exponent = 6 db/m max gain = 1000	linear = 0.1 pulsewidth^{-1} exponent = 8 db/m max gain = 1000
Gain Function (sandy loam)	linear = 0.01 pulsewidth^{-1} exponent = 10 db/m max gain = 1000	linear = 0.1 pulsewidth^{-1} exponent = 10 db/m max gain = 1000	linear = 0.1 pulsewidth^{-1} exponent = 10 db/m max gain = 1000
Gain Function (silt loam)	linear = 0.01 pulsewidth^{-1} exponent = 10 db/m max gain = 1000	linear = 0.1 pulsewidth^{-1} exponent = 10 db/m max gain = 1000	linear = 1 pulsewidth^{-1} exponent = 10 db/m max gain = 1000

[a] zero-time was corrected using a linear extrapolation of peak (i.e., negative trough) air wave arrivals to zero-offset time for each CMP sounding .

Table 4.3 Mean interval thicknesses and standard deviations (SD) using Equation (4.8).

Soil Texture		**Sand**			**Sandy Loam**			**Silt Loam**		
		225	**450**	**900**	**225**	**450**	**900**	**225**	**450**	**900**
			MHz			***MHz***			***MHz***	
Calculated Interval Thicknesses (m)										
Interval 1	Mean	1.22	1.18	0.49	1.28	1.07	0.67	0.79	0.58	0.31
	SD	0.23	0.11	0.02	0.21	0.19	0.10	0.11	0.10	0.04
Interval 2	Mean	1.41	1.01	0.80	1.30	1.06	0.67	1.12	0.70	0.35
	SD	0.19	0.13	0.03	0.29	0.25	0.19	0.16	0.17	0.04
Interval 3	Mean	1.15	1.12	0.76	1.38	1.13	0.76	1.09	0.88	0.46
	SD	0.23	0.18	0.09	0.32	0.28	0.18	0.21	0.21	0.08

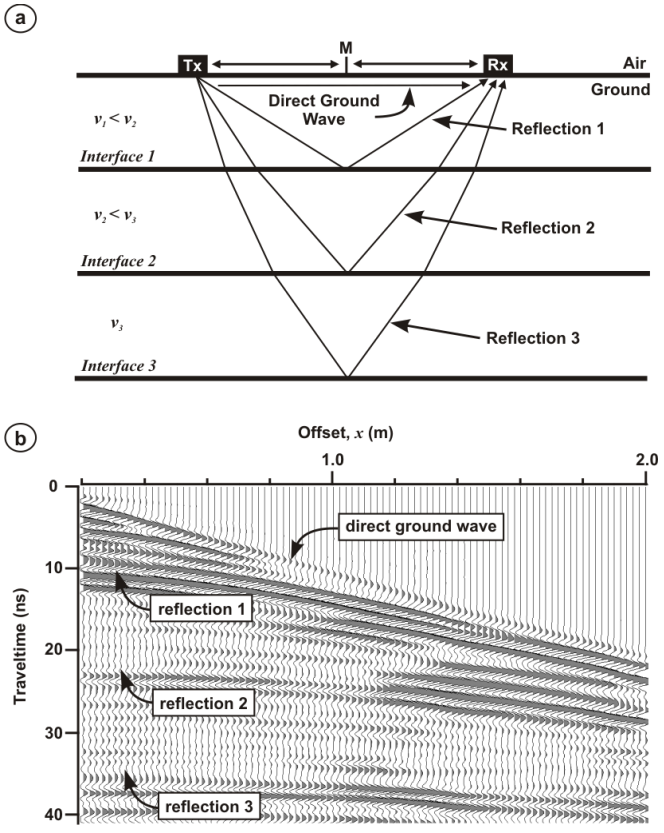

Figure 4.1 (a) Schematic CMP survey illustrating multiple reflection events and (b) corresponding CMP sounding.

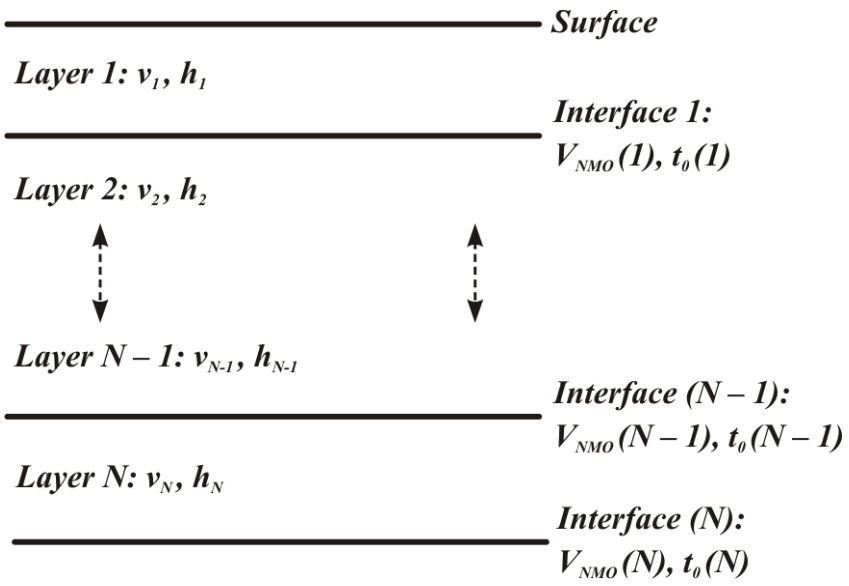

Figure 4.2 Diagram illustrating NMO velocity parameters for interval-velocity determination.

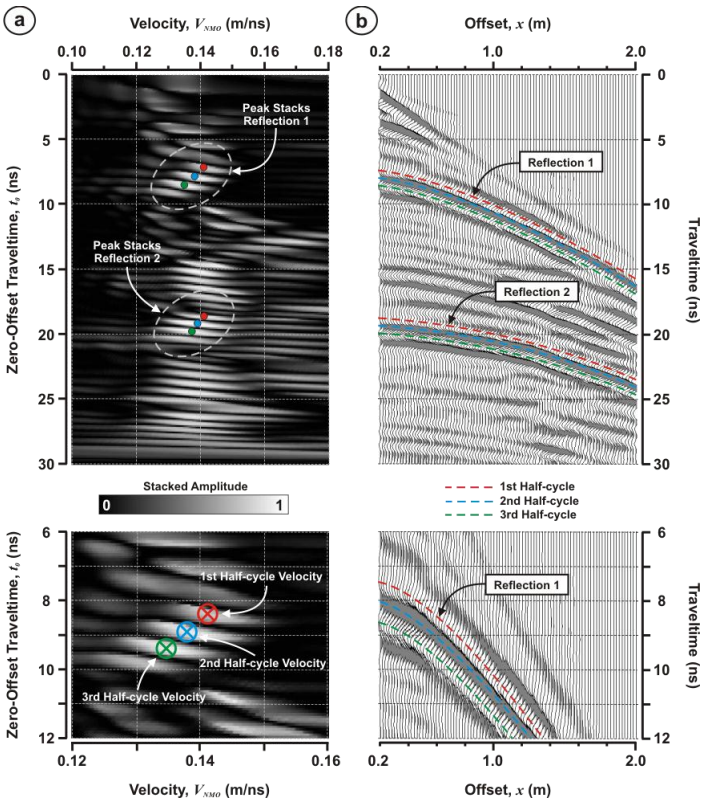

Figure 4.3 (a) Semblance response and (b) corresponding CMP sounding with two reflection events. Each reflection event is composed of three half-cycles that results in a series of peak stacks on the semblance plot. These peak stacks will exhibit a systematic slowing of velocity relative the initial first half-cycle velocity (modified from Booth et al., 2010).

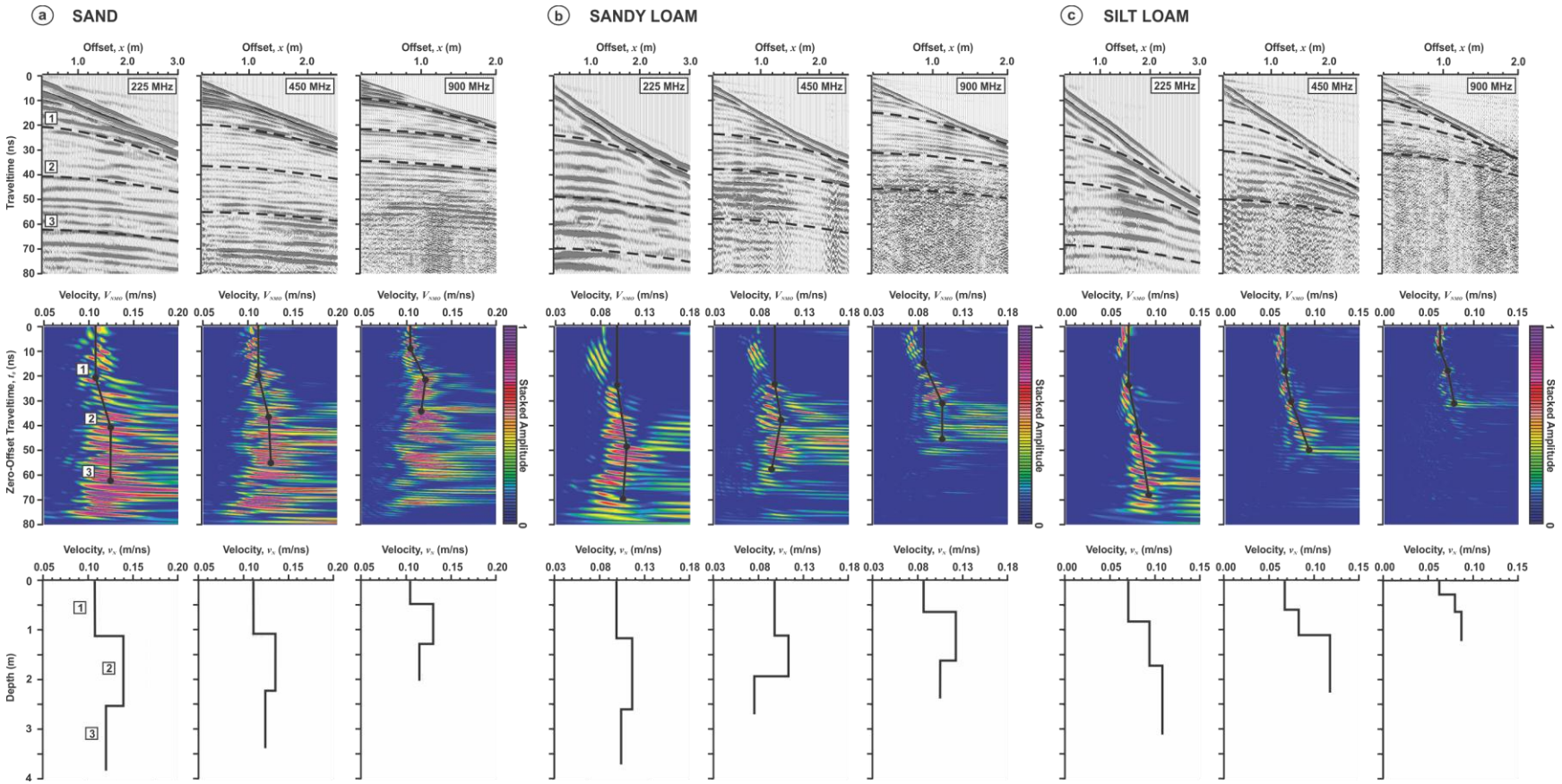

Figure 4.4 CMP soundings (upper series of panels), semblance plots (middle series of panels) with picked NMO velocity function, and calculated interval-velocity models (lower series of panels) obtained at the (a) sand (19 April 2007), (b) sandy loam (19 April 2007) and (c) silt loam (20 April 2007) sites with 225 MHz, 450 MHz and 900 MHz antennas.

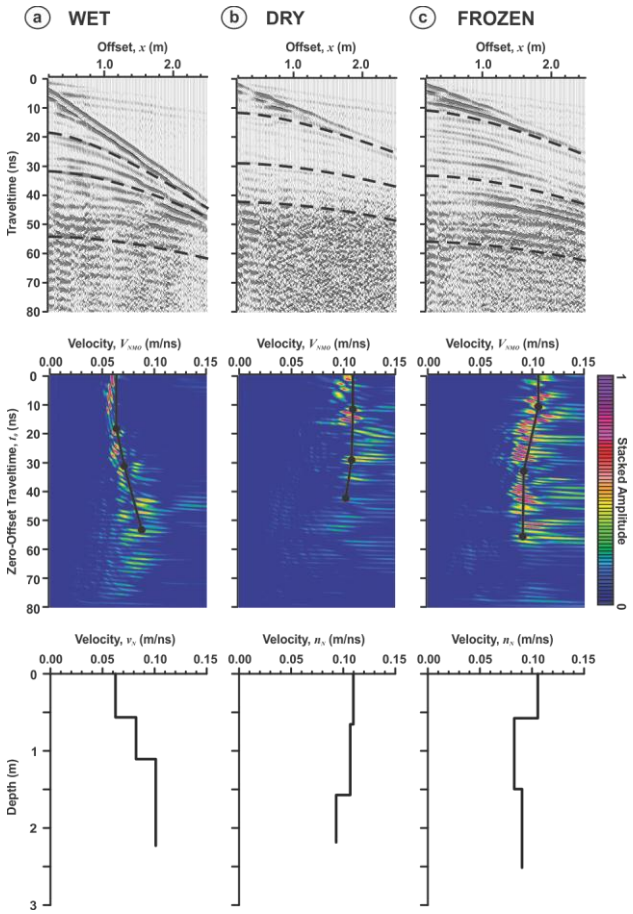

Figure 4.5 CMP soundings (upper series of panels), semblance plots (middle series of panels) with picked NMO velocity function, and calculated interval-velocity models (lower series of panels) corresponding to seasonally (a) wet (13 January 2007), (b) dry (31 August 2007) and (c) frozen (20 February 2007) soil conditions at the silt loam site using 450 MHz antennas.

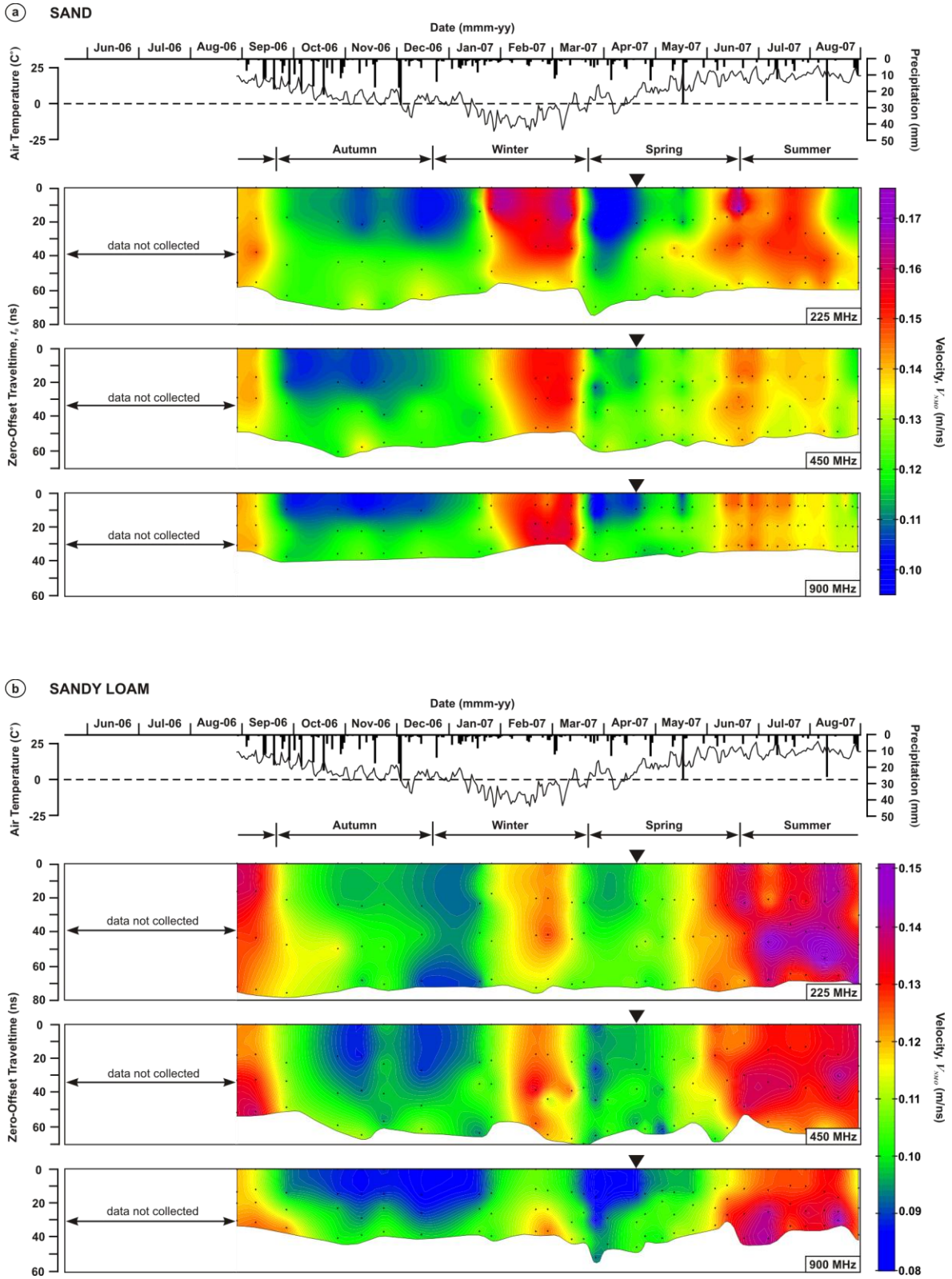
a
SAND
Date (mmm-yy)
Jun-06
Jul-06
Aug-06
Sep-06
Oct-06
Nov-06
Dec-06
Jan-07
Feb-07
Mar-07
Apr-07
May-07
Jun-07
Jul-07
Aug-07
Air Temperature (C°)
Precipitation (mm)
Autumn
Winter
Spring
Summer
data not collected
225 MHz
450 MHz
900 MHz
Zero-Offset Traveltime, t_z (ns)
Velocity, V_{RMO} (m/ns)
b
SANDY LOAM
Zero-Offset Traveltime (ns)

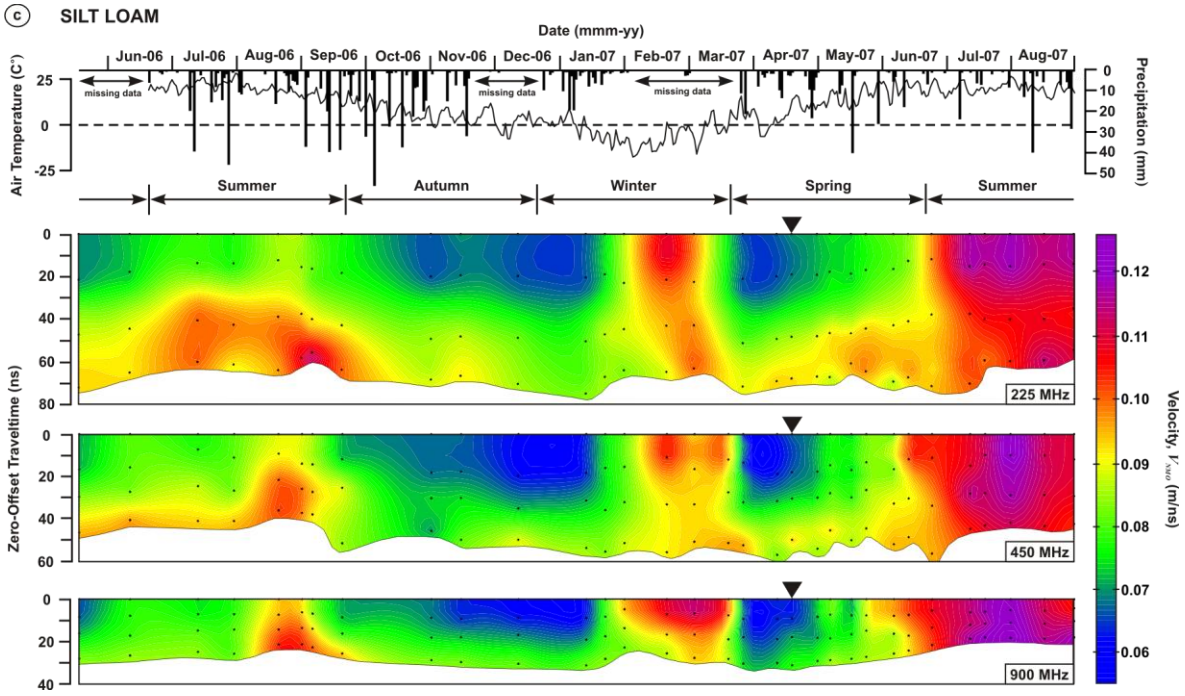

Figure 4.6 Temporal VNMO fields for the (a) sand (b) sandy loam and (c) silt loam sites measured with 225 MHz, 450 MHz and 900 MHz antennas. The location of the velocity data shown in Figure 4.4 (i.e., middle series of panels) is identified by the symbol (▼). Precipitation and air temperature data is also provided.

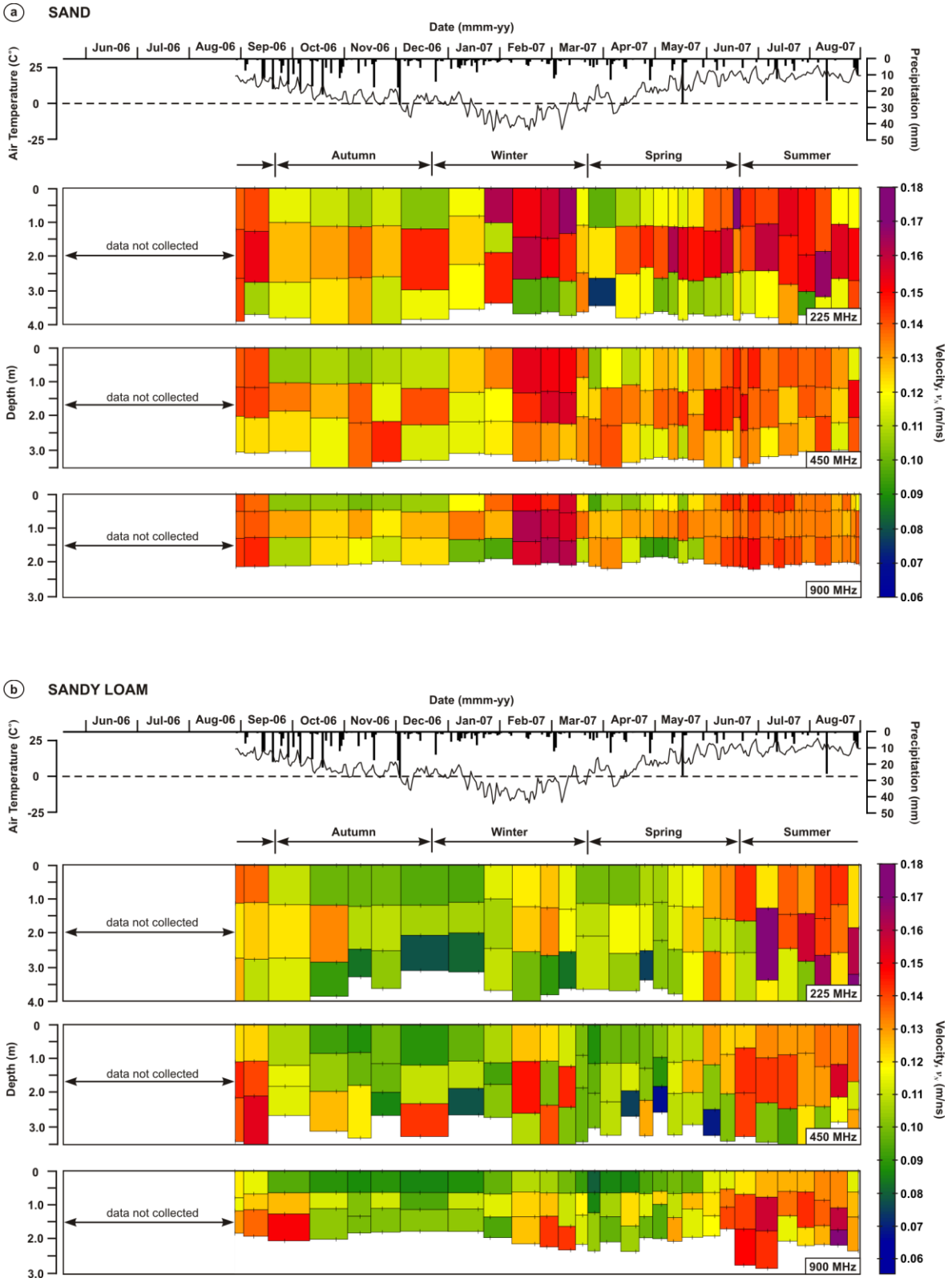
a
SAND
Date (mmm-yy)
Jun-06
Jul-06
Aug-06
Sep-06
Oct-06
Nov-06
Dec-06
Jan-07
Feb-07
Mar-07
Apr-07
May-07
Jun-07
Jul-07
Aug-07
Air Temperature (C°)
Precipitation (mm)
Autumn
Winter
Spring
Summer
data not collected
225 MHz
450 MHz
900 MHz
Depth (m)
Velocity, v_s (m/ns)
b
SANDY LOAM

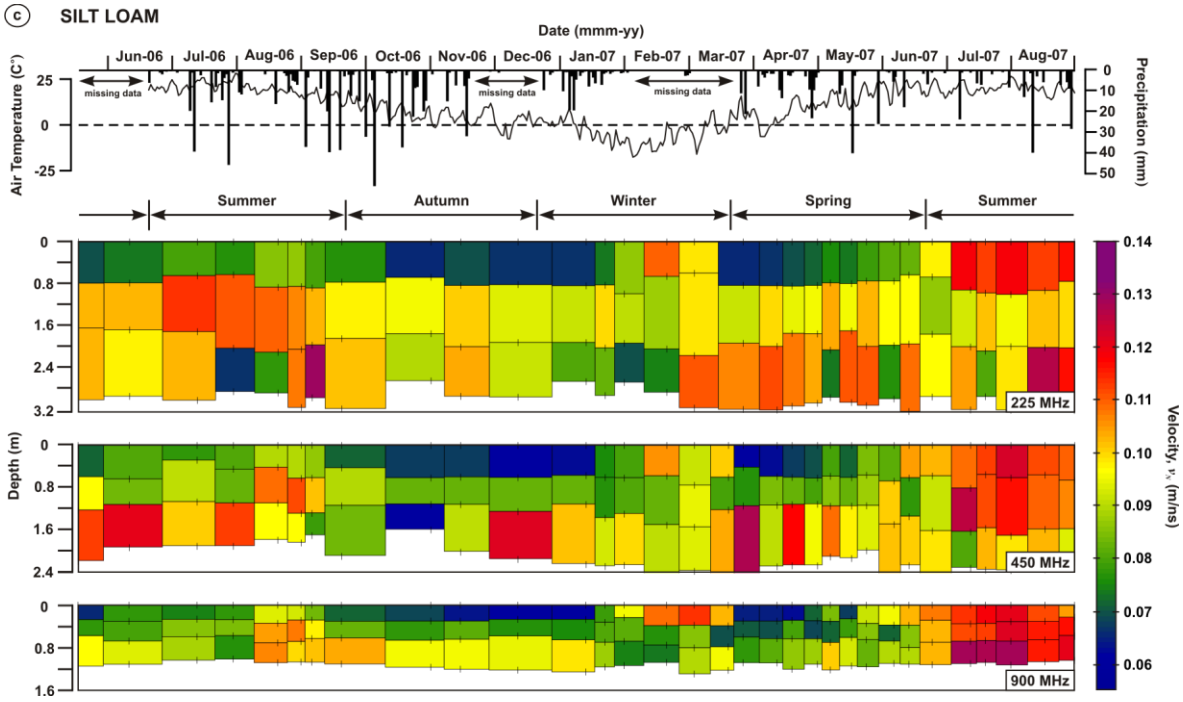

Figure 4.7 Temporal interval-velocity fields for the (a) sand, (b) sandy loam and (c) silt loam sites measured with 225 MHz, 450 MHz and 900 MHz antennas. The temporal position of each interval-velocity model is denoted by a series of vertical dashes which define the upper and lower boundary for each interval. It should be noted that some the lower interval boundaries plot outside the depth range presented. Precipitation and air temperature data is also provided.

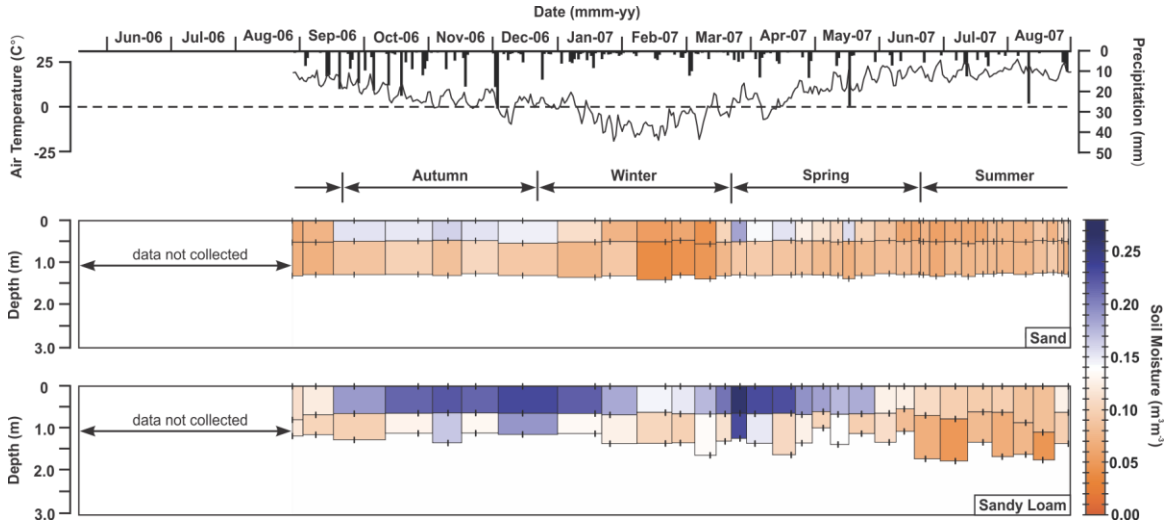

Figure 4.8 Temporal interval water content fields determined using Equation (4.8) for intervals 1 and 2 at the sand and sandy loam sites with 900 MHz antennas. Precipitation and air temperature data is also provided.

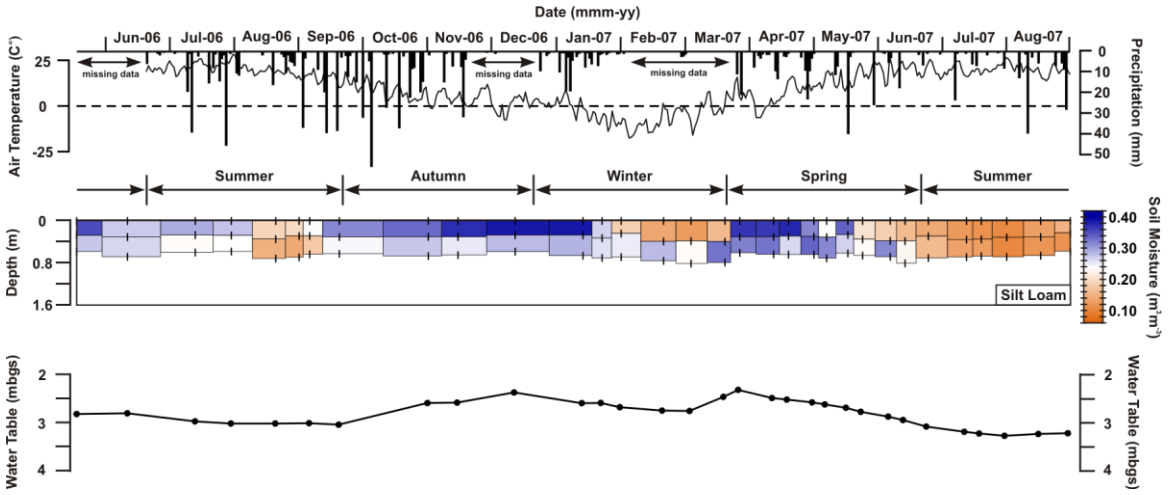

Figure 4.9 Temporal interval water content field determined using Equation (4.8) for intervals 1 and 2 at the silt loam site with 900 MHz antennas. Precipitation, air temperature and depth to water table are also shown.

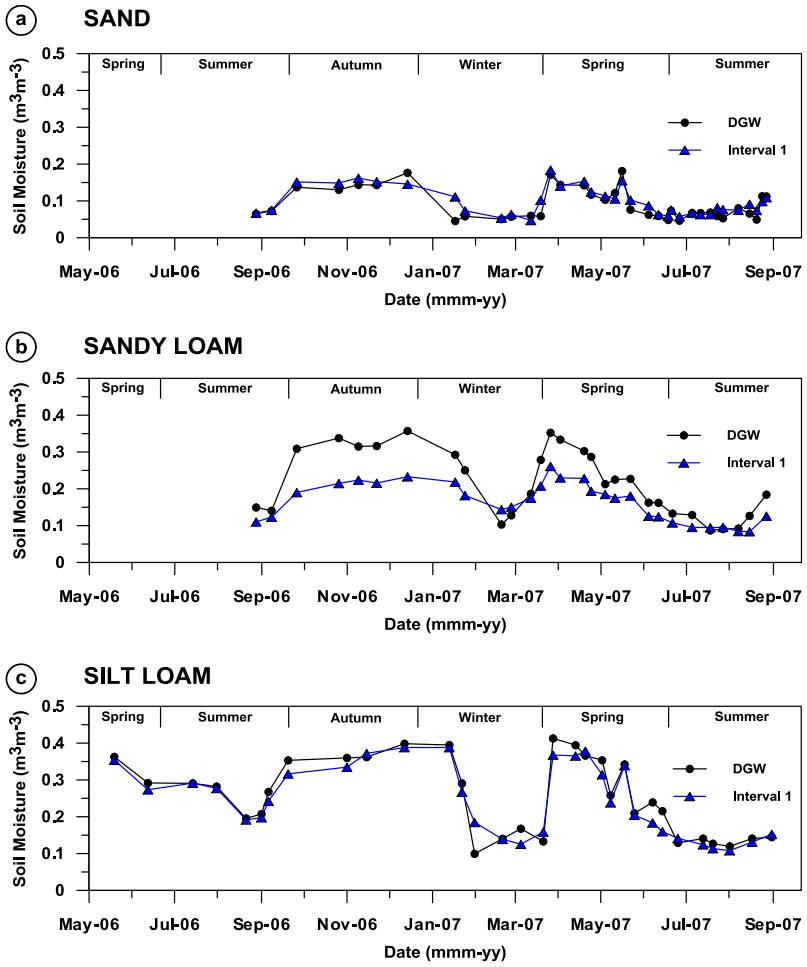

Figure 4.10 Comparison between direct ground wave (DGW) and interval 1 NMO based water content estimates using 900 MHz antennas at the (a) sand, (b) sandy loam and (c) silt loam sites.

Chapter 5
High-Resolution GPR Monitoring of Soil Moisture Dynamics – Field Results and Interpretation[4]

5.1 Executive Summary

Surface ground-penetrating radar (GPR) techniques have been used by a number of previous researchers to characterize soil moisture content in the vadose zone. However, limited temporal sampling and low resolution near the surface in these studies greatly impeded the quantitative analysis of vertical soil moisture distribution and its associated dynamics within the shallow subsurface. To further examine the capacity of surface GPR, we have undertaken an extensive 26 month field study using concurrent high-frequency (i.e., 900 MHz) reflection profiling and common-midpoint (CMP) soundings to quantitatively monitor soil moisture distribution and dynamics within the shallow vadose zone. This unique data set permitted us to assess the concurrent use of these techniques over two contrasting annual cycles of soil conditions. Reflection profiles provided high resolution traveltime data between four stratigraphic reflection events while cumulative results of the CMP sounding data set produced precise depth estimates for those reflecting interfaces, which were used to convert interval traveltime data into soil water content estimates. The downward propagation of major infiltration episodes associated with seasonal and transient events were well resolved by the GPR data; these data show the progressive attenuation and delay of episodic events with depth. In addition, GPR data reveal variations in the nature of infiltration events between contrasting annual cycles. The use of CMP soundings permitted the determination of direct ground wave velocities, which provided high-resolution information along the air-soil interface. This improved near-surface resolution enabled better characterization of short-duration wetting/drying and freezing/thawing processes, and hence, permitted better evaluation of the nature of the coupling between shallow and deep moisture conditions.

[4] Steelman, C.M., and Endres, A.L. (in review). High-resolution GPR monitoring of soil moisture dynamics 1. Field results and interpretation. Submitted to *Water Resources Research* 16/09/2011, submission number: 2011WR011413.

5.2 Introduction

Advancing our understanding of near-surface hydraulic processes hinges on our ability to measure in-situ soil moisture conditions. Soil moisture measurements are important for determining hydrological state conditions, soil hydraulic parameters, and soil water fluxes in the vadose zone (Vereecken et al., 2008). A comprehensive understanding of shallow moisture processes is also necessary for the evaluation and management of climate effects on water resources (Seneviratne et al., 2010).

Conventional moisture monitoring techniques such as gravimetric sampling, thermal neutron probes and time-domain reflectometry (TDR) provide highly localized information and are generally invasive; further, these methods are not well suited for efficient acquisition of spatial data. While remote sensing imagery provides spatial information, it has low resolution and lacks the depth of investigation necessary to estimate vertical hydraulic fluxes. As a result, surface hydrogeophysical methods are increasingly recognized (e.g., Vereecken et al., 2008; Robinson et al., 2008) as an important source of soil moisture information at the field scale due to their larger sampling volume (i.e., dm^3–m^3 scale), non-invasive nature, good depth of investigation (1–10 m) and high resolving power. In particular, ground-penetrating radar (GPR) techniques have been proven to be very useful for monitoring vadose zone soil water content at the field scale (Huisman et al., 2003a). While GPR data are dependent on the same electromagnetic (EM) properties that govern TDR response, its larger sampling volume and non-invasive nature makes it unaffected by measurement errors associated with macropores (e.g., root and worm holes) and air gaps along sensors that impact TDR measurements (Robinson et al., 2003).

Two major issues in vadose zone hydrology are the characterization of the vertical soil moisture distribution within this region and the nature of its coupling with soil moisture variations at the surface (Vereecken et al., 2008). Two standard surface GPR techniques have the capacity to provide this type of information. Common-midpoint (CMP) soundings supply offset distance-traveltime data for subsurface reflection events; the normal moveout (NMO) analysis of these data give velocity profile information that can be used to infer vertical soil moisture variation (e.g., Greaves et al., 1996; Garambois et al., 2002; Turesson, 2006). However, the quality of the results from this approach are sensitive to numerous factors (Jacob and Hermance, 2004; Becht et al., 2006; Barrett et al., 2007; Booth et al., 2010); this makes it difficult to obtain consistent results over the annual cycle of hydrological conditions, particularly during dynamic moisture periods (Steelman and Endres, in review) [Chapter 4].

Recent applications of reflection profiling to extract vertical soil moisture information have been promising (i.e., Lunt et al., 2005; Wollschläger and Roth, 2005; Grote et al., 2005). This approach is less susceptible to measurement errors compared to NMO analysis; hence, it is potentially a more suitable technique to monitor highly variable soil conditions. While this method can monitor relative soil moisture changes through the use of reflection traveltime variations, the extraction of true soil moisture values requires independent information regarding the depth of the reflecting interfaces. In these previous works, this information was obtained from boreholes or excavations. In addition, limited temporal sampling and low resolution near the surface in these earlier studies restricted quantitative analysis of vertical soil moisture distribution and associated dynamics within the shallow vadose zone.

To further examine the capacity of surface GPR techniques to characterize soil moisture dynamics in a non-invasive manner, we have undertaken an extensive 26 month field study covering two complete annual cycles of soil conditions (i.e., dry summer, wet spring and autumn, frozen winter soil conditions) typical of mid-latitude climates. Concurrent reflection profiles and CMP soundings were acquired on a daily to weekly interval using high-frequency 900 MHz antennas. The reflection profiles provided high resolution traveltime data for stratigraphic reflection events while the analysis of our complete CMP sounding data set produced precise depth estimates for those reflecting interfaces. As a result, we clearly demonstrated the ability of surface GPR methods to give high quality estimates of soil moisture in the upper 3 meters of the vadose zone over a wide range of soil moisture conditions characterized by highly variable moisture dynamics. This unique multi-year data set not only allowed us to quantitatively investigate seasonal moisture processes (i.e., infiltration, drainage, freeze and thaw), but also variation between contrasting annual cycles (e.g., wet versus dry summer conditions).

In addition, the use of CMP soundings permitted the determination of direct ground wave (DGW) velocities. Our previous work at this site (Steelman and Endres, 2010) [Chapter 2] clearly showed the capacity of DGW method employing CMP data to monitor soil moisture immediately below the air-soil interface (i.e., upper ~0.2 m) over the complete annual cycle. The improved resolution near the surface provided by the DGW method enables better characterization of short-duration wetting (infiltration) and drying (evapotranspiration) processes which, when combined with our reflection results, allowed us to more closely examine the coupling between soil moisture profile through the vadose zone and surface soil moisture variations.

To further assess the information about soil moisture dynamics derived from surface GPR monitoring, our GPR soil moisture estimates were also compared with results obtained from an unsaturated numerical flow modeling package, HYDRUS-1D, using laboratory derived hydraulic parameter estimates of soil samples extracted from the site. The results of this comparison are given in Steelman and Endres (in review) [Chapter 6].

5.3 Surface GPR Techniques

Surface GPR techniques use transmitting and receiving antennas that are positioned along the surface (i.e., the air-ground interface). The two commonly-used surface GPR techniques are reflection profiling and CMP sounding (Figure 5.1). A brief description of these two techniques is given below; detailed information concerning their theoretical foundation, instrumentation, data acquisition and processing is found in a number of excellent sources (e.g., Neal, 2004; Annan, 2005; Jol, 2009).

Reflection profiling (Figure 5.1a) is done with a constant (i.e., fixed) offset antenna array that is placed at sampling points located at regular intervals along a survey line, providing a cross-sectional image composed of reflection events originating from subsurface interfaces that delineate contrasting EM properties. The two-way traveltimes for reflections from these interfaces are obtained from the radargram acquired at each sampling point. Temporal variations in the interval traveltime between two given stratigraphic reflecting interfaces in the vadose zone are due to EM wave velocity changes accompanying water content variations between these interfaces. However, only relative changes in water content within these intervals can be inferred from these traveltime data; absolute water content estimates require independent information about the interval thicknesses.

CMP soundings (Figure 5.1b) systematically change the offset between the transmitting and receiving antennas while maintaining a fixed midpoint location, resulting in a separation of coherent events in the wavefield (e.g., direct air wave, direct ground wave and subsurface reflections). The traveltime-offset distance relationships for the subsurface reflections are determined using NMO analysis techniques (Yilmaz, 2001) that were originally developed for the processing of seismic reflection data. An estimate of interval velocity and layer thickness between two successive stratigraphic reflection events can be determined using the Dix (1955) equation. In addition, the DGW that propagates just below the air-soil surface between the antennas is readily identified and analyzed using CMP data (e.g., Steelman and Endres, 2010).

5.4 Experimental Description

5.4.1 Field Site

GPR measurements were collected within an active agricultural field located on the Waterloo Moraine. This site (528878E, 4814702N) is located 3 km west of Waterloo, Ontario, Canada. The Waterloo Moraine is described as an irregular tract of gently rolling to hummocky terrain with some exposures of ice-contact stratified sand and gravel deposits (Russell et al., 2007). The measurement location is positioned atop a local sand hill characterized by interbedded fine to coarse sand. The local water table is believed to be 15–20 m below ground surface based on nearby water bodies and geophysical measurements. While haying operations were conducted during the study period, other agricultural disturbances, such as plowing and tilling, were not performed during or in the recent past (i.e., within the preceding 2–5 years) prior to this study. Precipitation and atmospheric temperature for this site was monitored using the University of Waterloo weather station located approximately 7 km east of the site.

This stratified clean sand deposit permitted superior GPR depth penetration using high-frequency antennae and provided numerous stratigraphic reflection events suitable for repeated traveltime measurement. Figure 5.2 shows the location of the 2.0 m intensive monitoring profile relative to the larger X–X' and Y–Y' reflection profiles which illustrate the local stratigraphy in the immediate vicinity of the intensive monitoring profile.

5.4.2 Seasonal Weather Conditions

Data collected at the University of Waterloo weather station shows daily average high/low temperature range and cumulative precipitation for each month during the years 2006–2008 (Figure 5.3); these data highlight the seasonal conditions that occurred during the August 2006–October 2008 study period. Overall, the 2006 period was the third hottest year on record in nearly 100 years for the Region of Waterloo with an average temperature of 8.5°C (i.e., 1.6°C above the 1970–2000 average for the region). During this year, six months registered temperatures significantly above average, while five were slightly higher than average. October was the only month with slightly below average temperatures. This annual period also had consistently above average precipitation (1076.6 mm verses 904.0 mm 1970–2000 annual average).

In contrast, the 2007 period was characterized by extremely low precipitation (671.9 mm) with cooler (only 0.6°C above 1970–2000 average) temperatures compared to 2006. This lack of

precipitation can be seen throughout the year with six of the months recording significantly below average values, including a record low 26.6 mm during June which is about one-third of the average. December was the only month with higher than average precipitation. The following 2008 period experienced above average precipitation (1159.5 mm compared to the 904.0 mm 1970–2000 annual average). This year had the third highest precipitation recorded since 1915 and was significantly wetter than the 2007 period.

During 2008, seven months had above average precipitation and five were below average. Most notable was the month of July when 181.0 mm fell; this was the wettest July since 1991. Further, two very significant precipitation events happened during this month: a 1 in 25 year storm when 78.0 mm of rain occurred over 6 hours on July 11th and a 1 in 10 year rainfall on July 22nd when 23.0 mm fell over a 15 minute period. Annual average temperature for 2008 was slightly cooler (i.e., only 0.2 °C above 1970–2000 average) than 2007.

Of particular importance in this multi-year study were the contrasting seasonal conditions encountered during different annual cycles. For example, the summer 2007 period was both hot (0.9°C warmer than average) and dry (143.4 mm verses 30 year average of 274.0 mm); in addition, it was not characterized by major storm events. Conversely, the 2008 summer period was the 5th wettest measured in the region since 1915 (416.2 mm verses the 30 year average of 274.0 mm) with slightly warmer than average temperatures (0.5°C warmer than average). Further, 45 days of precipitation occurred in 2008 compared to 33 days in 2007; many of these 2008 precipitation events were intense, short-duration storms, including the two July events noted above, which were quickly followed by sunny conditions. The 2006 and 2007 autumn periods also differed significantly. The 2006 autumn period was wet (293.8 mm verses the 30 year average of 220.9 mm). In comparison, the 2007 period was dry (213.0 mm verses the 30 year average), particularly during the month of October when temperatures were also abnormally warm.

Warmer than average temperatures in late-2006 delayed the onset of wintertime conditions until mid-January 2007, and only 104.5 cm of snowfall occurred over this winter period. However, temperatures dropped significantly by February and remained well below zero until late-March, preventing the occurrence of intra-seasonal thaw events. In contrast, the 2007–2008 winter season was initiated earlier in late-November 2007 and experienced a record breaking snowfall of 257.5 cm, exceeding the previous record of 245.3 cm set in 1924. Highly variable temperatures occurred throughout this winter period, including a record breaking high of 13.3°C on January 8th that was the

4th highest January temperature measured in the region since records first began in 1915. This January 6th–11th period of above freezing temperatures was accompanied by approximately 50 mm of rainfall including 9.9 mm on January 8th and 33.2 mm on January 9th; the latter of which was the wettest January day since 1995. This wetting period resulted in a major intra-seasonal thaw event. Additional short-duration warming and cooling cycles during early-February and mid-March 2008 resulted in numerous freeze-thaw cycles prior to seasonal thaw in early-April.

5.4.3 GPR Acquisition and Analysis

A coincident pair consisting of a reflection profile and CMP sounding was acquired along a fixed 2.0 m survey line during each field session over the entire course of our study period between 28 August 2006 and 20 October 2008. A total of 165 GPR data sets were obtained at intervals ranging from 1 day to 4 weeks. It was determined that 162 reflection profiles and 159 CMP soundings were suitable for our analysis primarily due to the presence of dispersive wavefields during shallow freeze/thaw events (e.g., van der Kruk et al., 2009; Steelman et al., 2010) that significantly obscured reflection arrivals.

The GPR data in this study was collected using a Sensors and Software PulseEKKO™ 1000 (Sensors & Software Inc., Mississauga, Ontario, Canada) GPR system equipped with 900 MHz antennas. All GPR data was acquired using a time window of 100 ns, sampling interval of 0.1 ns and 64 stacks per trace. The reflection profiles and CMP soundings were collected using a manual trigger mode and the antennas remained stationary during the recording time. For the reflection profiles, the transmitter and receiver antennae were maintained at a constant 0.17 m separation (i.e., using manufacturer's brackets) and with stations every 0.02 m along the 2.0 m line. The CMP data was acquired for offsets between 0.2 to 2.0 m with a 0.02 m separation increment; the sounding midpoint was centered on the reflection profile.

The GPR data were processed using Reflex-Win™ software program (Sandmeier Software, Karlsruhe, Germany). The processing sequence applied to these data sets is summarized in Table 5.1. While numerous stratigraphic reflection events were persistently identified along the 2.0 m monitoring profile in both reflection and CMP data, only a small subset of these events were suitable for consistent traveltime and NMO velocity analysis. Suitable reflection events were (1) laterally continuous with consistent vertical separation across the monitoring profile, (2) corresponded to major stratigraphic boundaries (i.e., likely unconformities defining major stratigraphic packages), (3)

clearly identifiable in both reflection and CMP data sets, and (4) exhibited sufficient traveltime separation for reliable interval velocity/depth determination. Figure 5.4 shows the four reflection events selected for our study. These seasonally persistent reflection events allowed us to define four distinct soil intervals at fixed depths, within which soil conditions could be continuously monitored throughout the study period.

The two-way traveltime for each of the four designated stratigraphic events were determined at every station along the 2.0 m reflection profile, producing 101 individual traveltime measurements for each interface. This process was performed using an automated picking procedure in Reflex-Win™ that is based on maximum amplitude to ensure consistent identification of events across the profile. Traveltimes along the 2.0 m profile were averaged to obtain a single representative value for each event. By averaging over the 2.0 m profile, we are implicitly assuming the major elements of the soil moisture flux in our vadose zone can be represented by a one-dimensional vertical system. This contention is supported by our observation that comparable results were obtained using smaller lateral averaging intervals (i.e., 0.25 and 0.50 m). In addition, averaging over the entire 2.0 m profile maintained spatial consistency between the CMP sounding and reflection profiling data and produced more reliable traveltime measurements in the presence of noise when reflection identification and amplitude picking was more difficult (e.g., interference from surface scattering during thaw periods).

These data were then differenced to obtain interval two-way traveltime (Δt_N) which was then converted into interval velocity using the following relationship:

$$v_N = \frac{1}{\Delta t_N}\left\{2h_N \cos\left[\tan^{-1}\left(\frac{a}{2z_N}\right)\right]^{-1}\right\}. \qquad (5.1)$$

The depth to reflection z_N, antenna separation distance a, and interval thickness h_N are constants for each interval. This expression assumes straight raypath segments between the antennas and the reflecting interface, ignoring raypath bending at intermediate interfaces due to Snell's Law. This assumption is reasonable given the relatively small antenna separation distance used in the profiling compared to depths of the selected interfaces.

The estimates of interval thicknesses and reflection depths were obtained from the cumulative results of the NMO velocity analyses of the individual CMP soundings. The analysis procedure of an individual CMP sounding is illustrated in Figure 5.5. The four seasonally persistent stratigraphic

reflection events present on the reflection profile (Figure 5.5a) were identified on the corresponding CMP sounding (Figure 5.5b). Using the NMO velocity analysis component in the Reflex-Win™ software program, a semblance plot (Figure 5.5c) was generated from the CMP data from which NMO velocity (V_{NMO}) and two-way zero-offset traveltime (t_o) values were determined for each of the four reflection events. The software used these NMO velocities and traveltimes in conjunction with Dix's (1955) equation to construct interval velocity-depth models (Figure 5.5d) from which layer thickness values are obtained.

As previously noted, the level of uncertainty in the interval velocity-depth model obtained from the NMO velocity analysis of an individual CMP sounding is sensitive to numerous factors. In particular, these results are strongly dependent on the magnitude of the vertical EM wave velocity gradients present in the subsurface (Becht et al., 2006). Given the highly variable nature of water content in the shallow vadose zone, one would expect significant variations in vertical velocity gradients over the annual cycle of hydrological conditions. Uncertainties in the NMO velocity and zero-offset traveltime values increase as the interval thickness between selected reflecting interfaces thins due to the differencing process involved with Dix's (1955) equation (e.g., Hajnal and Sereda, 1981). Moreover, interval measurement resolution diminishes with increasing reflector depth (e.g., Jacob and Hermance, 2004; Booth et al., 2011; Steelman and Endres, in review).

Figure 5.6 shows the range of layer thickness values obtained from the 159 individual CMP soundings. One can readily see the impact of factors such as velocity gradient and interface depth on the variability of the individual results. To further reduce the uncertainty level in the layer thickness used to infer interval velocities from Equation 5.1, we have elected to use the mean value for each layer; these mean values and their 95% confidence interval are given in Table 5.2. In addition, the CMP data were used to determine the DGW velocity for each field date using the technique described in Steelman and Endres (2010). The DGW velocity was used to monitor soil moisture within the upper few decimeters of the vadose zone.

5.4.4 Direct Sampling

Pitting and coring was used to obtain detailed soil property information directly below the fixed survey line after the study was completed. The exposed upper 2 m section (Figure 5.7) is primarily characterized by well-sorted sequences of fine to coarse grained sand layers ranging between a few centimeters to decimeters in thickness. The dark coloured coarse sand in the upper 0.25 m represents

the plough zone and contains approximately 1.5% (wt/wt) organics and 3% silt fraction. The soil root zone is primarily contained within this region of the soil; however, some larger alfalfa roots did extend to greater depths as seen on the right hand side of Figure 5.7. While these detruding darker coloured root zones may act as preferential flow paths within the sandy soil matrix, they were not prevalent along our intensive monitoring profile.

In an effort to determine the source of the reflection events used to monitor vertical traveltime with units visible in the section, we horizontally inserted metal rods (markers 1–7 in Figure 5.7) at various stratigraphic boundaries across the exposure. A reflection profile was then repeated along the 2.0 m profile at the edge of the pit; the apex of the diffraction hyperbolas corresponding to these rods were then compared to the positions of the four reflection events. This survey established the identification of reflections 1 and 2 across the soil section. It was found that rods 5 and 7 corresponded to reflection 1 and were located 0.56 m and 0.53 m below ground surface, respectively. In addition, rod 6 corresponded to reflection 2 and was located 1.33 m below ground surface. These results are in good agreement with the depths obtained from the interval velocity-depth models.

Bulk soil samples (markers A–H in Figure 5.7) were extracted at various depths using small aluminum cylinders inserted along the exposed section of soil. These samples were used to obtain estimates of porosity assuming an average grain density of 2.65 g/cm^3. Falling head permeameter tests were performed on repacked samples (i.e., 4 runs per sample) to obtain an average saturated hydraulic conductivity. Water retention curves were then measured using the hanging water column method (Stephens, 1996) where the initial drainage curve was used to estimate Brooks and Corey (1964) unsaturated hydraulic conductivity parameters. Their relationship expressed in terms of effective water content S_e is defined as follows:

$$S_e = \begin{cases} \left(\dfrac{h}{h_b} \right)^{-\lambda} & h > h_b \\ 1 & h \le h_b \end{cases}, \tag{5.2}$$

where

$$S_e = \frac{\theta - \theta_r}{\theta_s - \theta_r}. \tag{5.3}$$

The effective water content varies as a function of suction head h, while parameters h_b and λ are characteristic properties of the medium representing the air-entry pressure head and pore-size distribution, respectively. The saturated and residual water contents are represented by θ_s and θ_r, respectively. A summary of the soil property information obtained from the soil section is provided in Table 5.3.

5.5 Results and Interpretation

5.5.1 Interval Velocity Estimation

For non-magnetic, low-loss materials, the EM wave velocity v primarily depends on the relative dielectric permittivity κ of the medium (i.e., the effective permittivity of the bulk material ε relative to the free space permittivity ε_o) such that $v = c/\sqrt{\kappa}$ where c is the EM wave velocity in free space (0.2998 m/ns). Because the permittivity of liquid water (κ_w = 78–88) contrasts strongly with other common components of the soil system (i.e., mineral soil grains κ_s = 4–6 and air κ_a = 1), as well as ice (κ_i = 3.2) (Cassidy, 2009), EM wave velocity in a soil is strongly dependent on its liquid water content.

The interval velocity values obtained from two-way traveltime measurements and interval-thickness estimates are shown with corresponding DGW velocity data in Figure 5.8. The shaded regions encompassing the interval velocity data represent the 95% confidence interval based on random measurement errors (i.e., spatial variations in Δt_N), while the region encompassing the DGW data represents the standard error derived from the slope of the best fitting line (Steelman and Endres, 2010). It should be noted that the uncertainties in interval thickness (shown Table 5.2) are systematic and are not included in the 95% confidence intervals. The relative effect of systematic uncertainties on soil moisture estimates will be discussed in the following section.

The results for Interval 1 (Figure 5.8b) covering the uppermost 0.50 m clearly display numerous short-term events superimposed onto significant long-term seasonal trends. In general, velocities were higher during summer and winter and lower during spring and autumn periods. These trends reflect the generally wet spring and autumn conditions in contrast to the dry summer and frozen winter conditions. The short-duration features in velocity observed in Interval 1 throughout the spring to autumn periods are largely in response to precipitation events while short-term events in the winter correspond to rapid freeze-thaw cycles. The DGW velocity data (Figure 5.8a) are very similar in

form, indicating that much of the velocity variation in Interval 1 is probably due to soil moisture changes in the upper 0.20 m.

Comparison of the Interval 1 (Figure 5.8b) results with those for Intervals 2–4 (Figures 5.8c–e, respectively) clearly show the progressive attenuation of both the short-duration events and seasonal trends with greater depths. In addition, systematically increasing temporal delays can be seen as the trends and events propagate downwards through the profile. The details of this coupling are directly reflected in observed soil moisture variations described below in Section 5.5.3.

5.5.2 Estimation of Soil Water Content

Soil water content estimation from EM velocity requires an appropriate petrophysical relationship to convert the bulk permittivity κ of the material into a volumetric water content θ measurement. Steelman and Endres (2011) [Chapter 3] showed that the Complex Refractive Index Model (CRIM) (e.g., Birchak et al., 1974; Wharton et al., 1980; Dobson et al., 1985) provides reliable estimates of water content for the range of conditions considered in this study, and is given by

$$\theta = \frac{\sqrt{\kappa} - (1-\phi)\sqrt{\kappa_s} - \phi\sqrt{\kappa_a}}{\sqrt{\kappa_w} - \sqrt{\kappa_a}}. \tag{5.4}$$

Here, ϕ represents soil porosity, while κ_a, κ_s and κ_w represent the permittivities of the air, solid mineral and water phase constituents, respectively.

Interval velocity values in Figure 5.8 were used with Equation (5.4) to estimate the interval soil water content. A depth weighted mean porosity ϕ = 0.39 from Table 5.2 was used while the fixed dielectric permittivity values assigned to the air, solid mineral and liquid water constituents were κ_a = 1, κ_s = 5 and κ_w = 84.9, respectively. Our dielectric value for water corresponds to a temperature T = 8˚C which represents the average annual temperature in this region. While variable soil temperatures are expected near the surface, an absence of in-situ soil temperature data restricts our ability to temporally constrain the κ_w parameter. A sensitivity analysis using κ_w values between 88.1 (T = 0˚C) and 78.5 (T = 25˚C) indicates maximum variations in water content estimates of <0.01 m^3m^{-3} when assuming a constant ground temperature of 8˚C and κ_s = 5. It should be noted that this maximum temperature variation coincides with very wet conditions (i.e., up to 0.20 m^3m^{-3}) and is reduced at lower moisture contents.

While temperature changes during the course of the study may contribute a small degree of uncertainty in water content estimate, more significant uncertainties are possible due to the solid phase permittivity and soil porosity parameters used in Equation (5.4), as well as uncertainties in our interval thickness estimates; however, these sources of uncertainty are systematic and do not vary during the study period. Although our permittivity value for solid phase is reasonable for quartz grain, values for sand range between 4 and 6 (Cassidy, 2009). Further, soil porosity can vary with depth due to changes in grain size distribution. Our simplifying assumptions about the soil system will introduce some degree of systematic uncertainty in our water content estimates. A simple uncertainty propagation analysis using the upper-lower bound method (i.e., using uncertainty ranges in each variable to calculate maximum and minimum values in water content) resulted in the following systematic uncertainties in water content: DGW = ±0.021 m^3m^{-3}; Interval 1 = ±0.024 m^3m^{-3}; Interval 2 = ±0.024 m^3m^{-3}; Interval 3 = ±0.028 m^3m^{-3}; Interval 4 = ±0.032 m^3m^{-3}. While this simple uncertainty propagation method does not yield a standard uncertainty estimate (i.e., 68% confidence interval), it does give a conservative estimate of the maximum systematic error in our water content measurements.

5.5.3 Soil Moisture Profile Dynamics

Interval moisture content estimates are presented in Figure 5.9 with the daily precipitation and average air temperatures observed at the University of Waterloo weather station. In addition, corresponding water storage estimates (mm) based on the thickness of each interval and an average porosity ϕ = 0.39 are also given in Figure 5.9. These water storage plots are shown to highlight the water flux between adjacent soil intervals.

For Intervals 2–4, the values of the estimated soil moisture range between 0.05 m^3m^{-3} and 0.12 m^3m^{-3}. The limiting low moisture values are in good agreement with residual saturations obtained from the laboratory measurements (Table 5.3), which indicates that our soil moisture estimates are minimally impacted by potential systematic uncertainties associated with phase permittivity, porosity and interval thickness. An exception occurred in Interval 2 during February–March 2007 when values down to 0.03 m^3m^{-3} were found. During this period, a transient event inferred to be the base of the frost table was observed well within Interval 2; the characteristics of such reflection events are described in Steelman et al. (2010) [Chapter 8]. Hence, these lower moisture estimates reflect the conversion of high permittivity liquid pore water to low permittivity ice in the portion of Interval 2 above the frost table.

In contrast, water content estimates for Interval 1 varied over a greater range from 0.03 m^3m^{-3} to 0.18 m^3m^{-3}. Water content values obtained from the gravimetric sampling of the upper 0.50 m at our site (Steelman and Endres, 2010) were consistent with the GPR derived estimates; this agreement is another indication to minimal influence of the previously mentioned potential systematic uncertainties. The extended lower limit is due to frozen soil conditions and the effects of desiccation near the surface during dry summer periods. The higher upper limit is the product of extensive wetting that happens at times of snow melt and thawing.

The GPR reflection-derived soil moisture values for Interval 1 clearly show long-term seasonal trends overlain by numerous short-term events. In general, it can be seen that the inferred interval soil moisture in Interval 1 increases in early spring (e.g., late March–early April) due to infiltration resulting from the seasonal thaw marking the end of frozen soil conditions. Afterwards, soil moisture tends to decrease through the late spring and summer period, followed by increasing moisture values during the autumn. The winter is marked by an apparent decrease in soil moisture due to the conversion of pore water into ice.

The comparison of corresponding seasons in Interval 1 values clearly shows the influence of differing annual cycle conditions. The dry and hot 2007 spring-summer period is characterized by a well-defined moisture decrease after the seasonal thaw that is punctuated by a few relatively low amplitude, short-duration moisture changes associated with the few significant rainfall events that occurred. For the wet 2008 spring-summer period, the seasonal trend is partially obscured by numerous high amplitude short-term moisture variations accompanying the many large precipitation events that happened during this time. In addition, the lowest moisture level monitored in Interval 1 during the summer of 2007 (i.e., 0.036 m^3m^{-3}) is well below that observed in 2008 (i.e., 0.057 m^3m^{-3}). Soil water storage was persistently higher along the profile during the 2008 summer period and was punctuated by a number of infiltration pulses.

During the autumn of 2006, sustained precipitation during the months of September and October resulted in an early moisture increase in Interval 1 that was maintained throughout the remainder of that wet autumn. In contrast, the soil moisture exhibited a more gradual increase during the drier 2007 autumn conditions until the occurrence of significant precipitation in November; this behavior is believed to reflect the seasonal slowing of evapotranspiration.

The onset of persistent freezing conditions in the 2006–2007 winter period did not occur until mid-January, but remained largely uninterrupted until the seasonal thaw in late March. These conditions

correlate well with the duration of low apparent moisture observed in Interval 1. Differing conditions were encountered in 2007–2008 winter, when persistent freezing conditions initiated in late November and were punctuated by intra-seasonal thaw events until the seasonal thaw in late March–early April. Again, these conditions are well represented in Interval 1 response where the low apparent moisture values that develop during this period are interrupted by a large moisture increase during the major early January thaw event.

The long-term seasonal trends observed in deeper Intervals 2–4 are similar to those described for Interval 1, but display progressively decreased magnitude with depth. In addition, episodes of infiltration associated with major thaw (t) and precipitation (p) events can be seen to propagate downward in Figure 5.9, significantly impacting soil water storage in the deeper portions of the profile. These short duration infiltration pulses are both more attenuated and increasingly delayed as they move down through the soil column.

Again, the comparison of corresponding seasons demonstrates the effects of differing annual cycle conditions. During the dry 2007 spring-autumn period, only infiltration due to the seasonal thaw (t^1) and the late autumn precipitation (p^2) was observed, there was no detectable infiltration pulses associated with the three major rainfall events which occurred during the August–September period. The evolution of the deeper soil moisture is completely characterized by the long-term seasonal patterns of a slow spring decline and autumn increase in water storage. In contrast, the wet spring-summer 2008 period exhibits several large mid-summer infiltration pulses (i.e., p^3 and p^4) accompanying major storm events. Dynamic changes in water storage can be seen down the profile during these events as water percolated through the system. Infiltration in the wet 2006 autumn period commenced much earlier than in the drier 2007 autumn (i.e., p^1 verses p^2), and higher soil moisture persisted along the entire profile through the autumn of 2006.

The contrast in the moisture profiles during the two winter periods is also striking. In the 2006–2007 winter season, the effects of substantial frost table extension into Interval 2 can be inferred from its very low apparent moisture during the February–March 2007 timeframe. The 2006–2007 winter is also characterized by a lack of infiltration due to significant intra-seasonal thaw events. Further, the development of the seasonal frost zone in Intervals 1 and 2 coincides with a period of accelerated moisture loss in Interval 3, which effectively reduced the amount of water stored in the lower soil profile. During the 2007–2008 winter period the frost table development appears to have been more restricted; and its impact on the estimated Interval 2 soil moisture values is not readily discernable. In

contrast to 2006–2007 winter season, the water stored in Intervals 3 and 4 continued to increase after the formation of seasonal frost zone at the surface due to the late precipitation (p^2). The major intra-seasonal thaw event in January 2008 (t^2) produced a large infiltration event that, in conjunction with the late autumn 2007 infiltration (p^2), resulted in elevated soil moisture throughout the section. These pre-existing higher moisture levels appear to partially obscure the effect of the subsequent 2008 seasonal thaw pulse (t^3) in Intervals 3 and 4.

5.5.4 Resolving Near-Surface Soil Moisture Dynamics

Soil moisture estimates based on the DGW velocity values derived from CMP data provide information about conditions in the upper 0.20 m region directly below the air-soil interface. These values are compared in Figure 5.10 with the soil moisture estimates for Interval 1 that covers the upper 0.50 m of the vadose zone, including the DGW sampling volume. The difference between these two sets of moisture estimates is shown to further highlight the relationship between their respective measurement scales. The weather conditions observed at the University of Waterloo station are also included.

These data clearly demonstrate the higher sensitivity of DGW measurements to changes in shallow soil conditions compared to Interval 1. This increased sensitivity is particularly evident in the DGW response to short-duration wetting and drying processes. During the dry 2007 spring-autumn conditions, the large variations in the DGW moisture values associated with the significant rainfall events are generally much more subdued features in the Interval 1 data. While these types of events are more prominent in the Interval 1 data during the wet 2008 spring-autumn conditions, they are still lower amplitude events than those seen in the DGW data.

Further, the expression of some longer term seasonal trends differs between these two data sets. The DGW data indicate higher moisture conditions during the mid-late autumn period in both 2006 and 2007, as well as wetter post thaw conditions in early April 2007. In addition, the onset of shallow frost development is better defined in the DGW data by the rapid appearance of low apparent moisture values with freezing conditions. The highly dynamic freeze-thaw cycles that occurred in mid-late March 2008 (i.e., onset of seasonal thaw) resulted in dispersive wave propagation which temporarily impacted our ability to obtain DGW moisture estimates, resulting in small gaps in the data series; however, these dispersive conditions did not significantly affect our ability to obtain a measurement for Interval 1.

Although short-duration transient events are observed in the uppermost layer (Interval 1), both the magnitude and nature of these events differed from that of the shallower DGW results. This highlights the importance of adopting higher resolution measurements which can better capture highly dynamic surface moisture conditions. Knowledge of surface moisture conditions (e.g., within the root zone) is of utmost importance for understanding the coupling between the vertical soil moisture distribution and soil moisture variations as the surface. As shown in Figure 5.10, DGW measurements obtained from the CMP data improves our resolving capability of shallow surface moisture conditions, and hence hydrologic processes such as evapotranspiration.

5.6 Conclusions

This study represents the first attempt to fully assess the concurrent use of two surface GPR techniques (i.e., reflection profiling and common-midpoint soundings) to characterize vertical soil moisture dynamics within the vadose zone, and the nature of its coupling with soil moisture variations at the surface over such a wide range of hydrological conditions. The 900 MHz reflection profiles provided high resolution traveltime information for selected stratigraphic reflection events that were used to monitor the soil moisture variations in the intervals between the reflecting interfaces. The CMP soundings supplied depth information that permitted the determination of interval EM wave velocity, and the subsequent estimation of interval soil moisture. The cumulative analysis of our complete CMP sounding data set significantly reduced the inherent uncertainty in the depth estimates obtained from individual CMP soundings, which in turn better constrained our moisture estimates. The comparison of our cumulative depth estimates for the upper two interfaces with the results of the post-excavation reflection profiling clearly demonstrates the value of this approach.

Our multi-year surface GPR data set allowed us to non-invasively characterize shallow soil moisture dynamics on various time scales. Long-term seasonal trends, such as the overall moisture decrease during the late spring-summer period, are defined in our data and observed to decrease in magnitude with depth. The downward propagation of major infiltration episodes associated with seasonal (i.e., spring recharge) and transient (i.e., major rainfalls and intra-winter thaws) events are also resolved by our geophysical data. In addition, our GPR data shows variations in the nature of these seasonal trends and infiltration events between contrasting annual cycles, such as the dry versus the wet summers.

Comparison of the soil moisture estimates for the uppermost layer (Interval 1) with those estimates for the deeper layers (Interval 2–4) clearly demonstrates how high resolution surface GPR techniques can determine the impact that the coupling between the vertical soil moisture distribution and soil moisture variations at the surface has on soil moisture dynamics in the vadose zone, as well as how this coupling varies with contrasting annual cycles. Further, it can be seen that DGW measurements from the CMP data, with its better near-surface resolution, allowed us to more closely examine the nature of this coupling. We would anticipate that combination of water content estimates from the DGW and interval traveltimes will prove useful for quantifying the effects of near-surface phenomena such as evapotranspiration.

As impressive as the results of this study are, it is necessary to further assess the quality of the soil moisture estimates obtained from these data. In the absence of detailed in-situ soil moisture measurements, we propose that this issue can be examined using the results of a standard unsaturated flow numerical modeling package, such as HYDRUS-1D, that are based on the laboratory characterization of soil samples obtained from our coring and pit. Steelman and Endres (in review) [Chapter 6] gives the outcome of this comparison, showing that the GPR soil moisture estimates are consistent with the modeling predictions.

5.7 Tables and Figures

Table 5.1 Processing sequence applied to CMP and reflection profile data.

Process	Parameters
Dewow	Time window = 1.111 ns
Mean Filter	Mean range = 4 points
Zero-Time Correction[a]	Independent correction based on peak air-wave arrival and zero-offset position
Time Cut	Uniform time window = 80 ns
Gain Function	Linear gain = 0.1 [1/pulsewidth]; exponent = 8 [db/m]; max gain = 1000
f-k Filter[b]	Manually defined area using bandpass filter to remove scattering events; linear taper width (*f* and *k*) = 10
Bandpass Frequency	Lower cutoff–lower plateau–upper plateau–upper cutoff 100–200–1100–1400 MHz
Running Avg[c]	Average traces = 3

[a] Reflection zero-time were also corrected for antenna offset; CMP zero time determined using linear extrapolation to zero-offset

[b] Applied to selected reflection profiles (17, 21 and 28 March 2008) exhibiting strong surface scattering during thaw conditions

[c] Applied to reflection profiles

Table 5.2 Average interval thickness[a] based on the cumulative results of the NMO analyses.

Depth Interval	Interval Thickness, h_N		Lower Interface Depth, z_N
	Mean	95% C.I.	
	m		
DGW	0.20[b]	-	N/A
Interval 1	0.504	0.005	0.50
Interval 2	0.814	0.007	1.32
Interval 3	0.790	0.018	2.11
Interval 4	0.821	0.032	2.93

[a] Obtained from 159 interval velocity-depth models
[b] Approximate sampling depth based on comparisons with gravimetric soil samples (Steelman and Endres, 2010)

Table 5.3 Measured hydraulic parameters.

Sample	Depth [m]	ϕ [-][a]	h_b [m][b]	λ [-][b]	θ_r [m^3m^{-3}][b]	$K_s \times 10^{-4}$ [m s^{-1}][c]
A	0.2	0.37	0.259	0.933	0.071	1.32
B	0.4	0.37	0.254	1.305	0.052	2.37
C	0.5	0.39	0.260	1.509	0.044	2.20
D	0.6	0.35	0.250	2.141	0.051	2.47
E	0.8	0.40	0.211	2.263	0.059	4.10
F	1.0	0.42	0.251	2.231	0.073	4.09
G	1.3	0.41	0.268	2.533	0.049	2.80
H	1.6	0.45	0.258	3.674	0.095	3.26
Mean[d]	-	0.39	0.252	1.716	0.060	2.42
95% C.I.[e]	-	0.03	0.014	0.692	0.014	0.78

[a] Based on in situ soil bulk density samples
[b] Brooks–Corey parameters fitted to initial drainage curve
[c] Average value from four repeated falling head permeameter tests
[d] Weighted mean value
[e] Confidence interval determined using Student's T-distribution

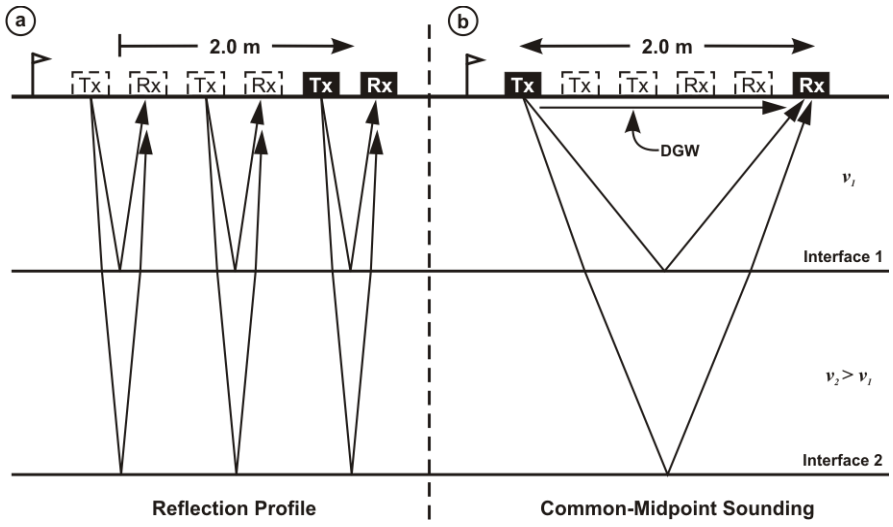

Figure 5.1 Schematic diagram illustrating the (a) reflection profiling and (b) common-midpoint (CMP) sounding techniques.

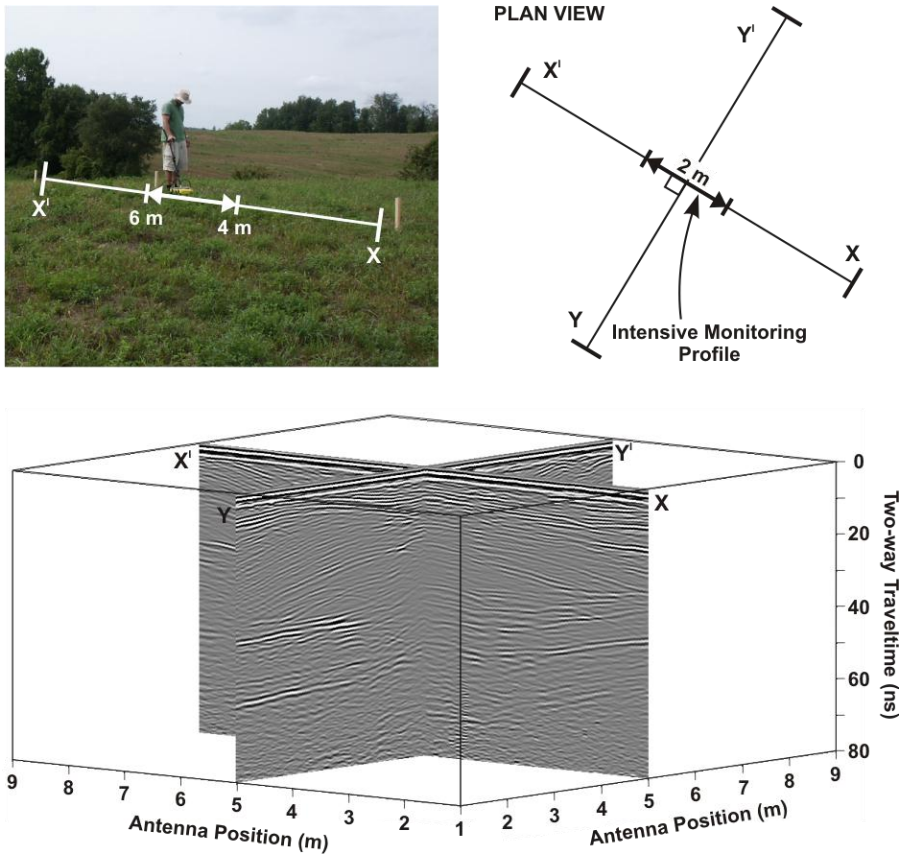

Figure 5.2 Reflection profiles collected parallel (X–X') and perpendicular (Y–Y') to intensive monitoring profile showing the shallow stratigraphy of the test site.

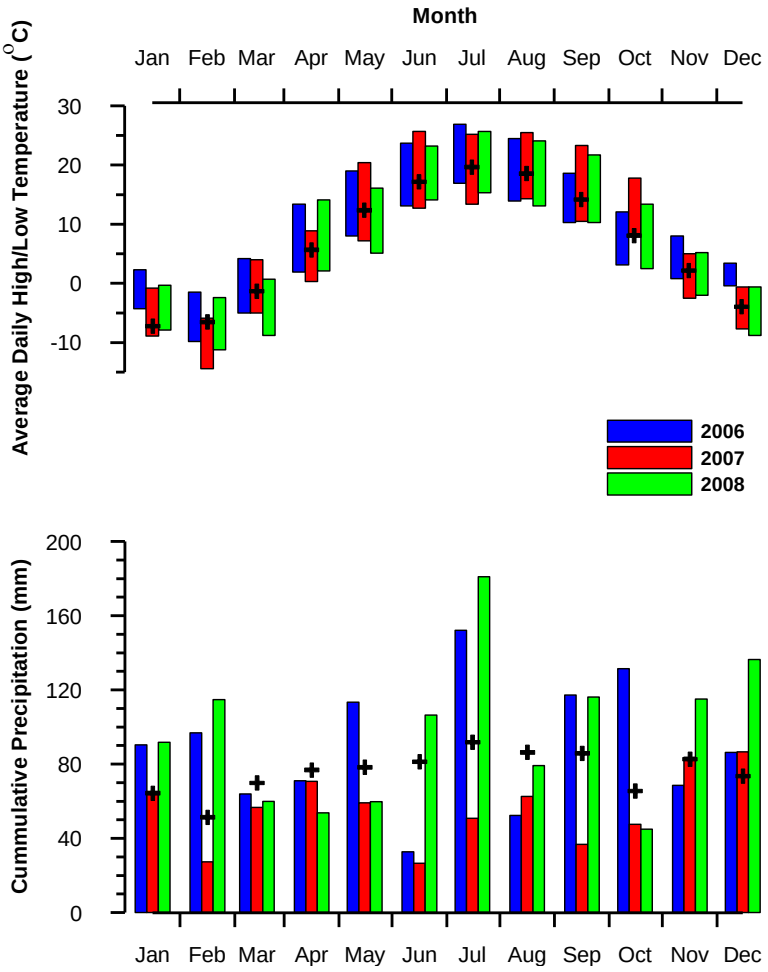

Figure 5.3 Monthly precipitation and average temperature range for 2006, 2007 and 2008 annual periods. The 30 year (1970–2000) average precipitation and mean monthly temperature for Waterloo-Wellington region are shown by (+) symbol.

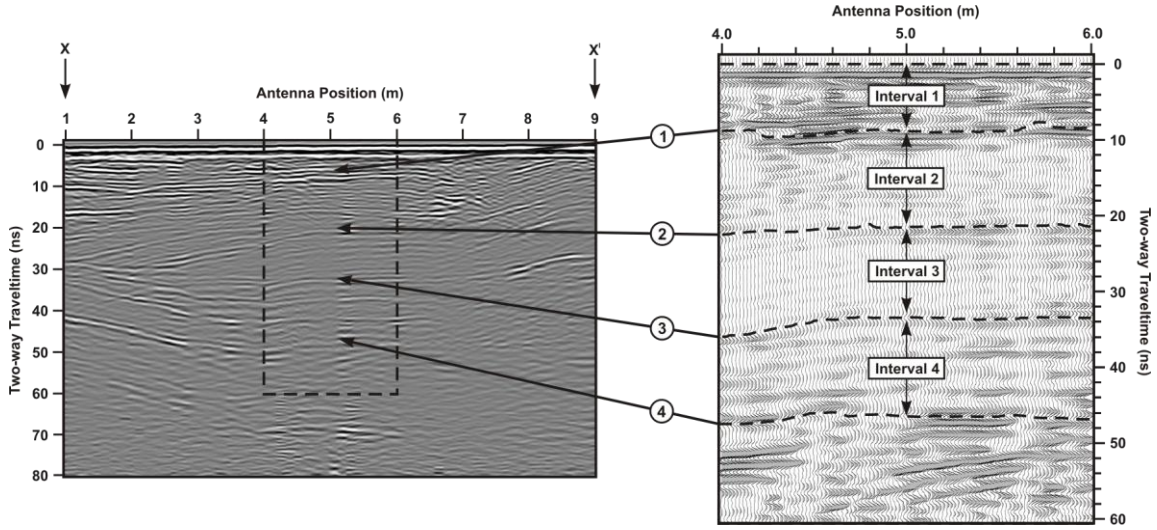

Figure 5.4 Portion of X–X' profile representing intensive monitoring 2.0 m profile with the four major stratigraphic reflections used for interval traveltime analysis identified.

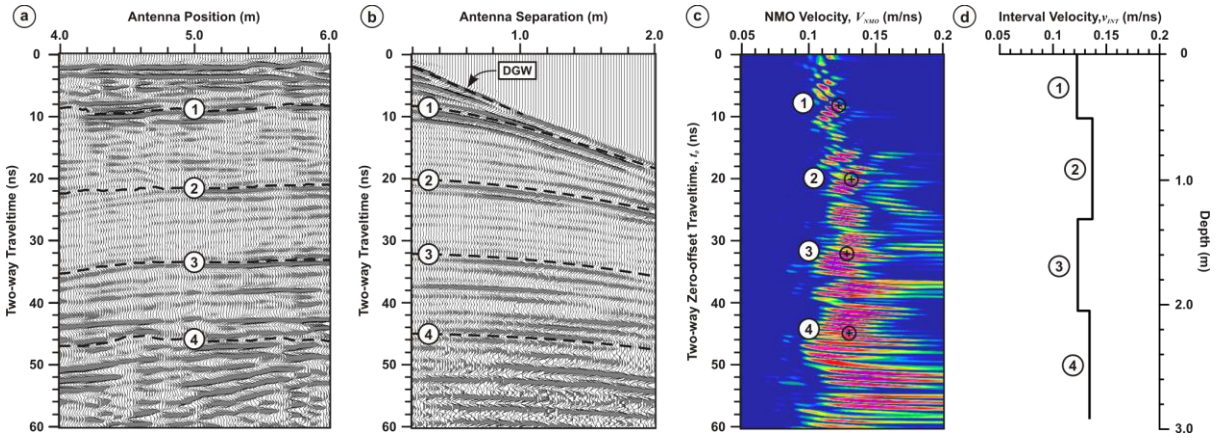

Figure 5.5 Typical data processing sequence corresponding to a single GPR data set, where pre-established stratigraphic reflections were identified on concurrently collected (a) reflection and (b) CMP data sets. Average two-way traveltimes corresponding to the four reflection events were determined along the profile. DGW velocity was determined using least-squares linear analysis while a (c) semblance plot was calculated to obtain NMO velocities and two-way zero-offset traveltimes corresponding to the four reflections; the Dix (1955) equation was used to construct an (d) interval velocity-depth model. This process was repeated for each GPR data set.

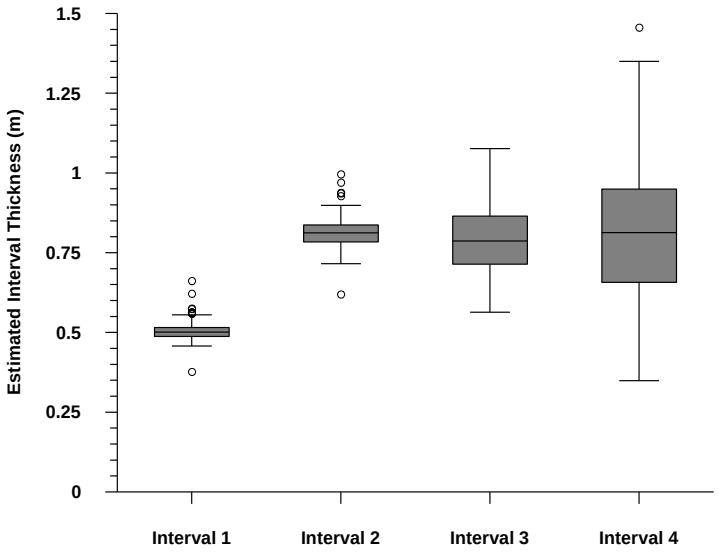

Figure 5.6 Interval thickness results obtained from the 159 interval velocity-depth models.

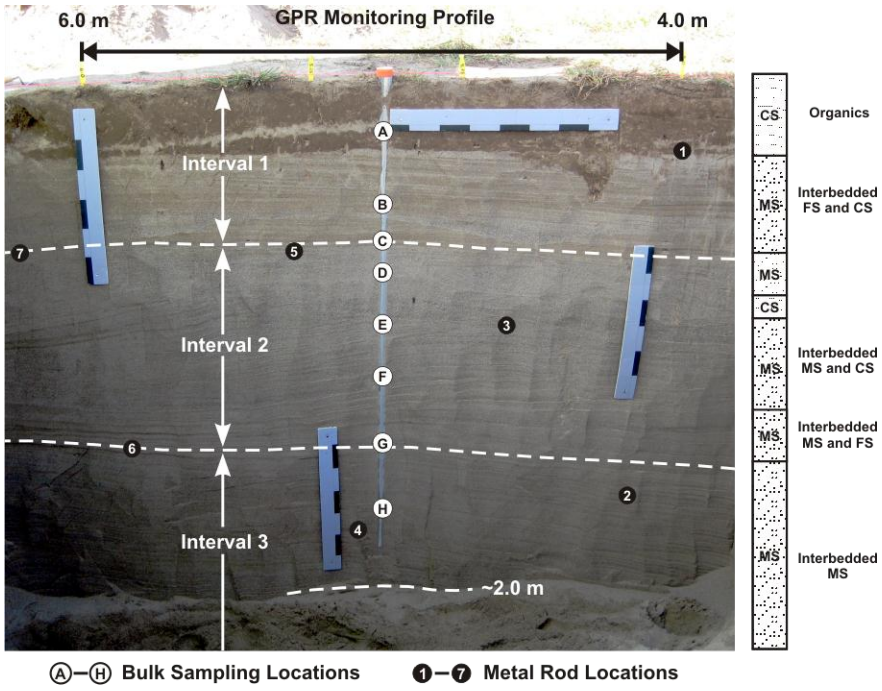

Figure 5.7 Vertical soil section exposing the upper 2 m below the intensive monitoring profile. Locations of bulk soil samples (A–H) and metal rods (1–7) are superimposed. Black and grey scales define 0.1 m intervals.

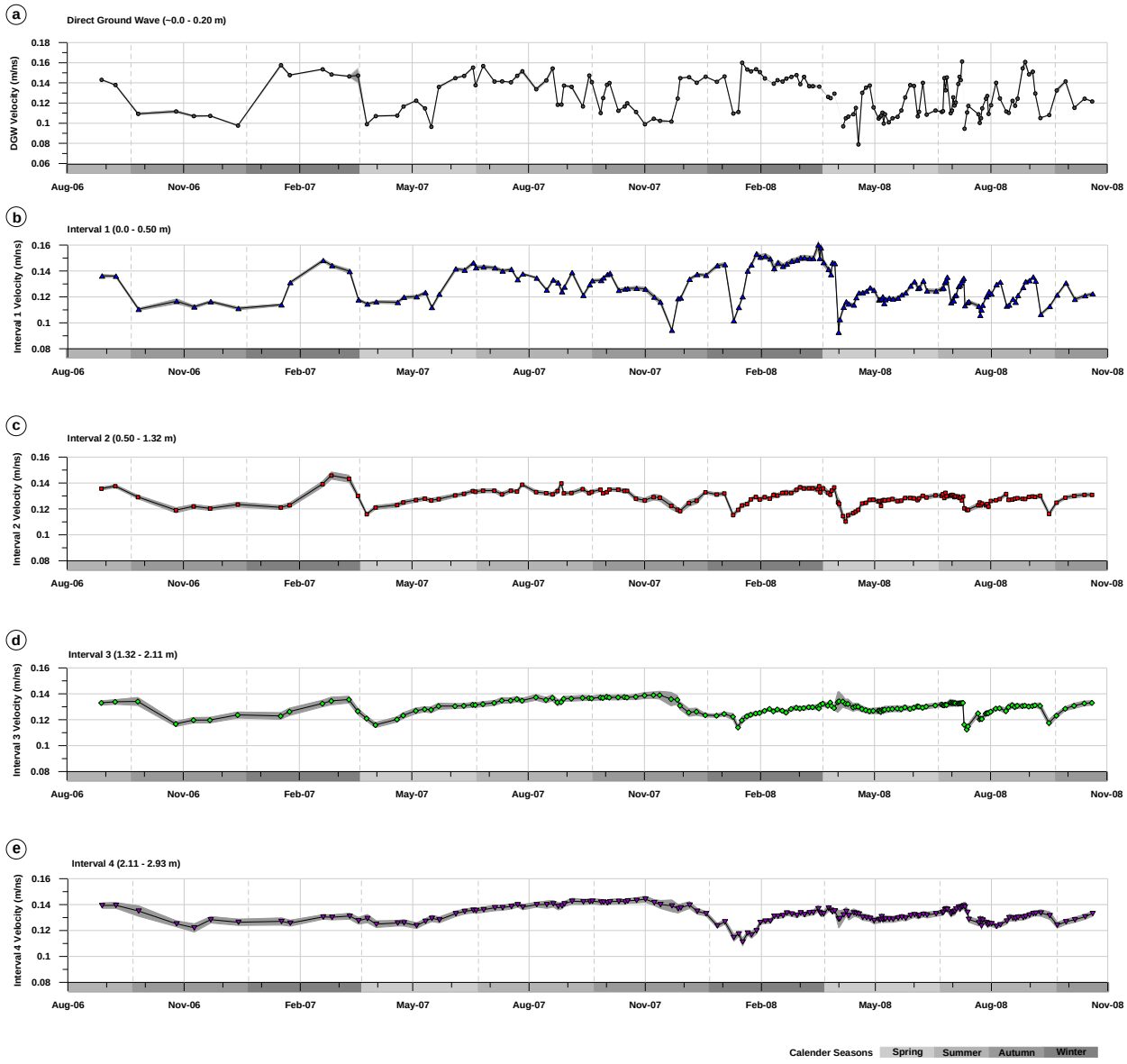

Figure 5.8 Temporal variations in (a) DGW velocity from CMP soundings and (b–e) interval velocity from reflection traveltimes.

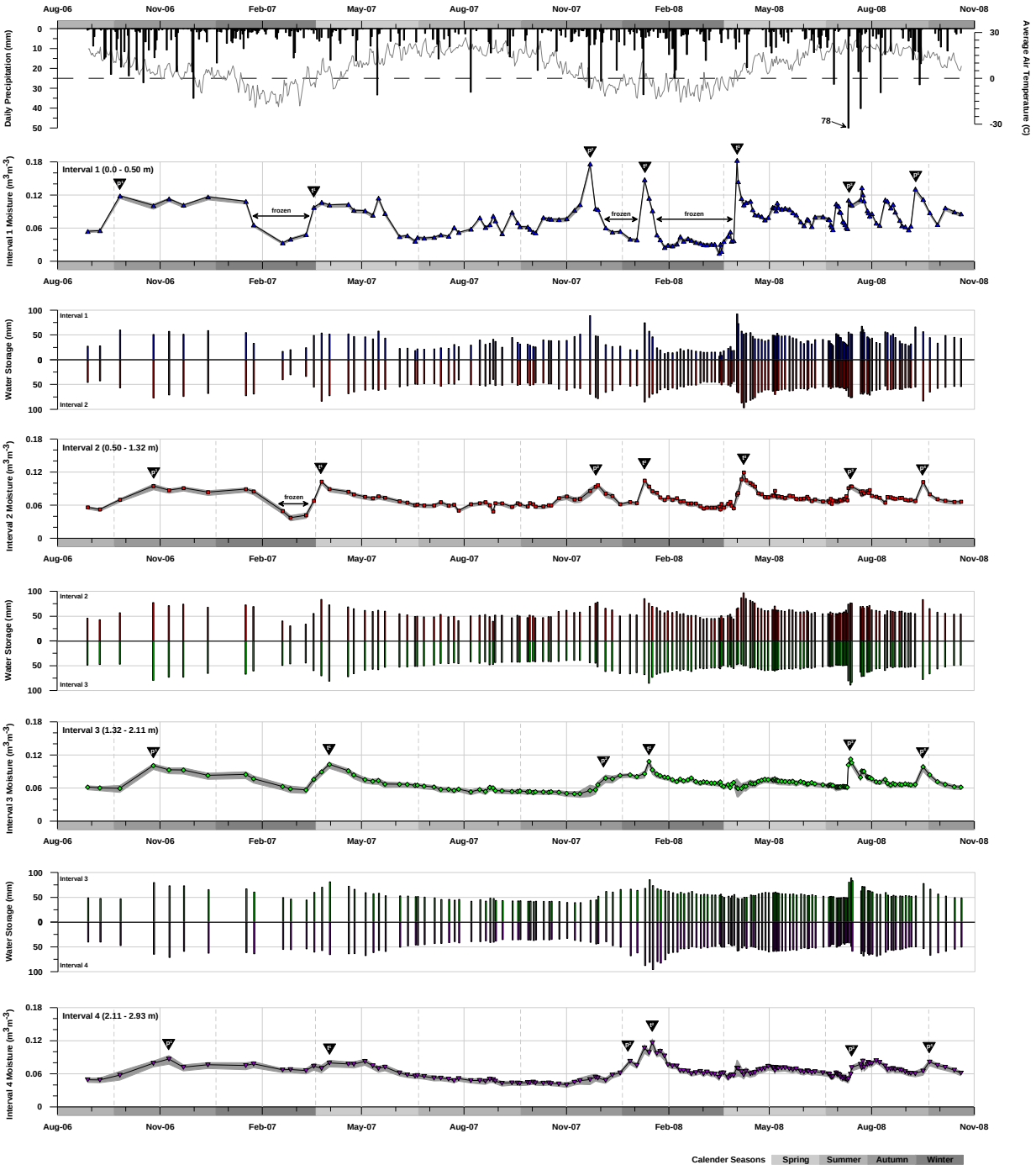

Figure 5.9 Interval moisture content estimates based on the GPR reflection data with water storage (mm) determined using interval thickness and average porosity ϕ = 0.39. Daily precipitation and average air temperatures are also shown.

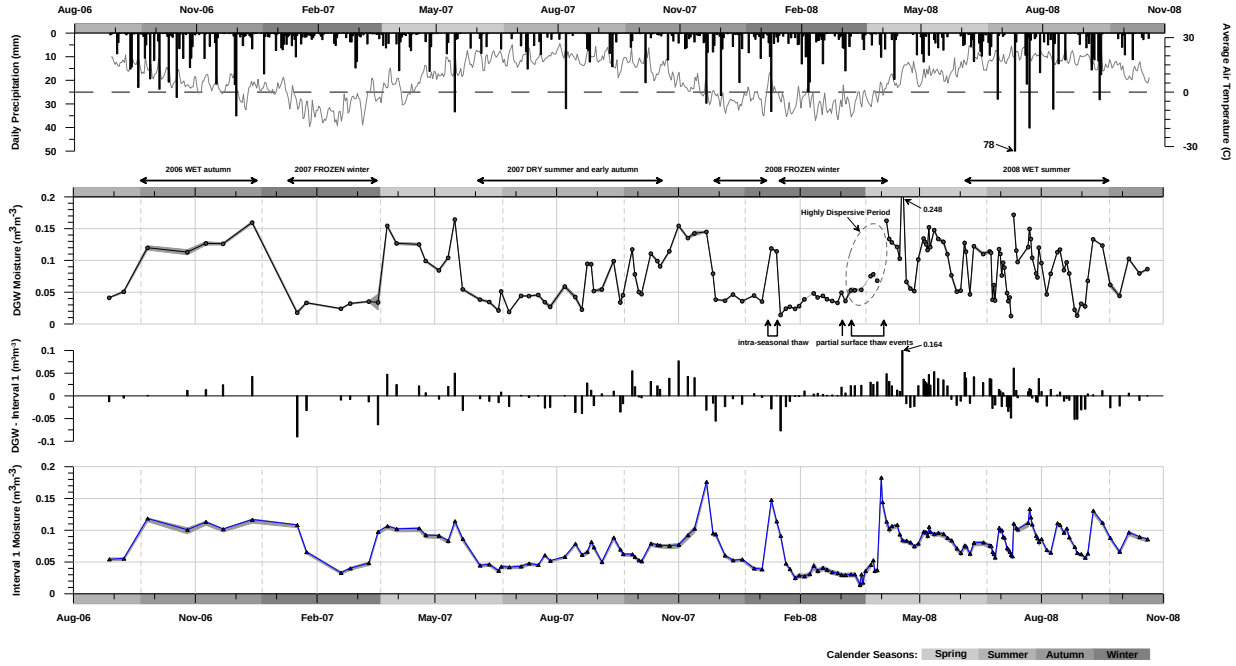

Figure 5.10 Soil moisture contents corresponding to DGW and Interval 1 velocity measurements. Daily precipitation and average air temperatures are also shown.

Chapter 6
High-Resolution GPR Monitoring of Soil Moisture Dynamics – Comparison with Unsaturated Flow Model[5]

6.1 Executive Summary

High-resolution surface ground-penetrating radar (GPR) techniques (i.e., reflection profiling and common-midpoint soundings) were used to quantitatively examine vertical soil moisture distribution and its associated dynamics within the shallow subsurface over an extensive 26 month period. This unique data set permitted an examination of the nature of GPR-derived soil moisture profiles collected during two contrasting annual periods characterized by dry and wet soil conditions in the upper 3 meters of vadose zone. The nature of transient infiltration pulses, evapotranspiration episodes, and deep drainage patterns observed in the GPR data series were examined by comparing them with vertical soil moisture flow simulations based on a one-dimensional variably saturated model (HYDRUS-1D). Using laboratory derived soil hydraulic property information from soil samples and a number of simplifying assumptions about the system, a very good agreement was achieved between measured and simulated soil moisture conditions without model calibration; this is a strong indication of the overall quality of the GPR-derived soil moisture measurements. The only notable difference between simulated and GPR water content estimate occurred during very dry conditions near the air-soil interface. Since the GPR-derived values were consistent with shallow gravimetric data, this difference suggests that processes controlling water contents at levels below the residual value obtained from gravitational drainage are not well implemented in the HYDRUS-1D model. Nevertheless, the overall good agreement between our forward simulations and field measurements over the vertical profile validates the capacity of surface GPR to provide detailed information about hydraulic state conditions in the upper few meters of vadose zone. It is proposed that surface-GPR could be a viable soil hydraulic parameter estimation technique if sufficient wetting and drying cycles are observed.

[5] Steelman, C.M., Jones, J.P., and Endres, A.L. (in review). High-resolution GPR monitoring of soil moisture dynamics 2. Comparison with unsaturated flow model. Submitted to *Water Resources Research* 16/09/2011, submission number: 2011WR011413.

6.2 Introduction

Geophysical methods offer a range of non-invasive to minimally invasive techniques with the capacity to provide soil moisture information that is typically unattainable using conventional point measurement sensors (Robinson et al., 2008). In particular, ground-penetrating radar (GPR) has received unprecedented attention over the past decade as a viable high-resolution soil moisture sensor in vadose zone environments (Huisman et al., 2003a). GPR systems transmit high-frequency electromagnetic waves that respond primarily to the dielectric permittivity of the medium, and can be deployed in a variety of configurations (e.g., air-launched, surface and downhole systems) depending on the application.

While GPR has been shown to provide detailed hydrological information between boreholes (e.g., Alumbaugh et al., 2002; Cassiani and Binley, 2005; Kowalsky et al., 2005; Deiana et al., 2007), less attention has been given to surface based measurements and its ability to provide quantitative vadose zone information. Although some surface GPR studies (i.e., Lunt et al., 2005; Wollschläger and Roth, 2005) have demonstrated the methods ability to provide vertical soil moisture data in the field, limited temporal sampling and low resolution near the surface has restricted quantitative analysis of hydrological state conditions, hydraulic parameters and water fluxes in the vadose zone. Using a laboratory-scale sandbox, Moysey (2010) showed how transient surface GPR data collected during controlled wetting and drying cycles could be used to determine soil hydraulic properties.

To further examine the capacity of surface GPR techniques to characterize vertical soil moisture dynamics within the shallow vadose zone, Steelman and Endres (in review) [Chapter 5] conducted an extensive 26 month field study covering two complete and contrasting annual cycles of soil conditions typical of mid-latitude climates. To the best of our knowledge, that study represents the first attempt to fully assess the use of two surface GPR techniques (i.e., reflection profiling and common-midpoint soundings) to characterize vertical soil moisture dynamics within the vadose zone and the nature of its coupling with soil moisture variations at the surface over such a wide range of hydrological conditions. In their study, concurrent reflection profiles and common-midpoint (CMP) soundings were acquired on a daily to weekly interval using high-frequency 900 MHz antennas along a fixed 2.0 m survey line. Reflection profiles provided high resolution traveltime data between four stratigraphic reflection events while analysis of the complete CMP sounding data set produced precise depth estimates for those reflecting interfaces. The use of CMP soundings also permitted the determination of direct ground wave (DGW) velocities which provided high-resolution information along the air-

soil interface; this information allows more detailed examination of the nature of the coupling between vertical soil moisture profile and surface soil conditions.

While Steelman and Endres (in review) [Chapter 5] clearly demonstrated the apparent ability of surface GPR methods to give high quality estimates of soil moisture distribution in the upper 3 meters of the vadose zone, the nature of these GPR-derived moisture data needs to be assessed in the context of other hydrological information. Ideally, this comparison would be done using in situ soil moisture measurements. However, these data are limited to gravimetric sampling in the upper 0.50 cm, done as part of our DGW study (i.e., Steelman and Endres, 2010) [Chapter 2], due to our decision to minimally impact the subsurface at this site during the course of our study. As an alternate approach, we propose that our GPR soil moisture estimates can be compared with predictions obtained from a well-accepted hydrological modeling package, HYDRUS-1D (Simunek et al., 2008).

In this paper, we further examine those GPR-derived soil moisture profiles by comparing them with vertical soil moisture flow simulations using the one-dimensional variably saturated model, HYDRUS-1D, parameterized with hydraulic property measurements obtained from direct soil samples extracted along the vertical profile. Simulations were performed during two separate unfrozen periods from 1 April to 1 November 2007 and 2008, respectively characterized by unusually dry and wet seasonal soil conditions. Numerical results are compared with GPR soil moisture data to assess the capacity of surface GPR to monitor highly variable soil moisture conditions in the upper vadose zone. In addition, these simulated moisture data are used to examine the nature of short-duration events (i.e., transient infiltration pulses through the upper vadose zone; evapotranspiration episodes within the root zone) and longer period moisture trends (i.e., deep drainage patterns) observed in the GPR-derived soil moisture time series.

This multi-year GPR data set presents a unique opportunity to advance our knowledge of vadose zone moisture dynamics as they are incorporated into numerical models. Using laboratory derived soil hydraulic property information and a number of simplifying assumptions about the system we were able to achieve very good agreement between measured and simulated soil moisture conditions without any model calibration. This observed agreement is a strong indication of the overall quality of those GPR-derived soil moisture measurements, and hence, the suitability of surface GPR for field-scale soil hydraulic parameter and seasonal moisture flux estimation.

6.3 Site Description and Data Acquisition

The field site (528878E, 4814702N) is located within an active agricultural field located 3 km west of Waterloo, Ontario, Canada. While haying operations were conducted during the study period, other agricultural disturbances, such as plowing and tilling, were not performed during or in the recent past (i.e., within the preceding 2–5 years) prior to this study. Our soil moisture measurements were performed on a topographic high characterized by interbedded fine to coarse sand that extends to an approximate depth of 10 m based on GPR reflection profiling using 100 MHz antennas and electrical resistivity measurements collected over the area. The local water table is believed to be 15–20 m below ground surface based on nearby water bodies and geophysical measurements.

A detailed description of the GPR data acquisition, processing and analysis is given in Steelman and Endres (in review) [Chapter 5] and are briefly summarized below. Coincident pairs consisting of a reflection profile and CMP sounding were acquired using 900 MHz antennas along a fixed 2.0 m survey line on each field date at 1 day to 4 week intervals between 28 August 2006 and 20 October 2008. The study period encompassed two complete annual cycles of soil conditions (i.e., dry summer, wet spring and autumn, frozen winter soil conditions). DGW velocity measurements from CMP data provided highly resolved soil moisture information within the upper 0.2 m of soil (Steelman and Endres, 2010). Using reflection profiling along a 2.0 m survey line, deeper moisture information was obtained from average two-way interval traveltimes between four well-defined stratigraphic interfaces located in the upper 3 m of vadose zone. Normal-moveout velocity analysis of our complete CMP sounding data set produced precise depth estimates for those reflecting interfaces, which were used to determine interval thicknesses. Calculated interval velocities using reflection traveltime data were converted into volumetric water content using the Complex Refractive Index Model (CRIM) (Wharton et al., 1980), using a depth weighted mean porosity $\phi = 0.39$ and fixed permittivities for air ($\kappa_a = 1$), soil ($\kappa_s = 5$) and water ($\kappa_w = 84.9$) phases.

The 26 month soil moisture data set shown in Figure 6.1 was originally presented in Steelman and Endres (in review) [Chapter 5]. This paper focuses on two unfrozen soil periods between 1 April and 1 November 2007 and 2008, which include 35 and 75 observation dates, respectively. Meteorological data was collected using the University of Waterloo weather station located approximately 7 km east of the site. The station continuously measures precipitation, air temperature, relative humidity, barometric pressure, wind speed, incoming and outgoing shortwave radiation every 15 minutes.

Detailed soil property information was collected directly below the measurement profile after the study was completed; eight soil samples were extracted from the upper 1.6 m for in-situ soil bulk density and hydraulic parameter estimation in the lab. The exposed vertical section of soil was characterized by a 0.25 m dark coloured plough horizon composed of coarse sand containing approximately 1.5% (wt/wt) organics and 3% silt fraction. Underlying this plough zone were clean, well-sorted sequences of fine to coarse grained sand layers ranging between a few centimeters to decimeters in thickness. The depositional nature of these units is consistent with an ice-contact stratified moraine deposit. Grass roots were primarily observed within the dark coloured upper plough zone; however, some isolated roots did detrude into the clean underlying sand. Although we were unable to excavate below a depth of 2 m, field-scale geophysical measurements indicate the presence of similarly structured sand deposits to an approximate depth of 10 m.

6.4 Numerical Simulations

6.4.1 Conceptual Framework

Numerical simulations were performed using the HYDRUS-1D software package, version 4.08 (Simunek et al., 2008), which simulates water, heat and solute transport in one-dimensional variably-saturated porous media. In this study, we consider only one-dimensional water flow and neglect the effects of temperature gradient, air phase and solute concentration on liquid flow. As a result, one-dimensional fluid flow in a partially saturated rigid porous medium was described using a modified form of the Richards equation:

$$\frac{\partial \theta}{\partial t} = \frac{\partial}{\partial z}\left[K\left(\frac{\partial h}{\partial z} + 1 \right) \right] - S, \tag{6.1}$$

where θ is the volumetric water content [-], h is the pressure head [m], t is time [d^{-1}], z is the vertical coordinate (positive upwards), K is the unsaturated hydraulic conductivity function [m d^{-1}] and S is a sink term [m^3m^{-3} d^{-1}] representing the actual evapotranspirative flux. The volume of water removed from a unit volume of soil per unit time was described by Feddes et al. (1978) root-water uptake model:

$$S(h) = \alpha(h) S_p. \tag{6.2}$$

This model applies a dimensionless root-water uptake water stress response function $\alpha(h)$ of the soil water pressure head with the range $0 \leq \alpha \leq 1$ to scale the potential evapotranspirative flux rate S_p. Here, S_p is defined by a linear root distribution function over a prescribed root zone depth L_R and potential transpiration rate (Simunek et al., 2009).

The unsaturated hydraulic conductivity function can be defined by parameterizing the Brooks and Corey (1964) unsaturated hydraulic model to measured pressure-saturation data. Their pressure head (h) formulation for soil water retention $\theta(h)$ and hydraulic conductivity $K(h)$ is defined as:

$$S_e = \begin{cases} |\alpha h|^{-n} & h < -1/\alpha \\ 1 & h \geq -1/\alpha \end{cases} \tag{6.3}$$

$$K = K_s S_e^{\frac{2+3n}{n}}, \tag{6.4}$$

respectively, where S_e is effective saturation:

$$S_e = \frac{\theta - \theta_r}{\theta_s - \theta_r}. \tag{6.5}$$

Here, θ_s [-] and θ_r [-] represent the saturated and residual water contents, respectively, while K_s [m d^{-1}] is the saturated hydraulic conductivity, α [m^{-1}] is the inverse of the air-entry pressure (i.e., $\alpha = 1/h_b$), and n [-] is a pore-size distribution index. The parameters α and n represent empirical coefficients that control the shape of the hydraulic functions.

6.4.2 Hydraulic Model

A highly simplified conceptual hydraulic model is proposed that ignores macropore flow through the root zone, seasonal plant canopy and root dynamics, heat and vapor flux, hysteresis in soil water function and overland flow. Further, we assume that the observed water flux can be adequately represented using the modified Richards equation, Brooks and Corey parameterization and a free-drainage lower boundary condition. We also make the assumption that the site can be approximated below the plough zone using a homogeneous hydraulic parameter distribution such that the effects of vertical stratigraphic variations on soil moisture distribution and hydraulic parameters are negligible at our measurement scale. In an attempt to minimize potential boundary effects on water flow in the upper 3 meters of soil the lower boundary was set 10 m below the surface which is a reasonable

assumption given our field-scale geophysical measurements. Our one-dimensional model (schematic shown in Figure 6.2) was divided into six soil layers each discretized into 0.01 m intervals to a depth of 10 m (i.e., 1001 nodes). Soil Layers 1–4 correspond to the measured GPR Intervals 1–4. Layer 1 is separated into two zones (i.e., Layer 1a and 1b) to differentiate the upper plough zone, occupying the upper 0.25 m of soil, from the underlying clean sand soil. It should be noted that our DGW measurements effectively samples the upper 0.2 m of Layer 1a. Finally, Layer 5 in the schematic represents the models extension to the lower boundary.

Bulk soil samples extracted along the exposed soil section (see approximate locations in Figure 6.2) were used to obtain field estimates of soil bulk density and porosity assuming an average grain density of 2.65 g/cm^3. Repacked samples were then used to estimate saturated hydraulic conductivity using a falling head permeameter (i.e., 4 runs per sample), while water retention curves were obtained using the hanging water column method (Stephens, 1996). These initial drainage curves were fitted using both the Brooks and Corey (1964) and van Genuchten (1980) unsaturated hydraulic models; however, we found that the Brooks and Corey model yielded a much better fit to the measured data, particularly at the air-entry pressure and residual saturation portions of the curve. As a result, Equations (6.3) and (6.4) were used to describe the measured pressure-saturation data; the best-fit curves to these data are shown in Figure 6.3. Because the GPR soil moisture estimates were obtained using an average porosity of 0.39 along the profile [as in Chapter 5], this value was also used to describe the saturated portion of the pressure-saturation and hydraulic conductivity functions for the numerical simulations. While the sample from the upper plough zone clearly yielded a different set of hydraulic parameters (dotted black line in Figure 6.3), the remaining samples from the underlying clean sand gave similar results; hence, these clean sand data were averaged to obtain a single representative parameter set (solid black line in Figure 6.3).

Soil water flow was simulated using a transient atmospheric upper boundary condition controlled by daily precipitation measurements and calculated daily average estimates of potential evapotranspiration using meteorological data from the nearby weather station. Although our meteorological data was not collected directly at the site, these input and output data are considered good approximations to the actual conditions at the site given the duration of the study. Potential evapotranspiration was calculated using the FAO recommended Penman-Monteith combination equation (FAO, 1990):

$$ET_o = \frac{1}{\lambda}\left[\frac{\Delta\left(R_n - G\right)}{\Delta + \gamma\left(1 + r_c/r_a\right)} + \frac{\rho c_p\left(e_a - e_d\right)/r_a}{\Delta + \gamma\left(1 + r_c/r_a\right)}\right], \tag{6.6}$$

where ET_o is the potential evapotranspiration rate [mm d^{-1}], λ is the latent heat of vaporization [MJ kg^{-1}], R_n is the net radiation at the surface [MJ m^{-2} d^{-1}], G is the soil heat flux [MJ m^{-2} d^{-1}], ρ is the atmospheric density [kg m^{-3}], c_p is the specific heat of moist air [1.013×10^{-3} MJ Kg^{-1} $°C^{-1}$], e_a is the saturation vapor pressure [kPa] at temperature T, e_d is the actual vapor pressure [kPa], r_c is the crop canopy resistance [s m^{-1}], r_a is the aerodynamic resistance [s m^{-1}], Δ is the slope of the vapor pressure curve [kPa $°C^{-1}$], and γ is the psychrometric constant [kPa $°C^{-1}$]. A detailed description of these parameters and their estimation is provided in Simunek et al. (2009). For this study, the soil heat flux G was assumed to be zero based on the use of a daily time step, while the leaf area index (LAI) for the field crop was determined using

$$LAI = 5.5 + 1.5\ln\left(h_c\right) \tag{6.7}$$

with a constant crop height, h_c, of 0.1 m. Calculated daily potential evapotranspiration (ET_o) fluxes were partitioned into potential evaporation (E_o) and transpiration (T_o) using (Ritchie, 1972):

$$T_o = ET_o\left(1 - e^{-k\,LAI}\right) \tag{6.8}$$

$$E_o = ET_o e^{-k\,LAI}, \tag{6.9}$$

where k represents the canopy extinction coefficient which was set to 0.398.

Root water uptake in the model was simulated using the Feddes et al. (1978) model (Equation 6.2) using parameters for pasture according to Wesseling (1991), which were made available in HYDRUS software. Visual inspection of the root zone during excavation showed that roots were mainly concentrated in the upper 0.15 m; however, a few isolated alfalfa roots in adjacent areas did extend to greater depths beyond the upper plough zone. Nevertheless, a simplified soil root zone was represented in the model between 0.02–0.15 m. Finally, a constant minimum absolute pressure head of 150 m was set at the soil surface for the simulation period as recommended by Simunek et al. (2009).

6.5 Forward Simulation Results using Direct Sampling Data

Laboratory-derived hydraulic parameter estimates (e.g., θ_r, α, n, K_s) were used to carry out forward vertical flow simulations using HYDRUS-1D software package. Based on our direct sampling data from the upper 1.6 m, we elected to describe the system as a simple two-layer model: a 0.25 m upper layer representing the more organic rich plough zone that contains the soil roots overlying a clean homogeneous sand unit extending to a depth of 10 m. The upper layer (Layer 1a) parameters were defined using the single uppermost sample (θ_r = 0.071 m^3m^{-3}; α = 3.86 m^{-1}; n = 0.933; K_s = 1.32×10^{-4} m/s), while average parameter values from the seven underlying samples (θ_r = 0.058 m^3m^{-3}; α = 4.00 m^{-1}; n = 2.128; K_s = 3.01×10^{-4} m/s) described the clean sand unit (Layers 1b–5). A single porosity value of 0.39 was used to represent the saturated water content, θ_s, along the entire vertical profile.

Numerical simulations were carried out during unfrozen soil conditions from 1 April to 1 November 2007 and 2008, i.e., days 91–306 and 92–306, respectively. A uniform water content of 0.10 m^3m^{-3} was initialized along the 10 m profile at the start of each simulation; this value is consistent with water contents measured during wet spring thaw conditions. Measured daily precipitation and calculated potential evapotranspiration using Equation (6.6) defined the water flux at the upper boundary; water was allowed to freely drain through the system using a free-drainage lower boundary condition (Simunek et al., 2009). To compare simulated water contents with those obtained from GPR measurements, the average nodal water content within each model layer was determined for each time step. The upper 0.2 m of Layer 1a was used to represent the DGW sampling depth. The average layer water contents from the simulations with corresponding GPR water content data for the 2007 and 2008 periods are plotted in Figure 6.4.

The initial 30 days of the simulation represents the spin-up period as the soil profile equilibrates to atmospheric conditions. The dry 2007 (Figure 6.4a) simulation period shows only long-term seasonal moisture changes along the deeper profile (i.e., Intervals 2–4) while the wet 2008 (Figure 6.4b) simulation is punctuated by a number of major short-term moisture pulses resulting from large precipitation events that propagate down through the section. Further, the number of simulated moisture fluctuations near the surface (i.e., DGW zone and Interval 1) during 2007 is far less and with much lower magnitude than those observed during the 2008 period. These model responses are consistent with our GPR measurements. While we do not expect a perfect match between simulated and measured moisture conditions given the proximity of the weather station to the site and our simplifying assumptions in potential evapotranspiration calculations, these data still show very good

agreement over the simulated periods. This conformity is well illustrated during the 2008 period where higher GPR sampling captured many of the shorter-duration fluctuations in the simulated water content profile. The excellent agreement observed between measured and simulated moisture profiles without model calibration is a strong indication of the high potential value of these GPR-derived soil moisture measurements to the characterization of vadose zone hydrological conditions.

Soil moisture conditions in the DGW zone and Interval 1 reflect short-duration variations in water content due to rainfall followed by evapotranspiration processes. These processes are much more prominent in the DGW data as its thinner thickness better isolates the shallow near-surface region (i.e., within the root zone) where these processes dominate. It can be seen that low limit values of GPR-derived water content for the DGW zone and Interval 1 during dry periods (<0.04 m^3m^{-3}) were significantly less than those values obtained from the model using the laboratory hydraulic parameters (~0.08 m^3m^{-3}); this divergence in lower-limit values resulted in slightly higher root-mean-squared-errors (RMSE) of ~0.04 m^3m^{-3} and ~0.02 m^3m^{-3} for DGW and Interval 1 water contents, respectively. While our laboratory residual water content is greater than that indicated by the GPR measurements, these lower GPR values are consistent with the 2007 gravimetric sampling (Steelman and Endres, 2010).

The deeper Intervals 2–4 show strikingly different soil moisture dynamics for the two contrasting annual periods. For instance, the 2007 period is defined by gradually declining water contents during the entire simulation period which indicates that minimal, if any, water passed through the upper root zone and contributed to deep drainage. This is demonstrated by fact that two major precipitation events (i.e., p^1 and p^2) did not result in distinct moisture pulses below Interval 2. In contrast, the 2008 period shows consistently higher water contents during the entire monitoring period including three short-duration moisture increases (i.e., p^3, p^4 and p^5) in response to major infiltration events. These three precipitation events resulted in transient infiltration pulses that propagated through the monitored portion of the profile. The magnitude and character of these pulses were dependent on the rate, intensity and duration of the precipitation event. For instance, the p^1 and p^2 events were the result of 39 mm and 32 mm of rainfall over a 4 and 7 day period, respectively. In comparison, the more significant p^3, p^4 and p^5 events were the result of 82 mm, 76 mm and 108 mm of rainfall over 2, 5 and 13 day periods, respectively.

RMSE for these deeper intervals were much lower than those bounded by the air-soil interface. The best fit was obtained for Interval 2 data with an RMSE less than 0.01 m^3m^{-3}. Although slightly

higher RMSE (i.e., <0.02 m^3m^{-3}) were observed for Interval 3 and 4 data, these data maintained very good agreement throughout the simulated periods. While Interval 3 and 4 data maintained very good agreement throughout the simulated periods, the higher RMSE (i.e., <0.02 m^3m^{-3}) in these deeper intervals may be the result of a slight divergence in our assumption of a uniform hydraulic parameter distribution below the excavated portion of the profile.

Given the good agreement between the modeling results and the GPR soil moisture estimates, the soil water fluxes were calculated at various points along the simulated profile to better understand the nature of GPR response in the context of the hydrological conditions during the 2007 and 2008 periods. While the GPR data provided high-resolution soil moisture information at various points in time along the vertical profile, the value of these data becomes more apparent once we understand the dynamic nature of the resultant moisture fluxes. Hence, cumulative water flux was determined for the following: (1) soil surface (precipitation minus evaporation), (2) root water uptake (transpiration), (3) flux passing root zone (i.e., surface flux minus root water uptake) and (4) flux passing lower layer boundary (i.e., bottom of Layer 4). These flux results are plotted in Figure 6.5. As expected, the dryer 2007 period exhibited very little moisture flux through the soil profile; note the minimal, if any, contributions of p^1 and p^2 events to deep moisture drainage (i.e., red line). Rather, much of the surface flux (i.e., -191 mm) during this period was captured through root water uptake (i.e., +181 mm), a small portion of water (i.e., -31 mm) did manage to drain past the bottom of Layer 4; however, most of this water would have come from initial spring drainage. In comparison, the wetter 2008 period had markedly higher fluxes at the surface (i.e., -399 mm) which led to higher root water uptake (i.e., +254 mm). These wetter conditions allowed -142 mm of water to migrate past the bottom of Layer 4 (i.e., red line) which largely occurred during two extended wetting periods in July (p^3 and p^4) and September (p^5). These numerical flux results demonstrate the capacity of GPR to monitor various scales of wetting and drying cycles, and its potential for field-scale hydraulic parameter estimation when coupled with a numerical flow model (e.g., Moysey, 2010).

6.6 Effects of Simplified Vegetative Cover

Although our moisture simulations are in very good agreement with GPR-derived water contents over the larger intervals (Intervals 1–4) more significant deviations were observed in the upper 0.2 m (i.e., corresponding to DGW measurement). Soil moisture variations along the air-soil interface are controlled by atmospheric forces, plant canopy, and root growth dynamics. For instance, the actual evapotranspiration is controlled by root depth (L_R), canopy height (h_c) and LAI, which affects the

partitioning of water between evaporation at the soil surface and transpiration through root water uptake. While the net moisture flux to the atmosphere is not expected to vary significantly given the high potential evapotranspiration rates calculated during the two simulation periods, natural changes in plant conditions during the course of the season (e.g., rooting depth and plant growth) may explain some of the observed deviations between measured and simulated water contents at the surface.

A simple scenario analysis using different rooting depths and crop heights (i.e., 0.05–0.25 m) was conducted to evaluate the effects of plant properties on the wetting and drying cycles in the soil, and cumulative moisture fluxes during the 2007 and 2008 period; these results are given in Table 6.1. Although significant differences in flux are evident across the air-soil interface due to variations in the partitioning between evaporation and transpiration, the relative effect of plant conditions on deep moisture drainage is relatively minor. For instance, differences in cumulative downward water flux past the lower interval are ~8 mm during the dryer 2007 period and ~24 mm during the wetter 2008 period. These differences only had a slight effect on wetting and drying cycles; further, RMSE differences between short (i.e., L_R = 5 cm; h_c = 5 cm) and tall (i.e., L_R = 25 cm; h_c = 25 cm) grass for the upper 0.2 m was less than 0.007 m^3m^{-3} and 0.005 m^3m^{-3} for the 2007 and 2008 periods, respectively; and were significantly less with increasing sampling depth.

The higher discrepancies observed between simulated and measured water contents in the upper 0.2 m could also be partially explained by the HYDRUS-1D simplified ground cover condition which assumes a constant and densely distributed plant canopy during the simulation period; a similar assumption is made about the root zone. For instance, haying operations were performed in late-June which led to a drastic reduction in plant canopy height and ground cover fraction that was not implemented in the simulations. Persistently lower plant canopies and greater ground exposure was observed through the drier July and August period, which was attributed to a change in dominant vegetative cover from taller pasture grass to short and patchy blade grass.

While these vegetative groundcover assumptions may explain some of the surface discrepancies, the most fundamental cause is the fact that HYDRUS-1D uses the residual water content from the Brooks and Corey relationship (i.e., the limiting value during gravitational drainage) as the limiting value for overall water content. It is most likely that these lower values observed at the surface by both the DGW and gravimetric sampling are due to evaporative drying that removes the residual water phase in a manner analogous to the oven drying done in the lab. Hence, it is obvious that HYDRUS-1D does not account for this process; and any attempt to adjust the residual water content

to better match dry surface soil conditions resulted in more significant discrepancies over the wetter range of soil condition. These GPR data clearly highlight the importance of processes that are inadequately incorporated into this numerical modeling package.

6.7 Conclusions

The strong agreement between simulated and measured interval water content with depth indicates that our surface-based GPR measurements yielded very reliable soil moisture estimates within the upper 3 m of vadose zone during a wide-range of unfrozen soil conditions. Here, numerical flow simulations were conducted using HYDRUS-1D for two contrasting annual periods characterized by dry and wet soil conditions from 1 April to 1 November 2007 and 2008, respectively. The GPR data show that short time-scale soil moisture variations during the dryer 2007 period were limited to the upper root zone with little impact on deeper moisture conditions. In contrast, the wetter 2008 period was characterized by numerous large-scale precipitation events that were well-defined in the GPR measurements. The GPR data also demonstrated that the persistently wetter conditions during the 2008 annual period resulted in greater moisture variability near the surface and numerous moisture pulses that propagated through the soil profile. All of these hydrological responses were well predicted by the HYDRUS-1D model. The very good correlation between model and GPR water content estimates is very significant as these uncalibrated simulations are based on laboratory derived soil hydraulic property information and a number of simplifying assumptions about the system.

The important difference between model and GPR water content estimates was the contrast in lower limiting value for the root zone interval during very dry conditions. Since the GPR-derived values are consistent with shallow gravimetric data that was available, this difference suggests that processes controlling water contents at levels below the residual value obtained from gravitational drainage are not well implemented in HYDRUS-1D. While this factor had little, if any, impact on the very good match obtained between model and GPR water contents for the lower intervals, our analysis indicates that inappropriate use of the lower GPR value, particularly from DGW data from the root zone, as the residual water content in a saturation-capillary pressure relationship would significantly impact the extraction of hydrological parameters from models calibrated using GPR data.

Geophysical techniques with the capacity to estimate soil moisture in the vadose zone can be used to calibrate field-scale hydrologic models. Wollschläger et al. (2009) inversely modeled a limited

time series of in-situ soil water contents measurements obtained from time-domain reflectometry using HYDRUS-1D to obtain field-scale hydraulic parameters. More recently, Moysey (2010) demonstrated how high-frequency GPR reflection data from a laboratory-scale sandbox infiltration experiment coupled with HYDRUS-1D could be used to estimate soil hydraulic properties. Our HYDRUS-1D comparison study builds upon these previous works by examining moisture changes over a much deeper portion of vadose zone under natural field conditions. The water content measurements were also obtained from discrete, well-defined depth intervals. Further, our study compared two contrasting annual periods (i.e., dominantly dry verses dominantly wet) characterized by highly dynamic wetting and drying cycles.

Our forward simulations using the soil samples extracted from the upper half of the profile indicates that surface-GPR could be a viable soil hydraulic parameter estimation technique if sufficient wetting and drying cycles are observed along the observed profile. Moreover, the integration of DGW measurements from a well-described root zone (i.e., a priori knowledge of plant growth dynamics) could be used to define evapotranspiration flux. The data collected during the wetter 2008 period is particularly suited for such analysis due to the presence of major infiltration events which led to significant wetting and drying cycles along the profile, and the high surface moisture variability due to precipitation followed by evapotranspiration. However, meaningful field-calibration of our data may require improved representation of meteorological conditions and a better understanding of soil surface dynamics (i.e., plant growth and ground cover) during the simulation period.

This numerical study not only establishes the capacity of surface GPR to provide detailed information about hydraulic state conditions in the shallow vadose zone, but it also demonstrates its suitability for field-scale soil hydraulic parameter and seasonal moisture flux estimation. Given the importance of non-destructive field-scale unsaturated hydraulic property estimation, future work will focus on inverse parameter estimation modeling techniques using surface-based GPR soil moisture measurements.

6.8 Tables and Figures

Table 6.1 Simulated cumulative soil water flux (mm).

	Crop Parameters	Soil Surface	Root Uptake	Root Zone	Lower Layer
2007	L_R = 5 cm; h_c = 5 cm	-131	116	-16	-37
	L_R = 15 cm; h_c = 10 cm[a]	-191	181	-10	-31
	L_R = 25 cm; h_c = 25 cm	-207	199	-8	-29
2008	L_R = 5 cm; h_c = 5 cm	-324	160	-164	-161
	L_R = 15 cm; h_c = 10 cm[a]	-399	254	-145	-142
	L_R = 25 cm; h_c = 25 cm	-464	325	-139	-137

[a] Cumulative flux results plotted in Figure 6.5.

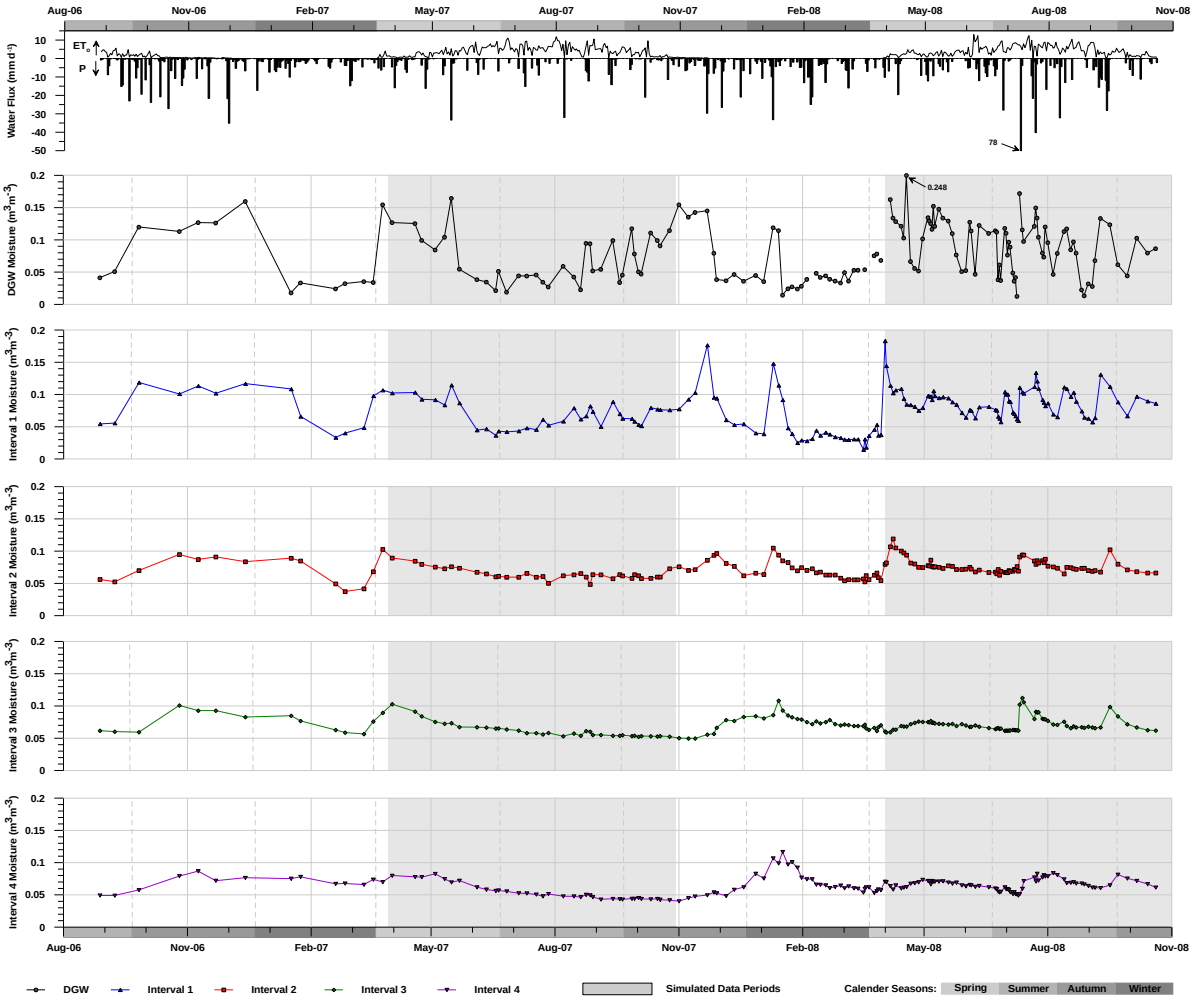

Figure 6.1 GPR-derived soil moisture content estimates from reflection and CMP direct ground wave data originally presented in Steelman and Endres (in review) [Chapter 5]. GPR measurement scales include DGW (0–0.2 m), Interval 1 (0–0.50 m), Interval 2 (0.50–1.32 m), Interval 3 (1.32–2.11 m) and Interval 4 (2.11–2.93 m). Daily measured precipitation and calculated potential transpiration using nearby weather station is also shown.

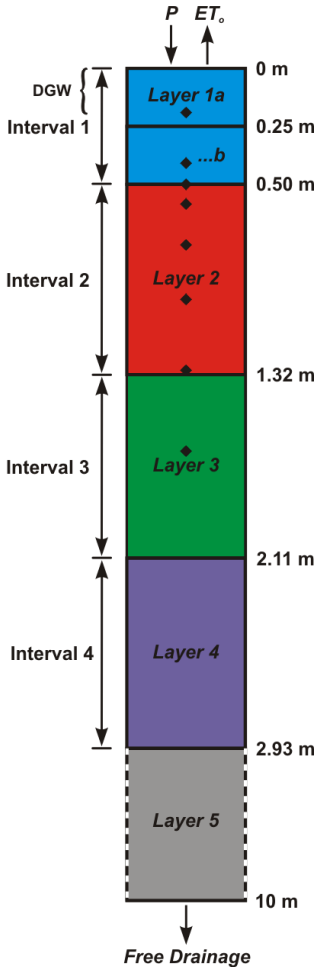

Figure 6.2 Schematic illustrating model setup for HYDRUS-1D simulations. Approximate soil sampling locations used for hydraulic parameter estimation shown by symbols (♦).

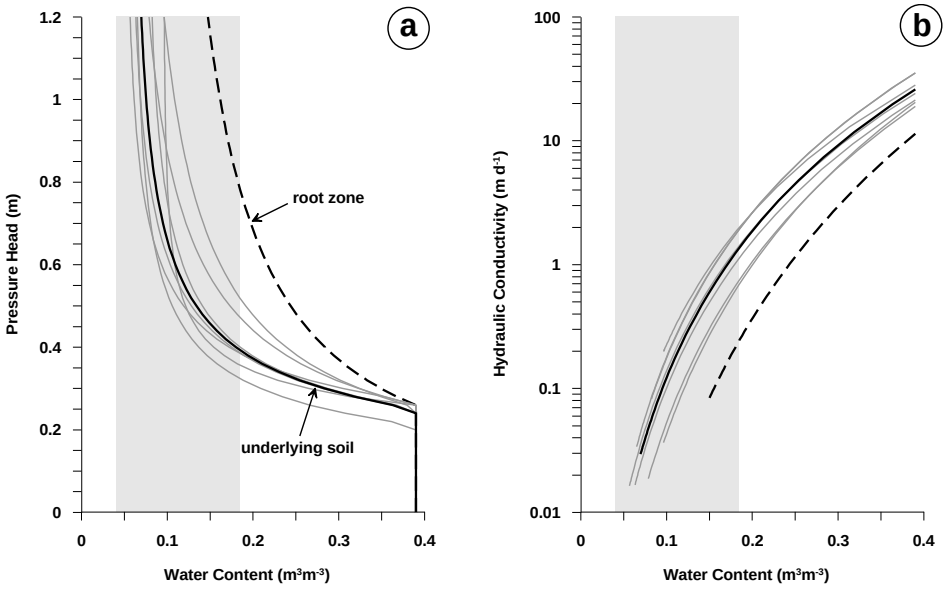

Figure 6.3 (a) Pressure-saturation and (b) unsaturated hydraulic conductivity functions based on Brooks-Corey parameterization using an average porosity ϕ = 0.39. Dotted line represents the single upper plough zone sample while the dark solid line represents an average of the seven samples underlying the root zone.

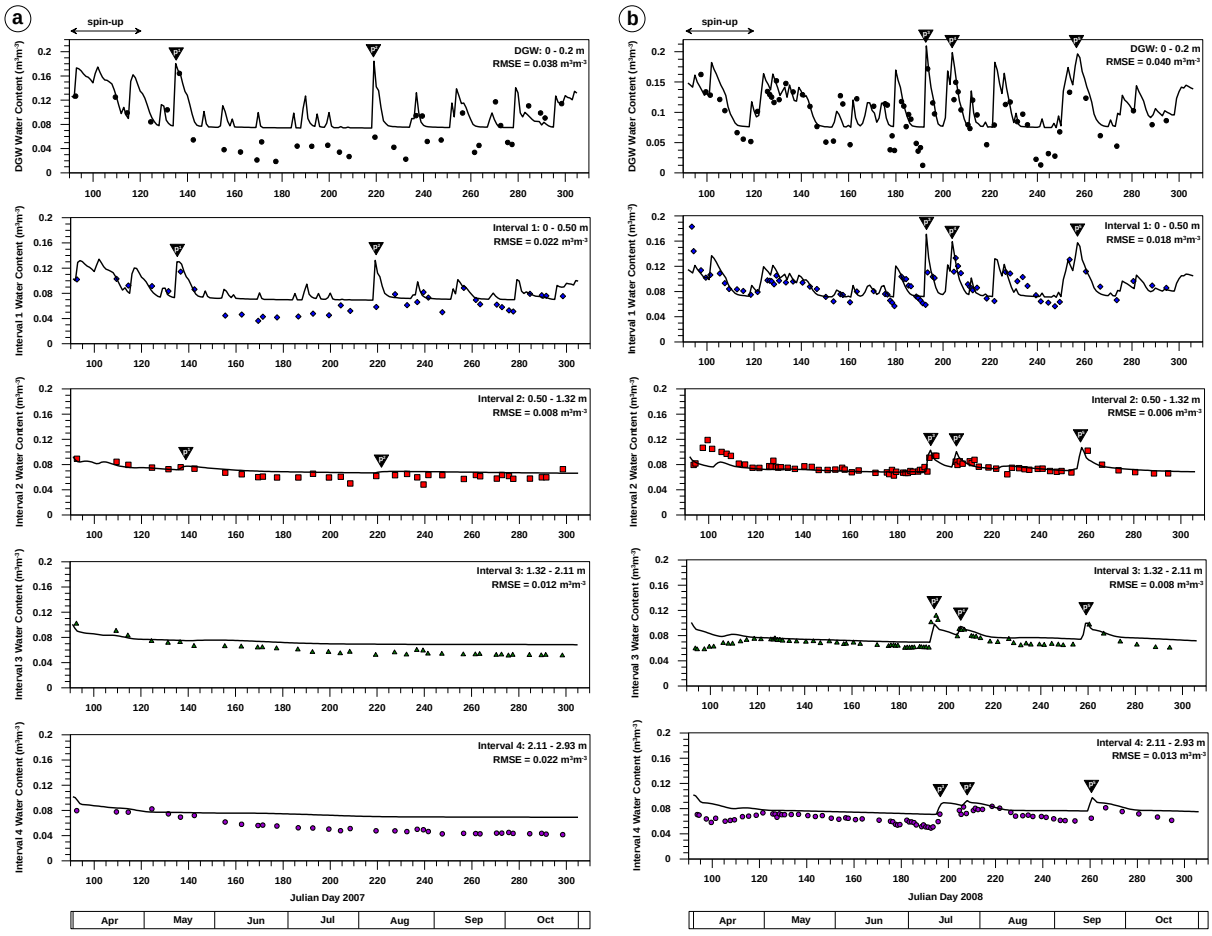

Figure 6.4 Simulated soil moisture content (solid lines) with corresponding GPR moisture data points for the (a) 2007 and (b) 2008 periods. Root-mean-squared-error (RMSE) for each measurement is also shown for the post spin-up period.

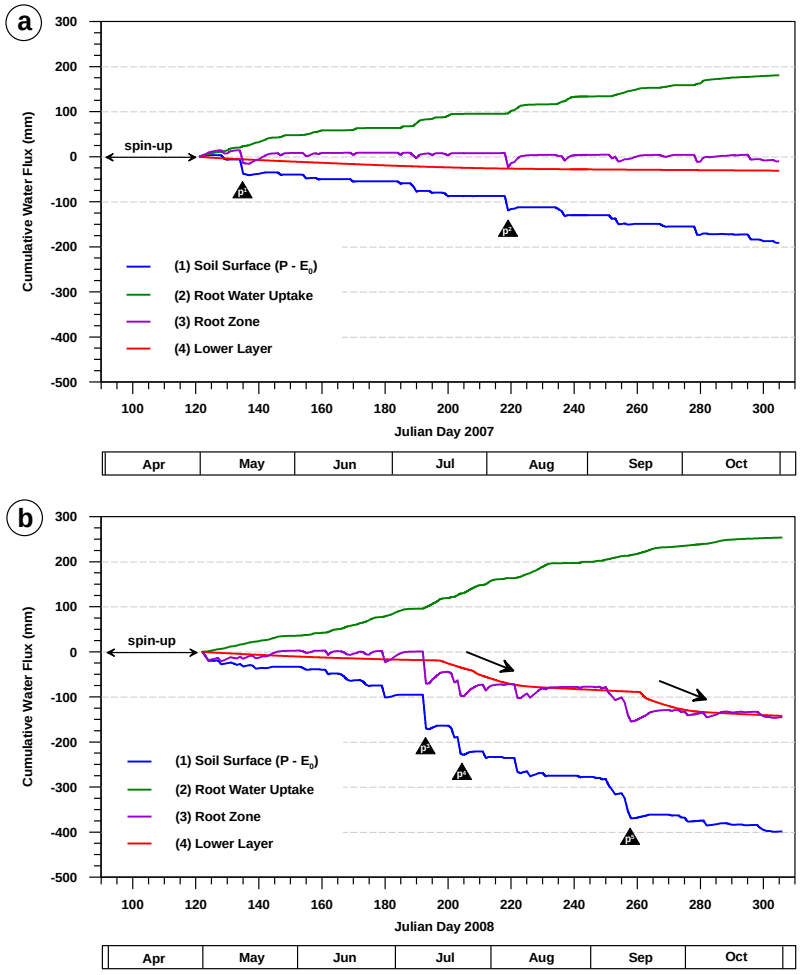

Figure 6.5 Simulated cumulative water flux passing (1) soil surface (precipitation minus evaporation), (2) root water uptake (transpiration), (3) root zone (surface minus root water uptake) and (4) bottom of Layer 4 for (a) 2007 and (b) 2008 periods.

Chapter 7
Evolution of High-Frequency Ground-Penetrating Radar Direct Ground Wave Propagation during Thin Frozen Soil Layer Development[6]

7.1 Executive Summary

High-frequency ground-penetrating radar direct ground waves were used to monitor the seasonal development of a thin, high velocity frozen soil layer over a wet low velocity unfrozen substratum. During the freezing process, the progressive attenuation of a low velocity direct ground wave and the subsequent development of a high velocity direct ground wave were observed. Numerical simulations showed that low velocity direct wave event occurring after freezing commences is due to energy leaking across the frozen layer from the spherical body wave in the unfrozen half space. This leaky phase progressively dissipates until the frozen layer reaches a thickness equivalent to one quarter of the dominant wavelength in the frozen ground. The appearance of the high velocity direct wave is governed by its destructive interference with the reflection events from the base of the frozen layer. This interference obscures the high velocity direct wave event until the frozen layer thickness reaches one half of the dominant wavelength in the frozen ground. These changes in direct wave transmission permit frozen layer monitoring for thicknesses that are significantly less than those feasible using the reflection event from the frozen-unfrozen boundary.

7.2 Introduction

While numerous researchers have characterized glacial and permafrost environments using ground-penetrating radar (GPR) techniques (Woodward and Burke, 2007; Kneisel et al., 2008), there has been very limited, if any, examination of the use of GPR for monitoring seasonal soil frost development. Seasonal frost zones form in mid-latitude climates during periods of sub-zero (˚C) temperatures, and typically develop in the upper meter of soil (Shanley and Chalmers, 1999; Hardy et al., 2001). Soil frost zones are an important component in spring runoff and ground water recharge studies (Shanley

[6] Steelman, C.M., and Endres, A.L. (2009). Evolution of high-frequency ground-penetrating radar direct ground wave during thin frozen soil layer development. *Cold Regions Science and Technology, 57*, 116 – 122, doi:10.1016/j.coldregions.2009.01.007.

and Chalmers, 1999; Nyberg et al., 2001). The depth and distribution of seasonal frost zones influence the dynamics of spring infiltration. Johnsson and Lundin (1991) found that infiltrating snow melt was temporarily restricted by the presence of ice occupying the intermediate-sized pores, which resulted in increased surface runoff. Therefore, knowledge of the temporal and spatial distribution of soil frost zones is an important component in modeling groundwater/surface water recharge.

Typical techniques for monitoring soil frost zones are invasive (e.g., thermistors, frost tubes) and represent point measurements which cannot easily be extrapolated to the field scale. Furthermore, these methods cannot measure the amount of liquid water present within the frozen soil. Time-domain reflectometry (TDR) has been shown as a viable technique to monitor the development of seasonal frost zones and melt water infiltration due to its ability to measure liquid water content (e.g., Patterson and Smith, 1980; Patterson and Smith, 1981; Stein and Kane, 1983; Hayhoe and Bailey, 1985). However, the TDR technique requires the installation of numerous horizontally and vertically positioned rods within the soil, thereby, limiting its suitability for spatial investigations. We propose that high frequency (450 MHz and higher) GPR is particularly well suited for monitoring the freezing process within the shallow subsurface (<1.0 m) due to its non-invasive nature and ability to measure the liquid water component in frozen soil.

GPR typically uses a transmitting antenna positioned along the surface (i.e., air-ground interface) which radiates short pulses of unguided electromagnetic waves commonly between 10 MHz and 1 GHz. These propagating electromagnetic fields respond to changes in material electrical properties. The propagation velocity (v) of electromagnetic waves within GPR bandwidth can be determined from its relative dielectric permittivity (κ) (i.e., the permittivity relative to the free space value) using the equation:

$$v = \frac{c}{\sqrt{\kappa}} \tag{7.1}$$

where c is the electromagnetic velocity in free space (3×10^8 m/s). Within this frequency bandwidth, the relative permittivity of liquid water is approximately 80 while ice has a permittivity of approximately 3.2. Hence, the transformation of water to ice during freezing can significantly lower the bulk dielectric permittivity of the soil (Seyfried and Murdock, 1996), resulting in a corresponding velocity increase.

Previous researchers have illustrated the suitability of GPR to measure volumetric water content in the shallow soil zone by measuring the propagation velocity of the direct ground wave (e.g., Huisman et al., 2003a and references therein). The direct ground wave is an interfacial wave that is transmitted directly from the transmitter to the receiver and which propagates as a coherent pulse within electrically thick layers. Galagedara et al. (2005b) investigated direct ground wave propagation using numerical two-layer models (e.g., high over low velocity and low over high velocity). The purpose of their investigation was to determine the effective sampling depth of the direct ground wave by progressively thinning the upper layer until the direct ground wave detected the lower layer (i.e., observed change in velocity). Although their results indicate a change in apparent velocity as the thickness of the upper layer decreased, they did not explain the nature of the direct ground wave propagation during the presence of a thin (i.e., thicknesses near or less than half of the effective wavelength of the GPR pulse) upper soil layer.

Other studies (e.g., Arcone, 1984; Liu and Arcone, 2003; Arcone et al., 2003; van der Kruk et al., 2006) have examined the propagation of electromagnetic waves through thin-surface waveguides which propagate as modal and dispersive waveforms at velocities that may not correspond to the layer's dielectric properties (Arcone et al., 2003). Dispersive propagation typically occurs during the presence of a thin low velocity layer overlying a higher velocity layer (e.g., wet soil over frozen soil). Dispersive propagation can also occur during the presence of a high velocity layer over a low velocity layer as long as the layer dielectric contrast is very large (e.g., ice over water). Arcone (1984), Lui and Arcone (2003) and van der Kruk et al. (2007) examined the propagation of dispersed electromagnetic waves through a high velocity (ice) layer overlying a low velocity (water) layer. However, they did not examine the propagation of direct ground waves through very thin (<0.5 m) high velocity frozen soil zones overlying unfrozen substratum.

In our work, GPR direct ground wave measurements were used to monitor and evaluate the formation of a shallow frozen soil layer within an active agricultural field. We focus in this paper on the propagation characteristics of the direct ground wave during early soil frost development and propose a potential method of inferring a thin frost layer thickness which is otherwise unattainable without the use of invasive measures. Our results show that the direct ground wave transmission varied systematically during the early freezing process. In particular, a progressive attenuation of a low velocity direct wave was followed by the gradual development of a high velocity direct wave during the progressive thickening of a seasonal soil frost zone underlain by wet soil. We examine the

nature and duration of the direct ground wave transmission phenomenon observed during the formation of a thin frozen soil layer over a wet unfrozen soil layer using a numerical two-dimensional electromagnetic wave modeling software (GPRMAX2D) (Giannopoulos, 2005).

7.3 Ground-Penetrating Radar Field Investigation

The field site is located in Oxford County south of Woodstock, Ontario, Canada (4770360N, 519841E). These surveys were conducted in a localized valley portion of an active agricultural field characterized as a glaciofluvial outwash channel. Core logs in the vicinity show that the survey location is characterized by approximately 0.5–0.7 m of silt loam (17% sand, 79% silt, 4% clay) grading downward into a silty gravel with sand. The water table is located 2–3 m below ground surface. An on-site weather station identified consistent subzero atmospheric temperatures between 14 January 2007 and 21 March 2007 with a total water equivalent precipitation of 31 mm. The snow pack at the site was typically less than 0.30 m during the winter season which was removed prior to the GPR surveys.

GPR surveys are typically performed using bistatic antennas which allow the user to operate in both multi-offset and common-offset configurations. Multi-offset configurations such as common mid-point (CMP) soundings simultaneously separate the transmitting and receiving antenna at regularly defined intervals (Figure 7.1a). These surveys produce a traveltime-offset sounding at a point location that can be used to obtain velocity-depth information. Accurate identification and characterization of the direct ground wave, direct air wave and reflections can be achieved using the CMP method (Figure 7.1b). Reflection profiling surveys use a common-offset antenna separation to collect traveltime imaging of reflecting interfaces. The depth to these reflectors is determined from the signal propagation velocity which can be obtained from CMP soundings.

Coincident CMP soundings and constant-offset reflection profiles were conducted along a fixed survey line using a Sensors and Software PulseEKKO™ 1000 GPR system (Sensors and Software Inc., Mississauga, Ontario, Canada) equipped with 450 MHz bistatic antennas. The GPR data was collected using a time window of 100 ns, sampling interval of 0.1 ns and 64 stacks per trace. CMP data was acquired over the range of antenna offsets from 0.20 m to 2.50 m using a 0.02 m step interval; corresponding reflection profiles were collected along a 2.0 m line using a spatial step size of 0.02 m centered on the CMP. Prior to analysis, all data sets were dewowed to remove low frequency signal saturation. Bandpass temporal filtering was applied to the data sets using frequencies of 50,

200, 900 and 1100 MHz (i.e., low cut frequency, lower plateau, upper plateau and high cut frequency) to remove high and low frequency noise. A spreading and exponential compensation (SEC) gain was applied to the CMP soundings and reflection profiles.

The CMP field data (Figure 7.2a–d) showed an initial attenuation of the direct ground wave signal during early soil freezing conditions, followed by a re-establishment of the direct wave after approximately one month. The CMP survey conducted on 13 January 2007 (Figure 7.2a) during unfrozen wet soil conditions displayed a strong, well-developed low velocity direct ground wave (DGW^{WG}) with a measured velocity of 0.0607 m/ns ±0.0001 m/ns. The CMP survey on 22 January 2007 (Figure 7.2b) was conducted during early frost development and showed a severely attenuated DGW^{WG} event. This lower velocity DGW^{WG} was observed between offsets of 0.80–1.70 m with a measured velocity of 0.0633 m/ns ±0.0022 m/ns. The CMP survey conducted on 31 January 2007 (Figure 7.2c) showed the early development of a high velocity direct ground wave (DGW^{FG}) event at offsets less than 0.60 m; its velocity was determined to be 0.1180 m/ns ±0.0110 m/ns. The final CMP survey performed on 20 February 2007 (Figure 7.2d) showed a well-developed high velocity DGW^{FG} event with a measured velocity of 0.1140 m/ns ±0.0005 m/ns.

The reflection profiles corresponding to the previous CMP surveys are given in Figure 7.3a–d. It should be noted that the direct ground wave velocities used to obtain a depth scale may not be an accurate representation of unfrozen soil underlying the shallow frost zone. The depth scales in Figures 7.3b and 7.3c represent the upper portion of soil, i.e., frozen portion of soil characterized by the direct ground wave. Reflection profile monitoring of the freezing process depends on the imaging of the reflection from the interface at the base of the frozen zone. To be well defined at shallow depths, this event must have sufficient two-way traveltime to avoid interference with the complex first arrival consisting of the direct air and ground waves. During the earlier portion of the freezing process, this condition does not appear to be achieved; and this reflection event is not observed (Figures 7.3b and 7.3c). During these periods, however, Figures 7.3b and 7.3c show a distinct decrease in early time amplitudes, which represent the direct air, direct ground and reflections off the base of the frozen layer. It is only after a substantial period of freezing conditions that the base of the frozen layer is imaged by the reflection profiling (Figure 7.3d). Using the frozen soil velocity from the direct ground wave, we estimate the depth of this event to be approximately 0.5 m. Although a change in early time amplitudes were observed in the reflection profiles, the CMP soundings provided a means to monitor freezing at shallower depths.

7.4 Numerical Simulations: Results

Numerical simulations were conducted using GPRMAX2D, a finite-difference time-domain (FDTD) two-dimensional algorithm (Giannopoulos, 2005), to investigate the propagation characteristics of the CMP direct ground wave during the development of a thickening high velocity (frozen) layer over a low velocity (wet unfrozen) substratum analogous to the silt loam soil at the Woodstock site.

The propagation of GPR waves for sources present on the air-ground interface is described by Annan (1973) and Radzevicius et al. (2003). Including a thin shallow layer, however, significantly complicates the wave propagation. Figure 7.4 illustrates the events present in such a situation where a point electromagnetic source (S) radiating spherical waves upward into the air (A) and downward into a layer of frozen ground (G^{FG}) and a halfspace of wet ground (G^{WG}). Due to the higher velocity of air and frozen ground with respect to the underlying layer, lateral waves (head waves) are present in the frozen ground (L^{FG}) and the wet ground (L^{WG}), respectively. Due to the lower velocity of wet and frozen ground with respect to the overlying layer, evanescent waves are present in the frozen ground (E^{WG}) and air (E^{FG}), respectively. These evanescent waves exponentially dampen with increasing distance from the interface. If the frozen ground layer is thin enough, the evanescent wave generated on the wet and frozen ground interface can still be measured in the air as being the low velocity direct ground wave. The direct ground wave in the frozen ground (DGW^{FG}) is a combination of the spherical wave in the frozen ground (G^{FG}) and the evanescent wave in air (E^{FG}) which is present due to the boundary conditions that enforce continuity of the horizontal electric field. The direct ground wave in the wet ground (DGW^{WG}) is a combination of the spherical wave in the wet ground (G^{WG}) and the evanescent wave that is present in the frozen ground and air (E^{WG}). Primary (P) and multiple (M) reflections off the base of the frozen layer result in multiple lateral waves in the wet ground and multiple waves in air (not all shown in Figure 7.4).

The synthetic CMP surveys were centered within a 10 m × 10 m domain (x, y) with a spatial discretization of 0.005 m. The frozen soil layer was assigned a relative dielectric permittivity of κ = 5, relative magnetic permeability of μ = 1 and electrical conductivity of σ = 4 mS/m. The wet layer was assigned a permittivity of κ = 20, permeability of μ = 1 and conductivity of σ = 8 mS/m. These permittivity values were derived from observed direct ground wave velocities obtained during seasonally wet and late frozen soil conditions, while the conductivities were based on EM-38 ground conductivity meter measurements done in the horizontal dipole mode at those corresponding times.

Synthetic CMP surveys were performed for a series of frozen layer thicknesses between 0.0 and 0.75 m at 0.025 m increments. Survey simulations were started with a transmitter to receiver separation of 0.2 m and extended to a maximum separation of 2.5 m using a step-size of 0.02 m. The electromagnetic wave propagation was computed for a 30 ns time window using an 11.8 ps time step increment. An infinite line source perpendicular to the modeling plane was used to approximate the dipole source used in the field experiment. A Ricker excitation function was used to describe the source pulse with a center frequency of 450 MHz. In addition, these modeling results were examined using simple ray optics to determine the traveltimes of the primary and multiply reflection events.

Figure 5a–f shows synthetic CMP surveys for frozen layer thicknesses between 0.0 cm and 30.0 cm. Model results show that a reduced amplitude low velocity DGW^{WG} event persists with the introduction of a thin 2.5 cm frozen layer (Figure 7.5b). Further thickening of the frozen layer to 5.0 cm (Figure 7.5c) caused the low velocity DGW^{WG} event to become severely attenuated. Our numerical results indicate that this event essentially dissipated once the frozen layer reached 7.5 cm which corresponds with one quarter of the dominant wavelength in the frozen ground. There is no observable high velocity DGW^{FG} event for either of these very thin frozen layer cases.

The synthetic CMP with a frozen layer thickness of 10.0 cm (Figure 7.5d) showed the initial development of an observable high velocity DGW^{FG} event at short antenna offsets; however, this event undergoes severe destructive interference with the superimposed primary (P) and multiple (M) reflection events from the base of the frozen layer. The interference with the reflection events obscured high velocity DGW^{FG} signal until the frozen layer thickness reached 15.0 cm (Figure 7.5e), where DGW^{FG} began to separate from the primary reflection event. In this case, a discrete high velocity DGW^{FG} event is observed at antenna offsets less than 0.3 m. This layer thickness (15 cm) corresponds with one half of the dominant wavelength in the frozen ground (i.e., in-situ wavelength). Further thickening of the frozen layer to 30 cm (Figure 7.5f) shows well resolved high velocity DGW^{FG} events between antenna offsets of 0.2–0.8 m; superposition of the high velocity DGW^{FG} event and the primary reflection off the base of the frozen layer occurs beyond this range.

Additional analyses of the wavefield were performed using two-dimensional snapshots of a single point source to investigate the effects of the progressive thickening of a frozen layer on the propagation of the various ground wave events. Snapshots captured at 15 ns are displayed in Figure 7.6a–f for frozen layer thicknesses between 0.0 and 30.0 cm. Figure 7.6a show the correspondence between the low velocity DGW^{WG} event at the surface and the spherical wave propagating outward

through the unfrozen halfspace. The presence of a thin 2.5 cm frozen layer (Figure 7.6b) did not significantly affect the spherical wave propagating in the unfrozen halfspace; the low velocity DGW^{WG} event at the surface is the result of energy leaking across the frozen layer from the spherical body wave in the unfrozen half space. Further thickening of the frozen layer to 5.0 cm (Figure 7.6c) significantly attenuated the spherical body wave and its leaky mode that is observed as the low velocity DGW^{WG} event along the surface. As the frozen layer continues to thicken to 10.0 cm and greater (Figures 7.6d–f), development of high velocity DGW^{FG} event occurs as it increasingly separates from the trailing reflection and multiple events from the base of the frozen layer.

7.5 Discussion and Conclusions

In this study, we have examined the use of high frequency GPR direct ground waves for monitoring the seasonal development of the thin surficial frozen soil layer. Our field results clearly show that the nature of the direct wave propagation observed on the CMP surveys evolved during the freezing process. Prior to the onset of freezing conditions, a strong low velocity direct ground wave indicative of wet unfrozen soil conditions was present. Initially during the freezing process, there was a systematic attenuation of a low velocity direct ground wave in the CMP data. The subsequent CMP surveys observed development of a high velocity direct ground wave over a progressively longer range of antenna offset distance. In contrast, reflection profiles were only able to monitor the freezing process after the formation of an adequately thick frozen zone permitted imaging of the reflection from the base of this zone.

To investigate this observed evolution in direct wave propagation, numerical simulations were conducted for a progressively thickening frozen soil layer over a wet substratum. Our numerical results showed that the observed evolution in direct wave propagation are consistent with synthetic results obtained with a progressively thickening high velocity (frozen) layer over a low velocity (unfrozen wet) substratum model. These modeling results indicate that low velocity direct wave event found in the field CMP data after freezing commences is due to energy leaking across the frozen layer from the spherical body wave in the unfrozen half space. This leaky phase is essentially dissipated once the frozen layer reaches a thickness equivalent to one quarter (i.e., 7.5 cm) of the dominant in-situ wavelength. The appearance of the high velocity direct wave is governed by destructive interference with the superimposed primary and multiple reflection events from the base of the frozen layer. This interference obscured the high velocity direct wave event until the frozen layer thickness reached one half (i.e., 15 cm) of the dominant in-situ wavelength.

Much of the work concerning the use of GPR direct waves for near surface characterization is based on the velocity estimation. The earlier modelling study by Galagedara et al. (2005b) did not explicitly consider either the existence of a leaky mode or the effects of a destructive interference pattern associated with direct ground wave propagation during the presence of a thin high velocity layer underlain by a low velocity layer. Our numerical results indicate that direct ground wave identification, and the associated direct ground wave velocity estimation would be problematic for frozen layer thicknesses less than one half the in-situ wavelength.

Arcone (1984) showed that modal propagation could exist for a thin layer bounded by two confining layers with contrasting dielectric permittivities (e.g., ice bounded by air and water), and would essentially propagate as lossless dispersive waves for layer thickness near or less than the in-situ wavelength. Inversion of these dispersed modes can yield layer thickness and layer dielectric properties (van der Kruk et al., 2007). In the case of a frozen soil layer bounded by air and unfrozen soil, however, the dielectric contrast was not sufficient to induce total internal reflection (i.e., modal propagation) within the frozen soil layer. As a result, much of the direct wave energy leaked across the frozen-unfrozen interface and caused significant attenuation of direct ground wave energy. Smith (1984) shows comparable observations to those presented in this paper. Based on numerical electric field patterns for electric horizontal dipoles positioned at various heights above an interface between lossless dielectric media (i.e., antenna was positioned at various heights in air overlying a dielectrically higher material), Smith showed that the evanescent waves generated by the dipole can start propagating in the lower layer if the thickness of the overlying layer is not too large. In other words, if the thickness of the upper layer is too large, the waves will not propagate in the lower layer or will propagate with much smaller amplitudes.

The results of this study clearly demonstrate the capability of high frequency CMP surveys for monitoring and evaluating the development of a thin frozen soil layer, which would otherwise require the use of invasive techniques. In particular, changes in direct ground wave propagation during the presence of a thin frozen soil layer permit layer monitoring for thicknesses that are less than those feasible using conventional GPR reflection profiling. Additional work using measurements from a number of well instrumented field sites is needed to assess the application of this technique to the characterization of frozen soil for a wide range of conditions.

7.6 Tables and Figures

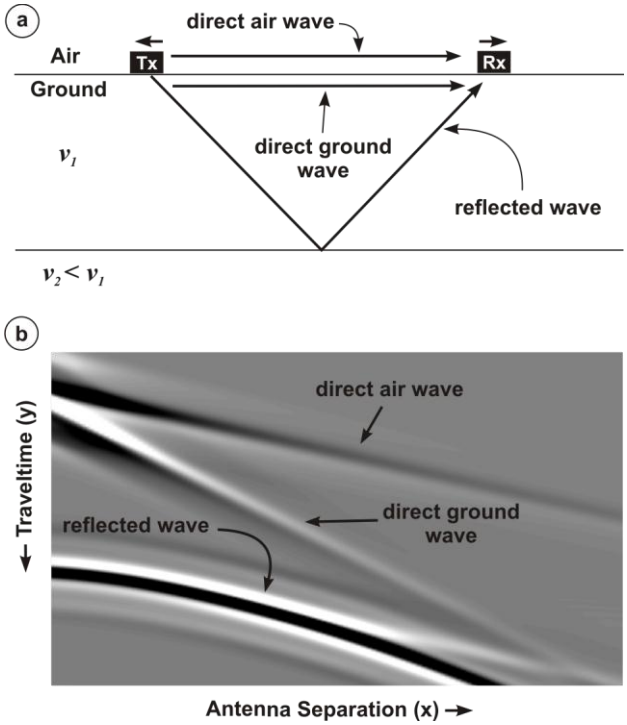

Figure 7.1 (a) Schematic diagram illustrating CMP survey conducted at a fixed measurement point with (b) corresponding CMP sounding.

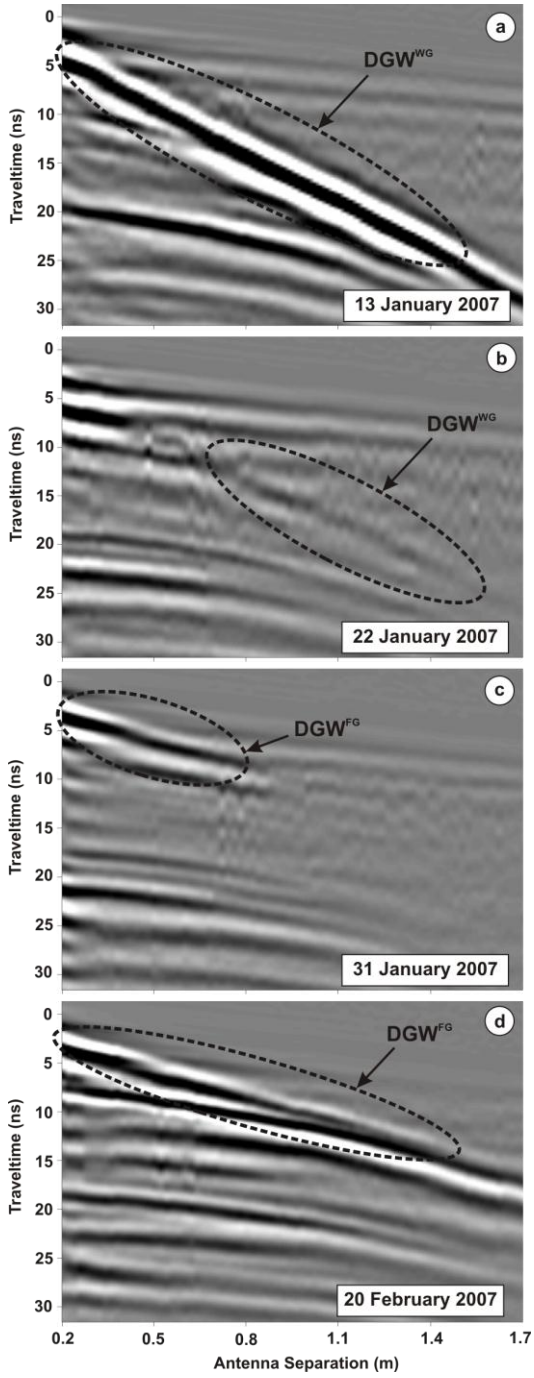

Figure 7.2 Field CMP surveys showing the evolution of the direct ground wave during the development of a surficial frozen soil layer over a wet soil layer using 450 MHz antennas.

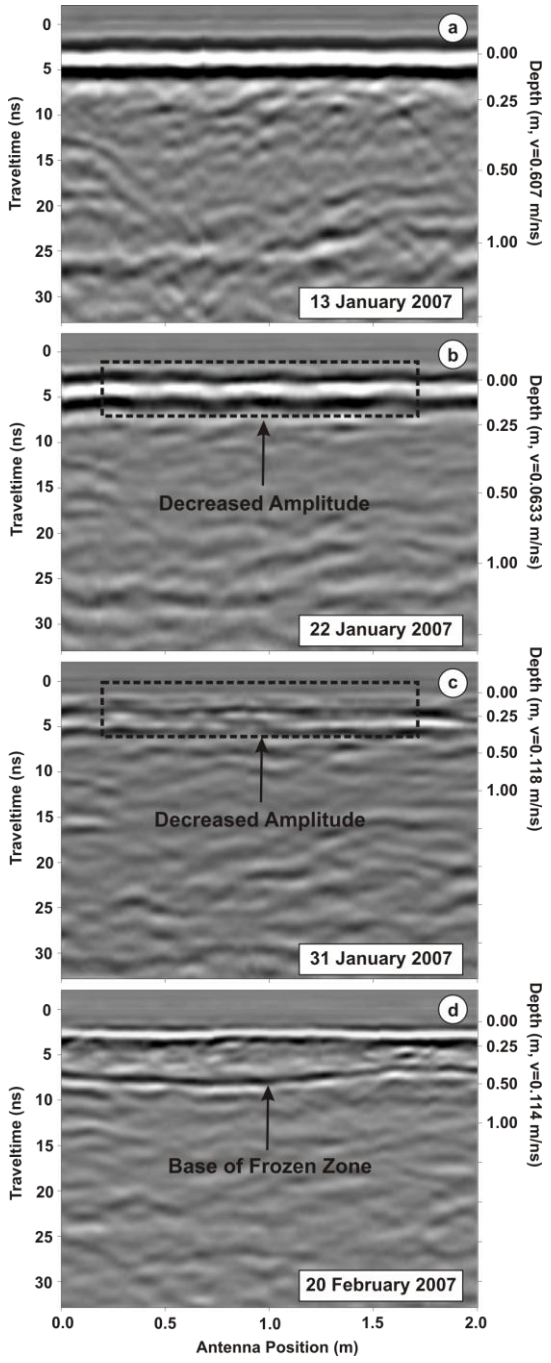

Figure 7.3 Reflection profiles collected along CMP line using 450 MHz antenna during the development of a surficial frozen soil layer over a wet soil layer. Depths were determined using the corresponding CMP direct ground wave velocity. The strong reflection event generated by the interface at the base of the frozen zone was observed on 20 February 2007; its depth is approximately 0.5 m.

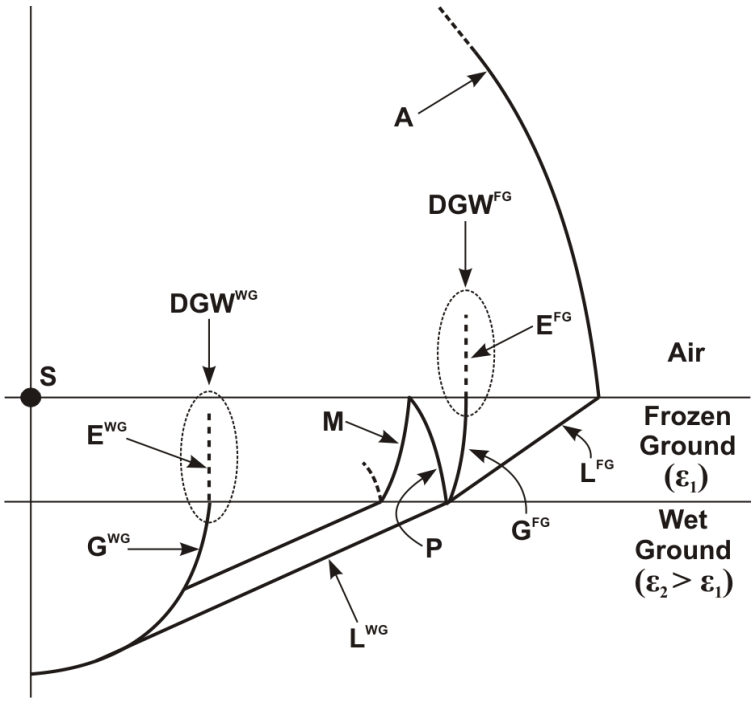

Figure 7.4 Schematic diagram illustrating wavefields corresponding to a point electromagnetic source for a thin shallow frozen soil layer overlying a wet soil halfspace.

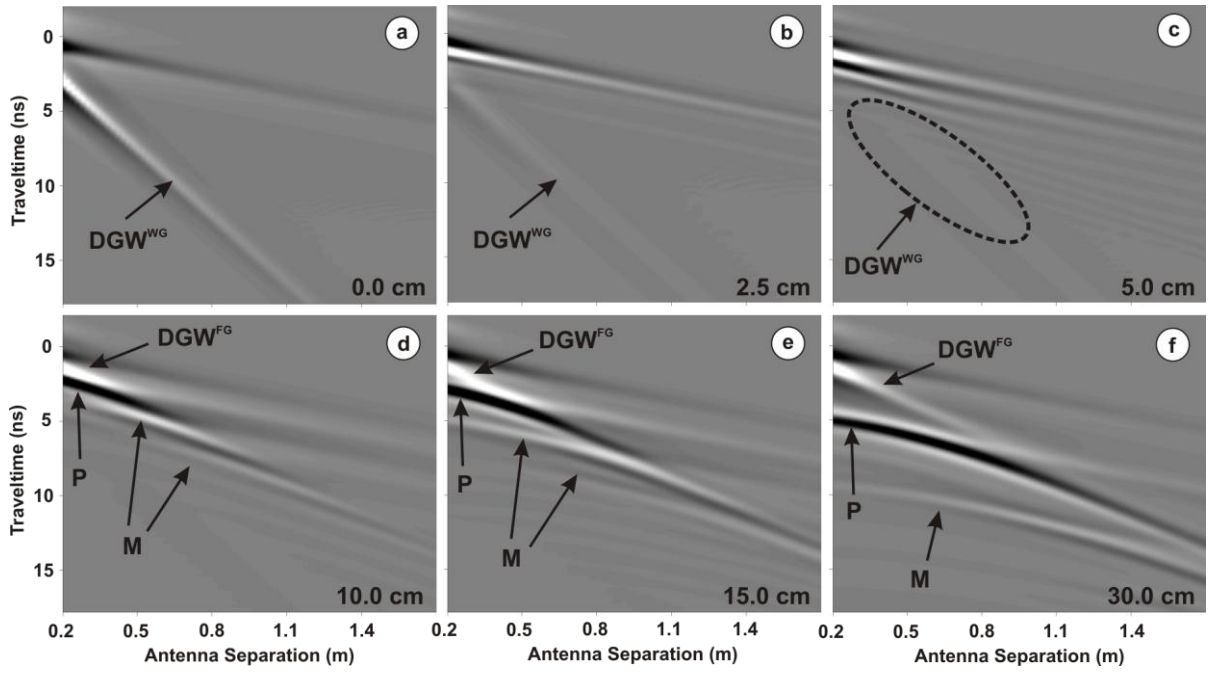

Figure 7.5 Synthetic CMP sections for frozen layer thicknesses between 0–30 cm over a wet soil layer. Results show the progressive evolution of the direct ground wave as frozen soil layer thickness increases. During the freezing process, the modelling results show the progressive attenuation of a low velocity DGW^{WG} (a–c) and the subsequent development of a high velocity DGW^{FG} (d–f).

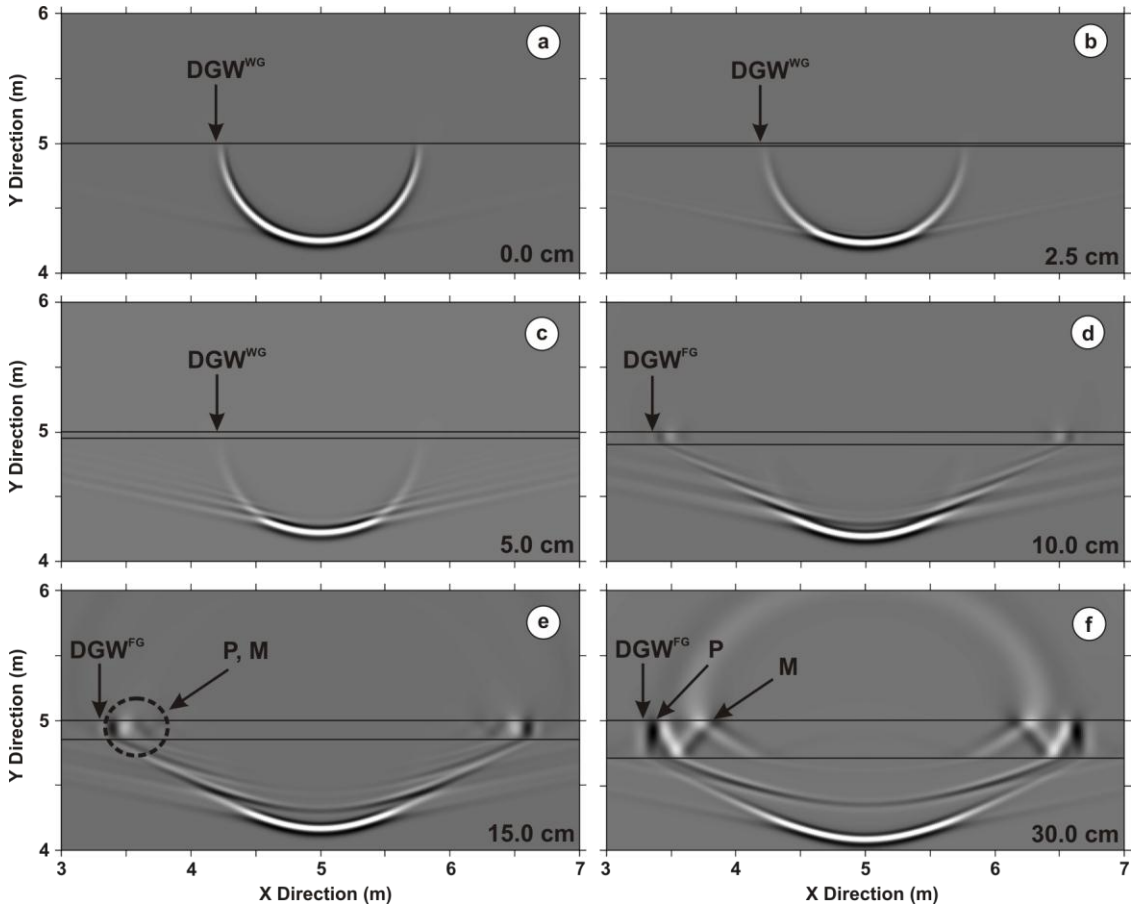

Figure 7.6 Two-dimensional snapshot at 15 ns for a progressively thickening frozen soil layer (0–30 cm) over a wet soil halfspace. The presence of a thin 2.5 cm frozen layer (b) did not significantly affect the spherical wave propagating in the unfrozen halfspace; the low velocity DGW^{WG} event at the surface is the result of energy leaking across the frozen layer from the spherical body wave in the unfrozen half space. Significant attenuation of the spherical body wave and its leaky mode was observed at layer thickness of 5.0 cm (c). As the frozen layer thickened to 10.0 cm and greater (d–f), development of high velocity DGW^{FG} event occurs as it separates from the primary (P) and multiple (M) reflection events.

Chapter 8
Field Observations of Shallow Freeze and Thaw Processes using High-Frequency Ground-Penetrating Radar[7]

8.1 Executive Summary

We have used reflection profiles and common-midpoint soundings with 900 MHz ground-penetrating radar (GPR) to monitor freezing and thawing processes during winter seasonal periods at two separate sites located in Ontario, Canada. GPR responds to the large contrast in dielectric permittivity between liquid water and ice. The profiles reveal the long-term development of a very shallow (<0.5 m) soil frost zone overlying unfrozen wet substratum. During the course of the winter season, long-term traveltime analysis yielded physical properties of the frozen and unfrozen layers as well as the spatial distribution of the base of the soil frost zone. Short-term shallow thawing events overlying frozen substratum formed a dispersive waveguide for both the CMP and reflection profile surveys. Inversion of the dispersive wavefields for the CMP data yielded physical property estimates for the thawed and frozen soils and thawed layer thickness. We have shown that GPR can be used to monitor very shallow freezing and thawing events by responding to changes in the relative dielectric permittivity of the soil water phase (e.g., liquid water verses ice). The non-invasive collection of such data permits interpretation of dynamic temporal and spatial freeze-thaw events which are important for characterizing a range of hydrological processes.

8.2 Introduction

The seasonal freezing and thawing of near-surface sediments affect hydrological processes such as the infiltration of meltwater, surface water runoff and soil water distribution. The temporal and spatial distribution of seasonally frozen and thawed zones significantly influences the dynamics of seasonal soil water content distribution. The seasonal frost zones pertaining to this study are those which form in mid-latitude (temperate) climates during periods of sub-zero (˚C) atmospheric conditions; they are typically constrained to the upper few meters of soil and are exclusively present during the winter seasonal period. Since these frost zones develop in the near surface, they are susceptible to changes

[7] Steelman, C.M., Endres, A.L., and van der Kruk, J. (2010). Field observations of freeze and thaw processes using high-frequency ground penetrating radar. *Hydrological Processes, 24*, 2022–2033, doi:10.1002/hyp.7688.

in atmospheric conditions. As a result, seasonal freeze-thaw processes greatly vary during the course of the winter season.

A comparison of coupled soil water and heat model simulations with field measurements of soil water content, unfrozen water content, soil temperature and drainage water flow by Johnsson and Lundin (1991) showed that the hydraulic complexities associated with seasonal freezing and thawing of the pore water significantly influence the drainage potential of soils. Field investigations by Nyberg et al. (2001) showed that frost zones affect surface runoff dynamics. Further, an extensive field study conducted by Bayard et al. (2005) showed that soil frost formation could significantly reduce the amount of deep percolation and subsequent groundwater recharge by up to 25%. Bayard et al. also demonstrated that surface runoff, subsurface runoff and percolation are primarily influenced by the presence or absence of pore and basal ice. Undoubtedly, novel field techniques capable of characterizing and monitoring temporal and spatial aspects of freeze-thaw processes would provide valuable information for larger-scale studies of groundwater and surface water recharge.

Freeze-thaw processes are typically characterized using invasive point-measurement techniques (e.g., thermistors, frost tubes) which cannot easily be extrapolated to the field-scale. For example, time-domain reflectometry (TDR) is capable of monitoring the development of seasonal freezing and thawing (e.g., Johnsson and Lundin, 1991; Nyberg et al., 2001; Bayard et al., 2005) because it is used to infer the liquid water fraction within frozen soil (Patterson and Smith, 1981; Stein and Kane, 1983; Hayhoe and Bailey, 1985). However, TDR requires numerous horizontally and vertically positioned rods at representative soil depths, limiting its suitability for spatial investigations. On the other hand, relatively non-invasive geophysical methods (e.g., electrical resistivity tomography (ERT), capacitively coupled ERT, electromagnetic induction, and ground-penetrating radar (GPR)) can also provide high-resolution information of freeze-thaw processes (Kneisel et al., 2008). Here we use GPR because of its unique ability to delineate the boundary between frozen and unfrozen soil and capacity to estimate the amount of liquid water in frozen ground.

GPR has been used to characterize a wide range of glacial and frozen conditions (Woodward and Burk, 2007; Kneisel et al., 2008) such as the spatial and temporal distribution of ground ice, depth to permafrost table and thickness of the active layer above the permafrost (e.g., Annan and Davis, 1978; Delaney et al., 1990; Arcone et al., 1998; Hinkel et al., 2001; Moorman et al., 2003; De Pascale et al. 2008). Recently, Kneisel et al. (2008) was able to image an upper and lower thermal interface delineating the lateral distribution of a seasonally unfrozen soil layer within a frozen soil environment

of a water deltaic area. Wollschläeger et al. (2008) used multi-channel GPR to simultaneously map the depth to permafrost table and average moisture content in the active layer at a continuous permafrost site. The successful application of GPR in these environments is based upon the large contrast in dielectric properties between liquid water and ice, permitting the inference of the thermal state of soil water in the subsurface.

Despite all this work, there has been very limited use of GPR to characterize shallow (e.g., <1.0 m) temperate freeze-thaw processes. Recently, Steelman and Endres (2009) [Chapter 7] demonstrated that GPR ground waves could be used to monitor the seasonal development of frozen soil. This paper expands upon the well-established use of GPR for characterizing permafrost environments to the monitoring of seasonal (i.e., long-term) development and dissipation of a shallow soil frost zone overlying unfrozen wet substratum during the winter season using high-frequency GPR (i.e., 900 MHz). We inferred vertical changes in the thermal state of soil water from common-midpoint (CMP) soundings and imaged its spatial variations using fixed-offset reflection profiling. We also have investigated short-term (i.e., 1–5 day) mid-winter thawing events which form relatively thin thawed soil layers that produced dispersive waveguides. Analysis of the observed dispersive wavefields yielded information about near-surface soil conditions in zones that are below the resolution of the conventional CMP and reflection profiling surveys.

8.3 GPR Background

GPR uses a transmitting antenna positioned along the surface (i.e., the air-ground interface) that radiates short pulses of electromagnetic (EM) waves commonly in the frequency band between 10 MHz and 1 GHz. These propagating EM waves respond to changes in material electrical properties and are recorded with a separate receiving antenna also located on the surface. The separate antennas allow the performance of both fixed-offset reflection profiling and multi-offset CMP soundings. The conventional reflection profiling technique provides a cross-sectional image of subsurface interfaces that delineate spatial changes in electrical properties. CMP surveys systematically separate a transmitting and receiving antenna about a central fixed point, which results in a separation of coherent events in the wavefield (e.g., direct air wave, direct ground wave and reflections). The direct ground wave propagates along the air-ground interface and is effectively sensitive to a depth of approximately one-half dominant wavelength in ground while reflection events are affected by conditions along raypaths down to a given reflecting interface.

The propagation velocity (v) of EM waves within GPR bandwidth primarily depends on the relative dielectric permittivity (κ) of the material (i.e., the measured dielectric permittivity relative to the free space permittivity). This relationship is defined by the equation

$$v = \frac{c}{\sqrt{\kappa}}, \tag{8.1}$$

where c is the electromagnetic velocity in free space (0.2998 m/ns). Many successful applications of GPR rely on the large electrical contrast between liquid water and the remaining subsurface components. Within the GPR bandwidth, the dielectric permittivity for most geophysical applications ranges between κ = 1 (air) and κ = 78–88 (freshwater at 25˚C and 0˚C, respectively). Table 8.1 provides a summary of dielectric permittivities and EM wave velocities for some reported materials. The large dielectric value of liquid water relative to ice (κ = 3.2) under natural soil conditions provides a basis for monitoring freeze-thaw processes using EM wave velocity measurements. Further, an estimate of liquid water content during these processes can be obtained using an appropriate petrophysical relationship (e.g., Patterson and Smith, 1981; Stein and Kane, 1983; Nyberg et al., 2001).

The vertical resolution of GPR is determined by the pulse length of the emitted signal (Annan, 2005). Practically, pulse length is equal to 1.5 times the wavelength, where wavelength is equal to the product of the EM wave velocity and dominant pulse period. The vertical resolution is approximately equal to one-half the in-situ pulse length. Consequently, higher frequency pulses provide better resolution than lower frequency pulses. However, higher frequencies attenuate more rapidly and thus have a shallower depth of investigation. Hence, there is an inherent frequency trade-off between depth of investigation and signal resolution. Given the very shallow depth (<1.0 m) of the freeze-thaw processes we monitored and the relatively low attenuation in frozen soils, we were able to use a high-frequency GPR system with excellent resolving power to image these phenomena.

Normal-moveout (NMO) velocity analyses applied to CMP soundings (e.g., Greaves et al., 1996) provide information about the subsurface EM wave velocity profile. The hyperbolic form of the offset-distance-traveltime relationship for reflection events is the basis for methods used to determine the NMO velocity related to a specific reflection event. Commonly used velocity analyses employ a semblance statistic which is a measure of signal coherency along the hyperbolic trajectory of a reflection event. The semblance statistic is expressed as the normalized output-to-input energy ratio

on a velocity versus time plot, where semblance peaks represent NMO velocities and two-way zero-offset times corresponding to reflection events (Yilmaz, 2001).

The NMO velocity for a given reflection is an average velocity value for the overlying material through which this event propagates. An interval velocity for the material located between two reflecting events can be obtained from the NMO velocity information using the Dix (1955) equation:

$$v_{\text{int}} = \sqrt{\frac{v_L^2 t_L - v_U^2 t_U}{t_L - t_U}}, \tag{8.2}$$

where v_L and v_U are the NMO velocities of the lower and upper reflecting boundaries, while t_L and t_U are the corresponding two-way zero-offset traveltimes. The corresponding interval thickness between persistent reflection events is obtained from the measured traveltimes and interval velocity.

The amplitude of a reflected GPR pulse will depend on the interface reflection coefficient (R), which primarily depends on the contrast between electrical properties across the interface (Annan, 2005). The reflection coefficient for a downward traveling normally incident signal is defined by

$$R = \frac{\sqrt{\kappa_U} - \sqrt{\kappa_L}}{\sqrt{\kappa_U} + \sqrt{\kappa_L}}, \tag{8.3}$$

where κ_U is the dielectric permittivity of the upper (i.e., incident) layer while κ_L is the dielectric permittivity of the lower (i.e., refracting) layer. Reflection coefficients (i.e., relative amplitudes) range between 1 and −1, where the negative sign convention denotes a reversal in the polarity of the reflected signal, and hence, an inversion in the contrast between electrical properties across the interface. Further, the magnitude of R is directly related to the permittivity contrast at the interface; hence, large amplitude reflections indicate boundaries with a strong permittivity contrast.

8.4 Site Description

The GPR field studies were conducted at two field sites located in southern Ontario, Canada (Figure 8.1). The Woodstock site (519845E, 4770361N) is characterized by silt loam soil (17% sand, 79% silt, 4% clay), while the Waterloo site (528878E, 4814702N) is characterized by sandy soil (97% sand, 3% silt). The mean annual air temperature and precipitation (1971–2000) in the region surrounding the Woodstock site is 7.5 ˚C and 954 mm; the atmospheric conditions over the same period for the region surrounding the Waterloo site is 6.7˚C and 908 mm, respectively (Environment

Canada, 2008). In general, seasonal conditions in southern Ontario are characterized by frozen soil conditions during the months of December–March and unfrozen conditions for the remainder of the year.

The Woodstock site is situated in a localized valley portion of an active agricultural field characterized as a glaciofluvial outwash channel (Cowan, 1975). Core logs in the vicinity show that the monitoring location is characterized by approximately 0.5–0.7 m of silt loam grading downward into a silty gravel with sand. The water table is located 2–3 m below ground surface. The Waterloo site is situated on a relative topographic high within an active agricultural field located on top of the Waterloo moraine. It is characterized as an irregular tract of gently rolling to hummocky terrain with some exposures of ice-contact stratified sand and gravel deposits (Bajc et al., 2004). The regional water table at the Waterloo site is located approximately 15–20 m below ground surface.

8.5 Methods and Data Processing

Continuous daily measurements of precipitation and atmospheric temperature for the Woodstock and Waterloo sites were collected at nearby weather stations during the 2007 and 2008 winter seasons, respectively. Conditions at the Woodstock site were monitored using an on-site meteorological station located approximately 0.5 km from the field site. Conditions at the Waterloo site were monitored from the University of Waterloo weather station located approximately 7 km east of the field site.

GPR data sets were collected at both sites during the development of the seasonal soil frost zone and subsequent seasonal thaw (e.g., January–March). The relatively thin snow pack at each site (e.g., <0.3 m) was removed prior to conducting the GPR surveys; the snow was returned after completing the GPR surveys to minimize effects of snowpack thickness on the freezing process. CMP soundings and reflection profiling were concurrently conducted along a fixed survey line using a Sensors and Software PulseEKKO™ 1000 GPR system (Sensors and Software Inc., Mississauga, Ontario, Canada) equipped with 900 MHz (nominal frequency) bistatic antennas. These antennae generally yielded center frequencies between 500–800 MHz. The GPR data were collected using a time window of 100 ns, sampling interval of 0.1 ns and 64 stacks per trace.

CMP soundings and reflection profiling at the Woodstock site were conducted on eight different dates between 13 January 2007 and 13 April 2007. Discrete CMP data were acquired over the range of antenna offsets from 0.2 m to 2.0 m using a 0.02 m recording step interval; corresponding

reflection profiles were collected along a 2.0 m line using a spatial step size of 0.02 m. CMP soundings and reflection profiling at the Waterloo site were conducted between 11 November 2007 and 26 April 2008; however, the GPR data pertaining to this study are focused on a single mid-winter thawing event occurring between 24 January and 8 February 2008. For this site, CMP data were acquired over the range of antenna offsets from 0.2 m to 4.0 m using a 0.02 m step interval; corresponding reflection profiles were collected along an 8.0 m line using a spatial step size of 0.02 m. For both data sets, the midpoint location of the CMP surveys coincides with the center of the corresponding reflection profile.

The following processing sequence was applied to the GPR data sets using Reflex Win™ software program (Sandmeier Software, Karlsruhe, Germany) prior to interpretation: (1) low-pass frequency filtering to remove low-frequency noise and dc offsets, (2) time zero correction, (3) bandpass temporal filtering with 100 and 1400 MHz cutoff frequencies, (4) spreading and exponential compensation gains to compensate for geometrical spreading and attenuation losses and (5) time-to-depth conversion for reflection profiles at the Woodstock site. It should be noted that identical gains were applied to a sequence of time-lapse GPR measurements collected at a particular location (e.g., the same gain function was applied to the CMP soundings collected at the Woodstock site), thereby permitting a comparison of relative reflection amplitudes.

Figure 8.2 illustrates a single GPR waveform trace that shows numerous pulse arrivals corresponding to various subsurface events. GPR profiles are represented by a sequence of waveform traces collected at regularly defined intervals for some distance along the surface. Traces are plotted with respect to position on the horizontal axis and pulse traveltime (or equivalent depth) on the vertical axis. In this paper, waveforms are represented by an equivalent grey-scale banding where positive and negative pulse amplitudes correspond to white and black colour scale, respectively.

Although reflection profiles provide information on subsurface geometry, the technique does not provide a direct measure of soil dielectric permittivity (i.e., physical property measurement). As discussed above, soil dielectric permittivity measurements can be obtained through velocity analysis of CMP data. Velocity-depth information was obtained through a one-dimension velocity analysis of the CMP data using Reflex Win™ software program. This analysis was done by calculating the semblance statistic for the processed CMP soundings. Using these semblance plots, we determined the NMO velocities and two-way zero-offset traveltimes corresponding to three strong reflections along the vertical soil profile. Successive pairs of NMO velocity and zero-offset traveltime were then

substituted into Equation (8.2) to construct the interval-velocity-depth model. Using Equation (8.1), we were able to infer soil dielectric permittivity from EM wave velocity measurements and evaluate the thermal state of soil water (i.e., differentiate between liquid water and ice).

Table 1 summarizes the large difference between typical frozen soil and unfrozen soil dielectric permittivity and their corresponding EM wave velocity range. Although frozen soil is analogous to dry soil (i.e., they have similar dielectric permittivity ranges), GPR surveys collected immediately prior to freezing conditions and gravimetric soil sampling confirm the presence of very wet soil conditions. Therefore, a progressive increase in EM velocity after initiation of soil freezing would correspond to the transformation of liquid soil water into ice below the soil surface. Using these velocity data, we can also convert the measured reflection profile two-way traveltimes to depth.

8.6 Field Observations

Conditions during the 2007 winter seasonal period at the Woodstock site are well described in terms of a single, long-term freeze and thaw cycle. The daily average temperatures were persistently subzero between 9 January 2007 and 21 March 2007. Temporal GPR data collected at the Woodstock site during this period show the development of a relatively thick, seasonal frost layer and the occurrence of the subsequent infiltration event during the seasonal thaw.

In contrast, a number of short-term (i.e., 1–5 day) mid-season thawing events occurred during the 2008 winter seasonal period at the Waterloo site. The formation of a relatively thin, thawed layer (e.g., layer thickness near or less than the dominant wavelength of GPR) over a frozen substratum gave rise to a dispersive waveguide. Analysis of the dispersed waves yielded estimates of the properties of the unfrozen and frozen layers.

8.6.1 Seasonal Velocity Variations

CMP data collected at the Woodstock site during the 2007 winter seasonal period are shown in Figure 8.3. The CMP soundings (upper series of panels) were analyzed using the semblance statistic (middle series of panels) which was then used to construct an interval-velocity-depth profile (lower series of panels) for each of the soundings. These vertical velocity profiles were derived from three coherent reflection events; the NMO velocity picks corresponding to these reflection events are shown on the semblance plots. The velocities shown on the semblance plots correspond to the upper soil interval.

The initial CMP sounding (Figure 8.3a) was conducted on 13 January 2007 during unfrozen wet soil conditions; gravimetric sampling in the upper 0.5 m of soil yielded a volumetric water content measurement of 0.42 m^3m^{-3}. Although daily average atmospheric temperatures were consistently below zero after 9 January 2007, the seasonal snowpack was not yet developed at this time. The GPR data displays a strong, well-developed low velocity direct ground wave (DGW) consistent with the presence of high liquid soil water content in the vicinity of the ground surface. During this period, the upper soil interval was characterized by a relatively low velocity of 0.0621 m/ns which is consistent with wet unfrozen soil conditions (see Table 8.1).

The CMP sounding collected on 22 January 2007 (Figure 8.3b) was conducted after the formation of a relatively thin (e.g., <0.05 m) snowpack. The occurrence of an attenuated DGW is indicative of the formation of a thin frozen soil layer (i.e., thin relative to dominant GPR wavelength) over an unfrozen substratum (Steelman and Endres, 2009). This inference is supported by a velocity increase to 0.0786 m/ns in the uppermost soil interval which is consistent with the presence of higher velocity frozen soil within this layer.

The CMP sounding acquired on 31 January 2007 (Figure 8.3c) shows the effects of the continued freezing process with the development of a high velocity DGW and a further velocity increase in the upper soil interval to 0.0957 m/ns. This CMP sounding also contains a reflection event at approximately 4 ns noted at 0.2 m antenna offset which corresponds to an approximate depth of 0.24 m; its polarity is consistent with a velocity decrease with depth (e.g., high velocity frozen layer over lower velocity unfrozen substratum). Given its polarity and the associated high velocity in the near-surface, this event is interpreted to be the initial formation of the base of the soil frost zone (BFZ).

The following CMP soundings collected on 20 February 2007 (Figure 8.3d) and 5 March 2007 (Figure 8.3e) both continue to show well-developed high velocity DGW and high velocity conditions in the upper soil interval (i.e., 0.108 m/ns and 0.114 m/ns, respectively). The strong BFZ reflection event in the CMP sounding data remains at an approximate traveltime of 7 ns at 0.2 m antenna offset. This high amplitude event is now readily observed in the semblance plots and shows the BFZ at a depth of 0.40–0.43 m. The snowpack was at its maximum height (e.g., 0.3–0.5 m) during this period.

The CMP sounding done on 21 March 2007 (Figure 8.3f) was conducted at the end of the seasonally sub-zero period and after the seasonal snowpack was completely melted. In addition, an intense short-term overland flow event that covered our site with about 0.5 m of meltwater was observed on 13 March 2007. However, the velocity for the upper soil interval decreased only slightly

(i.e., to 0.102 m/ns), and the BFZ event was still observed at a depth of 0.42 m. Hence, the frozen soil layer had persisted after the seasonal snowpack melt and subsequent overland flow event. The final two CMP soundings collected on 28 March 2007 (Figure 8.3g) and 13 April 2007 (Figure 8.3h) show a return to low velocity conditions (e.g., 0.0641 m/ns) indicative of wet unfrozen soil conditions; corresponding gravimetric sampling in the upper 0.5 m of soil yielded volumetric water contents of 0.45 m^3m^{-3} and 0.42 m^3m^{-3}, respectively.

8.6.2 Spatial Imaging of Freeze-Thaw Process

While CMP soundings can be used to obtain substratum physical properties, they do not provide information about the spatial development of freeze-thaw interfaces because they are localized. In contrast, GPR reflection profiles provide a cross-sectional image of the subsurface. Those profiles corresponding to the CMP soundings discussed above are presented in Figure 8.4. The vertical axis for these profiles has been converted into a depth estimate for the reflecting boundaries using the corresponding interval-velocity data provided in Figure 8.3.

Figure 8.4a shows the reflection profile obtained during the unfrozen soil conditions on 13 January 2007. The strong first arrivals are a superposition of the direct air and DGW. By the time of the profiling on 22 January 2007 (Figure 8.4b), the freezing process had commenced; however, the soil frost front was too shallow to generate a distinct reflection event below the composite first arrival direct air coupling. In this case, the interference between these overlapping events obscures the frost front reflection during shallow phase transition.

The profile of 31 January 2007 (Figure 8.4c) images a discontinuous frost line reflection across the transect at an approximate depth of 0.22–0.24 m. This event correlates with the BFZ reflection noted at 4 ns on the corresponding CMP data (Figure 8.3c). After a substantial period of freezing conditions, the reflection profile of 20 February 2007 (Figure 8.4d) shows a well-developed BFZ reflection event between 0.28–0.40 m across the transect. By 5 March 2007 (Figure 8.4e), the BFZ event continued to 0.38–0.43 m depth and displays a significant increase in amplitude.

The profile of 21 March 2007 (Figure 8.4f) continues to image the BFZ event at 0.28–0.42 m, supporting the CMP sounding results that indicated the continued presence of a frozen surface layer. However, its relative amplitude appears to be slightly diminished compared to the profile of 5 March.

The reflection profile acquired one week later on 28 March 2007 (Figure 8.4g) shows significant changes in reflection character. In particular, the polarity of the strong reflection is opposite to that of

the reflection from the BFZ, and so indicates a reversal in the sense of the electrical properties contrast for this interface (i.e., lower velocity layer overlying relatively higher velocity substratum). We interpret this change to represent an infiltration front associated with the release of liquid water due to the thawing of the near-surface frozen zone. Simply, rapid thawing of the frozen zone had resulted in a comparatively wetter soil zone overlying the seasonally unfrozen substratum. The reflection profile also shows partial dissipation (smearing) of this infiltration front from 4.25 m to 5.0 m positions which illustrates its dynamic spatial response. These results illustrate the ability of GPR to differentiate between a range of soil phase conditions during the course of the winter period. The final reflection profile conducted on 13 April 2007 (Figure 8.4h) shows a return to uniformly thawed conditions similar to those encountered at the start of this sequence on 13 January 2007 (i.e., Figure 8.4a).

8.6.3 Near-Surface Waveguide

During the Waterloo mid-season freeze-thaw cycles, wave dispersion was readily observed in the GPR data. Dispersion means that different pulse frequencies are propagating at different phase velocities (i.e., the transmitted GPR pulse disperses such that its shape smears out with distance). Within these waveguide layers, the internally reflected radar energy produces interfering multiples that appear as a package of dispersed waves. The overall pulse waveform propagates at a group velocity which is also frequency dependent (Arcone et al., 2003; van der Kruk et al., 2006).

Arcone (1984) showed that GPR wave dispersion develops for a thin layer bounded by two reflecting layers (e.g., ice layer bounded by air and water), which propagates as nearly lossless dispersive waves for layer thickness near or less than the in-situ wavelength at velocities that may not correspond to the layer's dielectric properties. Arcone et al. (2003) also showed how dispersive waves develop between two refracting layers.

The thicknesses of our thawed layers were below the resolving power of the reflection profile and CMP velocity analyses. However, the effects of these waveguides are observed in both profiling and CMP data. Analysis of these dispersed modes yields layer thickness and dielectric properties (e.g., van der Kruk et al., 2007). van der Kruk et al. (2009) [Appendix B] demonstrate the dispersion inversion technique for estimating thin frozen and thawed soil properties using 900 MHz CMP data sets.

Figure 8.5 compares profiles collected during seasonally unfrozen (Figure 8.5a), frozen (Figure 8.5b) and during a brief thaw event (Figure 5c); the frozen and thaw profiles were recorded only 15 days apart. Figure 8.5a shows the CMP profile collected during wet unfrozen conditions on 13 November 2007 and is characterized by a low-velocity signal (i.e., 0.102 m/ns) in the upper 0.5 m of soil; gravimetric sampling at this time yielded a volumetric water content measurement of 0.16 m^3m^{-3}. In comparison, Figure 8.5b shows a CMP profile collected on 24 January 2008 at the Waterloo site after a period of prolonged freezing. The profile is characterized by a well-developed high velocity DGW and a high amplitude hyperbolic reflection at approximately 7 ns which yields an NMO velocity of 0.15 m/ns. This significant increase in near-surface velocity relative to wet conditions indicates the formation of a soil frost zone. Sub-zero air temperatures persisted until 5 February 2008, at which time a short-duration thawing period occurred, subsequently followed by a return to sub-zero atmospheric conditions and further snowfall accumulation on 6 and 7 February 2008. The CMP sounding collected on 8 February 2008 (Figure 8.5c) is completely different. It is characterized by dispersive propagation (i.e., dispersive signal), which was commonly observed for 1–5 days following the initiation of surface thawing conditions. The presence of waveguide dispersion in our data set is consistent with a thin thawed layer overlying frozen substratum (van der Kruk et al., 2009). While the semblance plot for this profile is more complex due to the dispersive wavefield, it also suggests a reduction in velocity (i.e., 0.124 m/ns) within the upper soil interval compared to the frozen period, which would indicate thawed soil conditions. However, it should be noted that the measured velocity is dependent on the range of offsets used in the semblance analysis. This is caused by the presence of interfering multiples and indicates that semblance analysis does not provide reliable estimates of shallow waveguide properties (van der Kruk et al., 2010).

Here, we employ the inversion procedure introduced by van der Kruk et al. (2006, 2009) for thin low velocity (thaw) layers overlying higher velocity (frozen) substratum. The inversion procedure involved calculating the phase-velocity spectra (i.e., dispersion curve) which we have assumed to correspond with the fundamental propagation mode. This dispersion curve was then inverted for a single layer model to obtain the relative dielectric permittivity and the thickness of the thawed layer and the dielectric permittivity of the underlying refracting layer (i.e., frozen substratum). The inversion results shown in Figure 8.6 yielded a thawed layer dielectric permittivity and thickness of 10.3 (i.e., v = 0.09 m/ns) and 0.06 m, respectively, and a refracting layer dielectric permittivity of 4.3 (i.e., v = 0.14 m/ns) which is consistent with our measured frozen soil value on Jan 24 (i.e., v = 0.15 m/ns).

The thawing process also produced small-scale heterogeneities that resulted in near-surface scattering which were observed on the reflection profiles in the form of steeply inclined wavefields. Because these scattered waves travel in the shallow thawed waveguide, they also exhibit a dispersive character. Previous field studies by Moorman et al. (2003) and Arcone et al. (2003) noted similar steeply dipping waveguide events within GPR profiles collected across relatively thin shallow thaw zones overlying frozen sediment. Moorman et al. attributed these near-surface events to shallow point source reflectors which they used to delineate small ice lenses; however, they did not note that these events were dispersive in character.

Figure 8.7 shows the reflection profiles corresponding to the CMP surveys collected at the Waterloo site. The profile for 16 November 2007 (Figure 8.7a) was collected during wet unfrozen soil conditions. The profile collected on 24 January 2008 (Figure 8.7b) represents a typical image acquired when a well-developed frozen surface is present. In this profile, we noted the arrival of a high amplitude horizontal reflection that cut across the dipping stratigraphic events between 7 to 9 m positions at approximately 6–8 ns on the traveltime profile; it can be clearly observed that this event was not present on 13 November survey. This strong reflection event can be traced across the entire 1 m to 9 m position range at approximately 7 ns and is at points superimposed over preexisting horizontal stratigraphic reflections. Based on these observations and the measured velocity data from the CMP sounding, this strong reflection event is interpreted to represent the BFZ. At this time, no near-surface scattering is present on the profile.

However, the profile collected on 8 February 2008 (Figure 8.7c) is characterized by numerous near-surface dispersive propagation events. While the BFZ event appears to be laterally continuous, the reflector is somewhat less pronounced (partially due to interfering scattering events) and occurs at a slightly later traveltime (e.g., 9–10 ns) that is consistent with the presence of overlying layer of lower velocity thawed material. Inverse analysis of these scattering events observed during the profiling should yield physical property measurements analogous to that obtained from the CMP soundings and is an objective of our future research.

8.7 Conclusions

While numerous studies have shown GPR to be an effective tool for characterizing glacial and permafrost environments, we used high-frequency GPR to monitor the temporal and spatial development of soil freezing and thawing processes in a temperate climate. Our inference of soil

freezing was based upon the large contrast in dielectric property between liquid water and ice which was readily evident in our GPR measurements.

We observed a significant velocity increase and decrease in the shallow soil zone that was consistent with seasonal freezing (i.e., transformation of liquid water into ice) and thawing (i.e., transformation of ice into liquid water) periods, respectively. These velocity changes were obtained from semblance analysis of CMP profiles that showed strong reflections coming from the frozen/unfrozen interface and the unfrozen/frozen interface. These reflection events were interpreted to represent the thermal interface, i.e., the base of the soil frost and thawing zone. In addition to the CMP data the corresponding reflection profiles enabled us to monitor the spatial distribution of thermal interfaces. While continuous monitoring during the wintertime period showed a relatively stable interface across the reflection profile, differences in reflection amplitude were observed. Surveys conducted after a major surface runoff event showed a persistent soil frost zone, suggesting that the frost zone may have limited the infiltration capacity of the soil during that period. GPR surveys conducted during spring thaw showed a strong reflection event along a portion of the reflection profile which exhibited an opposite polarity compared to the previously observed interface. Also, the CMP velocity indicated a return to pre-frozen soil conditions for this soil zone. These observations indicate the presence of a high liquid water content zone overlying less wet substratum. As a result, we interpreted this interface to represent a spatially dynamic infiltration front.

GPR surveys conducted during a mid-winter thawing period were characterized by dispersive waveguide propagation. An inversion technique yielded physical properties of the thawed and frozen soil. The corresponding reflection profiles showed similar dispersive scattering events associated with shallow heterogeneities along the thawed waveguide layer. Although we used high-frequency GPR to examine thawed waveguides, similar analysis could be conducted using relatively lower antenna frequencies. For example, increasing thawed layer thicknesses would yield dispersive waveforms for comparatively larger signal wavelengths (i.e., decreasing frequencies). Hence, one could evaluate the temporal evolution of a thickening thaw zones using a range of antenna frequencies. Improved inversion results could also be obtained by increasing the antenna offset range, thereby better defining the phase-velocity spectrum of the dispersive waveform.

Although we have demonstrated the capacity of high-frequency GPR for characterizing shallow freeze-thaw processes in temperate climates, further field studies should be conducted with soil temperature and moisture sensors installed along a vertical profile. Such a study would provide a

more detailed evaluation of the affect of water phase transformation on the GPR response, particularly during highly transient periods. Nevertheless, our field study shows the potential of high-frequency GPR for improving ones understanding of overland flow potential and groundwater recharge during these dynamic seasonal periods.

8.8 Tables and Figures

Table 8.1 Reported values of relative dielectric permittivity and EM wave velocity for common geological material within GPR bandwidth. Cassidy (2009).

Material	Dielectric Permittivity, κ	Corresponding Velocity (m/ns)
Air	1	0.3
Freshwater ice	3.2	0.17
Frozen sediment	2–8	0.11–0.21
Soil – sand, dry	3–6	0.12–0.17
Soil – sand, wet	10–30	0.055–0.095
Soil – loamy, dry	4–6	0.12–0.15
Soil – loamy, wet	10–20	0.067–0.095
Water	78 (25˚C)–88 (0˚C)	0.032–0.034

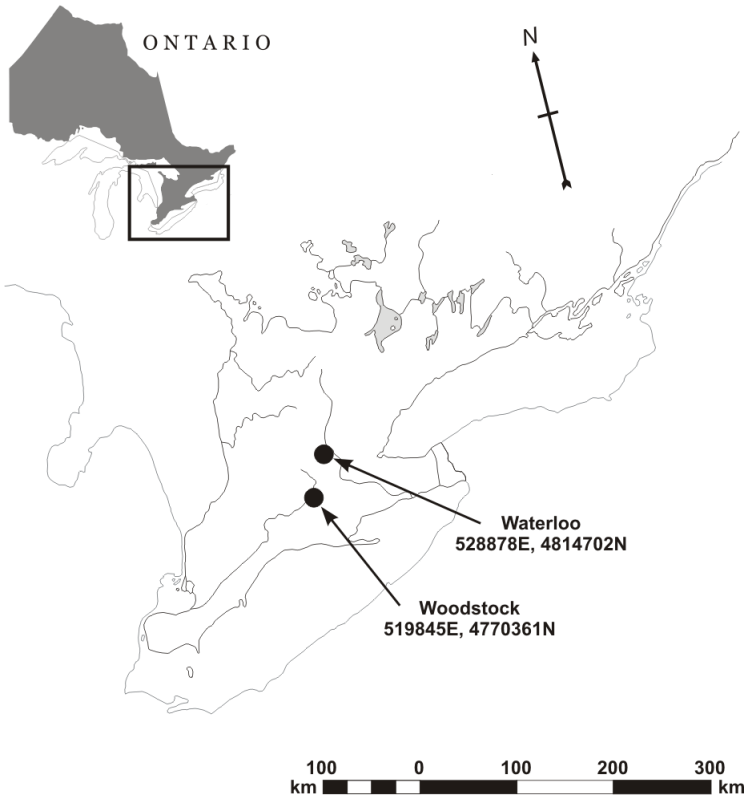

Figure 8.1 Study site locations in southern Ontario, Canada (revised from Natural Resources Canada, 2003).

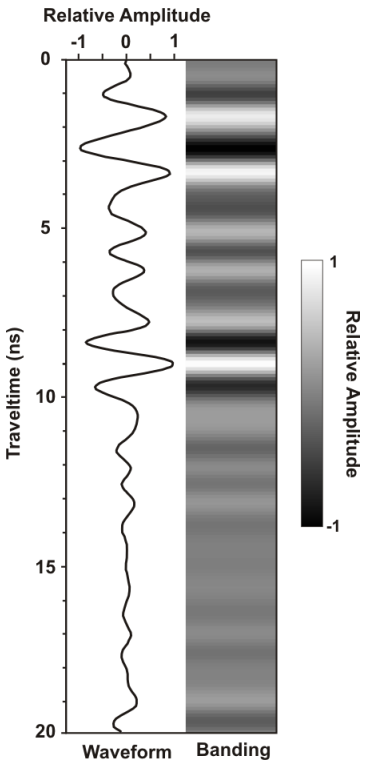

Figure 8.2 Illustration of GPR waveform and equivalent amplitude banding. Positive and negative reflection amplitudes are scaled in white and black, respectively.

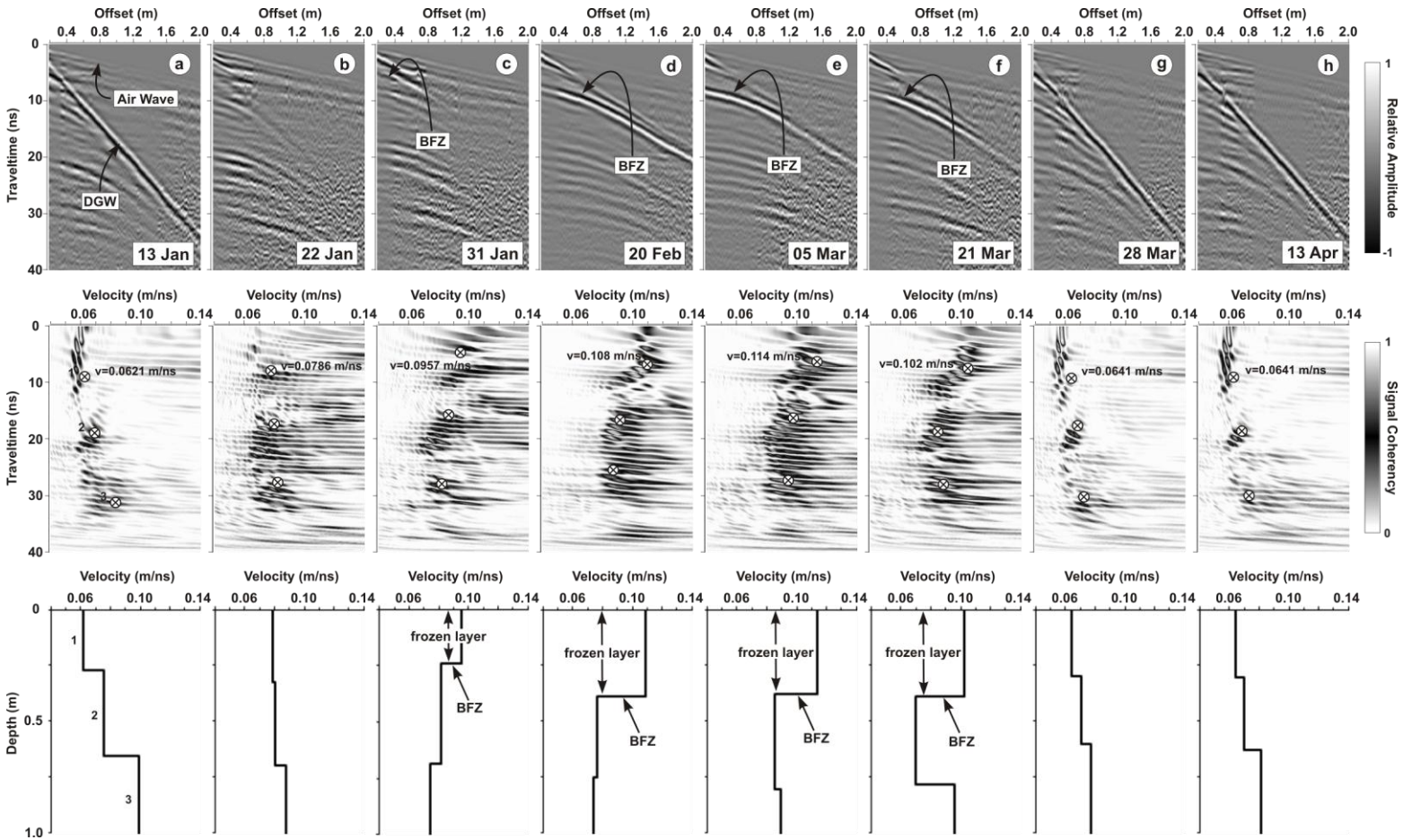

Figure 8.3 CMP soundings (upper series of panels), semblance plots (middle series of panels) and interval velocity models (lower series of panels) obtained at the Woodstock study site during the development of a surficial frozen soil layer and subsequent seasonal thaw. The three NMO velocity picks identified on the semblance plots were used to calculate the interval velocity models. Surveys were conducted on (a) 13 January 2007, (b) 22 January 2007, (c) 31 January 2007, (d) 20 February 2007, (e) 5 March 2007, (f) 21 March 2007, (g) 28 March 2007 and (h) 13 April 2007. The direct ground wave (DGW) and interpreted base of frost zone (BFZ) are identified.

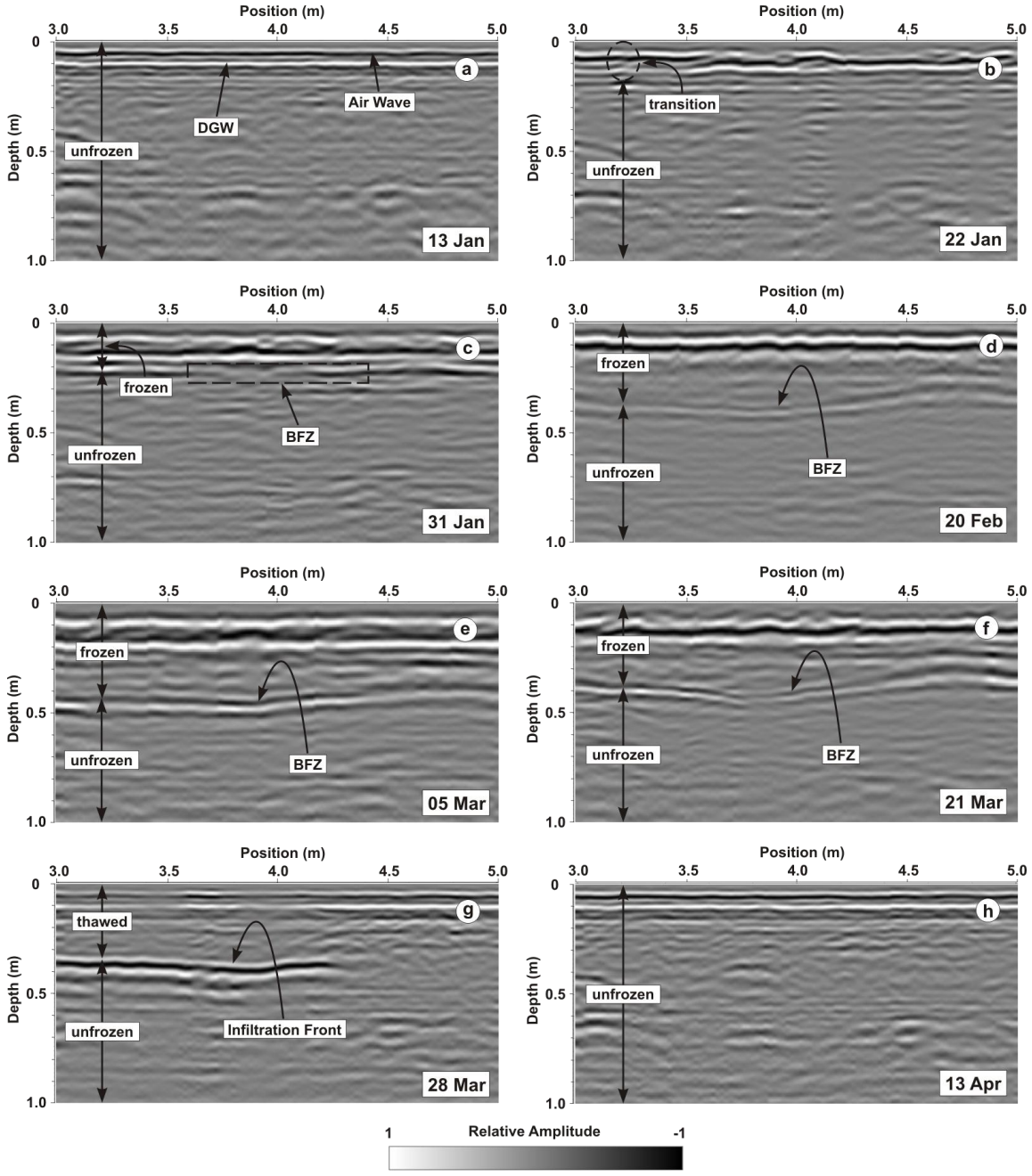

Figure 8.4 Reflection profiles collected at the Woodstock site. Profiles were concurrently collected with the CMP soundings on (a) 13 January 2007, (b) 22 January 2007, (c) 31 January 2007, (d) 20 February 2007, (e) 5 March 2007, (f) 21 March 2007, (g) 28 March 2007 and (h) 13 April 2007. Vertical time axis was converted to depth using the velocity information obtained from CMP velocity analysis.

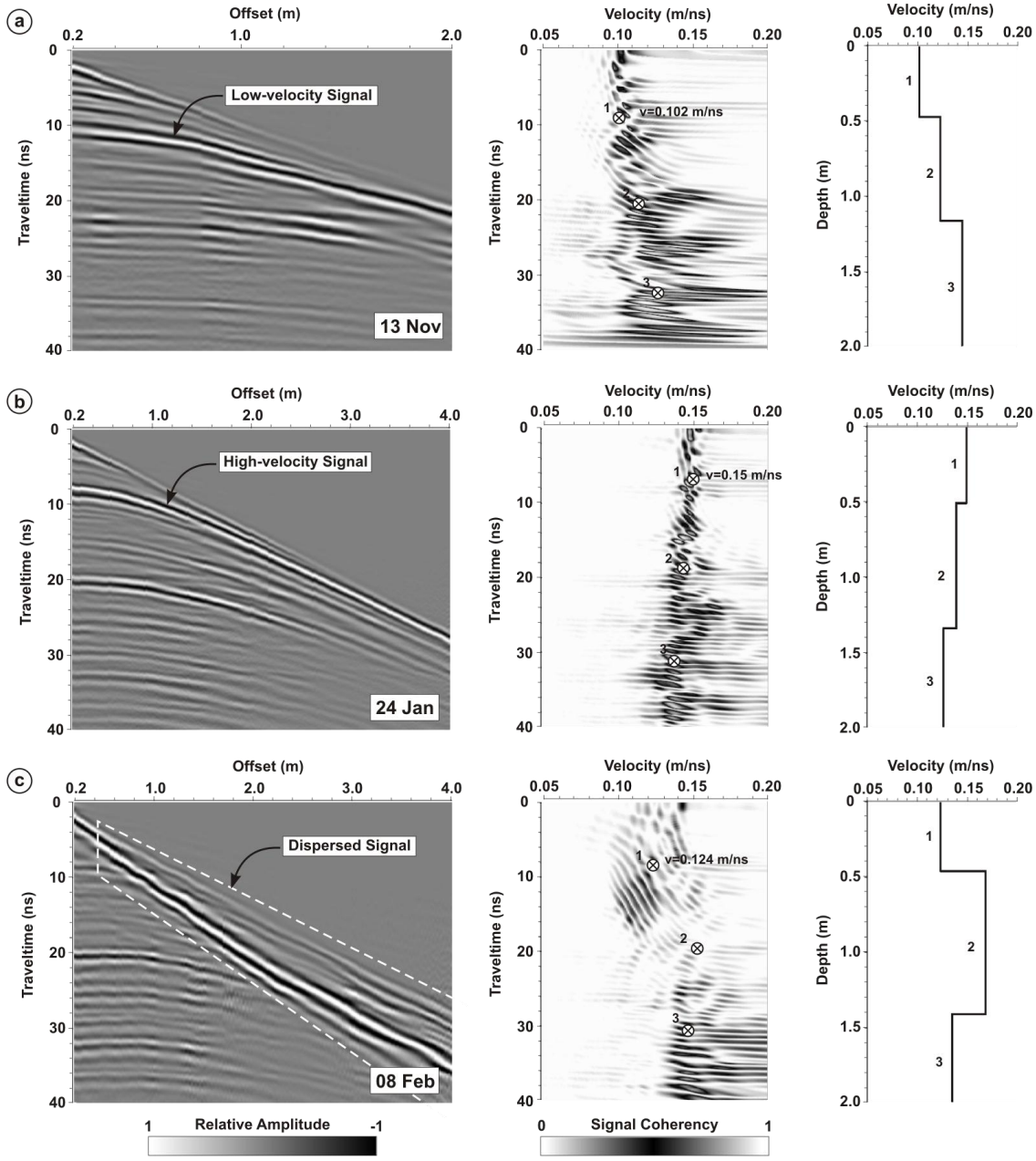

Figure 8.5 CMP soundings collected at the Waterloo site on (a) 13 November 2007 during unfrozen soil conditions, (b) 24 January 2008 during frozen soil conditions and on (c) 8 February 2008 following a mid-seasonal thawing event.

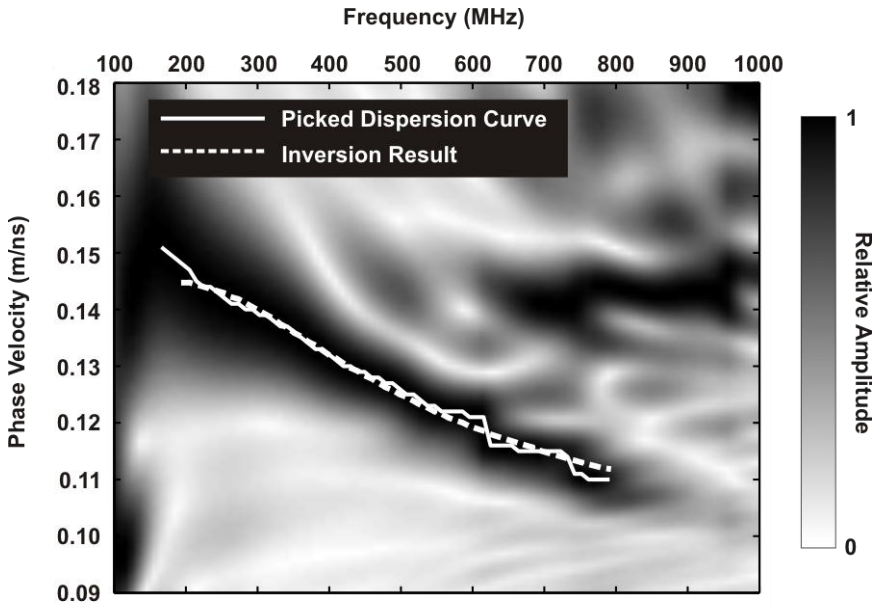

Figure 8.6 Phase velocity spectra of the CMP data collected on 8 February 2008 at the Waterloo site (i.e., Figure 8.5c). The solid line represents the picked dispersion curve while the dotted line is the dispersion curve calculated for the model parameters obtained from the inversion.

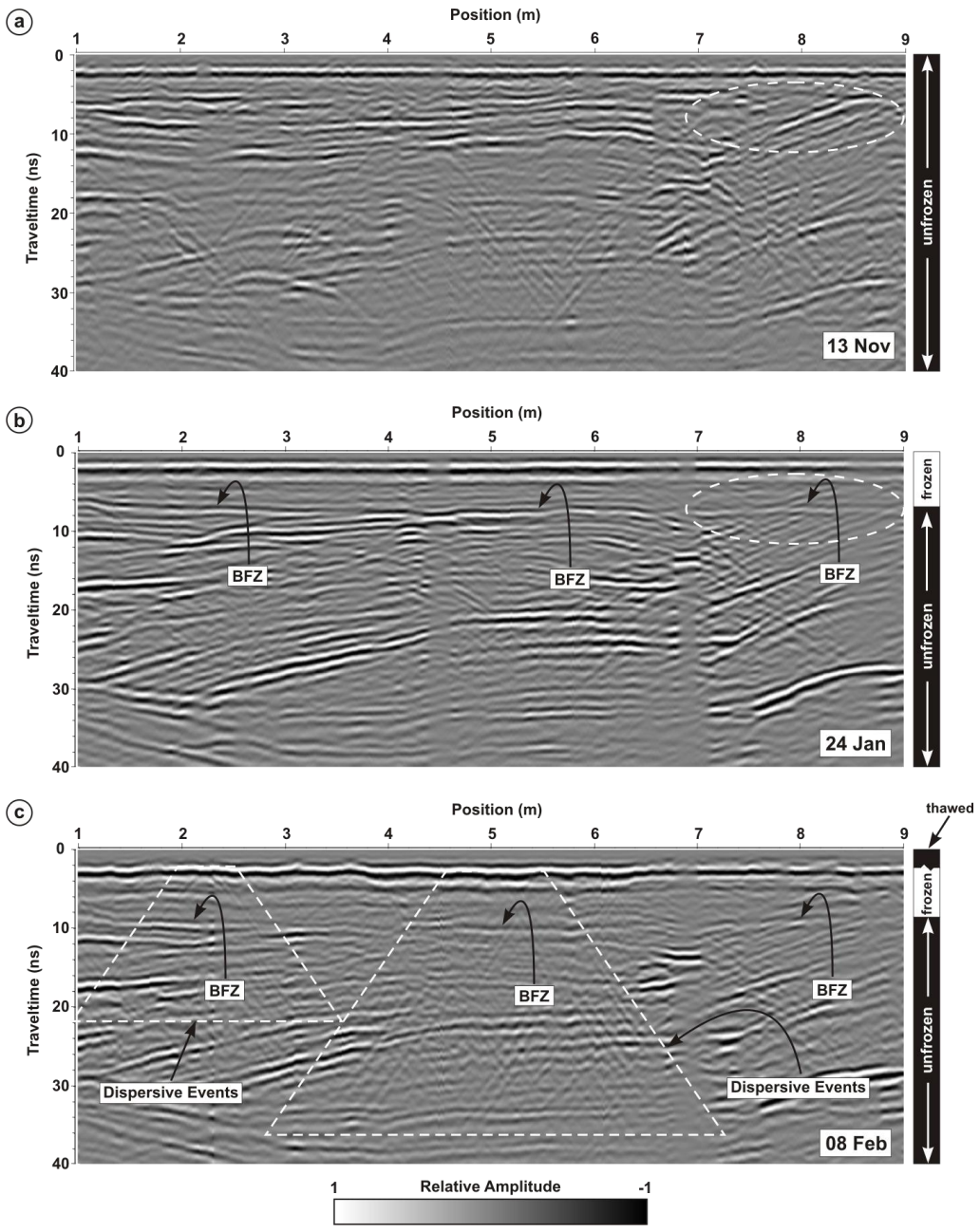

Figure 8.7 Reflection profiles collected at the Waterloo site on (a) 13 November 2007 during unfrozen soil conditions, (b) 24 January 2008 during surficially frozen soil conditions and on (c) 8 February 2008 following a mid-seasonal thawing period.

Chapter 9
Summary and Recommendations

9.1 Summary of Main Contributions

The goal of this thesis was to examine the capacity of surface ground-penetrating radar (GPR) for the characterization of highly dynamic soil moisture processes while developing novel measurement strategies that provide valuable hydrological information about the vadose zone. To achieve this, an exhaustive long-term soil moisture monitoring campaign was initialized at three sites characterized by different soil textural and geomorphological settings. Reflection profiling and common-midpoint (CMP) sounding measurements were concurrently collected at fixed locations using multiple high-frequency antennas (i.e. 225, 450 and 900 MHz). These GPR measurements were performed at intervals ranging from 1 day to 4 weeks over different periods between May 2006 and October 2008 and captured a wide range of naturally occurring soil moisture variations during dry summer, wet autumn and spring, and frozen winter conditions.

A complete description of the hydrologic system hinges on the ability to measure across a range of depth scales. For instance, the highly dynamic nature associated with surface soil conditions requires both high temporal and vertical resolution. The integration of deeper measurements is needed to fully understand the relationship between the soil moisture profile and surface soil conditions. GPR's non-invasive nature and capacity to measure over a range of depth scales makes it highly suited for shallow hydrologic characterization of the vadose zone.

Chapter 2 presented an extensive field study using multi-frequency (i.e., 225 MHz, 450 MHz and 900 MHz) direct ground wave (DGW) measurements to monitor a complete annual cycle of soil water content variations typical of mid-latitude climates at three sites with different soil textures. The use of CMP surveys facilitated interpretation of the near-surface electromagnetic wavefields, and hence, their impact on DGW moisture predictions. The main findings of this chapter were:

- significant temporal variations were observed in both the near-surface wavefield and multi-frequency DGW velocities corresponding to both seasonal and shorter term variations in soil conditions;

- while all of the measurement sites displayed similar temporal responses, the rate and magnitude of these velocity variations corresponded to varying soil water contents which were controlled by the soil textural properties;
- although systematic differences in DGW velocity as a result of frequency dispersion for the 225–900 MHz range was not observed, measurements obtained using higher frequency antennas (i.e., 450 MHz and 900 MHz) were less susceptible to near-surface wavefield interference;
- CMP surveys enabled determination of appropriate antenna offset range for DGW velocity measurements by showing the nature of the interference caused by the superposition of other events, such as the air wave phases and subsurface refractions, upon the DGW event;
- significant variations can occur in the nature of the near-surface electromagnetic wavefields over both long and short time scales that significantly impact the usable range of antenna offsets for DGW velocity determination and corresponding soil moisture estimation.

In Chapter 3, the suitability of different relationships for GPR soil water content estimation were investigated under natural field conditions for a complete range of seasonal soil conditions. Soil volumetric water contents were estimated from the dielectric permittivities derived from the DGW velocities using a range of petrophysical relationships (i.e., empirical relationships, volumetric mixing formulae and effective medium approximations) and compared with values obtained from thermogravimetric sampling. The main findings of this chapter were:

- while a range of antenna frequencies were used (i.e., 225 MHz, 450 MHz and 900 MHz), the lack of frequency dispersion produced very similar results for each frequency analyzed;
- the accuracy of soil water content predictions obtained from the various petrophysical relationships within each category (i.e., empirical relationship, volumetric mixing formulas and effective medium approximation) varied considerably;
- further improvements in water content were obtained using the field calibrated third-order polynomial relationship, based on the GPR permittivity measurements and gravimetric water contents;

- when considering the complete data set, the best fitting empirical relationship (Topp et al., 1980), volumetric mixing formula (Roth et al., 1990) and effective medium approximation (Coated Rock Grain Model) yielded comparable estimates of soil water content.

Chapter 4 presents an extensive field study using multi-frequency (i.e., 225 MHz, 450 MHz, 900 MHz) CMP soundings to monitor a complete annual cycle of soil water contents at three sites. Normal-moveout (NMO) velocity analysis is applied to CMP data to monitor vertical soil moisture dynamics typically observed in mid-latitude climates. This chapter demonstrated the capacity of GPR to characterize seasonal moisture dynamics while highlighting the importance of collecting high resolution data within the upper few meters of vadose zone. The main findings of this chapter were:

- NMO velocity measurements successfully characterized major seasonal trends associated with dry summer, wet spring and autumn, and frozen winter soil conditions;
- interval-velocity determination permitted soil moisture measurements at discrete depth intervals that, when combined with DGW data permitted an examination of the nature of the coupling between surface and deeper moisture conditions during the annual cycle;
- high-frequency 900 MHz antennas yielded the most reliable velocity and water content measurements with respect to depth of investigation and resolving power;
- although the application of CMP soundings permitted simultaneous measurement of surface and deeper soil moisture conditions, comparisons with coincident DGW measurements highlighted the need for better resolution of the very shallow near-surface. This could be achieved by augmenting the NMO velocity profiling process with DGW data obtained from a single CMP sounding.

Chapter 5 presented a 26 month field study in which high-frequency 900 MHz reflection traveltime measurements were used to monitor vertical soil moisture distribution in the upper 3 meters of vadose zone. The monitoring period covered two complete annual cycles of soil moisture variation, including dry summer, wet spring and autumn, and frozen winter soil conditions. Concurrent reflection and CMP soundings were collected on a daily to weekly interval. The reflection profiles provided high resolution traveltime data for four stratigraphic reflection events, while the analysis of the complete CMP sounding data set produced precise depth estimates for those reflecting interfaces. The addition of DGW measurements from the CMP data improved near-surface resolution of short-duration wetting and drying events. The main findings of this chapter were:

- first documented attempt to fully assess the concurrent use of two surface GPR techniques (i.e., reflection profiling and common-midpoint soundings) to characterize vertical soil moisture dynamics within the vadose zone;
- CMP soundings supplied depth information that permitted the determination of interval EM wave velocity, and the subsequent estimation of interval soil moisture;
- cumulative analysis of our complete CMP sounding data set significantly reduced the inherent uncertainty in the depth estimates obtained from individual CMP soundings, which in turn better constrained our moisture estimates;
- downward propagation of major infiltration episodes associated with seasonal (i.e., spring recharge) and transient (i.e., major rainfalls and intra-winter thaws) events were well resolved by the geophysical data;
- DGW measurements from the CMP data, with its better near-surface resolution, allowed a closer examination of the nature of the coupling between surface and deeper soil conditions;
- the combination of water content estimates from the DGW and interval traveltimes will prove useful for quantifying the effects of near-surface phenomena such as evapotranspiration.

Chapter 6 examined the nature of the soil moisture estimates presented in Chapter 5 by comparing the field data with vertical soil moisture flow simulations based on a one-dimensional variably saturated model, HYDRUS-1D. The nature of transient infiltration pulses, evapotranspiration episodes, and deep drainage patterns observed in the GPR data series were examined. The main findings of this chapter were:

- the very good agreement achieved between measured and uncalibrated simulated soil moisture conditions using laboratory derived soil hydraulic property information from soil samples and a number of simplifying assumptions about the system was a strong indication of the overall nature of the GPR-derived soil moisture measurements;
- the important difference between model and GPR water content estimates was the contrast in lower limiting value for the root zone interval during very dry conditions;
- this difference suggests that processes controlling water contents at levels below the residual value obtained from gravitational drainage are not well implemented in HYDRUS-1D;

- while this factor had little impact on the match between model and GPR water contents for the lower intervals, it indicates that inappropriate use of the lower GPR value, particularly from DGW data from the root zone, as the residual water content in a saturation-capillary pressure relationship would significantly impact the extraction of hydrological parameters from models calibrated using GPR data;
- findings indicate that surface-GPR could be a viable soil hydraulic parameter estimation technique if sufficient wetting and drying cycles are observed along the observed profile.

In Chapter 7, high-frequency DGW measurements were used to monitor and evaluate the formation of a shallow frozen soil layer within an active agricultural field. This chapter focused on the propagation characteristics of the DGW during early soil frost development using GPRMAX2D software, and proposed a potential method of inferring a thin frost layer thickness that would otherwise be unattainable without the use of invasive measures. The main findings of this chapter were:

- DGW transmission varied systematically during the early freezing process. In particular, the progressive attenuation of a low velocity direct wave was followed by the gradual development of a high velocity direct wave during the progressive thickening of a seasonal soil frost zone underlain by wet soil;
- numerical results indicate that direct ground wave identification, and the associated direct ground wave velocity estimation would be problematic for frozen layer thicknesses less than one half the in-situ wavelength;
- results indicate that low velocity direct wave event found in the field CMP data after freezing commences was due to energy leaking across the frozen layer from the spherical body wave in the unfrozen half space; this leaky phase was essentially dissipated once the frozen layer reaches a thickness equivalent to one quarter of the dominant in-situ wavelength;
- the appearance of the high velocity direct wave was governed by destructive interference with the superimposed primary and multiple reflection events from the base of the frozen layer. This interference obscured the high velocity direct wave event until the frozen layer thickness reached one half of the dominant in-situ wavelength;

In Chapter 8, reflection profiles and CMP soundings with 900 MHz antennas were used to monitor temporal and spatial development of soil freezing and thawing processes in a temperate climate. This chapter showed that GPR can be used to monitor very shallow freezing and thawing events by responding to changes in the relative dielectric permittivity of the soil water phase (e.g., liquid water verses ice). The non-invasive collection of such data permitted interpretation of dynamic temporal and spatial freeze-thaw events which was important for characterizing a range of seasonal hydrological processes. The main findings of this chapter were:

- reflection profiles revealed the long-term development of a very shallow (<0.5 m) soil frost zone overlying unfrozen wet substratum; long-term traveltime analysis yielded physical properties of the frozen and unfrozen layers as well as the spatial distribution of the base of the soil frost zone;
- surveys conducted after a major surface runoff event showed a persistent soil frost zone, suggesting that the frost zone may have limited the infiltration capacity of the soil during that period;
- GPR surveys conducted during spring thaw showed a strong reflection event along a portion of the reflection profile which exhibited an opposite polarity compared to the previously observed interface. Also, the CMP velocity indicated a return to pre-frozen soil conditions for this soil zone. These observations indicate the presence of a high liquid water content zone overlying less wet substratum; as a result, the reflection interface was interpreted to represent a spatially dynamic infiltration front;
- short-term shallow thawing events overlying frozen substratum formed a dispersive waveguide for both the CMP and reflection profile surveys. Inversion of the dispersive wavefields for the CMP data yielded physical property estimates for the thawed and frozen soils and thawed layer thickness.

The main findings of this thesis have established the effectiveness of high-frequency GPR as a non-invasive soil moisture monitoring tool under a full range of naturally occurring moisture conditions with the temporal and vertical resolution necessary to examine vadose zone dynamics. Because this study encompassed a wide range of naturally occurring soil conditions including numerous short and long duration wetting/drying and freezing/thawing cycles, unique geophysical responses were observed during highly dynamic soil moisture processes. Interpretation of these geophysical

responses was shown to yield both qualitative and quantitative information about the state of the hydrologic system in the upper vadose zone. The results of this thesis will have immediate implications to future hydrogeophysical investigations in vadose zone environments.

9.2 Recommendations for Future Studies

While these works provided valuable contributions to the hydrogeophysical field, additional investigations will be necessary to fully appreciate their contribution to the scientific community. In particular, the assimilation of soil moisture information obtained from surface GPR measurements into advanced land-surface hydrological models should be considered. An important component of this work will involve the integration of highly dynamic freeze and thaw processes that occur during wintertime conditions. A summary of main recommendations for future studies is provided below:

- GPR soil moisture monitoring methodologies/strategies considered in this thesis should be integrated into larger-scale hydrological studies, i.e., for both field calibration and validation of hydrological models. This should involve the integration of seasonal soil moisture distribution and dynamics, and freeze and thaw processes derived from GPR measurements;
- conduct numerical modeling study of longer-period freeze-thaw cycles (i.e., temporal evolution of thermal interface) based on current GPR observations to better understand the role of the seasonal frost zone in vadose zone hydrological processes, and incorporate this information into land-surface hydrologic models;
- conduct an instrumented field study using thermistors and auxiliary water content measurements during wintertime period to better characterize shallow thermodynamic processes (i.e., freeze-thaw cycles), and better understand the physical mechanisms controlling the observed GPR response. This would further validate the inverse solution of the dispersive wavefields observed in CMP sounding data and common-offset reflection profiles as a result of freezing and thawing soil waveguides;
- examine the relationship between DGW amplitude (i.e., CMP and reflection profiling data sets) and volumetric water content at the three sites;
- examination the sensitivity of NMO interval-velocity measurements to varying site conditions including the effects of vertical velocity gradient, semblance resolution, and antenna frequency to better understand uncertainties in measured velocity;

- develop inverse solution for common-offset reflection dispersion data observed during shallow surface thawing for spatial characterization of shallow frozen and thawed soil layer properties;
- examine potential field-scale inverse parameter estimation techniques using multi-year surface-based GPR soil moisture data set.

References

Alumbaugh, D., Chang, P.Y., Paprocki, L., Brainard, J.R., Glass, R.J., and Rautman, C.A. (2002). Estimating moisture contents in the vadose zone using cross-borehole ground penetrating radar: a study of accuracy and repeatability. *Water Resources Research, 38*, 1309, doi:10.1029/1002WR000754.

Annan, A.P. (1973). Radio interferometry depth sounding: part 1 – theoretical discussion. *Geophys*ics, *38*, 557–580.

Annan, A.P. (2005). Ground-Penetrating Radar. In D.K. Butler, (Ed.), *Near-Surface Geophysics*, (pp. 357–438). Tulsa (OK): Society of Exploration Geophysicists.

Annan, A.P., and Davis, J.L. (1978). High frequency electrical methods for the detection of freeze-thaw interfaces. In *Proceedings of the Third International Conference on Permafrost*, 1, 495–500.

Arcone, S.A. (1984). Field observations of electromagnetic pulse propagation in dielectric slabs. *Geophysics, 49*, 1763–1773.

Arcone, S.A., Lawson, D.E., Delaney, A.J., Strasser, J.C., and Strasser, J.D. (1998). Ground-penetrating radar reflection profiling of groundwater and bedrock in an area of discontinuous permafrost. *Geophysics, 63*, 1573–1584.

Arcone, S.A., Peapples, P.R., and Liu, L. (2003). Propagation of a ground-penetrating radar (GPR) pulse in a thin-surface waveguide. *Geophysics, 68*, 1922–1933.

Bajc, A.F, Endres, A.L., Hunter, J.A., Pullan, S.E, and Shirota, J. (2004). Three-dimensional mapping of quaternary deposits in the Waterloo Region, southwestern Ontario. In R.C. Berg, H.A.J. Russell, L.H. Thorleifson, (Eds.). *Three-Dimensional Mapping for Geological Applications Workshops* (pp. 12–15). Illinois State Geological Survey, Open File Series 2004-8, St. Catharines, Ontario, Canada, Associated with the 2004 Geological Association of Canada Meeting.

Barrett, B.E., Murray, T., and Clark, R. (2007). Errors in radar CMP velocity estimates due to survey geometry, and their implication for ice water content estimation. *Journal of Environmental Engineering Geophysics, 12*, 101–111.

Bayard, D., Stähli, M., Parriaux, A., and Flühler, H. (2005). The influence of seasonally frozen soil on the snowmelt runoff at two Alpine sited in southern Switzerland. *Journal of Hydrol*ogy, *309*, 66–84, doi: 10.1016/j.jhydrol.2004.11.012.

Becht, A., Appel, E., and Dietrich, P. (2006). Analysis of multi-offset GPR data: a case study in a coarse-grained gravel aquifer. *Near Surface Geophysics, 4*, 227–240.

Birchak J.R., Gardner, C.G., Hipp, J.E. and Victor J.M. (1974). High dielectric constant microwave probes for sensing soil moisture. *Proceedings of the IEEE, 62*, 93–98.

Bohidar, R.N., and Hermance, J.F. (2002). The GPR refraction method. *Geophysics, 67*, 1474–1485.

Booth, A.D., Clark, R., and Murray, T. (2010). Semblance response to a ground-penetrating radar wavelet and resulting errors in velocity analysis. *Near Surface Geophysics, 8*, 235–246.

Booth, A. D., Clark, R.A., and Murray, T. (2011). Influences on the resolution of GPR velocity analyses and a Monte Carlo simulation for establishing velocity precision. *Near Surface Geophysics, 9*, 399–411, doi:10.3997/1873-0604.2011019.

Brooks, R. H., and Corey, A.T. (1964). Hydraulic properties of porous media. Hydrogeology Papers, Colorado State University, Fort Collins, CO.

Brovelli, A., and Cassiani, G. (2008). Effective permittivity of porous media: a critical analysis of the complex refractive index model. *Geophysical Prospecting, 56*, 715–727, doi: 10.111/j.1365-2478.2008.00724x.

Cassiani, C., and Binley, A. (2005). Modeling unsaturated flow in a layered formation under quasi-steady state conditions using geophysical data constraints. *Advances in Water Resources, 28*, 467–477, doi:10.1016/j.advwatres.2004.12.007.

Cassiani, G., Giustiniani, M., Ferraris, S., Deiana, R., and Strobbia, C. (2009). Time-lapse surface-to-surface GPR measurements to monitor a controlled infiltration experiment. *Boll. Geof. Teor. Appl., 50*, 209–226.

Cassidy, N.J. (2009). Electrical and Magnetic Properties of Rocks, Soils and Fluids. In H.M. Jol, (Ed.), *Ground Penetrating Radar: Theory and Applications* (pp. 41–72). Amsterdam: Elsevier.

Castle, R.J. (1994). A theory of normal moveout. *Geophysics, 59*, 983–999.

Chen, Y., and Or, D. (2006). Geometrical factors and interfacial processes affecting complex dielectric permittivity of partially saturated porous media. *Water Resources Research, 42,* W06423, doi: 10.1029/2005WR004744.

Cosenza, P., Camerlynck, C., and Tabbagh, A. (2003). Differential effective medium schemes for investigating the relationship between high-frequency relative dielectric permittivity and water content of soil. *Water Resources Research, 42*, 1230, doi: 10.1029/2002WR001774.

Cowan, W.R. (1975). Quaternary geology of the Woodstock area. Southern Ontario. Ontario. Ministry of Natural Resources, Division of Mines..

Curtis, J.O. (2001). Moisture effects on the dielectric properties of soils. *IEEE Transaction on Geoscience and Remote Sensing, 39*, 125–128.

Davis, J.L., and Annan, A.P. (1989). Ground-penetrating radar for high-resolution mapping of soil and rock stratigraphy. *Geophysical Prospecting, 37*, 531–551.

Dean, T.J., Bell, J.P., and Baty, A.J.B. (1987). Soil moisture measurement by an improved capacitance technique, part I. sensor design and performance. *Journal of Hydrology, 98*, 67–78.

Dean, Jr. W.E. (1974). Determination of carbonate and organic matter in calcareous sediments and sedimentary rocks by loss on ignition: comparison with other methods. *Journal of Sedimentary Petrology, 44*, 242–248.

Deiana, R., Cassiani, G., Kemna, A., Villa, A., Bruno, V., and Bagliani, A. (2007). An experiment of non-invasive characterization of the vadose zone via water injection and cross-hole time lapse geophysical monitoring. *Near Surface Geophysics, 5*, 183–194.

Delaney, A.J., Arcone, S.A., Chacho Jr. E.F. (1990). Winter short-pulse studies on the Tanana River, Alaska. *Arctic, 43*, 244–250.

De Pascale, G.P., Pollard, W.H., and Williams, K.K. (2008). Geophysical mapping of ground ice using a combination of capacitive coupled resistivity and ground-penetrating radar, Northwest Territories, Canada. *Journal of Geophysical Research, 113*, F02S90. doi: 10.1029/2006JF000585.

Dix, C. H. (1955). Seismic velocities from surface measurements. *Geophysics, 20*, 68–86.

Dobson, M.C., Ulaby, F.T., Hallikainen, M.T., and El-Rayes M.A. (1985). Microwave dielectric behavior of wet soils, II dielectric mixing models. *IEEE Transactions on Geoscience and Remote Sensing, GE-23*, 35–46.

Du, S. (1996). Determination of water content in the subsurface with the ground wave of ground penetrating radar. Ph.D. thesis, Ludwig Maximilians Universität, Munich.

Ellis, D.V. (1987). *Well Logging for Earth Scientist.* New York: Elsevier.

Environment Canada. "National Climate Data and Information Archive – Canadian Climate Normals, 1971 – 2000". 2008-11-01, 2009-04-27 <http://www.climate.weatheroffice.ec.gc.ca/climate_normals/index_e.html>

Endres, A.L., and Bertrand, E.A. (2006). A pore-size scale model for the dielectric properties of water-saturated clean rocks and soils. *Geophysics, 71*, F185–F193, doi: 10.1190/1.2360192.

Endres, A.L., and Redman, J.D. (1996). Modelling the electrical properties of porous rocks and soil containing immiscible contaminants. *Journal of Environmental and Engineering Geophysics, 0*, 105–112.

Feddes, R.A., Bresler, E., and Neuman, S.P. (1974). Field test of a modified numerical model for water uptake by root systems. *Water Resources Research, 10*, 1199–1206.

Feng, S., and Sen P.N. (1985). Geometrical model of conductive and dielectric properties of partially saturated rocks. *Journal of Applied Physics, 58*, 3236–3243.

Food and Agricultural Organization of the United Nations (1990). Expert consultation on revision of FAO methodologies for crop water requirements. ANNEX V, FAO Penman-Monteith Formula, Rome, Italy.

Francesca, V., Osvaldo, F., Stefano, P., and Paola, R.P. (2010). Soil moisture measurements: comparison of instrumentation performances. *Journal of Irrigation and Drainage Engineering, 136*, 81–89.

Friedman, S.P. (1998). A saturation degree-dependent composite spheres model for describing the dielectric constant of unsaturated porous media. *Water Resources Research, 34*, 2949–2961.

Garambois S., Senechal, P., Perroud, H. (2002). On the use of combined geophysical methods to assess water content and water conductivity of the near surface. *Journal of Hydrology, 259*, 32–48.

Galagedara, L.W., Parkin, G.W., and Redman, J.D. (2003). An analysis of the ground-penetrating radar direct ground wave method for soil water content measurement. *Hydrological Processes, 17*, 3615–3628.

Galagedara, L.W., Parkin, G.W., Redman, J.D., von Bertoldi, P., and Endres, A.L. (2005a). Field studies of the GPR ground wave method for estimating soil water content during irrigation and drainage. *Journal of Hydrol*ogy, *301*, 182–197.

Galagedara, L.W., Redman, J.D., Parkin, G.W., Annan, A.P., and Endres, A.L. (2005b). Numerical modeling of GPR to determine the direct ground wave sampling depth. *Vadose Zone Journal, 4*, 1096–1106.

Gardner, C.M.K., Dean, T.J., and Cooper, J.D. (1998). Soil water content measurement with a high-frequency capacitance sensor. *Journal of Agricultural Engineering Research, 71*, 395–403.

Gerhards, H., Wollschläger, U., Yu, Q., Schiwek, P., Pan, X., and Roth, K. (2008). Continuous and simultaneous measurement of reflector depth and average soil-water content with multichannel ground-penetrating radar. *Geophysics, 73*, J15–J23.

Giannopoulos, A. (2005). Electromagnetic simulator for ground probing radar. GPRMAX2D version 2.0, User's Manual, University of Edinburgh, Scotland.

Greaves, R.J., Lesmes, D.P., Lee, J.M., and Toksöz, M.N. (1996). Velocity variations and water content estimation from multi-offset, ground-penetrating radar. *Geophysics, 61*, 683–695.

Grote, K., Hubbard, S., and Rubin, Y. (2003). Field-scale estimation of volumetric water content using ground-penetrating radar ground wave techniques. *Water Resources Research, 39*, 1321, doi:10.1029/2003WR002045.

Grote, K., Anger, C., Kelly, B., Hubbard, S., and Rubin, Y. (2010a). Characterization of soil water content variability and soil texture using GPR groundwave techniques. *Journal of Environmental and Engineering Geophysics, 15*, 93–110.

Grote, K., Crist, T., and Nickel, C. (2010b). Experimental estimation of the GPR groundwave sampling depth. *Water Resources Research, 46*, W10520, doi:10.1029/2009WR008403.

Grote, K., Hubbard, S., Harvey, J., and Rubin, Y. (2005). Evaluation of infiltration in layered pavements using surface GPR reflection techniques. *Journal of Applied Geophysics, 57*, 129–153, doi:10.1016/j.jappgeo.2004.10.002.

Haarder, E.B., Looms, M.C., Jensen, K.H., and Nielsen, L. (2011). Visualizing unsaturated flow phenomena using high-resolution reflection ground penetrating radar. *Vadose Zone Journal, 10*, 84–97, doi: 10.2136/vzj2009.0188.

Hagedoorn, J. (1954). A process of seismic reflection interpretation. *Geophysical Prospecting, 2*, 85–127.

Hajnal, Z., and Sereda, I.T. (1981). Maximum uncertainty of interval velocity estimates. *Geophysics, 46*, 1543–1547.

Hardy, J.P., Groffman, P.M., Fitzhugh, R.D., Henry, K.S., Welman, A.T., Demers, J.D., Fahey, T.J., Driscoll, C.T., Tierney, G.L., and Nolan, S. (2001). Snow depth manipulation and its influence on soil frost and water dynamics in a northern hardwood forest. *Biogeochemistry, 56*, 151–174.

Hayhoe, H.N., and Bailey, W.G. (1985). Monitoring changes in total and unfrozen water content in seasonally frozen soil using time domain reflectometry and neutron moderation techniques. *Water Resources Research, 21*, 1077–1084.

Heimovaara, T.J., Bouten, W. and Verstraten, J.M. (1994). Frequency domain analysis of time-domain reflectometry waveforms, 2. A four component complex dielectric mixing model for soils. *Water Resources Research, 30*, 201–209.

Henry, H.A.L. (2007). Soil freeze–thaw cycle experiments: trends, methodological weaknesses and suggested improvements. *Soil Biology and Biochemistry, 39*, 977–986, doi:10.1016/j.soilbio.2006.11.017.

Hinkel, K.M, Doolittle, J.A., Bockheim, J.G., Nelson, F.E., Paetzold, R., Kimble, J.M., and Travis, R. (2001). Detection of subsurface permafrost features with ground-penetrating radar, Barrow, Alaska. *Permafrost and Periglacial Processes, 12*, 179–190, doi: 10.1002/ppp.369.

Hubbard, S., Grote, K., and Rubin, Y. (2002). Mapping the volumetric soil water content of a California vineyard using high-frequency GPR ground wave data. *The Leading Edge*, *25*, 552–559.

Huisman, J.A., Hubbard, S.S., Redman, J.D., and Annan, A.P. (2003a). Measuring soil water content with ground penetrating radar: a review. *Vadose Zone Journal, 2*, 476–491.

Huisman, J.A., Snepvangers, J.J.J.C., Bouten, W., and Heuvelink, G.B.M. (2002). Mapping spatial variations in surface soil water content: comparison of ground-penetrating radar and time domain reflectometry. *Journal of Hydrology, 269*, 194–207.

Huisman, J.A., Snepvangers, J.J.J.C., Bouten, W., and Heuvelink, G.B.M. (2003b). Monitoring temporal development of spatial soil water content variation: comparison of ground penetrating radar and time domain reflectometry. *Vadose Zone Journal, 2*, 519–529.

Huisman, J.A., Sperl, C., Bouten, W., and Verstraten, J.M. (2001). Soil water content measurements at different scales: accuracy of time domain reflectometry and ground-penetrating radar. *Journal of Hydrol*ogy, *245*, 48–58.

Iwata, Y., Hirota, T., Hayashi, M., Suzuki, S., and Hasegawa, S. (2010). Effects of frozen soil and snow cover on cold-season soil water dynamics in Tokachi, Japan. *Hydrological Processes, 24*, 175–1765. doi: 10.1002/hyp.7621.

Jacob, R.W. and Hermance, J.F. (2004). Assessing the precision of GPR velocity and vertical two-way traveltime estimates. *Journal of Environmental and Engineering Geophysics*, *9*, 143–153.

Jacobsen, O.H., and Schjønning, P. (1993a). A laboratory calibration of time domain reflectometry for soil water measurements including effects of bulk density and texture. *Journal of Hydrology, 151*, 147–157.

Jacobsen, O.H., and Schjønning, P. (1993b). Field evaluation of time domain reflectometry for soil water measurements. *Journal of Hydrology, 151*, 159–172.

Johnsson, H., and Lundin, L.C. (1991). Surface runoff and soil water percolation as affected by snow and soil frost. *Journal of Hydrology*, *122*, 141–159.

Jones, S.B., and Friedman, S.P. (2000). Particle shape effects on the effective permittivity of anisotropic or isotropic media consisting of aligned or randomly oriented ellipsoidal particles. *Water Resources Research*, *36*, 2821–2833.

Jol, H.M., (Ed.). (2009). *Ground Penetrating Radar: Theory and Applications*. Amsterdam: Elsevier.

Jones, S.B., Wraith, J.M., and Or, D. (2002). Time domain reflectometry measurement principles and applications. *Hydrological Processes*, *16*, 141–153, doi: 10.1002/hyp.513.

Kenyon, W.E. (1984). Texture effects on megahertz dielectric properties of calcite rock samples. *Journal of Applied Physics*, *55*, 3153–3159.

Kneisel, C., Hauck, C., Fortier, R., and Moorman, B. (2008). Advances in geophysical methods for permafrost investigations. *Permafrost and Periglacial Processes*, *19*, 157–178.

Kowalsky, M.B., Finsterle, S., and Rubin, Y. (2004). Estimating flow parameter distribution using ground-penetrating radar and hydrological measurements during transient flow in the vadose zone. *Advances in Water Resources*, *27*, 583–599, doi:10.1016/j.advwatres.2004.03.03.

Lambot, S., Slob, E., Chavarro, D., Lubczynski, M., and Vereecken, H. (2008). Measuring soil surface water content in irrigated areas of southern Tunisia using full-waveform inversion of proximal GPR data. *Near Surface Geophysics, 6,* 403–410.

Lambot, S., Slob, E.C., van den Bosch, I., Stockbroeckx, B., and Vanclooster, M. (2004). Modeling of ground-penetrating radar for accurate characterization of subsurface electric properties. *IEEE Transactions on Geoscience and Remote Sensing, 42,* 2555–2568.

Lichtenecker, K., and Rother, K. (1931). Die herleitung des logarithmischen mischungsgesetzes aus allgemeinen prinzipien der stätionaren strömung. *Physikalische Zeitchrift, 32,* 255–260.

Liu, L., and Arcone, S.A. (2003). Numerical simulation of the wave-guide effect of the near-surface thin layer on radar wave propagation. *Journal Environmental Engineering Geophysics, 8,* 133–141.

Loeffler, O., and Bano M. (2004). Ground penetrating radar measurements in a controlled vadose zone: Influence of the water content. *Vadose Zone Journal, 3,* 1082–1092.

Lunt, I.A., Hubbard, S.S., and Rubin, U. (2005). Soil moisture estimation using ground-penetrating radar reflection data. *Journal of Hydrology, 307,* 254–269.

Luo, L.F., et al. (2003). Effects of frozen soil on soil temperature, spring infiltration, and runoff: results from the PILPS 2(d) experiment at Valdai, Russia. *Journal of Hydrometeorology, 4,* 334–351, doi:10.1175/1525-7541(2003)4<334:EOFSOS>2.0.CO;2.

Malicki, M.A., Plagge, R., and Roth, C.H. (1996). Improving the calibration of dielectric TDR soil moisture determination taking into account the solid soil. *European Journal of Soil Science, 47,* 357–366.

Moorman B.J., Robinson, S.D., and Burgess, M.M. (2003). Imaging periglacial conditions with ground-penetrating radar. *Permafrost and Periglacial Processes, 14,* 319–329, doi: 10.1002/ppp.463.

Moysey, S.M.J. (2010). Hydraulic trajectories in transient ground-penetrating-radar reflection data. *Geophysics, 75,* WA211–WA219, doi:10.1190/1.3463416.

Murray, T., Booth, A., Rippin, D.M. (2007). Water-content of glacier-ice: limitations on estimates from velocity analysis of surface ground-penetrating radar surveys. *Journal of Environmental Engineering and Geophysics, 12,* 87–99.

Nadler, A., Dasberg, S., and Lapid, I. (1991). Time domain reflectometry measurements of water content and electrical conductivity of layered soil columns. *Soil Science Society of America Journal, 55,* 938–943.

Natural Resources Canada, "The Atlas of Canada – Ontario", 2003-03-14, 2009-05-01 <http://atlas.nrcan.gc.ca/site/english/maps/reference/outlineprov_terr/ont_outline>

Neal, A. (2004). Ground-penetrating radar and its use in sedimentology: principles, problems and progress. *Earth Science Reviews, 66,* 261–330.

Neidell, N.S., Taner, M.T. (1971). Semblance and other coherency measures for multichannel data. *Geophysics, 36,* 482–497.

Norris, A.N., Callegari, A.J., and Sheng, P. (1985). A generalized differential effective medium theory. *Journal of Mechanics and Physics of Solids, 33,* 525–543.

Nyberg, L., Stähli, M., Mellander, P-E, and Bishop, K.H. (2001). Soil frost effects on soil water and runoff dynamics along a boreal forest transect: 1. field investigations. *Hydrological Processes, 15*, 909–926, doi: 10.1002/hyp.256.

Patterson, D.E., and Smith, M.W. (1980). The use of time domain reflectometry for the measurement of unfrozen water content in frozen soils. *Cold Regions Science and Technology, 3*, 205–210.

Patterson, D. E., and Smith, M.W. (1981). The measurement of unfrozen water content by time domain reflectometry: results from laboratory tests. *Canadian Geotechnical Journal, 18*, 131–144.

Ponizovsky, A.A., Chudinova, S.M., and Pachepsky, Y.A. (1999). Performance of TDR calibration models as affected by soil texture. *Journal of Hydrology, 218*, 35–43.

Radzevicius, S., Chen, C-C., Peters, L., and Daniels, J.J. (2003). Near-field dipole radiation dynamics through FDTD modeling. *Journal of Applied Geophysics, 52*, 75–92, doi:10.1016/S0926-9851(02)00241-0.

Ritchie, J.T. (1972). Model for predicting evaporation from a row crop with incomplete cover. *Water Resources Research, 8*, 1204–1213.

Robinson, D.A., Campbell, C.S., Hopmans, J.W., Hornbuckle, B.K, Jones, S.B., Knight, R., Ogden, F., Selker, J., and Wendroth, O. (2008). Soil moisture measurement for ecological and hydrological watershed-scale observatories: a review. *Vadose Zone Journal, 7*, 358–389, doi:10.2136/vzj2007.0143.

Robinson, D.A., Gardner, C.M.K., and Cooper, J.D. (1999). Measurement of relative permittivity in sandy soils using TDR, capacitance and theta probes: comparison, including the effects of bulk soil electrical conductivity. *Journal of Hydrology, 223*, 198–211.

Robinson, D.A., Jones, S.B., Wraith, J.M., Or, D., and Friedman, S.P. (2003). A review of advances in dielectric and electrical conductivity measurement in soils using time domain reflectometry. *Vadose Zone Journal, 2*, 444–475.

Roth, K., Schulin, R., Flühler, H., and Attinger, W. (1990). Calibration of time domain reflectometry for water content measurements using a composite dielectric approach. *Water Resources Research, 26*, 2267–2273.

Roth, C.H., Malicki, M.A., and Plagge, R. (1992). Empirical evaluation of the relationship between soil dielectric constant and volumetric water content as the basis for calibrating soil moisture measurements by TDR. *Journal of Soil Science, 43*, 1–13.

Russell, H.A.J., Sharpe, D.R., and Bajc, A.F. (2007). Sedimentary signatures of the Waterloo Moraine, Ontario, Canada. In M.J. Hambrey, P. Christoffersen, N.F. Glasser, and B. Hubbard (Eds.), *Glacial Sedimentary Processes and Products* (pp. 85–108), Special Publication Number 39 of the Internatioinal Association of Sedimentologists.

Samouelian, A., Cousin, I., Tabbagh, A., Bruand, A., and Richard, G. (2005). Electrical resistivity survey in soil science: a review. *Soil Tillage Research, 83*, 173–193.

Schaap, M.G., Leij, F.J., and van Genuchten, M.Th. (2001). Rosetta: a computer program for estimating soil hydraulic parameters with hierarchical pedotransfer functions. *Journal of Hydrology, 251*, 163–176.

Sen, P.N., Scala, C., and Cohen, M.H. (1981). A self-similar model for sedimentary rocks with application to the dielectric constant of fused glass beads. *Geophysics, 46*, 781–795.

Sen, P.N. (1984). Grain shape effects on dielectric and electrical properties of rocks. *Geophysics*, *49*, 586–587.

Seneviratne, S.I., Corti, T., Davin, E.L., Hirschi, M., Jaeger, E.B., Lehner, I., Orlowsky, B., and Teuling, A.J. (2010). Investigating soil moisture-climate interactions in a changing climate: a review. *Earth Science Reviews, 99,* 125–161, doi:10.1016/j.earscirev.1010.02.004.

Seyfried, M.S., and Murdock, M.D. (1996). Calibration of time domain reflectometry for measurements of liquid water in frozen soils. *Soil Science, 161,* 87–98.

Simunek, J., Sejna, M., and van Genuchten M.Th. (2008). Code for simulating the one-dimensional movement of water, heat, and multiple solutes in variably saturated porous media. (Computer software, version 4.08), PC-Progress, Prague, Czech Republic.

Simunek, J., Sejna, M., Saito, H., Sakai, M., and. van Genuchten M.Th (2009). The HYDRUS-1D software package for simulating the one-dimensional movement of water, heat, and multiple solutes in variably-saturated media, version 4.08. Department of Environmental Sciences, University of California Riverside, Riverside, California, USA.

Shah, P.M., Levin, F. K. (1973). Gross Properties of Time-Distance Curves. Geophysics, 38, 643–656.

Shanley, J.B., and Chalmers, A. (1999). The effect of frozen soil on snowmelt runoff at Sleepers River, Vermont. *Hydrological Processes, 13,* 1843–1857.

Sheets, K.R., and Hendrickx, J.M.H. (1995). Noninvasive soil-water content measurement using electromagnetic induction. *Water Resources Research, 31,* 2401–2409.

Sihvola, A.H. (2000). Mixing rules with complex dielectric coefficients. *Subsurface Sensing Technologies and Applications, 1,* 393–415.

Sihvola, A.H. (1999). *Electromagnetic Mixing Formulas and Applications*. IEEE Electromagnetic Waves Series 47. London (UK): The Institute of Electrical Engineers.

Smith, G.S. (1984). Directive properties of antennas for transmission into a material half-space. *IEEE Transactions on Antennas and Propagation, AP–32,* 232–246.

Stein, J., and Kane, D.L. (1983). Monitoring the unfrozen water content of soil and snow using time domain reflectometry. *Water Resources Research, 19,* 1573–1584.

Sperl, C. (1999). Determination of spatial and temporal variation of the soil water content in an agro-ecosystem with ground-penetrating radar. Ph.D. thesis, Technische Universität München, Munich.

Stein, J., and Kane, D.L. (1983). Monitoring the unfrozen water content of soil and snow using time domain reflectometry. *Water Resources Research, 19,* 1573–1584.

Steelman, C.M., and Endres, A.L. (2009). Evolution of high frequency ground penetrating radar direct ground wave propagation during thin frozen soil layer development. *Cold Regions Science and Technology, 57,* 116–122, doi:10.1016/j.coldregions.2009.01.07.

Steelman, C.M., and Endres, A.L. (2010). An examination of direct ground wave soil moisture monitoring over an annual cycle of soil conditions. *Water Resources Research, 46,* W11533, doi: 10.1029/2009WR008815.

Steelman, C.M., Endres, A.L. (2011). Comparison of petrophysical relationships for soil moisture estimation using GPR ground waves. *Vadose Zone Journal, 10,* 1–16, doi:10.2136/vzj2010.0040.

Steelman, C.M. and Endres, A.L. (in review). High-resolution GPR monitoring of soil moisture dynamics 1. field results and interpretation. Submitted to *Water Resources Research*, 16/09/2011, submission number: 2011WR011413.

Steelman, C.M., Jones, J.P., and Endres, A.L. (in review). High-resolution GPR monitoring of soil moisture dynamics 2. comparison with unsaturated flow model. Submitted to *Water Resources Research*, 16/09/2011, submission number: 2011WR011414.

Steelman, C.M., Endres, A.L., Assessing vertical soil moisture dynamics using multi-frequency GPR common-midpoint soundings. Submitted to *Journal of Hydrology* 7/10/2011 (accepted).

Steelman, C.M., Endres, A.L. and van der Kruk, J. (2010). Field observations of shallow freeze and thaw processes using high-frequency ground-penetrating radar. *Hydrological Processes*, *24*, 2022–2033, doi:10.1002/hyp.7688.

Stephens, D.B. (1996). *Vadose Zone Hydrology*. Boca Raton (FL): CRC Press.

Taner, M.T., Koehler, F. (1969). Velocity Spectra-Digital Computer Derivation and Application of Velocity Functions. *Geophysics*, *34*, 859–881.

Topp, G.C., Davis, J.L., and Annan, A.P. (1980). Electromagnetic determination of soil water content: measurements in coaxial transmission lines. *Water Resources Research*, *16*, 574–582.

Tillard, S., and Dubois, J-C. (1995). Analysis of GPR data: wave propagation velocity determination. *Journal of Applied Geophysics*, *33*, 77–91.

Turesson, A. (2006). Water content and porosity estimated from ground-penetrating radar and resistivity. *Journal of Applied Physics*, *58*, 99–111, doi: 10.1016/j.jappgeo.2005.04.004.

Tyč, S., Schwartz, L.M., Sen, P.N., and Wong, P. (1988). Geometrical models for the high-frequency dielectric properties of brine saturated sandstones. *Journal of Applied Physics*, *64*, 2575–2582.

van der Kruk, J., Arcone, S.A., and Liu, L. (2007). Fundamental and higher mode inversion of dispersed GPR waves propagating in ice layer. *IEEE Transactions on Geoscience and Remote Sensing*, *45*, 2483–2491.

van der Kruk, J., Jacob, R.W., and Vereecken, H. (2010). Properties of precipitation induced multi-layer surface waveguides derived from inversion of dispersive TE and TM data. *Geophysics*, *75*, WA263–WA273, doi:10.1190/1.3467444.

van der Kruk J., Steelman, C.M., Endres, A.L., and Vereecken, H. (2009). Dispersion inversion of electromagnetic pulse propagation within freezing and thawing soil waveguides. *Geophysical Research Letters*, *36*, L18503, doi: 10.1029/2009GL039581.

van der Kruk, J., Streich, R., and Green, A.G. (2006). Joint dispersion inversion of broadside and endfire CMP georadar data for properties of a thin-surface waveguide. *Geophysics*, *71*, K19–K29.

van Genuchten, M. Th. (1980). A closed-form equation for predicting the hydraulic conductivity of unsaturated soils. *Soil Science Society of America Journal*, *44*, 892–898.

van Overmeeren, R.A., Sariowan, S.V., and Gehrels, J.C. (1997). Ground penetrating radar for determining volumetric soil water content; results of comparative measurements at two sites. *Journal of Hydrology*, *197*, 316–338.

Vereecken, H., Huisman, J.A., Bogena, H., Vanderborght, J., Vrugt, J.A, and Hopmans, J.W. (2008). On the value of soil moisture measurements in vadose zone hydrology: a review. *Water Resources Research*, *44*, W00D06, doi: 10.1029/2008WR006829.

Wagner, W., Blöschl, G., Pampaloni, P., Calvet, J-C., Bizzarri, B., Wigneron, J-P., and Kerr, Y. (2007). Operational readiness of microwave remote sensing of soil moisture for hydrologic applications. *Nordic Hydrology*, *38*, doi: 10.2166/nh.2007.029.

Weiler, K.W., Steenhuis, T.S., J. Boll, and Kung, K.-J.S. (1998). Comparison of ground penetrating radar and time domain reflectometry as soil water sensors. *Soil Science Society of America Journal*, *62*, 1237–1239.

Wesseling, J.G., Elbers, J.A., Kabat, P., and van den Broek, B. J. (1991). SWATRE: instructions for input. Internal Note, Winand Staring Centre, Wageningen, Netherlands.

Wharton, R.P., Hazen, G.A., Rau, R.N., and Best, D.L. (1980). Electromagnetic propagation logging: advances in technique and interpretation. SPE Paper 9267.

Weast, R.C., Astle, M.J., and Beyer, W.H. (Ed.). (1985). *CRC Handbook of Chemistry and Physics.* (66^{th} ed.). Boca Raton (FL): CRC Press.

Weihermüller L., Huisman, J.A., Lambot, S., Herbst, M., and Vereecken, H. (2007). Mapping the spatial variation of soil water content at the field scale with different ground penetrating radar techniques. *Journal of Hydrol*ogy, *340*, 205–216, doi:10.1016/j.jhydrol.2007.04.013.

Wijewardana, Y.G.N.S., and Galagedara, L.W. (2010). Estimation of spatio-temporal variability of soil water content in agricultural fields with ground penetrating radar. *Journal of Hydrology, 391*, 24–33, doi:10.1016/j.jhydrol.2010.06.036.

Wollschläger, U., and Roth, K. (2005). Estimation of temporal changes of volumetric soil water content from ground-penetrating radar reflections. *Subsurface Sensing Technologies and Applications, 6*, 207–218, doi:10.1007/s11220-005-0007-y.

Wollschläeger U., Gerhards, H., Yu, Q., and Roth, K. (2008). Application of multi-channel ground-penetrating radar to determine thaw depth and moisture content of the active layer. *Eos Transaction of the AGU*, 89(53), Fall Meeting Supplemental Abstract C31E-0545.

Wollschläger, U., Pfaff, T., and Roth, K. (2009). Field-scale apparent hydraulic parameterization obtained from TDR time series and inverse modeling. *Hydrology and Earth Systems Science, 13*, 1953–1966.

Woodward, J., and Burke, M.J. (2007). Applications of ground-penetrating radar to glacial and frozen materials. *Journal of Environmental Engineering and Geophysics*, *12*, 69 – 85.

Wraith, J.A., Robinson, D.A., Jones, S.B., and Long, D.S. (2005). Spatially characterizing apparent electrical conductivity and water content of surface soils with time domain reflectometry. *Computers and Electronics in Agriculture, 46*, 239–261.

Yilmaz O. (2001). *Seismic Data Analysis: Processing, Inversion, and Interpretation of Seismic Data*. (Volume 1). Tulsa (OK): Society of Exploration Geophysicists.

Appendix A
Detailed Field Site Characterization

A.1 Field Study Description and Area Overview

Seasonal soil moisture conditions were monitored at three field sites near Woodstock (silt loam: 519845E, 4770361N) and Waterloo (sand: 528878E, 4814702N; sandy loam: 528938E, 4814594N), Ontario, Canada. Weather conditions in this region are representative of a mid-latitude temperate climate consisting of frozen soil conditions during the months of December–March and unfrozen soil conditions for the remainder of the year. Figure A.1 shows the average air temperature and cumulative precipitation for each month (i.e., 1971–2000) for the regions of Woodstock (Figure A.1a) and Waterloo-Wellington (Figure A.1b) (Environment Canada, 2008).

The soil moisture monitoring project was initiated in late-May 2006 within a localized valley portion of a field located 2 km south of Woodstock, Ontario. This study site is situated north of the Thornton Well Field which supplies drinking water to the City of Woodstock (Figure A.2). Recent hydrological investigations of this area have been conducted in response to rising nitrate groundwater concentrations in the municipal supply wells (Padusenko, 2001; Haslauer, 2005; Bekeris, 2007). Two additional soil moisture monitoring stations, separated ~125 m laterally and ~7 m vertically, were added in late-August 2006 in a field located 7 km west of Waterloo, Ontario (Figure A.3). This study area is situated over the Waterloo Moraine; these stratified moraine deposits contain the majority of the region's groundwater resources.

The three soil moisture monitoring stations consisted of a single 2.0 m profile that was periodically surveyed using a high-frequency ground-penetrating radar (GPR) system for the duration of the study period. These sites represent active agricultural fields used for hay production; the fields were not tilled during or in the recent past (2–5 years) prior to this study. The sites were chosen based on their varying soil textural properties (i.e., sand, sandy loam and silt loam surficial soil textures) and general site accessibility.

A.2 Field Site Characterization

A.2.1 Woodstock Site – Silt Loam

The quaternary geology has been described as an interlobate zone formed during the invasion of several distinct ice lobes which produced lithologicaly similar tills. Locally, the surficial Quaternary geology is dominated by the Zorra Till, a stiff, stoney silt till underlain by older Catfish Creek Till. Glaciofluvial outwash sand and gravel deposits also occupy this area (Cowan, 1975). The soil moisture monitoring profile is situated within a topographic low characterized by silt loam surficial soil. This area of the field also acts as a local drainage basin for overland flow during the spring melt season.

Field-scale electrical resistivity imaging and GPR reflection profiles were conducted across the field site to characterize the geological and hydrogeological conditions. Geophysical survey lines are shown in Figure A.4 and include five resistivity (lines 1–5) and three GPR (lines 1, 3 and 4) profiles. The resistivity and GPR data are shown in Figure A.5 and A.6, respectively. A core log collected in close proximity to the soil moisture monitoring station (see Figure A.4) reveled stratified sequences of sand and gravel units between 1.75–13.5 m below ground surface (mbgs); finer grained silt loam occupied the upper 0.5 m which graded into silty gravel and gravelly silt units to a depth of 1.75 m. The core was terminated at 13.75 m after penetrating a silty clay unit. An adjacent monitoring well indicated seasonal water table variations between 2.5 and 3.0 m below ground surface during the study period.

The resistivity profiles in Figure A.5 are characterized by a distinct laterally continuous low resistivity zone (blue) between 280–295 m above sea level (masl). This zone appears to be consistent with the sand and gravel units characterized in the core log and likely represents the upper most aquifer in the area. The overlying higher resistivity zones (red) appear to be more discontinuous across the profiles; these red zones likely correspond to unsaturated sand and gravel units while blue/green zones indicate transitions into finer textured silty soils (e.g., line 2). However, further field investigations would be needed to validate this hypothesis. GPR profiling using 100 MHz antennas (Figure A.6) along lines 1, 3 and 4 revealed the presence of a horizontal reflection event interpreted to represent the top of the capillary fringe (i.e., water table) at an approximate elevation of 298.5 masl (~2.5 mbgs) at the intersection of lines 3 and 4. While the GPR depth of penetration was limited to the upper 8 m, these data did show significantly higher reflectivity in the unsaturated zone and was

characterized by numerous reflection events. The water table reflection diminished significantly with increasing surficial elevation. This unsaturated/saturated interface delineated by the GPR is also consistent with the resistivity data.

A.2.1 Waterloo Site – Sand and Sandy Loam

The Waterloo Moraine is described as "an irregular tract of sand hills located centrally in the interlake peninsula of southwestern Ontario. It sits astride the interlobate zone between the Lake Ontario ice lobe from the east and the Huron-Georgian Bay ice lobe from the west and northwest… The bulk of the sand is associated with the overlying Maryhill Till (Port Bruce Stade), so the moraine was formed late in the history of glaciation. Late readvances deposited Maryhill Till from the east and Tavistock Till from the northwest as a patchy till cap on the moraine, much dissected by meltwaters during ice retreat" (Karrow and Paloschi, 1996). The field site is situated on the northwestern extent of the Waterloo Moraine over ice-contact stratified sand deposits (Bajc and Shirota, 2007). The local water table is inferred to be approximately 15–20 m below ground surface based on local water bodies.

Field-scale electrical resistivity imaging and GPR reflection profiles using 100 MHz antenna were collected across the Waterloo field site to better describe the geologic and hydrologic relationship between the two soil moisture monitoring locations. The locations of these geophysical surveys are shown in Figure A.7, and included 5 concurrently collected resistivity and GPR profiles. To facilitate geophysical interpretation these data sets have been superimposed in Figure A.8. Shallow core logs and pitting in the immediate vicinity of the two monitoring stations indicates that the field is dominated by glacial sand deposit with increasing fine fraction in the topographically low areas. For instance, topographically high areas were characterized by greater GPR investigation depths and higher resistivity values. The higher resistivity (red) zones delineate unsaturated sand dominated zones while lower resistivity (blue-green) zones highlight finer grained material with higher water content.

The north and north-western portions of the field are clearly composed of clean well-drained sand reaching thicknesses of 12 m. The sand site is situated atop the thickest portion of sand in this area of the field. In comparison, the south-eastern reaches of the field are characterized by a significant reduction in resistivity with increasing depth, particularly where the GPR signal is completely attenuated; this indicates a transition into finer grained material. Another notable feature in this data is the presence of an isolated low resistivity zone with concave reflection events between 45 and 87 m

on line 4. While this zone may represent an isolated perched water table, the local water table remains well below the two monitoring sites.

A.3 Tables and Figures

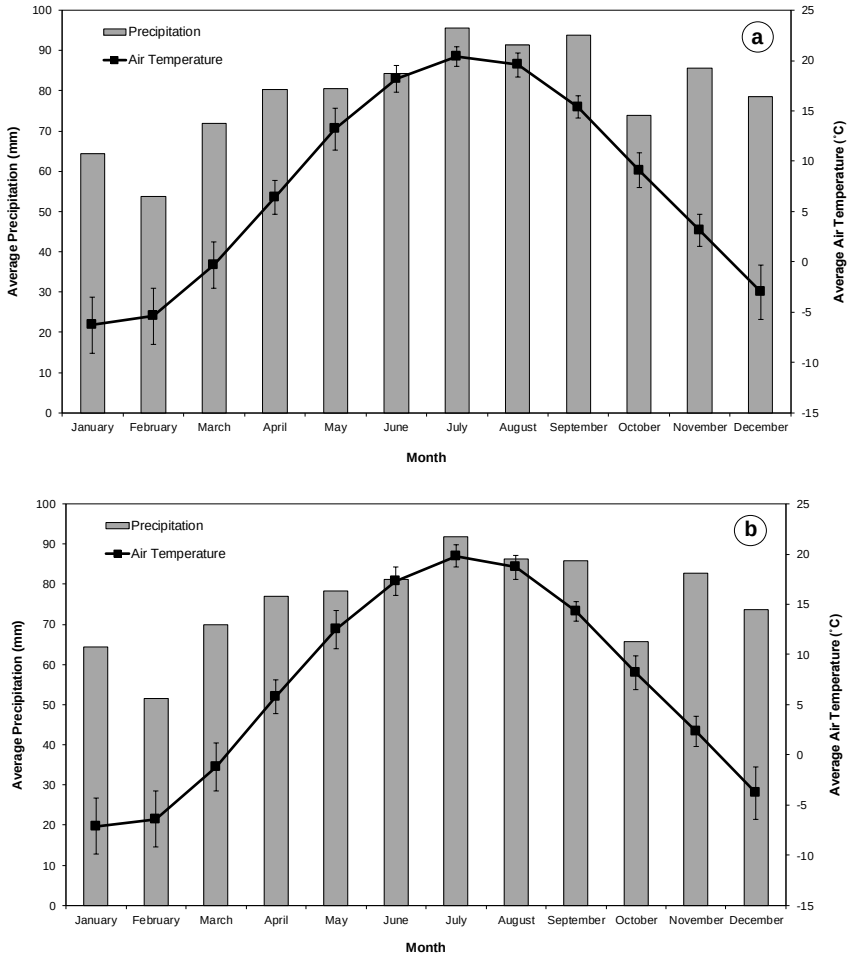

Figure A.1 Average precipitation and air temperature data (1971–2000) for (a) Woodstock and (b) Waterloo–Wellington regions (Environment Canada, 2008).

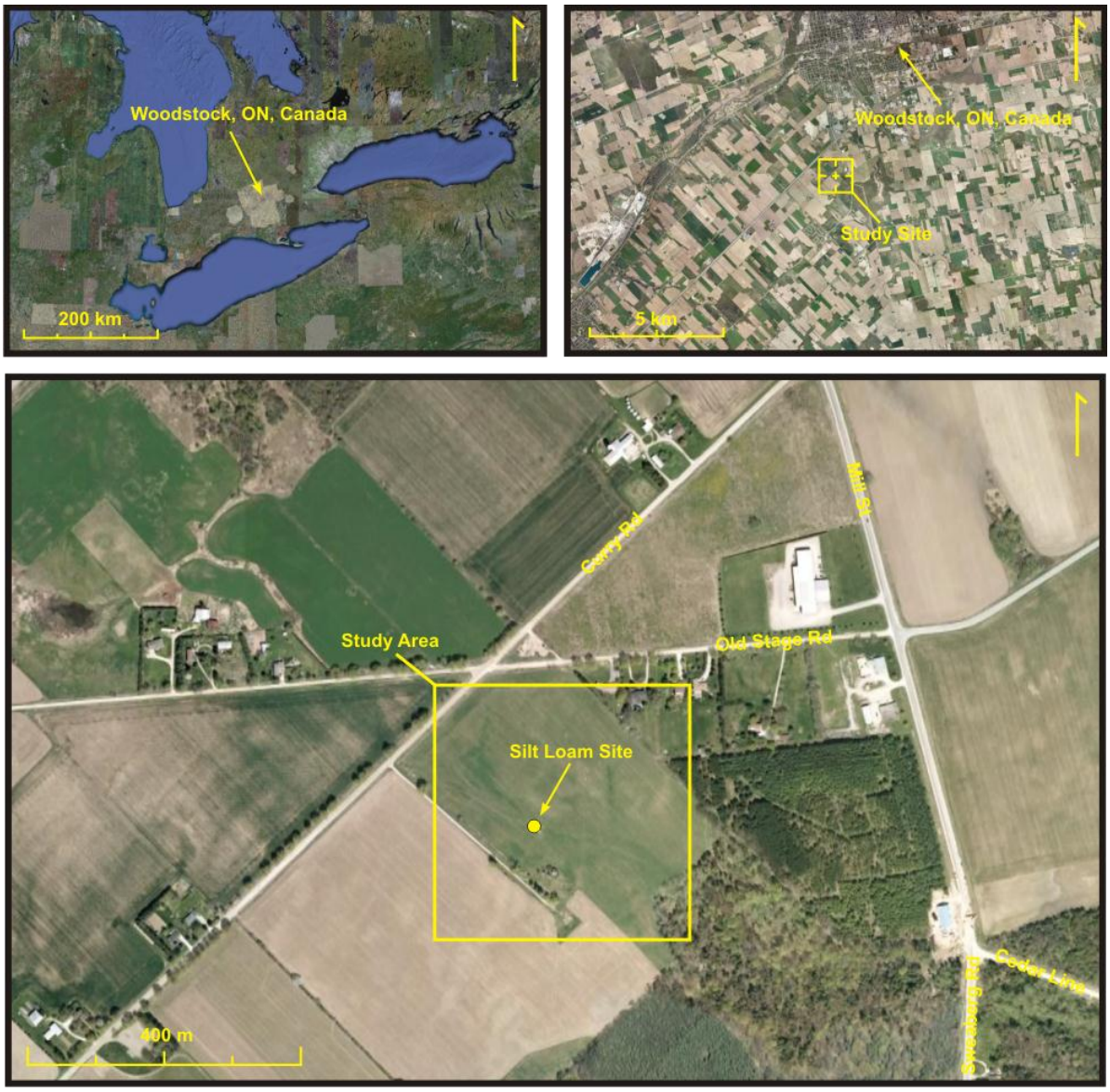

Figure A.2 Regional map of Woodstock silt loam soil moisture monitoring station.

Figure A.3 Regional map of Waterloo sand and sandy loam soil moisture monitoring stations.

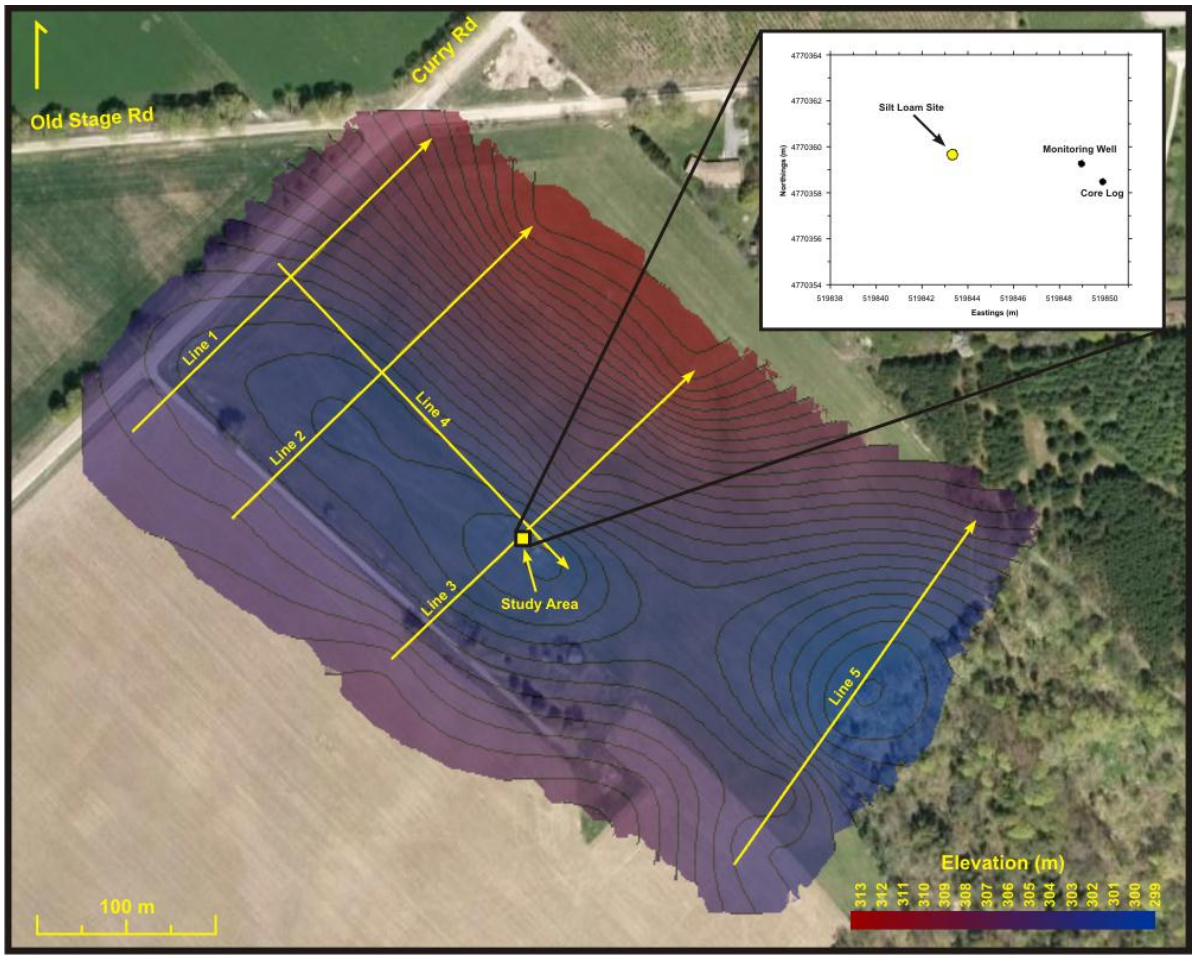

Figure A.4 Site map showing local topography around silt loam soil moisture monitoring area and locations of field-scale geophysical survey lines (GPR profiles and electrical resistivity imaging transects) used for site characterization.

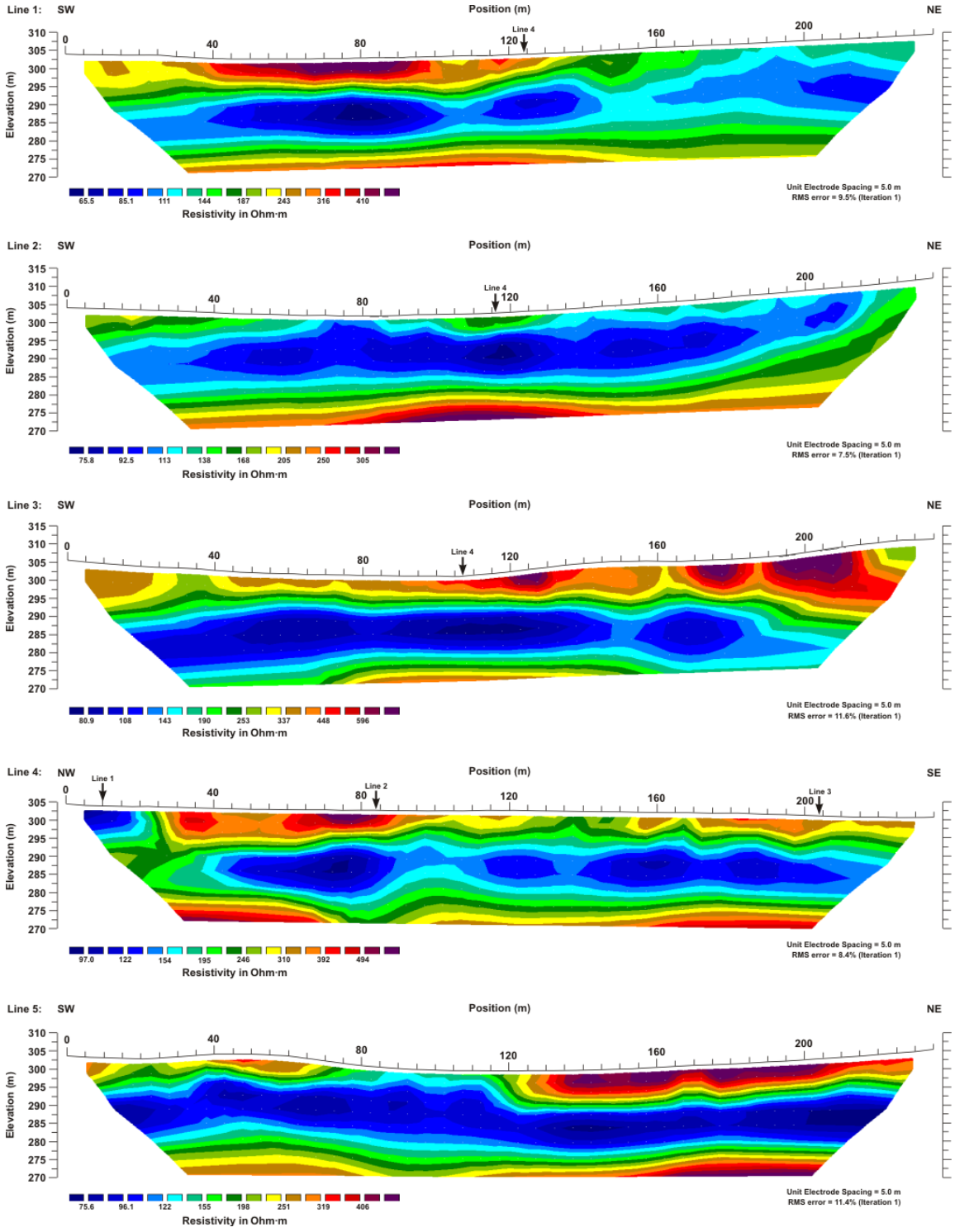

Figure A.5 Electrical resistivity imaging surveys (Wenner array) collected over the Woodstock site

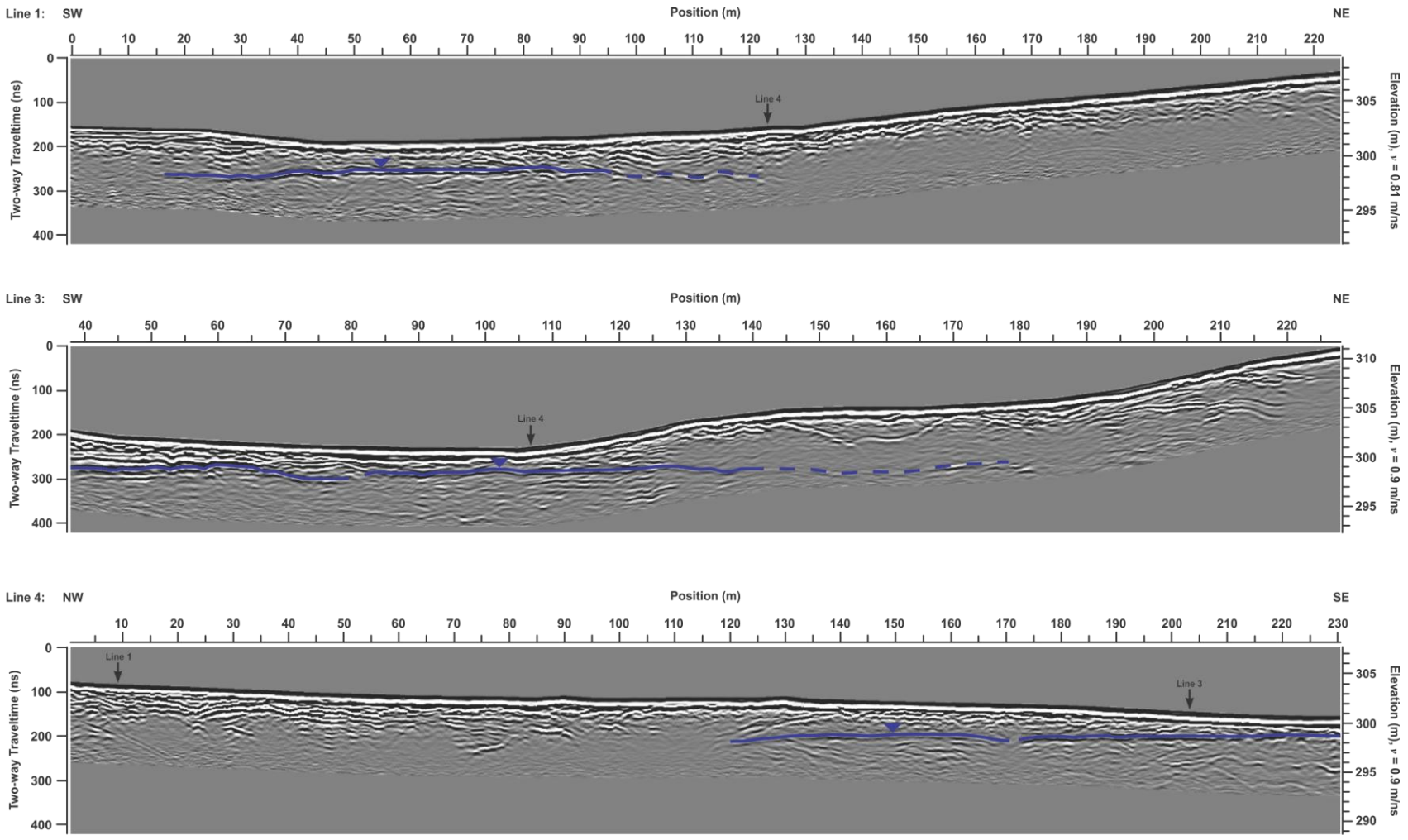

Figure A.6 GPR reflection profiles corresponding to lines 1, 3, and 4 showing local stratigraphy and water table position.

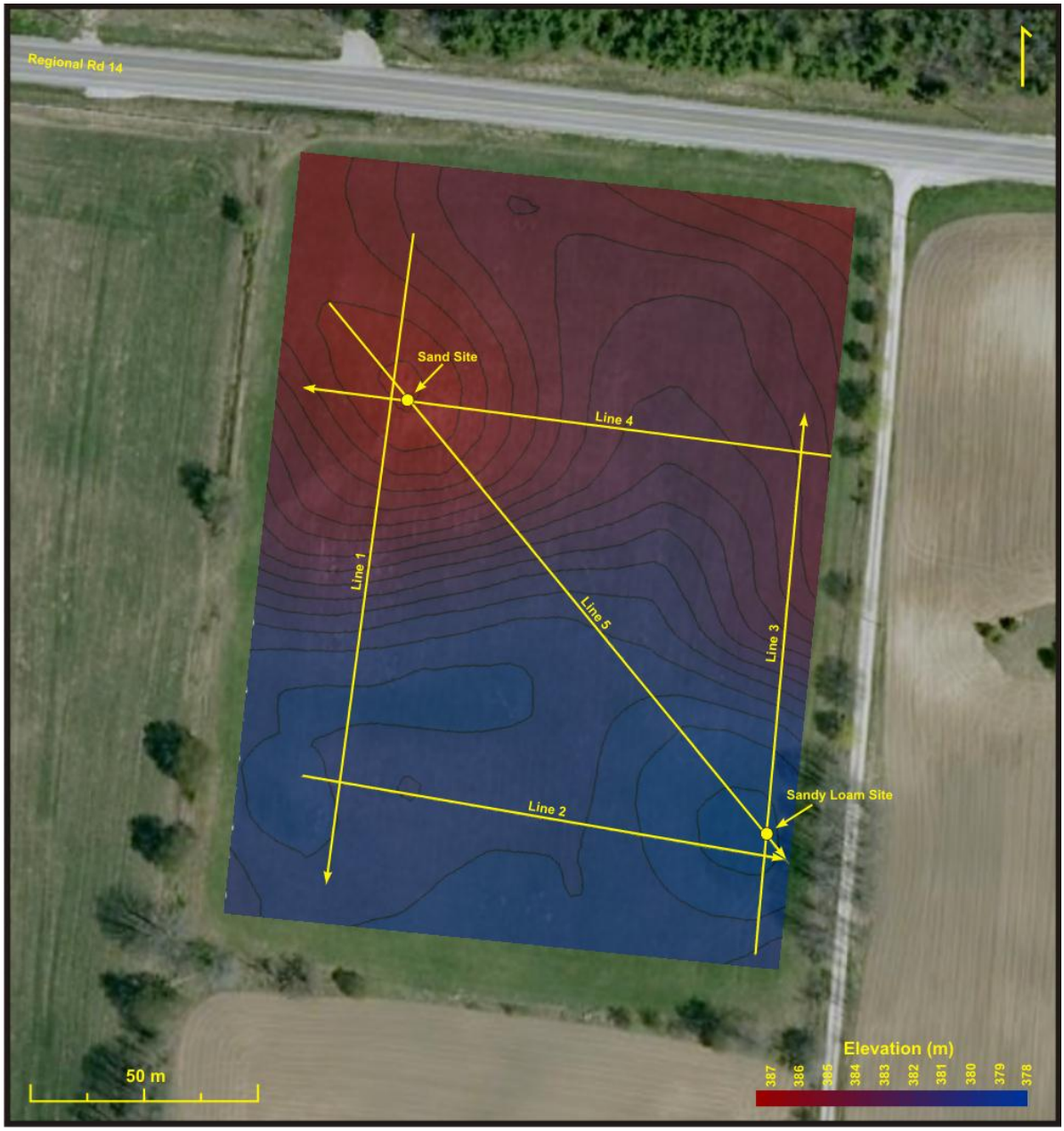

Figure A.7 Site map showing local topography around soil moisture monitoring sites and locations of field-scale geophysical survey lines (GPR profiles and electrical resistivity imaging transects) used for site characterization.

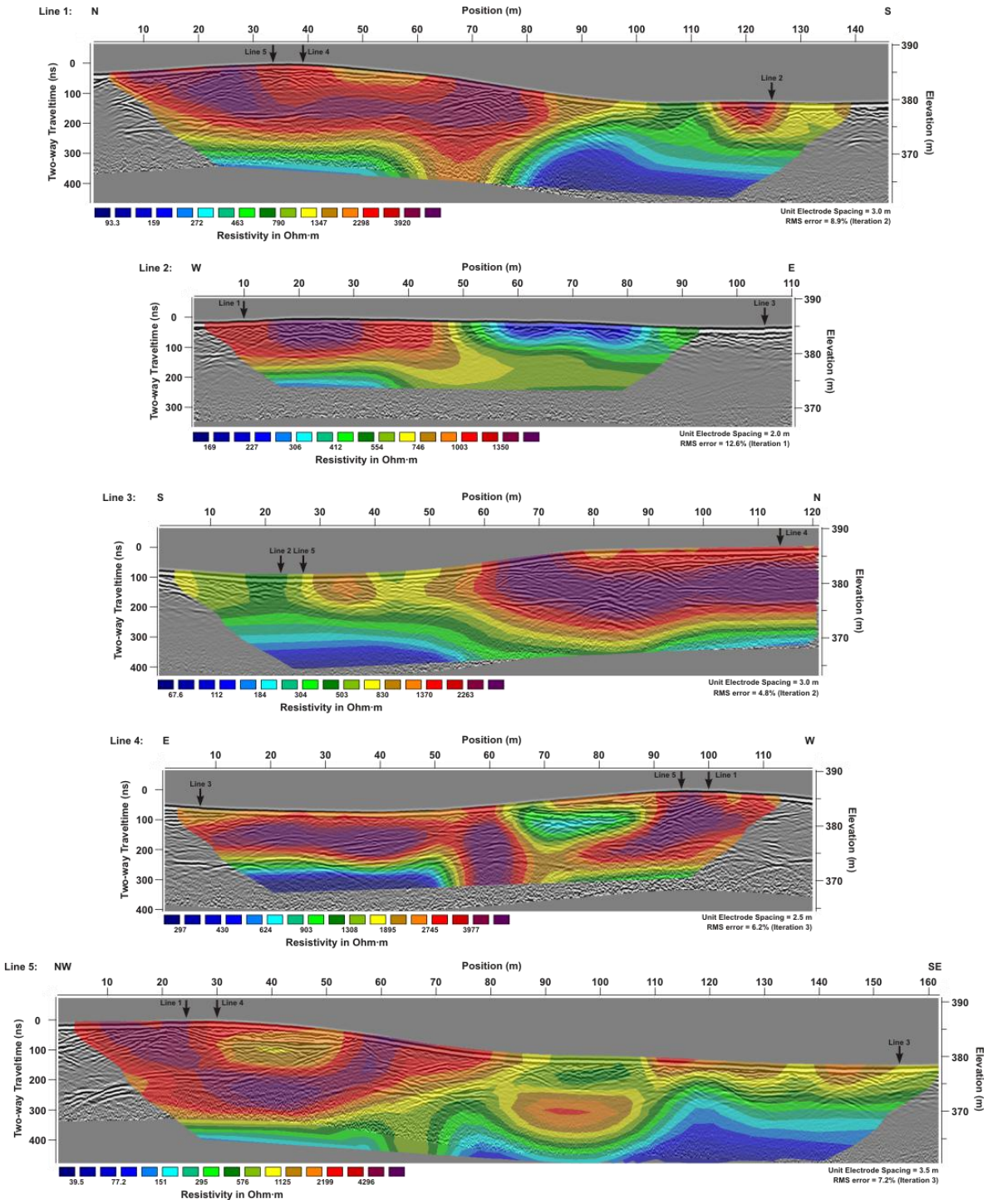

Figure A.8 Field-scale GPR profiles using 100 MHz antennas and electrical resistivity imaging (Wenner array) collected at the Waterloo site.

References

Bajc, A.F., and Shirota, J. (2007). Three-dimensional mapping of surficial deposits in the Regional Municipality of Waterloo, southwestern Ontario. Ontario Geological Survey, Groundwater Resources Study 3, 41p.

Bekeris, L. (2007). Field-scale evaluation of enhanced agricultural management practices using a novel unsaturated zone nitrate mass load approach. M.Sc. thesis, University of Waterloo, Department of Earth Sciences.

Haslauer, C.P. (2005). Hydrogeologic Analysis of a Complex Aquifer System and Impacts of Changes in Agricultural Practices on Nitrate Concentrations in a Municipal Well Field: Woodstock, Ontario. M.Sc. thesis, University of Waterloo, Department of Earth Sciences.

Padusenko, G.R. (2001). Regional hydraulic evaluation of a complex glacial aquifer system in an agricultural landscape: Implications for nitrate distribution. M.Sc. thesis, University of Waterloo, Department of Earth Sciences.

Cowan, W.R. (1975). Quaternary geology of the Woodstock area, Southern Ontario. Ontario. Ministry of Natural Resources, Division of Mines.

Environment Canada (2008). National Climate Data and Information Archive. 2010–09–02, http://www.climate.weatheroffice.ec.gc.ca/climate_normals/index_e.html (accessed on January 6, 2010).

Karrow, P.F., and Paloschi, G.V.R. (1996). The Waterloo kame moraine revisited: new light on the origin of some Great Lake region interlobate moraines. *Zeitschrift fuer Geomorphologie*, *40*, 305–315.

Appendix B

Dispersion Inversion of Electromagnetic Pulse Propagation within Freezing and Thawing Soil Waveguides[8]

Abstract

Freeze and thaw processes are important components in characterizing glacial, periglacial and frozen ground environments, and hence the response of cryospheric regions to climate change. High-frequency ground-penetrating radar is particularly well suited for monitoring the freezing and thawing processes within the shallow subsurface (i.e., < 1 m depth) due to its non-invasive nature and its sensitivity to the liquid water component in soil. The freezing of moist soil and thawing of frozen soil induce leaky and low-velocity waveguides, respectively. Within these waveguide layers, the internally reflected radar energy produces interfering multiples that appear as a package of dispersed waves. Here, we present a new method for characterizing very shallow freeze and thaw processes, in which the waveguide properties are obtained by inverting the observed dispersion curves. This new method can non-invasively monitor freezing and thawing processes in a wide range of glacial, periglacial and frozen ground studies.

B.1 Introduction

The freezing and thawing of near-surface material are important processes in cryospheric environments. The depth and distribution of frozen zones not only influence the dynamics of soil water distribution, but also have significant implications for modelling a wide-range of atmospheric and subsurface processes. We propose that high frequency (>250 MHz) ground-penetrating radar (GPR) is particularly well suited for monitoring the freezing and thawing process within the shallow subsurface because of its non-invasive nature and ability to obtain a measure of the liquid water component in frozen soil.

[8] van der Kruk, J., Steelman, C.M., Endres, A.L., and Vereecken, H. (2009). Dispersion inversion of electromagnetic pulse propagation within freezing and thawing soil waveguides. *Geophysical Research Letters*, *36*, L18503, doi:10.1029/2009GL039581, 2009.

GPR is often used to characterize glacial and permafrost environments (Woodward and Burke, 2007; Kneisel et al., 2008). While numerous studies have successfully used GPR to evaluate the spatial and temporal distribution of ground ice, depth to permafrost table and thickness of the active layer above the permafrost (e.g., Annan and Davis, 1978; Delany et al., 1990; Arcone et al., 1998; Hinkel et al., 2001; Moorman et al., 2003; De Pascale et al., 2008), only recently has high-frequency GPR been used to monitor seasonal frost development in mid-latitude climates (Steelman and Endres, 2009).

The permittivity of ice and water are approximately $3e_0$ and $80e_0$, respectively, where e_0 is the permittivity of free space. Due to this large contrast, the permittivity of wet soils can change dramatically during the freezing and thawing process. Arcone et al. (1998) found that the dielectric permittivity decreased by a factor of 4 or more at the saturated sediment-permafrost boundary. Due to this strong contrast in electromagnetic properties, Moorman et al. (2003) was able to use GPR to image periglacial conditions, while Bradford et al. (2005) successfully measured the thaw depth beneath peat-lined arctic streams.

When the thickness of the frozen sand overlying wet thawed sand or the thawed layer overlying the frozen sand is comparable to or smaller than the in situ wavelength of the electromagnetic (EM) waves emitted by the GPR system, the frozen or thawed sand layer act as a waveguide in which the EM energy is internally reflected; this results in a series of interfering multiples that manifest themselves as a package of dispersed waves which propagate large distances at phase and group velocities that may not correspond to material dielectric properties. These dispersed EM waves contain important information about the nature of the waveguide. However, standard travel-time techniques for estimating the velocity and thickness of the waveguide from a common-midpoint (CMP) measurement cannot be applied, because the different phases cannot be clearly identified.

The unfrozen soil underlying the shallow frozen layer will generate a strong reflection because it has a much higher relative permittivity. Total internal reflection only occurs at the upper interface beyond the critical angle. While the lower interface is a strong reflector, some energy is still transmitted across the interface; hence, it is a leaky waveguide (Figure B.1a). For the thawed layer case, the underlying frozen soil layer has a relatively lower permittivity, giving rise to a critical refraction. Here, the thawed layer has the lowest velocity and is called the low-velocity waveguide. Total internal reflection occurs at both interfaces when the angle of incidence is larger than the critical

angle of the lower interface (Figure B.1b). The freezing and thawing cycle in mid-latitude climates results in the presence of a leaky and a low-velocity waveguide at the same location over time.

For the leaky waveguide, Arcone (1984) investigated the electromagnetic properties of ice sheets overlying water. Given the average thickness of the waveguide, he determined the dielectric permittivities of the ice layer by assuming that the dominant frequencies of the dispersive coupled air-ice waves were accurate predictions of the waveguide cutoff frequencies. Recently, the derivation of dispersion curves from GPR data measured across ice sheets overlying water and their subsequent inversion have been described by van der Kruk et al. (2007). Procedures for inverting dispersion curves, which are analogous to techniques recently developed for analyzing surface waves recorded on multichannel seismic data, were derived for transverse-electric (TE) and transverse-magnetic (TM) GPR data. Liu and Arcone (2003) showed with finite-difference time-domain modeling that the TE mode emits more energy in the ground than the TM mode.

For the low-velocity waveguide, Arcone et al. (2003) studied the characteristics of EM waves traveling through a thin surface waveguide of low-velocity (high-permittivity) wet soil underlain by high-velocity (low-permittivity) dry sand and gravel. Given the average thickness of the waveguide, they were able to derive the relative permittivities of the two layers from the highly dispersed waveforms. Recently, the derivation of dispersion curves from GPR data and their subsequent inversion for subsurface-medium properties have been described by van der Kruk et al. (2006). Using these procedures, accurate model parameters were derived from synthetic and field data. To obtain meaningful models from GPR data characterized by discontinuous dispersed phases, a joint inversion of the TE and TM field data was necessary (van der Kruk et al., 2006). Including higher order modes in the inversion resulted in more accurate predictions of material physical properties (van der Kruk, 2006).

In this paper, we show that both the leaky and low velocity waveguides are induced by freezing moist sand and by thawing frozen sand, respectively. In both cases, the waveguide properties can be obtained by calculating phase velocity spectra, followed by determining the dispersion curves from the maxima in the spectra. We then invert the observed curves using a procedure based on single-layer subsurface models to obtain the physical properties of the thawed and frozen soils.

B.2 Dispersion Inversion

Dispersion is a typical feature of seismological data at all scales: Dispersed Rayleigh waves are commonly used to infer subsurface material properties. In shallow seismological studies, the dispersed Rayleigh waves recorded on multichannel data are first transformed from the time distance domain to the phase-velocity-frequency domain from which the optimum phase velocity versus frequency curve is determined. The derived dispersion curve is then inverted to obtain a layered subsurface model, which requires adjusting the model parameters until the difference between the observed dispersion curve and the theoretical dispersion curve for the model is minimized. In this way, shear-wave velocities (Xia et al., 1999; Park et al., 1999) can be determined. Recently, similar inversion techniques were applied to dispersive GPR data (van der Kruk, 2006; van der Kruk et al., 2006, 2007).

Here, we employ the method of Park et al. (1999) to calculate phase-velocity spectra of our GPR common midpoint (CMP) data. By selecting the maxima in the phase velocity spectra, we obtain dispersion curves that show phase velocity as a function of frequency. The medium properties are obtained by inverting these dispersion curves. Due to the strong nonlinear nature of the forward problem, we employ a combined global and local optimization algorithm. For a variety of starting models, we initiated a local minimization algorithm based on the simplex search method (Lagarias et al., 1998). For each starting model, a local minimum is obtained. The local minimum that produces the closest match between the model and observed dispersion curves is regarded as the global minimum. To avoid the possibility of obtaining a very low cost function when only a few frequencies are used in the inversion, we required that the theoretical dispersion curve match the observed dispersion curve over at least 90% of the frequency range. Because we approximate the reflection coefficient between the waveguide and the lower halfspace at -1 for the leaky waveguide, the inversion depends on e_1 and h (van der Kruk et al., 2007), whereas the inversion for the low-velocity waveguide depends on e_1, e_2 and h (van der Kruk et al., 2006).

B.3 Experimental Procedures

Common-midpoint gathers were collected during the 2007 and 2008 winter seasons at a test site near Waterloo, Ontario, Canada, using a Sensors and Software PulseEKKO 1000 GPR system (Sensors and Software Inc., Mississauga, ON, Canada) equipped with 900 MHz bistatic antennas. The GPR data were acquired with a spatial and temporal sampling of 0.02 m and 0.1 ns, respectively. Surveys

were conducted during the development of a seasonal frost layer and a period of seasonal thaw at a single measurement location characterized by well-sorted sandy soil. Since the freezing and thawing processes took place at very shallow depths, we used 900 MHz bistatic antennas. For larger depths, lower frequency antennas should be used.

B.3.1 Leaky Waveguide

Figure B.2a shows the GPR data measured across the leaky waveguide case of frozen sand overlying wet sand. Although many multiple reflections are apparent, it is not possible to uniquely identify each one. In contrast, the corresponding phase-velocity spectrum in Figure B.2b clearly shows the presence of 4 TE modes. The maximum amplitude is normalized to unity for each frequency. The picked dispersion curves (yellow lines in Figure B.2b) describe the loci of maximum amplitudes and hence are the solutions for the phase velocities. The high phase-velocity values close to that of air indicate a leaky waveguide, because leaky waveguide dispersion curves always have values between that of air and the material within the waveguide (van der Kruk et al., 2007). After analyzing the frequency separation between the dispersion curves and using the formula for the cut-off frequency (van der Kruk et al., 2007), we identified these phases as the TE_3, TE_5, TE_7, and TE^9 modes. Combining higher order modes better constrains the inversion in comparison to the separate inversion of each mode (van der Kruk, 2006). Therefore, we performed a joint TE_3-TE_5-TE_7-TE_9 inversion of the observed dispersion curves shown in Figures B.2a and B.2b. For each suite of inversions, we used 9 different starting models with all combinations of e_1 = 4, 12, and 20 and h = 0.05, 0.175, and 0.3 m. The optimal model parameters for the TE_3-TE_5-TE_7-TE_9 inversion are e_1 = 6.1 and h = 0.40 m. Several local minima had these or similar values indicating that this inversion is well constrained. The black dashed lines in Figure 2b show the model dispersion curves obtained from the TE_3-TE_5-TE_7-TE_9 inversion, which fit the four modes reasonably well, with slightly larger deviations at lower and higher frequencies. Because the effective frequency spectrum had a maximum around 800 MHz, the fit of the TE_7 mode is judged to be more important than the fit of the TE_3, TE_5 and TE_9 modes.

B.3.2 Low-Velocity Waveguide

Figures B.3a and B.3b show the broadside (TE) and endfire (TM) data, respectively, measured over thawing of the shallow part of the frozen ground. Both data sets clearly show shingling, which indicates significant dispersion. This dispersion is more evident in the corresponding phase velocity spectra (Figures B.3c and B.3d). Here, we could only identify the fundamental modes, which we

obtained by picking the maxima in the phase-velocity spectra. Since joint inversions of the complementary TE and TM data provide results that are more reliable than those provided by the separate TE or TM inversions (van der Kruk et al., 2006), we performed a joint TE_0-TM_0 inversion of the observed dispersion curves (yellow lines displayed in Figures B.3c and B.3d). Different local minima were obtained for 27 starting models (all combinations of e_1 = 10, 15, and 20, e_2 = 3, 6, and 9 and h = 0.05, 0.25 and 0.5 m). The optimal value of model parameters for the TE_0-TM_0 inversion are e_1 = 15.7, e_2 = 7.0 and h = 0.15 m. Again, several local minima had these or similar medium properties, indicating that this inversion is well constrained. We have plotted the computed TE_0 and TM_0 dispersion curves for the models on the TE and TM phase-velocity spectra of Figures B.3c and B.3d (black dashed lines); they show a reasonably good fit with the observed dispersion curves.

B.4 Conclusions

Both the leaky and low-velocity waveguides are induced by seasonally frozen sand overlying wet sand and thawed sand overlying frozen sand, respectively. In both cases, the waveguide properties (layer dielectric permittivity and thickness) can be obtained by calculating phase-velocity spectra, followed by determining dispersion curves. For the leaky waveguide of frozen sand overlying wet sand, we identified and used 4 higher-order TE modes to invert for waveguide properties. The low-velocity waveguide, caused by thawing of the shallow part of the frozen soil, showed clear dispersion of the fundamental TE and TM modes; a joint inversion was used to obtain the waveguide properties. Here, we used 900 MHz antennas to investigate the freezing and thawing processes at very shallow depths. Larger depths can be investigated as long as the waveguide thickness is comparable to the in situ wavelength. This new method of characterizing near-surface freeze and thaw processes can be extended to a wide-range of glacial, periglacial and frozen ground studies, thereby improving our ability to monitor the effects of climate change in these sensitive environments.

B.4 Tables and Figures

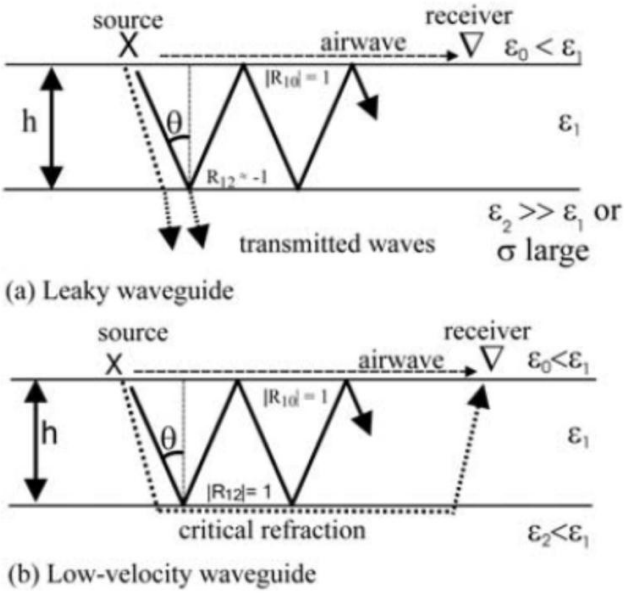

Figure B.1 Diagram of the (a) leaky and (b) low-velocity waveguides. Arrows show dominant ray paths of the EM waves.

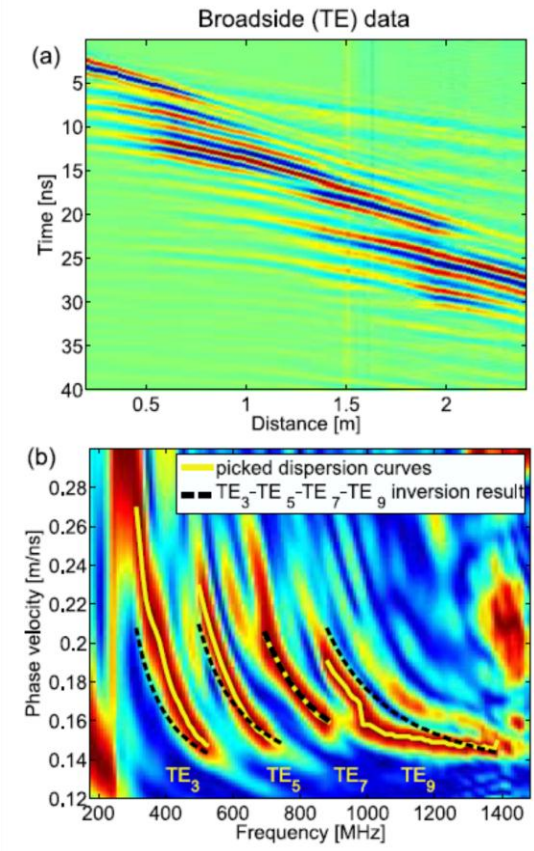

Figure B.2 (a) Measured broadside leaky waveguide data set clearly showing the many multiples traveling within the frozen ground layer. (b) Corresponding phase-velocity spectrum. The yellow lines are the observed dispersion curves used for the inversion. The dashed black lines show the dispersion curves for the model obtained from the TE_3-TE_5-TE_7-TE_9 inversion result.

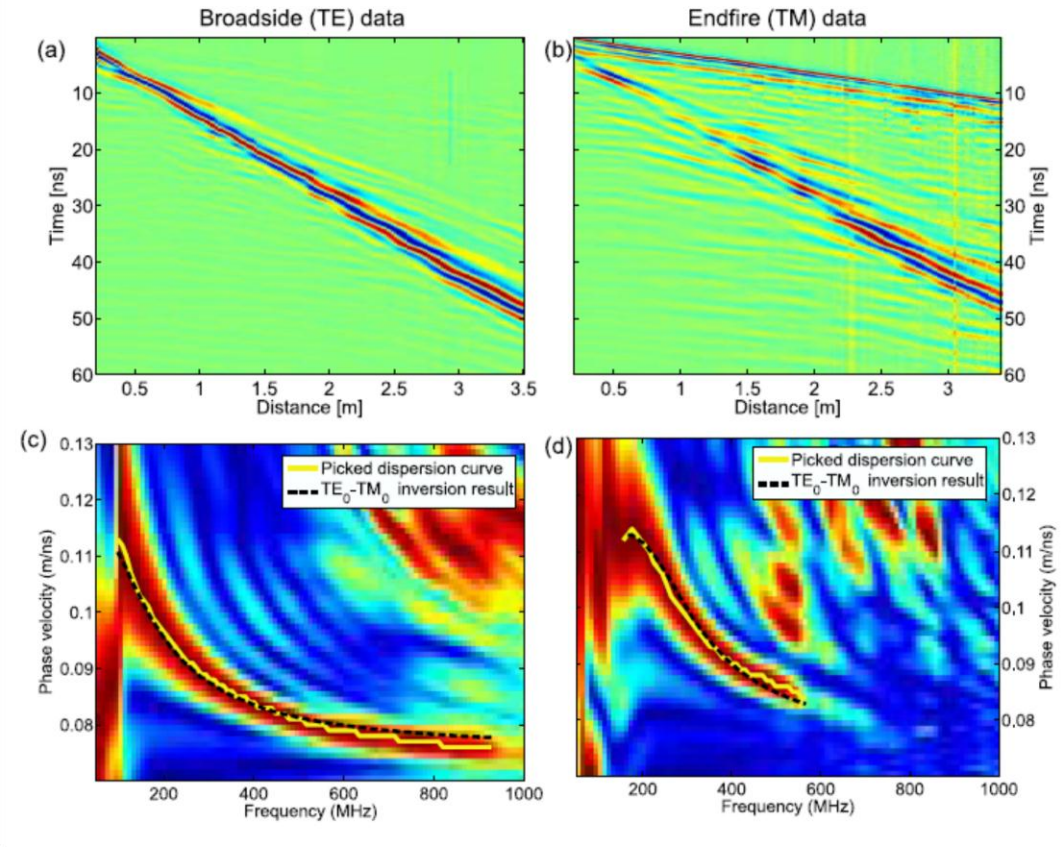

Figure B.3 Measured (a) broadside and (b) endfire low-velocity waveguide data sets clearly showing dispersion, and (c and d) corresponding phase-velocity spectra, respectively. The yellow line is the observed dispersion curve used for the inversion. The dashed black lines represent the dispersion curve for the model obtained from the TE_0-TM_0 inversion result.

References

Annan, A.P., and Davis, J.L. (1978). High frequency electrical methods for the detection of freeze-thaw interfaces. In *Proceedings of the Third International Conference on Permafrost*, pp. 495–500, National Research Council of Canada, Ottawa, Canada.

Arcone, S.A. (1984). Field observations of electromagnetic pulse propagation in dielectric slabs. *Geophysics, 40,* 285–298.

Arcone, S.A., Lawson, D.E., Delaney, A.J., and Strasser, J.D. (1998). Ground-penetrating radar reflection profiling of groundwater and bedrock in an area of discontinuous permafrost. *Geophysics, 63,* 1573–1584.

Arcone, S.A., Peapples, P.R., and Liu, L. (2003). Propagation of a ground penetrating radar (GPR) pulse in a thin-surface waveguide. *Geophysics, 68,* 1922–1933.

Bradford, J.H., McNamara, J.P., Bowden, W., and Gooseff, M.N. (2005). Measuring thaw depth beneath peat-lined arctic streams using ground penetrating radar. *Hydrological Processes, 19,* 2689– 2699.

Delaney, A.J., Arcone, S.A., and Chacho Jr. E.F. (1990). Winter shortpulse studies on the Tanana River, Alaska. *Arctic, 43,* 244–250.

De Pascale, G.P., Pollard, W.H., and Williams, K.K. (2008). Geophysical mapping of ground ice using a combination of capacitive coupled resistivity and ground-penetrating radar, Northwest Territories, Canada. *Journal of Geophysical Research, 113,* F02S90, doi:10.1029/2006JF000585.

Hinkel, K.M., Doolittle, J.A., Bockheim, J.G., Nelson, F.E., Paetzold, R., Kimble, J.M., and Travis, R. (2001). Detection of subsurface permafrost features with ground-penetrating radar, Barrow, Alaska. *Permafrost Periglacial Processes, 12,* 179–190.

Kneisel, C., Hauck, C., Fortier, R., and Moorman, B. (2008). Advances in geophysical methods for permafrost investigations. *Permafrost Periglacial Processes, 19,* 157–178.

Lagarias, J.C., Reeds, J.A., Wright, M.H., and Wright, P.E. (1998). Convergence properties of the Nelder-Mead simplex method in low dimensions. *Society for Industrial and Applied Mathematics, 9,* 800–808.

Liu, L., and Arcone, S.A. (2003). Numerical simulation of the wave-guide effect of the near-surface thin layer on radar wave propagation. *Journal of Environmental Engineering and Geophysics, 8,* 133–141.

Moorman, B.J., Robinson, S.D., and Burgess, M.M. (2003). Imaging periglacial conditions with ground-penetrating radar. *Permafrost and Periglacial Processes, 14,* 319–329.

Park, C.B., Miller, R.D., and Xia, J. (1999). Multichannel analysis of surface waves. *Geophysics*, *64*, 800–808.

Steelman, C.M., and Endres, A.L. (2009). Evolution of high-frequency ground-penetrating radar direct ground wave propagation during thin frozen soil layer development, *Cold Regions Science and Technology*, *57*, 116–122.

van der Kruk, J. (2006), Properties of surface waveguides derived from inversion of fundamental and higher mode dispersive GPR data, *IEEE Trans. Geosci. Remote Sens.*, *44*, 2908–2915.

van der Kruk, J., Streich, R., and Green, A.G. (2006). Properties of surface waveguides derived from separate and joint inversion of dispersive TE and TM GPR data. *Geophysics*, *71*, K19–K29.

van der Kruk, J., Arcone, S.A., and Liu, L. (2007). Fundamental and higher mode inversion of dispersed GPR waves propagating in an ice layer. *IEEE Transactions on Geoscience and Remote Sensing*, *45*, 2483–2491.

Woodward, J., and Burke M.J. (2007). Applications of ground-penetrating radar to glacial and frozen materials. *Journal of Environmental and Engineering Geophysics*, *12*, 69–85.

Xia, J., Miller, R.D., and Park, C.B. (1999). Estimation of near-surface shear-wave velocity by inversion of Rayleigh waves. *Geophysics*, *64*, 691–700.

Appendix C
Data CD

The material contained on this CD includes all field and laboratory data (original and processed) and is available from the Department of Earth and Environmental Sciences, upon request.